

Special Issue Reprint

Synthesis and Applications of Copper-Based Catalysts

Edited by
Yongjun Ji, Liwen Xing and Ke Wu

mdpi.com/journal/catalysts

Synthesis and Applications of Copper-Based Catalysts

Synthesis and Applications of Copper-Based Catalysts

Editors

Yongjun Ji
Liwen Xing
Ke Wu



Basel • Beijing • Wuhan • Barcelona • Belgrade • Novi Sad • Cluj • Manchester

Editors

Yongjun Ji
School of Light Industry
Beijing Technology and
Business University
Beijing
China

Liwen Xing
College of Chemistry and
Materials Engineering
Beijing Technology and
Business University
Beijing
China

Ke Wu
College of Chemistry and
Materials Engineering
Beijing Technology and
Business University
Beijing
China

Editorial Office

MDPI
St. Alban-Anlage 66
4052 Basel, Switzerland

This is a reprint of articles from the Special Issue published online in the open access journal *Catalysts* (ISSN 2073-4344) (available at: www.mdpi.com/journal/catalysts/special_issues/copper_catalysts).

For citation purposes, cite each article independently as indicated on the article page online and as indicated below:

Lastname, A.A.; Lastname, B.B. Article Title. <i>Journal Name</i> Year , Volume Number, Page Range.
--

ISBN 978-3-0365-9043-1 (Hbk)

ISBN 978-3-0365-9042-4 (PDF)

doi.org/10.3390/books978-3-0365-9042-4

© 2023 by the authors. Articles in this book are Open Access and distributed under the Creative Commons Attribution (CC BY) license. The book as a whole is distributed by MDPI under the terms and conditions of the Creative Commons Attribution-NonCommercial-NoDerivs (CC BY-NC-ND) license.

Contents

About the Editors	vii
Preface	ix
Ke Wu, Liwen Xing and Yongjun Ji Synthesis and Applications of Copper-Based Catalysts Reprinted from: <i>Catalysts</i> 2023 , <i>13</i> , 973, doi:10.3390/catal13060973	1
Chunyang Duan, Xiaojie Li, Yongjun Ji, Liuyang He, Jianhua Qian and Zenghua Zhao In-Situ Catalytic Preparation of Two-Dimensional BCN/Graphene Composite for Anti-Corrosion Application Reprinted from: <i>Catalysts</i> 2022 , <i>12</i> , 1618, doi:10.3390/catal12121618	5
Igor Yu. Kaplin, Ekaterina S. Lokteva, Artem V. Tikhonov, Konstantin I. Maslakov, Oksana Ya. Isaikina and Elena V. Golubina Copper–Cerium–Tin Oxide Catalysts for Preferential Oxidation of CO in Hydrogen: Effects of Synthesis Method and Copper Content Reprinted from: <i>Catalysts</i> 2022 , <i>12</i> , 1575, doi:10.3390/catal12121575	18
Yanlin Yu, Zhiming Liu, Wenxian Huang, Shan Zhou, Zuofu Hu and Ligen Wang Ab Initio Investigation of the Adsorption and Dissociation of O ₂ on Cu-Skin Cu ₃ Au(111) Surface Reprinted from: <i>Catalysts</i> 2022 , <i>12</i> , 1407, doi:10.3390/catal12111407	37
Zhi-Qiang Wang, Hui-Hui Liu, Xin-Ping Wu, Peijun Hu and Xue-Qing Gong Hydride Generation on the Cu-Doped CeO ₂ (111) Surface and Its Role in CO ₂ Hydrogenation Reactions Reprinted from: <i>Catalysts</i> 2022 , <i>12</i> , 963, doi:10.3390/catal12090963	45
Rui Dang, Xiufeng Xu, Mengmeng Xie and Jian Liu Synthesis of Self-Supported Cu/Cu ₃ P Nanoarrays as an Efficient Electrocatalyst for the Hydrogen Evolution Reaction Reprinted from: <i>Catalysts</i> 2022 , <i>12</i> , 762, doi:10.3390/catal12070762	57
Fenglan Fan, Lingjuan Wang, Lei Wang, Jinyu Liu and Minghui Wang Low-Temperature Selective NO Reduction by CO over Copper-Manganese Oxide Spinel Reprinted from: <i>Catalysts</i> 2022 , <i>12</i> , 591, doi:10.3390/catal12060591	69
Mengyi Han, Xue Tang, Peng Wang, Zhiyong Zhao, Xiaohua Ba and Yu Jiang et al. Metal-Organic Frameworks Decorated Cu ₂ O Heterogeneous Catalysts for Selective Oxidation of Styrene Reprinted from: <i>Catalysts</i> 2022 , <i>12</i> , 487, doi:10.3390/catal12050487	81
Alexei D. Averin, Svetlana P. Panchenko, Arina V. Murashkina, Varvara I. Fomenko, Daria S. Kuliukhina and Anna S. Malysheva et al. Recent Achievements in the Copper-Catalyzed Arylation of Adamantane-Containing Amines, Di- and Polyamines Reprinted from: <i>Catalysts</i> 2023 , <i>13</i> , 831, doi:10.3390/catal13050831	95
Fenghai Guo, Jayla A. Young, Mina S. Perez, Holden A. Hankerson and Alex M. Chavez Progress on the Cu-Catalyzed 1,4-Conjugate Addition to Thiochromones Reprinted from: <i>Catalysts</i> 2023 , <i>13</i> , 713, doi:10.3390/catal13040713	119

Xiaoli Chen, Yaqi Liu, Yan Liu, Dianxing Lian, Mohaoyang Chen and Yongjun Ji et al.
Recent Advances of Cu-Based Catalysts for NO Reduction by CO under O₂-Containing
Conditions
Reprinted from: *Catalysts* **2022**, *12*, 1402, doi:10.3390/catal12111402 **135**

About the Editors

Yongjun Ji

Yongjun Ji received his Ph.D. in Physical Chemistry in 2012 from East China Normal University, China. Then, he joined Prof. Yadong Li's group at Tsinghua University as a Postdoctoral Fellow. During 2014–2020, he worked as an associate research fellow in Prof. Fabing Su's group at the Institute of Process Engineering, Chinese Academy of Sciences. In June 2020, he joined the School of Light Industry, Beijing Technology and Business University as a full professor. His research interests include controlled synthesis of novel nanomaterials, mesocrystals, and single-atom catalysts, as well as their application in heterogeneous catalysis. Currently, he has published 75 papers in journals such as *Nature Communications*, *National Science Review*, *Matter*, *Advanced Materials*, *Advanced Functional Materials*, *Journal of Catalysis*, *ACS Catalysis*, *Applied Catalysis B: Environmental*, *Small*, *Nano Research*, and *Energy Storage Materials*. To date, his papers have been cited over 2000 times. Additionally, he has 26 pending patents in China, including 14 issued patents.

Liwen Xing

Liwen Xing received his bachelor's degree from Shanxi University, Taiyuan, China, in 2012; a master's degree from Capital Normal University, Beijing, China, in 2016; and a doctoral degree in Engineering from the University of Science and Technology Beijing, China, in 2020. Since Oct. 2020, Dr. Xing has been a Lectorate at the Department of Materials Science and Engineering, College of Chemistry and Materials Engineering, Beijing Technology and Business University, China. His research interests focus on the controlled synthesis and precise tailoring of solid-state materials for advanced applications in the field of electrocatalysis and sensing.

Ke Wu

Dr. Ke Wu is a Senior Lecturer of Chemistry at the Beijing Technology and Business University. Dr. Wu obtained his BS degree from the Nanjing Normal University (Nanjing, China) in 2014 and received his PhD in chemistry from the Peking University (Beijing, China) in 2019. He was a Boya postdoctoral fellow at Peking University before starting his independent academic career in 2021. Dr. Wu's research efforts focus on controlled synthesis, surface modulation, and catalytic applications of ceria-related nanomaterials for DeNO_x and biomass conversion.

Preface



The increasing demands for fine and high value-added chemicals have motivated the long-term exploration of high-performance catalysts with desired activity, selectivity, and durability. Owing to its high natural abundance and low cost, copper as well as its various derivatives has been widely employed as a catalytically active component in a diversity of organic transformations. On the other hand, the multiple accessible oxidation states of reactive Cu element (Cu⁰, Cu^I, Cu^{II}, and Cu^{III}) within Cu-based catalysts are likely to enable the target catalytic reactions that proceed via both single- and multi-electron transfers. As a result, Cu-based catalysts have also found many applications in redox reactions, such as CO oxidation, selective oxidation of organic compounds, selective catalytic reduction of NO_x by CO (CO-SCR), electrochemical hydrogen evolution reaction (HER), and electrochemical CO₂ reduction reaction (CO₂RR). While a great progress has been made, the prerequisite for successful application of Cu-based catalysts lies in the delicate design and regulation of the local electron structure of active sites. Besides that, the catalytic activity of real Cu-based catalysts can only be predicted to some extent via theoretical modeling and calculations. Therefore, it is still of great significance to continue the exploration of novel and more efficient Cu-based catalysts that deliver an enhanced performance.

This Special Issue, entitled “Synthesis and Applications of Copper-Based Catalysts”, provides an overview of recent progress in the synthesis and application of Cu-based materials, with particular emphasis on the latest advanced synthetic approaches, structure modulation strategies, and catalytic performance of copper-based catalysts in heterogeneous and homogeneous catalysis, which can contribute to the development of efficient Cu-based catalysts. We hope that our compilation of such meaningful research studies can provide researchers with new inspiration in this field.

Yongjun Ji, Liwen Xing, and Ke Wu
Editors

Editorial

Synthesis and Applications of Copper-Based Catalysts

Ke Wu ¹, Liwen Xing ^{1,*} and Yongjun Ji ^{2,*}

¹ College of Chemistry and Materials Engineering, Beijing Technology and Business University, Beijing 100048, China; wuke@btbu.edu.cn

² School of Light Industry, Beijing Technology and Business University, Beijing 100048, China

* Correspondence: xingliwen@btbu.edu.cn (L.X.); yjji@btbu.edu.cn (Y.J.)

The increasing demand for fine and high-value-added chemicals has motivated the lasting exploration of high-performance catalysts with desirable activity, selectivity, and durability. Owing to its high natural abundance and low cost, copper, as well as its various derivatives, has been widely employed as a catalytically active component in a diversity of organic transformations. On the other hand, the accessible multiple oxidation states of reactive Cu elements (Cu^0 , Cu^I , Cu^{II} , and Cu^{III}) within Cu-based catalysts can enable targeted catalytic reactions that proceed via both single- and multi-electron transfer. As a result, these Cu-based catalysts have also found many applications in redox reactions, such as CO oxidation, selective oxidation of organic compounds, selective catalytic reduction of NO_x by CO (CO-SCR), electrochemical hydrogen evolution reaction (HER), electrochemical CO_2 reduction reaction (CO_2RR), etc. While great progress has been made, Cu-based catalysts must be delicately designed and their local electron structure of active sites must be regulated. Besides, the catalytic activity of real Cu-based catalysts can be only predicted to some extent by theoretical modeling and calculations. Therefore, it is of great significance to continue the exploration of novel and more efficient Cu-based catalysts that deliver enhanced performance. Some recent and key advances in Cu-based catalysts are included in this Special Issue, as summarized below.

Duan et al. [1], reported a CVD in situ catalytic method to prepare a layer of BCN/Gr two-dimensional composite that directly grew on the surface of copper foil. The anti-corrosion performance characterized via electrochemical and salt spray experiments revealed that the in situ grown BCN/Gr two-dimensional composite exhibited stronger adhesion to the substrate and superior grain boundary dislocation, thus showing an enhanced anti-corrosion capability with the corrosion rate reduced by 91.4% and 57.1% compared with bare Cu foil and BCN-Gr composite synthesized through the transfer method, respectively. This work proposed a new 2D material for researching corrosion prevention mechanisms.

Results obtained by Kaplin et al. [2] demonstrated a one-pot precipitation method employing sacrificial CTAB templates and complexing agents of citric acid to incorporate copper into Ce-Sn and comparative Ce-Zr oxide supports to produce CuCeSn and CuCeZr catalysts. Compared with the counterparts prepared by post-impregnating double CeSn/CeZr oxides with copper salt, the one-pot synthesized CuCeSn and CuCeZr catalysts exhibited improved catalytic performance toward the continuous-flow preferential oxidation of CO in hydrogen excess (CO-PROX). Moreover, a small number of tin dopants in cerium-based catalysts were shown to have better reducibility than that of zirconium, and the switch from Sn^{4+} to Sn^{2+} can provide an additional redox pair, thus positively affecting its activity. In addition, the one-pot technique contributed to the uniform element distribution in the 20CuCeSn catalysts and promoted their micro- and mesoporosity. Besides, modulating the copper content was beneficial for tuning the CO conversion/ CO_2 selectivity ratio, which should be ascribed to predominantly distributed copper in the CeSn phase at low loading, while separate copper oxide phases appear at higher loadings, thus increasing the interfacial interaction between copper-containing and CeSn oxides.



Citation: Wu, K.; Xing, L.; Ji, Y. Synthesis and Applications of Copper-Based Catalysts. *Catalysts* **2023**, *13*, 973. <https://doi.org/10.3390/catal13060973>

Received: 31 May 2023

Revised: 2 June 2023

Accepted: 2 June 2023

Published: 5 June 2023



Copyright: © 2023 by the authors. Licensee MDPI, Basel, Switzerland. This article is an open access article distributed under the terms and conditions of the Creative Commons Attribution (CC BY) license (<https://creativecommons.org/licenses/by/4.0/>).

Surface adsorption and dissociation processes can play a vital role in the catalytic performance of metal alloys. Wang et al. [3] performed first-principles calculations to study the adsorption and dissociation of O₂ on the Cu-skin Cu₃Au(111) surface. According to the calculated results, the most energetically favorable adsorption configuration on the Cu-skin Cu₃Au(111) surface is b-f(h)-b. Meanwhile, two thermodynamically feasible dissociation paths are available for O₂ dissociation. One path is from b-f-b to two O atoms in adjacent *hcp* sites, and the other path is from b-h-b to two O atoms in adjacent *fcc* sites. Compared with the Cu(111) surface, the Cu-skin Cu₃Au(111) surface showed higher stability of O₂ adsorption and a lower dissociation energy barrier of the adsorbed O₂. These theoretical findings can offer useful guidance for the practical application of Cu-Au alloys as high-efficiency CO oxidation catalysts.

Ceria-based catalysts are highly efficient in the selective catalytic hydrogenation of CO₂ to methanol. However, the intrinsic reaction mechanism concerning the formation of active H species remains obscure. Gong et al. [4], performed DFT + U calculations to systematically investigate the impact of pristine and Cu-doped CeO₂(111) surfaces on the catalytic dissociation of H₂ to produce hydride species. The obtained results showed that doping a single Cu atom on the CeO₂(111) surface resulted in the creation of an oxygen vacancy, which played a decisive role in promoting the heterolytic dissociation of H₂ to produce H⁻ species. Moreover, the Cu dopant can also facilitate the adsorption of CO₂ and the subsequent hydrogenation of CO₂ to produce HCOO*, thus leading to the improved catalytic activity and selectivity of methanol. It is expected that this work can provide valuable guidance for rationally designing high-performance ceria and Cu-based catalysts toward CO₂ catalytic reduction reactions.

The hydrogen evolution reaction (HER), which is derived from electrochemical water splitting, is one of the most economical and environmentally benign avenues to produce green hydrogen. Dang et al. [5] synthesized self-supported Cu/Cu₃P nanoarrays through a low-temperature phosphidation process, which were directly grown on the surfaces of Cu nanosheets from Cu/CuO nanoarrays precursor. Typically, Cu/Cu₃P nanoarray-270 electrocatalysts show superior electrocatalytic activity and long-term stability for HER in an acidic electrolyte solution, accompanied by an onset overpotential of 96 mV and a small Tafel slope of 131 mV per decade. The unique nanoarray architecture of Cu/Cu₃P rendered abundant active sites and promoted diffusion of the products, contributing to a faster electron transfer rate and good electrical conductivity, thus resulting in enhanced electrocatalytic efficiency toward the HER. This novel strategy offers unique opportunities in HER and can be extended to more metal phosphides and metal-related nanostructures.

Selective catalytic reduction of NO with CO (CO-SCR) is regarded as a valid and economical denitrification technology to simultaneously eliminate NO and CO from flue gas. Spinel structural manganese–copper spinels are considered potential CO-SCR materials due to their excellent stability and redox properties. Thus, Liu et al. [6], synthesized foam-like Cu_xMn_{3-x}O₄ spinel ($x = 0, 1, 1.5, 2, 3$) with varying CuO/MnO_x contents via a citrate-based pechini method. Meaningfully, the redox balance that occurred on the Cu_xMn_{3-x}O₄ catalyst ($\text{Cu}^{2+} + \text{Mn}^{3+} \rightleftharpoons \text{Mn}^{4+} + \text{Cu}^{+}$) was shifted to improve the redox property and CO-SCR catalytic performance because of the doped Cu species, which promoted the generation of grain and growth of the spinel structural Cu_{1.5}Mn_{1.5}O₄ with increased surface area and particle size. Therefore, compared with pure Mn₂O₃, a higher content of Mn⁴⁺/Mn and more highly active oxygen-containing species were created on the surface of Cu_{1.5}Mn_{1.5}O₄ spinels, which is favorable for the adsorption of oxygen molecules, thus improving the adsorption capacity of CO and NO. Consequently, Cu_{1.5}Mn_{1.5}O₄ catalysts are capable of reaching 100% NO conversion together with 53.3% CO conversion at a low temperature of 200 °C, and this study provided a practicable method for the rational design and synthesis of reactive Mn-based catalysts toward CO-SCR.

The selective oxidation of styrene to benzaldehyde with highly efficient and environmentally friendly catalysts is significant in fine chemical industries. An advanced core–shell structural Cu₂O@Cu-BDC-NH₂ heterogeneous catalyst with a tunable Cu⁺/Cu²⁺ interface

and variable MOF loadings and Cu₂O crystal phases was prepared by Zhang et al. [7] via a facile in situ self-assembly method. Importantly, the alkaline properties of Cu₂O and the introduced –NH₂ group can dramatically prevent the excessive oxidation of target products, thus allowing the selective oxidation of styrene to proceed without a base condition. Meanwhile, the well-designed combination of Cu₂O and Cu-BDC-NH₂ further produced an appropriate Cu⁺/Cu²⁺ active interface and porous MOF shells, thus simultaneously facilitating the mass transfer and protecting the active Cu₂O component. Hence, the optimal Cu₂O@Cu-BDC-NH₂-8h exhibited a high styrene conversion of 85% and benzaldehyde selectivity of 76% with H₂O₂ as a non-polluting oxidant under an ambient condition of 40 °C. This work demonstrated a new perspective for developing cost-efficient and eco-friendly catalysts with moderate basicity toward the selective catalytic oxidation of styrene under base-free conditions.

At the beginning of the 21st century, the fast development of the copper-catalyzed amination of aryl halides provided an efficient approach to constructing the C(sp²)-N bond, which competed against the classic Buchwald–Hartwig amination reaction. Averin et al. [8] reviewed recent progress in the copper-catalyzed arylation and heteroarylation of adamantane-containing amines, diamines, and polyamines. With the primary purpose of classifying the dimension and limitation of the copper catalysis involved in the arylation and heteroarylation of the as-mentioned amines, this review addressed the following issues: the dependence of the most suitable catalytic systems on the property of reagents, the chance of N,N'-di(hetero) arylation of the diamines, oxadiazines, and polyamines, the utilization of unsupported copper nanoparticles, and the feather of the Chan–Lam amination using adamantane-containing amines, diamines, and oxadiazines.

Sulfur-containing heterocyclic compounds have attracted significant research interest in recent years owing to their abundant biological activities and universal use in biopharmaceuticals, pesticides, and material science fields. Guo et al. [9] provided a brief review of recent achievements involved in the preparation of a crucial series of sulfur-heterocycles-2-alkylthiochroman-4-ones and thioflavanones through Cu-catalyzed conjugate introduction of Grignard reagents to thiochromones. Moreover, the latest advance in the production of 2-alkynyl thiochroman-4-ones by the alkynylation and alkenylation of thiochromones with the aid of copper catalysts was also summarized. The recent progress comprises introducing alkyl, aryl, and alkenyl to thiochromones via 1,4-conjugate addition of Grignard reagents together with the formal conjugate addition of alkynyl groups to thiochromones catalyzed by Cu(I) salts. This work comprehensively reviewed the above-mentioned, providing a rapid understanding of 2-substituted thiochroman-4-ones.

Cost-effective Cu-based catalysts exhibit fascinating catalytic activity in CO-SCR; however, some technical problems including high reaction temperature and poor resistance to O₂, H₂O, and SO₂ still hinder their industrial implementation. Ji et al. [10] comprehensively reviewed Cu-catalyzed CO-SCR under O₂-containing conditions, including the catalytic performance of non-supported, supported mono-metallic, supported bimetallic, and supported multi-metallic Cu-based catalysts. Besides, the impact of O₂ concentration, reaction temperature, and the existence of H₂O and SO₂ on the CO-SCR performance was briefly summarized. The reaction mechanism, future challenges, and perspectives regarding CO-SCR were discussed as well. This review can be beneficial in offering guidance for designing effective Cu-based catalysts for the CO-SCR.

In summary, this Special Issue on “Synthesis and Applications of Copper-Based Catalysts” provided an overview of the recent progress in the synthesis and application of Cu-based materials, with particular emphasis on the latest advanced synthetic approaches, the structure modulation strategies, and catalytic performance of copper-based catalysts in heterogeneous and homogeneous catalysis, which can contribute to the development of efficient Cu-based catalysts. We hope that our compilation of this meaningful research progress can help to provide researchers with new inspiration in this field.

Finally, we are grateful to all authors for their valuable contributions and to the editorial team of *Catalysts* for their kind support, making this Special Issue possible.

Author Contributions: Conceptualization, K.W., L.X., and Y.J.; writing—original draft preparation, K.W. and L.X.; writing—review and editing, L.X. and Y.J. All authors have read and agreed to the published version of the manuscript.

Funding: This research was funded by the Research Foundation for Youth Scholars of Beijing Technology and Business University grant number QNJ2022-22 from L.X. and QNJ2022-23 from K.W.; the R&D Program of Beijing Municipal Education Commission grant number KM202310011005 from K.W.; the National Natural Science Foundation of China grant number 21978299 from Y.J.; the Research Foundation for Advanced Talents of Beijing Technology and Business University grant number 19008020159 from Y.J.

Conflicts of Interest: The authors declare no conflict of interest.

References

1. Duan, C.; Li, X.; Ji, Y.; He, L.; Qian, J.; Zhao, Z. In-Situ Catalytic Preparation of Two-Dimensional BCN/Graphene Composite for Anti-Corrosion Application. *Catalysts* **2022**, *12*, 1618. [CrossRef]
2. Kaplin, I.Y.; Lokteva, E.S.; Tikhonov, A.V.; Maslakov, K.I.; Isaikina, O.Y.; Golubina, E.V. Copper–Cerium–Tin Oxide Catalysts for Preferential Oxidation of CO in Hydrogen: Effects of Synthesis Method and Copper Content. *Catalysts* **2022**, *12*, 1575. [CrossRef]
3. Yu, Y.; Liu, Z.; Huang, W.; Zhou, S.; Hu, Z.; Wang, L. Ab Initio Investigation of the Adsorption and Dissociation of O₂ on Cu-Skin Cu₃Au(111) Surface. *Catalysts* **2022**, *12*, 1407. [CrossRef]
4. Wang, Z.-Q.; Liu, H.-H.; Wu, X.-P.; Hu, P.; Gong, X.-Q. Hydride Generation on the Cu-Doped CeO₂(111) Surface and Its Role in CO₂ Hydrogenation Reactions. *Catalysts* **2022**, *12*, 963. [CrossRef]
5. Dang, R.; Xu, X.; Xie, M.; Liu, J. Synthesis of Self-Supported Cu/Cu₃P Nanoarrays as an Efficient Electrocatalyst for the Hydrogen Evolution Reaction. *Catalysts* **2022**, *12*, 762. [CrossRef]
6. Fan, F.; Wang, L.; Wang, L.; Liu, J.; Wang, M. Low-Temperature Selective NO Reduction by CO over Copper-Manganese Oxide Spinel. *Catalysts* **2022**, *12*, 591. [CrossRef]
7. Han, M.; Tang, X.; Wang, P.; Zhao, Z.; Ba, X.; Jiang, Y.; Zhang, X. Metal-Organic Frameworks Decorated Cu₂O Heterogeneous Catalysts for Selective Oxidation of Styrene. *Catalysts* **2022**, *12*, 487. [CrossRef]
8. Averin, A.D.; Panchenko, S.P.; Murashkina, A.V.; Fomenko, V.I.; Kuliukhina, D.S.; Malysheva, A.S.; Yakushev, A.A.; Abel, A.S.; Beletskaya, I.P. Recent Achievements in the Copper-Catalyzed Arylation of Adamantane-Containing Amines, Di- and Polyamines. *Catalysts* **2023**, *13*, 831. [CrossRef]
9. Guo, F.; Young, J.A.; Perez, M.S.; Hankerson, H.A.; Chavez, A.M. Progress on the Cu-Catalyzed 1,4-Conjugate Addition to Thiochromones. *Catalysts* **2023**, *13*, 713. [CrossRef]
10. Chen, X.; Liu, Y.; Liu, Y.; Lian, D.; Chen, M.; Ji, Y.; Xing, L.; Wu, K.; Liu, S. Recent Advances of Cu-Based Catalysts for NO Reduction by CO under O₂-Containing Conditions. *Catalysts* **2022**, *12*, 1402. [CrossRef]

Disclaimer/Publisher’s Note: The statements, opinions and data contained in all publications are solely those of the individual author(s) and contributor(s) and not of MDPI and/or the editor(s). MDPI and/or the editor(s) disclaim responsibility for any injury to people or property resulting from any ideas, methods, instructions or products referred to in the content.

Article

In-Situ Catalytic Preparation of Two-Dimensional BCN/Graphene Composite for Anti-Corrosion Application

Chunyang Duan ^{1,*}, Xiaojie Li ¹, Yongjun Ji ², Liuyang He ¹, Jianhua Qian ¹ and Zenghua Zhao ^{1,*}¹ School of Petrochemical Engineering, Liaoning Petrochemical University, Fushun 113001, China² School of Light Industry, Beijing Technology and Business University, Beijing 100048, China

* Correspondence: duanchunyang@lnpu.edu.cn (C.D.); zzh799@126.com (Z.Z.)

Abstract: In-situ catalytic growth of two-dimensional materials shows great potential for metal surface protection because of the impermeability and strong interaction of the materials with metal surfaces. Two-dimensional hexagonal boron-carbon nitrogen (h-BCN) is composed of alternating boron, carbon, and nitrogen atoms in a two-dimensional honeycomb lattice, which is similar to graphene. The corrosion caused by defects such as grain boundary of two-dimensional materials can be weakened by dislocation overlap via the transfer method. However, two-dimensional composite films prepared using the transfer method have problems, such as the introduction of impurities and poor adhesion, which limit their corrosion resistance. In this study, a layer of BCN/Gr two-dimensional composite was directly grown on the surface of copper foil using the CVD in-situ catalysis method, and its anti-corrosion performance was characterized by electrochemical and salt spray experiments. The results showed that the directly grown two-dimensional composite had better adhesion to the substrate and the advantage of grain boundary dislocation, thus showing a better anti-corrosion capability.



Citation: Duan, C.; Li, X.; Ji, Y.; He, L.; Qian, J.; Zhao, Z. In-Situ Catalytic Preparation of Two-Dimensional BCN/Graphene Composite for Anti-Corrosion Application. *Catalysts* **2022**, *12*, 1618. <https://doi.org/10.3390/catal12121618>

Academic Editor: Bishweshwar Pant

Received: 27 October 2022

Accepted: 7 December 2022

Published: 9 December 2022

Publisher's Note: MDPI stays neutral with regard to jurisdictional claims in published maps and institutional affiliations.



Copyright: © 2022 by the authors. Licensee MDPI, Basel, Switzerland. This article is an open access article distributed under the terms and conditions of the Creative Commons Attribution (CC BY) license (<https://creativecommons.org/licenses/by/4.0/>).

Keywords: BCN/graphene composite; CVD; anti-corrosion

1. Introduction

With developments in modern science and technology, industrial production requires metal materials with higher stability and service life; thus the development of surface protection technology for metals is of great significance. Traditional anti-corrosion methods, such as protective coatings and sacrificial anodes, require very thick coating materials, which cause problems such as environmental pollution and easy peeling [1–4]. Therefore, it is of great significance to develop novel anti-corrosion materials with strong corrosion resistance. Two-dimensional (2D) materials directly grown on metal surfaces are not only impermeable, but they can be closely combined with the metal surface, thus fully meeting the requirements of novel metal protective coatings [5–9].

2D materials refer to nanomaterials with ordered structures on 2D planes. Their atomic thickness gives them excellent mechanical properties and light transmittance [10–12]. Graphene, the first 2D material that could be controllably prepared in the laboratory, is a honeycomb hexagonal plane crystal formed by the arrangement of single-layer sp^2 hybrid carbon atoms. Due to its 2D honeycomb lattice arrangement, it shows excellent impermeability [13,14], an extremely high theoretical specific surface area ($2630 \text{ m}^2/\text{g}$) [15,16], excellent light transmittance ($\sim 97.7\%$) [11], high Young's modulus ($\sim 1 \text{ TPa}$) [17], and good oxidation resistance [18,19]. These properties play an important role in its anti-corrosion mechanism, making graphene an excellent candidate for anti-corrosion materials [20]. However, the excellent conductivity of graphene can also promote the occurrence of electrochemical corrosion reactions, which compromise its long-term anti-corrosion ability [1,21].

2D hexagonal boron-carbon nitrogen (h-BCN), a novel 2D structure composed of alternating boron, carbon, and nitrogen atoms in a 2D honeycomb lattice, has recently

attracted considerable attention. Although 2D h-BCN has a similar structure to graphene, h-BCN is an excellent insulator due to its wide band gap, and its strong B-N, B-C, and C-N bond cooperation gives it strong mechanical strength [22,23], good high-temperature oxidation resistance, and thermal stability, showing strong oxidation resistance at 900 °C [24,25]. Therefore, 2D h-BCN nanomaterials directly grown on metal surfaces have the potential to effectively prevent corrosion molecules from diffusing to the surface of the metal substrate, thus improving corrosion resistance [26]. However, it is difficult to prepare a large area of single-crystal 2D material using the CVD method, and grain boundaries with poor adhesion and weak bond cooperation are unavoidable, which are usually the starting points for corrosion reactions of 2D materials in corrosive environments [1,6].

In order to eliminate the influence of the grain boundary of 2D materials and improve their corrosion resistance, some research has been devoted to the preparation of single-crystal 2D materials, but they are generally grown on the surface of single crystal substrates, which is difficult to achieve in actual preparations and applications on large areas [27,28]. Overlaying several layers of 2D materials by transfer is one way to weaken the influence of grain boundaries through grain boundary interlacing [29]. However, the adhesion between 2D films is poor, and impurities and breakage are introduced during the transfer process, which seriously affects its anti-corrosion performance [30]. In order to improve the performance of 2D materials in corrosion protection, this work proposed a new strategy of in-situ catalytic growth of composite 2D films prepared using the CVD method for metal corrosion protection. The boron carbonitride/graphene (BCN/Gr) 2D composites prepared by in-situ growth not only had very strong interlaminar forces, but also realized the dislocation of the grain boundary, which alleviated the corrosion caused by the grain boundaries. Salt spray experiments, electrochemical tests, and adhesion measurements showed that the in-situ grown BCN/Gr 2D composite films had excellent adhesion and improved corrosion resistance. Compared with as-grown BCN film and the BCN-Gr composite prepared by the transfer method, the corrosion rate of in-situ grown 2D BCN/Gr film was reduced by 91.4% and 57.1%, respectively. Therefore, this work not only provides a new 2D material for corrosion prevention, but also provides new experimental and theoretical support for research investigating the corrosion prevention mechanisms of 2D materials.

2. Results and Discussion

A home-built CVD furnace was used for the preparation of the 2D materials, such as BCN and BCN/Gr, and its preparation diagram is shown in Figure 1a. As shown in Figure 1a, the growth process had two heating zones, including the sub heating zone at the front end of the quartz tube and the main heating zone at the rear section of the quartz tube. The temperature in the main heating zone was regulated by the electric heating parts of the CVD furnace, and the temperature in the sub heating zone was controlled by the heating belt wound on the quartz tube. When BCN and BCN/Gr two-dimensional films were grown by CVD, methane and borane ammonia were used as the precursors. After exhausting the air in the tubular furnace with Ar, the temperature of the main heating zone was raised to 1000 °C, the mixed gas of methane and hydrogen was introduced, and methane molecules were decomposed into carbon atoms. Then, the temperature of the auxiliary heating zone was set to 90 °C, and the borane ammonia was decomposed by heat to produce $\text{-BH}_2\text{-NH}_2\text{-}$, which diffused to the main heating zone with the gas flow, and then was further decomposed into -B-N- under the high temperature in the main heating zone [26]. Finally, -B-N- was deposited on the copper substrate and re-bonded into BCN films with carbon atoms. The preparation of BCN/Gr 2D composite films combines the growth process of graphene and BCN in the same procedure with copper foil was used as catalyst and borane ammonia and methane as precursors. The graphene layer was first grown on the copper foil surface with CH_4 as the carbon source. First, methane was decomposed and provided C atoms. Since Cu has poor affinity to C, C atoms could diffuse on the surface and build up the thermodynamically stable honeycomb lattice by surface

nucleation and growth [31,32]. Then, the temperature of the sub heating zone was raised, the borane ammonia precursor was added on the basis of the CH_4 source, the BCN layer continued to grow on the surface of the graphene film, and the BCN/Gr 2D composite film was finally obtained.

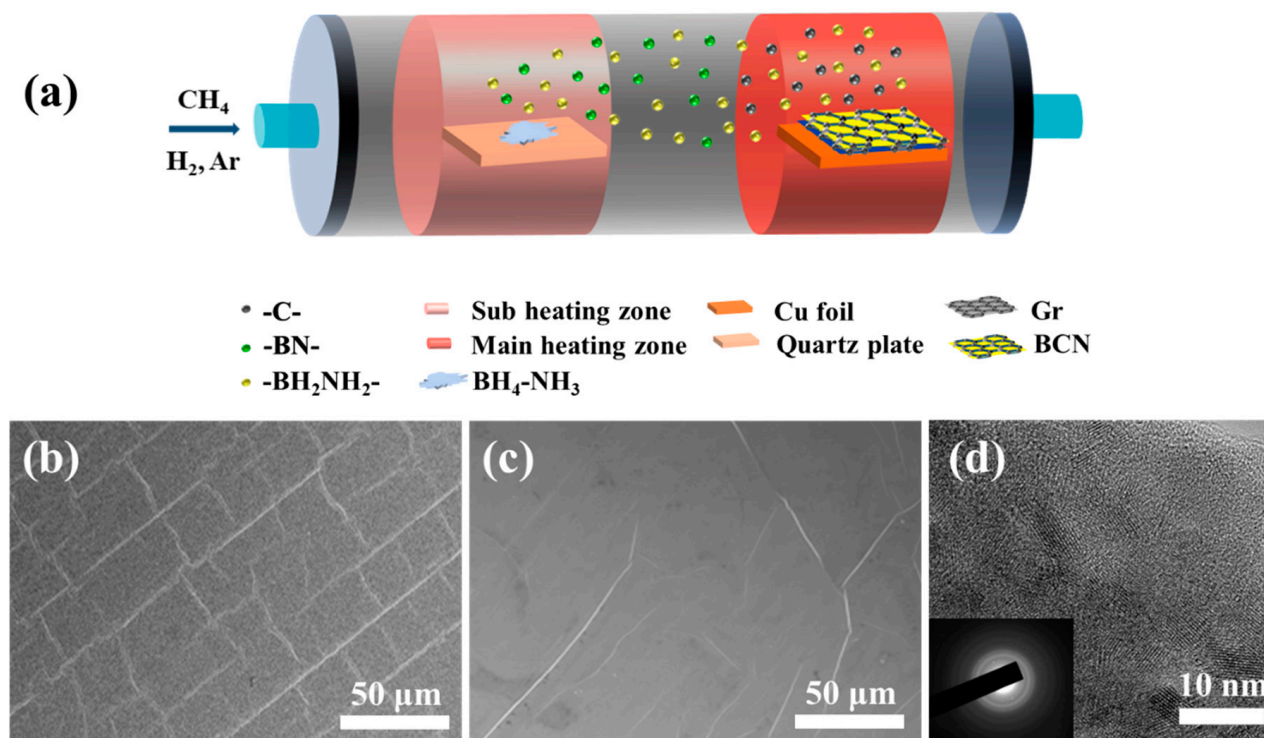


Figure 1. (a) Diagram of the home-built CVD furnace for the preparation of BCN and BCN/Gr; (b) SEM of the BCN two-dimensional film; (c) SEM of the BCN/Gr two-dimensional film; (d) TEM and electron diffraction pattern (inset) of the BCN/Gr two-dimensional film.

Figure S1 and Figure 1b,c show the SEM images of Gr, BCN, and BCN/Gr grown on Cu foils, respectively. It can be seen that the 2D films are continuous and complete, and there are a lot of wrinkles on the surface. These wrinkles may be due to the release of internal stress in the growth base (copper foil), which conforms to the characteristics of the 2D film [33]. In addition, the BCN/Gr 2D composite film shows (Figure 1c) a flatter surface structure than BCN (Figure 1b), which may be due to the reduction of copper foil roughness and the release of surface stress during the first step of growing the graphene layer. Figure 1d shows the TEM topography of BCN/Gr, which indicates that BCN/Gr is a complete continuous film and shows a clear laminar structure with irregular lattice distribution. As graphene grows below the BCN layer, it is difficult to directly observe the structure of the graphene layer. However, the clear laminar flow structure and staggered lattice shown in the TEM diagram may be derived from the interlacing of two different 2D structures (graphene and BCN). Among them, the electron diffraction pattern shown in the illustration in Figure 1d clearly shows the annular diffraction characteristics of BCN and Gr 2D structures [34–36]. Meanwhile, the EDS results also confirmed the even distribution of C and N elements in the as-prepared 2D film (Supporting Information Figure S2). The thickness of the in-situ grown BCN and BCN/Gr 2D films was characterized by TEM and AFM. The results showed that the thickness of the BCN 2D film was approximately 3–4 nm and the thickness of the BCN/Gr 2D composite film was 8–10 nm. The significant increase in the thickness of BCN/Gr may be due to the increase in the number of layers of BCN films grown on the graphene (Supporting Information Figure S3).

Raman spectroscopy and infrared spectroscopy are important characterization means to evaluate the bonding and structure of two-dimensional materials. In this study, we

analyzed the quality of BCN and BCN/Gr samples prepared at different growth times using these two techniques. Samples BCN1,2,3 and BCN/Gr1,2,3 represent samples with growth times of 10, 20, and 40 min, respectively. After etching the Cu substrate from the BCN and BCN/Gr layers by liquid phase etching (Supporting Information, Figure S4), the BCN and BCN/Gr 2D composite films were transferred to the surface of SiO₂ substrates for characterization. Figure 2a shows the Raman spectra of the BCN 2D films, showing wider D and G peaks, similar to those of graphene (Supporting Information, Figure S5). The shoulder peaks appearing at $\sim 1363\text{ cm}^{-1}$ corresponded to in-plane substitution, vacancy, or lattice distortion between grain boundaries in the sp^2 structure; and the peak at $\sim 1600\text{ cm}^{-1}$ reflected the tensile structural strength of sp^2 bonding [37]. Compared with graphene, the D and G peaks of the BCN 2D layer blue shifted to higher wavelength positions due to the combination of B and N bonds with C in BCN. For the infrared spectrum of BCN (Figure 2b), the peaks at 1392 cm^{-1} and 809 cm^{-1} were attributed to in-plane tension and out-of-plane bending vibrations of the B-C-N rings, respectively. The infrared peaks between 1070 and 1250 cm^{-1} indicated the existence of B-C bonds. The films rich in B had maximum absorption at $\sim 1100\text{ cm}^{-1}$, whereas the films rich in C had maximum absorption at $\sim 1250\text{ cm}^{-1}$ [22,38].

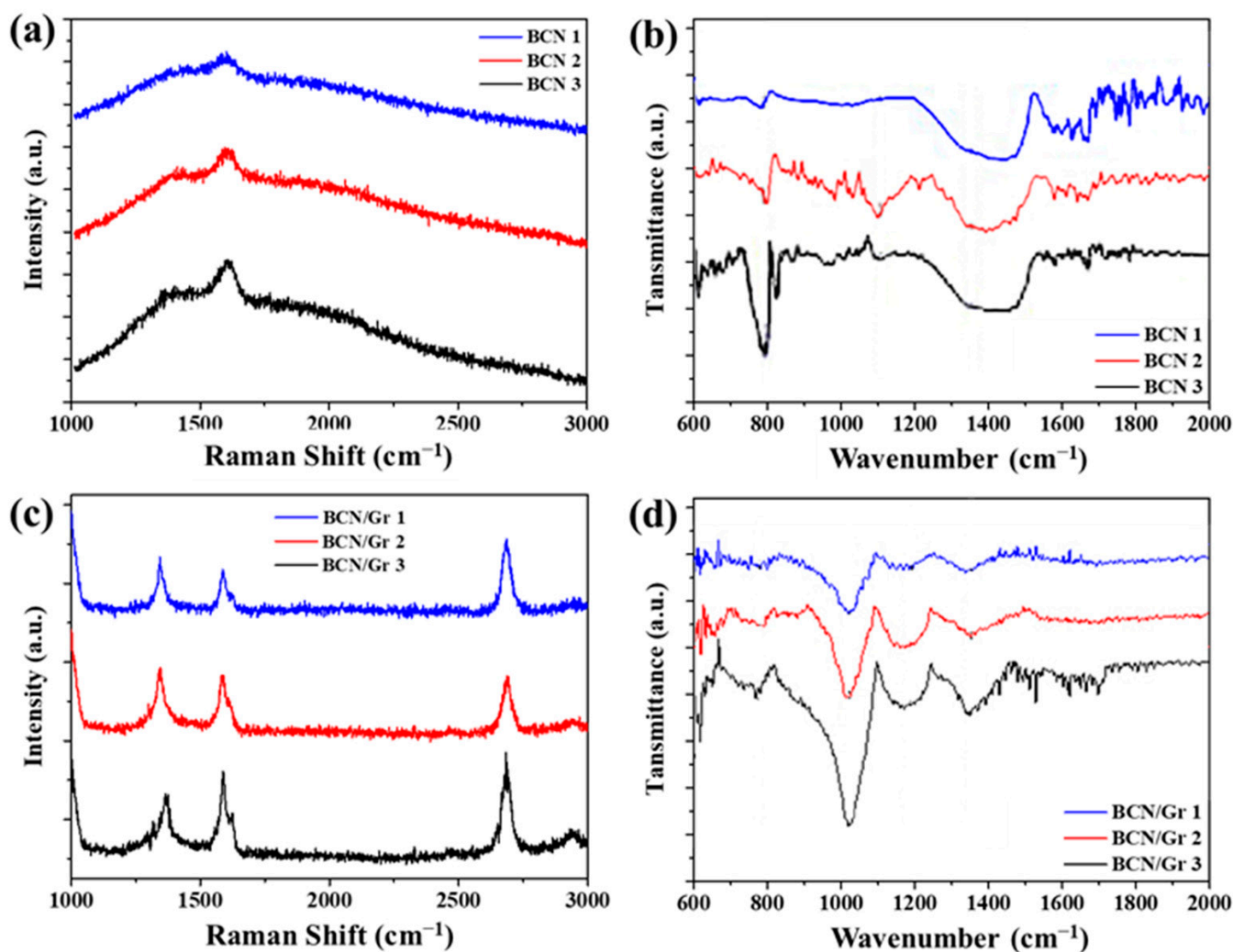


Figure 2. (a) Raman spectra of BCN two-dimensional films; (b) Infrared spectra of BCN two-dimensional films; (c) Raman spectra of BCN/Gr two-dimensional films; (d) Infrared spectra of BCN/Gr two-dimensional films.

Figure 2c shows the Raman spectra of the BCN/Gr 2D composite films. The characteristic peaks of graphene, such as G peaks and 2D peaks, are clearly visible. At the same time, the characteristic peaks of BCN can also be observed at $\sim 1363\text{ cm}^{-1}$ and $\sim 1600\text{ cm}^{-1}$. As the growth time increased, the G peaks gradually broadened, indicating that the peak strength at 1600 cm^{-1} was increasing and forming the wide characteristic peak of graphene. Meanwhile, the strength of the D peak was also gradually increasing, which proved that the content of BCN in the 2D composite films was increasing, thus confirming the formation of the BCN/Gr 2D composite material.

Figure 2d shows the infrared spectra of the BCN/Gr 2D composite films. It can be seen that in contrast to the infrared spectra of BCN (Figure 2b), the maximum characteristic peak of BCN/Gr (Figure 2d) moved to $\sim 1100\text{ cm}^{-1}$, which was attributed to B-C bonds. Meanwhile, with increasing growth time, the peak at $\sim 1100\text{ cm}^{-1}$ also increased, indicating the increasing B content of the BCN/Gr sample. The Raman and infrared spectra proved the successful preparation of BCN and BCN/Gr 2D composite materials.

It is reported that 2D materials protect the metal substrate through their impermeability and tight combination with the substrate [1,29,39]. However, two-dimensional film materials prepared using the CVD method have a large number of grain boundaries, which are considered to be the starting point of corrosion reactions. By transferring another layer of 2D film on its surface, the grain boundaries could be dislocated, thus preventing the diffusion of corrosion reactants to the metal substrate [29]. Therefore, we used the liquid etching method to transfer the BCN and graphene films onto the surface of an as-grown BCN/Cu foil surface and prepared BCN-BCN and BCN-Gr samples, respectively (Supporting Information, Figure S1). The graphene layer used for transfer was prepared using the CVD process, which is described in the Supporting Information (Figure S2). Figure 3a,c display schematic diagrams of the BCN-BCN and BCN-Gr samples, and Figure 3b,d shows their corresponding SEM results, respectively. As shown in Figure 3b,d, the boundaries of the transferred 2D films can be clearly observed. The transferred graphene and BCN films were relatively complete and not damaged during the transfer process. In addition, the BCN film (Figure 3b) was significantly thicker than the graphene film (Figure 3d). It can be seen that in this study, we prepared a variety of 2D films based on graphene, BCN, and BCN/Gr composite films through direct growth and transfer. In order to describe and characterize the samples more clearly, we summarized the samples and preparation methods in Table 1.

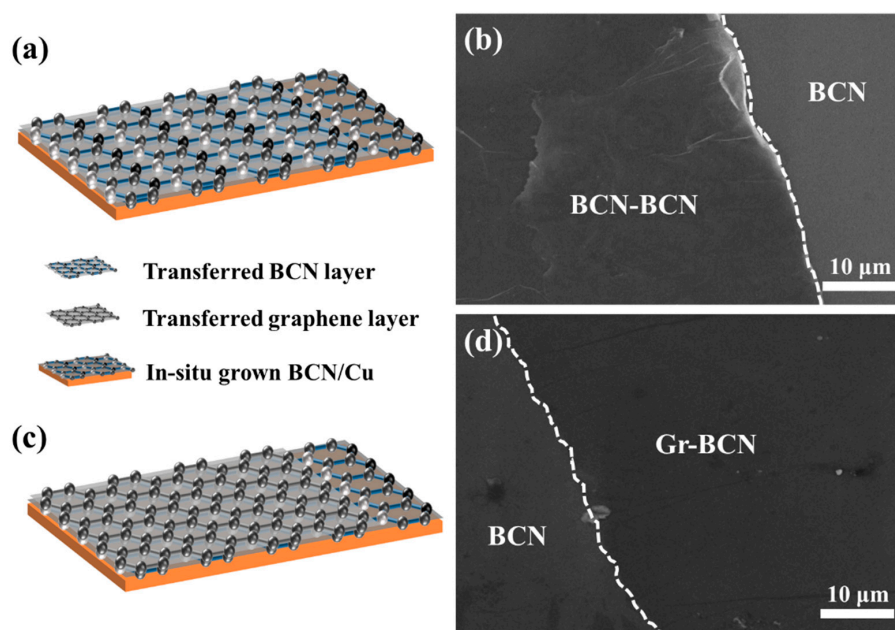


Figure 3. (a) Schematic diagram of BCN-BCN sample; (b) SEM of BCN-BCN sample; (c) Schematic diagram of BCN-Gr sample; (d) SEM of BCN-Gr sample.

Table 1. Samples prepared in this study.

Sample	Method	Growth Time of BCN (min)
BCN 1	CVD grown BCN	10
BCN 2		20
BCN 3		40
BCN/Gr 1	CVD grown BCN/Gr composite	10
BCN/Gr 2		20
BCN/Gr 3		40
BCN-Gr 1	CVD grown BCN + transferred BCN	10
BCN-Gr 2		20
BCN-Gr 3		40
BCN-BCN 1	CVD grown BCN + transferred Gr	10
BCN-BCN 2		20
BCN-BCN 3		40

Electrochemical testing is considered a convenient method to evaluate the corrosion resistance of protective coatings [40–42]. Figure 4a shows the schematic diagram of the three-electrode system for electrochemical testing, in which the platinum electrode is the counter electrode, the saturated calomel electrode is the reference electrode, the samples to be tested are the working electrodes, and the electrolyte is 5% NaCl solution. Figure 4b shows the Tafel curves of the different samples. According to the tangent line of the quasi-linear part of the Tafel curve, the corrosion voltage and corrosion current of the samples can be determined. At the same time, the corrosion rate (R_{corr}) can be calculated using the following formula [40,41]:

$$\text{Corrosion Rate} = \frac{I_{\text{corr}} \times K \times EW}{\rho A} \quad (1)$$

where the corrosion rate constant $K = 3272 \text{ mm/yr}$ and the density of Cu substrate $\rho = 8.94 \text{ g/cm}^3$. Since Cu loses 2 electrons due to oxidation, EW is 31.7 g and A is the test area (1 cm^2) of the sample during the test.

As shown in Figure 4b, the bare copper sample showed the maximum corrosion current and the most negative corrosion voltage, indicating that it was the most susceptible to corrosion. With the modification of different 2D films on Cu surfaces, the corrosion current decreased and the corrosion voltage moved in the positive voltage direction, indicating that the samples had stronger corrosion resistance. Compared with the simple growth of a layer of BCN film, further transferring a layer of 2D material on its surface significantly reduced its corrosion current and increased its corrosion voltage, reflecting promotion of the corrosion resistance of 2D materials through grain boundary dislocation. Meanwhile, the in-situ grown BCN/Gr 2D composite film showed a smaller corrosion current and the corrosion voltage moved approximately 15 mV in the positive voltage direction compared with the transferred sample, showing a stronger corrosion resistance ability.

Figure 4c shows the Nyquist diagram obtained by electrochemical impedance spectroscopy (EIS). Within the frequency range of 1~100 kHz, the measured diameter of the half arc could be considered as the interface of charge transfer resistance, representing the corrosion resistance of the protective coating. It can be seen from Figure 4c that the bare Cu substrate showed the minimum impedance, that is, the worst corrosion resistance. With surface modification, the impedance of the sample gradually increased and the BCN/Gr sample showed the strongest corrosion resistance, which was consistent with the results shown in the Tafel curves (Figure 4b). Figure 4d shows the potential dependent EIS results of the in-situ grown BCN/Gr 2D films. The results showed that when the polarization potential changed to the negative direction, the semicircle diameter of the impedance curve increased significantly, indicating that the interface charge transfer resistance increased and had a cathodic protection effect under negative potential. Figure 4e shows the corrosion rates of different samples calculated according to the above formula. The BCN/Gr sample

showed the lowest corrosion rate, that is, the best corrosion resistance. Compared with the bare Cu substrate, the corrosion rate of the BCN 2D material decreased from 0.35 to 0.14 mil/year, with a decrease of 60%. When another layer of BCN or graphene 2D film was transferred on the surface of the in-situ grown BCN 2D film, the corrosion rate was further reduced to 0.08 and 0.07 mil/year, which was nearly 50% lower than that of the single-layer modification. This result proved that the grain boundary dislocation of 2D materials improved corrosion resistance. Furthermore, the corrosion rate of the in-situ grown BCN/Gr 2D composite films further decreased to 0.03 mil/year, which was 91.4% lower than that of bare Cu foil and 57.1% lower than that of the BCN-Gr composite prepared using the transfer method. The further improvement of the anti-corrosion performance of the in-situ grown 2D composite may be due to the dislocation of the grain boundaries of the BCN and graphene layers. In addition, compared with the BCN-Gr two-dimensional composite film obtained by transfer, the interlayer gap of the in-situ grown composite might be smaller, which is more conducive to metal surface protection.

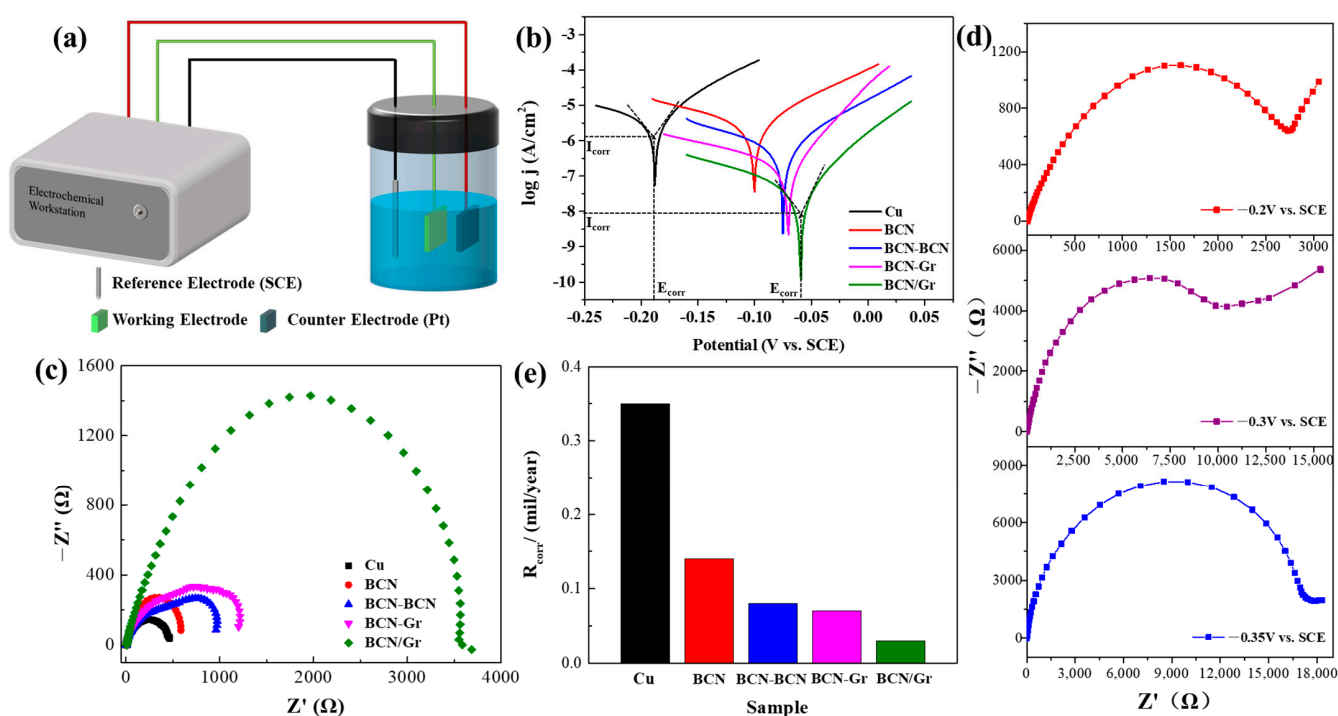


Figure 4. (a) Schematic diagram of the three-electrode system for electrochemical testing; (b) Tafel curves of the Cu foils with different modification layers; (c) Nyquist diagram obtained by electrochemical impedance spectroscopy of the different samples; (d) potential dependent EIS results of in-situ grown BCN/Gr 2D films; (e) Corrosion rates of the samples with different surface modification.

Salt spray testing mainly uses artificial simulated salt spray conditions to assess corrosion resistance ability. In the salt spray experiments, we cut bare copper sheet samples and samples with different surface modifications into 2 cm × 2 cm pieces and placed them into the salt spray box for salt spray testing. After 8 h of spray, the samples were removed and washed with deionized water, and their morphologies were observed after drying. Figure 5a–e shows the optical photos of bare copper foil, BCN, BCN-BCN, BCN-Gr, and BCN/Gr samples after salt spray testing for 8 h. It can be seen that the bare copper foil is most corroded, followed by the sample with a layer of BCN film. After another layer of 2D film was transferred on the surface of BCN, the corrosion was alleviated, and the in-situ grown BCN/Gr sample showed the best corrosion resistance ability, which was consistent with the previous electrochemical test results. Figure 5f–h shows the SEM images of BCN, BCN-Gr, and in-situ grown BCN/Gr samples after salt spray testing for 8 h. It can be clearly seen that the BCN layer grown on the Cu substrate (Figure 5f) was

severely cracked and peeled off from the substrate. At the initial stage of corrosion, the BCN film on the substrate surface could block the corrosion reaction from the Cu foil substrate, thus reducing corrosion. With the extension of time, Cl^- in the corrosive solution gradually passed through the protective layer, and a large amount of Cl^- was adsorbed on the surface of the matrix and reacted with Cu; thus, the BCN film started to be damaged and its anti-corrosion effect was greatly reduced, causing corrosion on the surface of the Cu substrate. As shown in Figure 5g, the BCN-Gr composite prepared by the transfer method had less corrosion and the decorative films were partially complete after the salt spray experiments. The transfer boundary was clear, only small pitting corrosion occurred, and a small amount of salt particles remained. Because of the grain boundary dislocation of the two-layer structure, even the surface layer (graphene) cracked and it was difficult for Cl^- to continue to diffuse through the bottom layer (BCN), causing damage to the Cu substrate. Finally, the in-situ grown BCN/Gr composite showed the best protection effect (Figure 5h). The corrosion mainly occurred at the grain boundary, and other locations were effectively protected except for some residual salt particles. The results of the salt spray experiments were consistent with the electrochemical experiments, confirming the protective effect of the in-situ grown BCN/Gr composite on the metal surface.

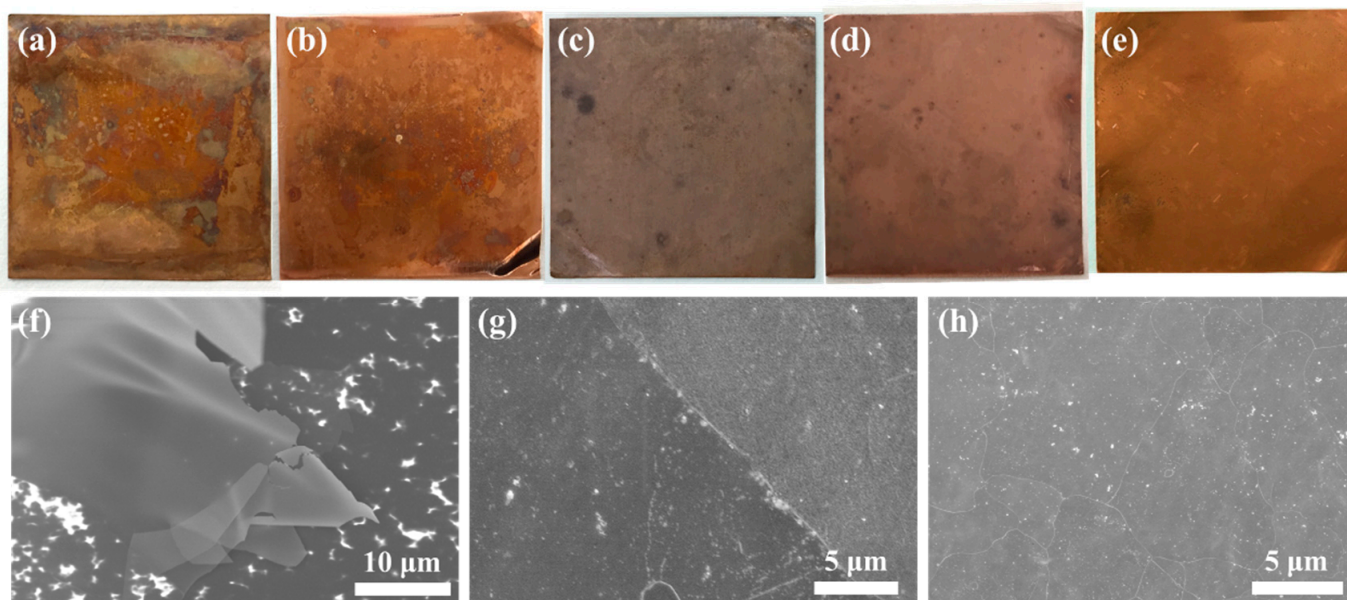


Figure 5. (a–e): Optical photos of bare copper foil (a), BCN (b), BCN-BCN (c), BCN-Gr (d), and BCN/Gr (e) samples after 8 h salt spray testing (sample size: 2 cm × 2 cm); (f–h) SEM images of BCN (f), BCN-Gr (g), and BCN/Gr (h) samples after 8 h salt spray testing.

2D films protect the metal substrate through their tight combination with the substrate and impermeability. Therefore, the combination of the 2D film with the metal substrate is an important factor affecting their anti-corrosion performance. Nano scratch testing is used to characterize the adhesion of 2D materials by testing the force required to peel the 2D film from the substrate [43]. Figure 6a shows the schematic diagram of adhesion test. In this study, a nano indentation instrument was used to evaluate adhesion. By applying 150 μN on the surface of 2D films/copper, nano scratch experiments were conducted, and the curves of transverse force and displacement were obtained (Figure 6b). As shown in Figure 6b, when the indenter peeled the 2D material from the metal substrate surface, significant changes in lateral force can be observed, and the variation in lateral force represents the adhesion between the 2D film and the metal substrate. Figure 6c shows the adhesion of the different samples calculated from the lateral force displacement curve. It can be seen that the BCN film showed the minimum adhesion, which may be related to the larger thickness of the BCN 2D film. After another layer of two-dimensional material

was transferred on the surface of BCN/Cu, the adhesion was increased. The adhesion of BCN-BCN was smaller than that of BCN-Gr, which may be because the BCN film was thicker than the graphene film, thus making it difficult for BCN to closely fit with the substrate. Furthermore, the adhesion of the in-situ grown BCN/Gr composite was significantly higher than that of the composite prepared by the transfer method. This might be attributed to the existence of chemical bonds between the directly grown BCN/Gr layer and the substrate, and the existence of van der Waals forces between the BCN and graphene layers, which shows a closer combination with the substrate. This close combination ensured that corrosive substances were less likely to penetrate into the metal substrate and prevented corrosion reactions.

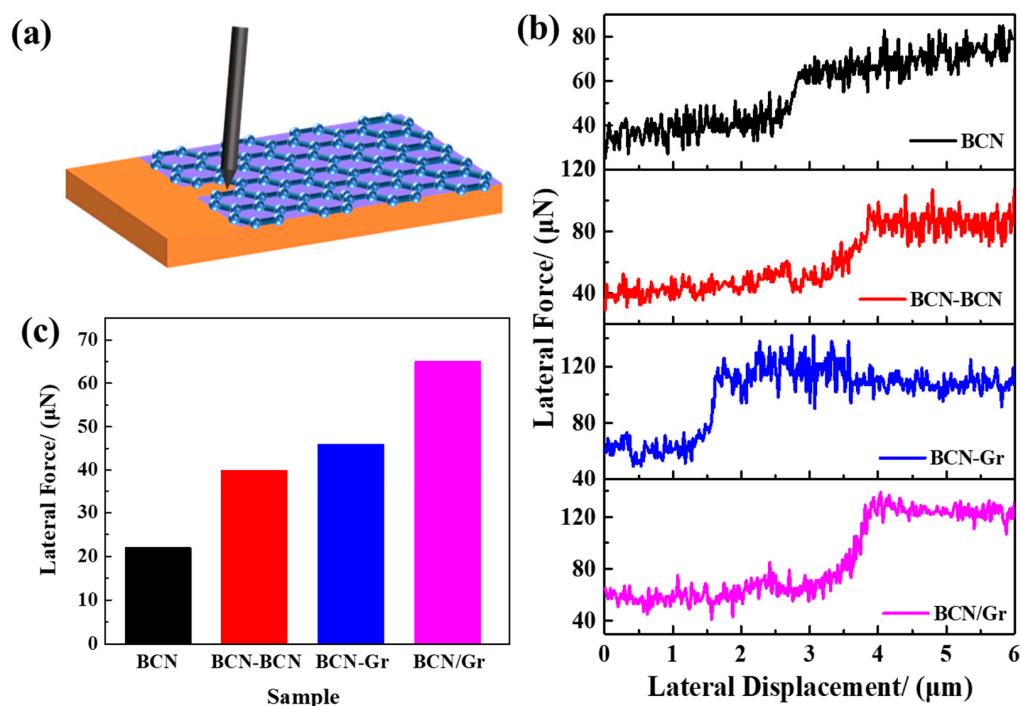


Figure 6. (a) Schematic diagram of adhesion test; (b) The curves of lateral force and displacement of the samples with different surface modifications; (c) Adhesion of different samples calculated from the lateral force-displacement curves.

3. Materials and Methods

3.1. CVD Growth of BCN 2D Films

BCN 2D films were grown using the CVD method, with methane and borane ammonia used as the precursors, Cu foil used as the substrate, and the carbon source flow rate and growth time as the variables. As shown in Figure 1a, the growth process had two heating zones. After exhausting the air in the tubular furnace with Ar, the temperature of the main heating zone was raised to 1000 °C, and the mixed gas of methane and hydrogen was introduced, in which the dehydrogenation of methane molecules produced carbon atoms. Then, the temperature of the auxiliary heating zone was set to 90 °C, and the borane ammonia was decomposed by heat to produce $\text{-BH}_2\text{-NH}_2\text{-}$, which diffused to the main heating zone with the gas flow, decomposed into -B-N- under the high temperature, and was deposited on the copper substrate with carbon atoms to generate the BCN films. The variables in this experiment were carbon source flow rate and growth time, which were $\text{CH}_4 = 20$ sccm, growth for 10 min; $\text{CH}_4 = 40$ sccm, growth for 20 min; and $\text{CH}_4 = 40$ sccm, growth for 40 min. The samples were named BCN1, BCN2, and BCN3, respectively.

3.2. In-Situ Catalytic Growth of BCN/Gr 2D Composite Films

The preparation of BCN/Gr two-dimensional composite films also used the CVD method, which combined the growth processes of graphene and BCN in the same procedure, with copper foil used as the catalyst and borane ammonia and methane as the precursors. First, we used methane as the carbon source to grow graphene two-dimensional films. During the growth process, clean copper sheets were first put into the main heating zone of the CVD furnace. Subsequently, the quartz tube was vacuumed. After the internal pressure of the system was pumped below 30 pa, it was filled with Ar to normal pressure, and vacuumed it again. This process was repeated three to four times until no air existed in the system. Then, Ar was introduced and its flow was adjusted to 100 sccm. After the inert atmosphere in the quartz tube was adjusted, the temperature of the main heating zone was raised to 1040 °C at a heating rate of 14 °C·min⁻¹, and H₂ was introduced. The flow rate was set at 15 sccm and the temperature was maintained for 30 min. Then, methane (20 sccm) was introduced and the carbon atoms were arranged on the surface of the Cu foil for 20 min. After the growth of the graphene layer, the temperature of the main heating zone was reduced to 1000 °C with the flow rates of methane and hydrogen maintained at 40 and 15 sccm, respectively. Then, heating tape was wound around the auxiliary heating zone to keep the temperature at 90 °C for the decomposition of borane ammonia. At 1000 °C, the flow rate of H₂ was 15 sccm, the flow rate of CH₄ was 40 sccm, and the growth time was set at 10, 20, and 40 min to finally realize the preparation of BCN/Gr composite films. The samples were named BCN/Gr1, BCN/Gr2, and BCN/Gr3, respectively. After the growth period was complete, the heating band was removed, the CH₄ and H₂ were turned off, and the sample was cooled in the furnace to room temperature. Then, the system was filled with Ar to normal pressure and the sample was removed.

3.3. Preparation of BCN-BCN and BCN-Gr 2D Composites by Transfer Method

With PMMA as the transfer carrier, the copper substrate under the BCN and graphene films was etched using the chemical etching method, the BCN and graphene films were transferred to the BCN/Cu grown under different conditions, and the PMMA was removed by acetone after drying. The samples that were prepared by transferring a layer of BCN on the basis of the BCN/Cu grown by the CVD method under different conditions were named BCN-BCN1, BCN-BCN2, and BCN-BCN3, respectively. The samples that were prepared by transferring a layer of graphene film on the basis of the BCN/Cu grown by the CVD method under different conditions were named BCN-Gr1, BCN-Gr2, and BCN-Gr3, respectively.

3.4. Electrochemical Test

A three-electrode system was used for electrochemical testing to evaluate the corrosion resistance of the samples. The platinum electrode was used as the counter electrode and the saturated calomel electrode was used as the reference electrode. The test was conducted in 5% NaCl solution. The test sample was sealed with silicone rubber, leaving a 1 cm² exposed area to be measured. After the silicone rubber was completely cured, the samples were used as the working electrode to obtain Tafel curves and electrochemical impedance spectroscopy (EIS) was conducted on the samples in the three-electrode system. The frequency range was set as 1~100 kHz during the EIS tests. Finally, the corrosion rates were calculated by determining the tangent lines of the Tafel curves.

3.5. Salt Spray Test

A salt spray box was used for salt spray testing. First, 5% NaCl solution was prepared and the pH value was adjusted to 6.5–7.2. Then, the samples to be tested were put into the salt spray box and the samples were inclined at an angle of 15–30° to the vertical plane. After spraying for 8 h, the samples were removed, and the salt particles attached to the surface were quickly washed with deionized water. Finally, further characterizations were carried out after the samples were dried.

3.6. Nano Scratch Test

A Hysitron TriboScope nano indenter was used to conduct the nano scratch experiments. The indenter used in the experiment was a Berkovich diamond indenter and the curvature radius of the tip was approximately 150 nm. A transverse force (150 μN) was applied on the two-dimensional film/Cu substrates, and the nano scratch experiments were carried out to obtain the curves of transverse force and displacement. When the indenter peeled the two-dimensional material from the substrate surface, significant changes in the lateral force were observed. The difference between the lateral force was identified as the adhesion between the material and the substrate.

4. Conclusions

In conclusion, BCN/Gr 2D composite with a complete structure was directly grown on the surface of copper foil by in-situ catalytic growth and delicately controlled precursors and reaction conditions. Through morphological analysis, electrochemical testing, adhesion measurements, and salt spray testing, it can be seen that the in-situ grown BCN/Gr 2D composite exhibited the best anti-corrosion ability with the advantages of grain boundary dislocation and strong adhesion with the metal substrate. As a result, the corrosion resistance of the in-situ grown BCN/Gr composite was greatly improved, with a corrosion rate 91.4% and 57.1% lower than that of bare Cu foil and BCN-Gr composite prepared by the transfer method, respectively, showing its potential in corrosion protection applications. This study not only proposes a new strategy for preparing new 2D composite films, but also provides a new approach for the application of 2D nanomaterials in corrosion protection.

Supplementary Materials: The following supporting information can be downloaded at: <https://www.mdpi.com/article/10.3390/catal12121618/s1>, Figure S1: SEM image of graphene grown on Cu foil; Figure S2: EDS of BCN/Gr 2D composite film; Figure S3: (a) TEM and (b) AFM of in-situ grown BCN film; (c) TEM and (d) AFM of BCN/Gr 2D composite film; Figure S4: Diagram of liquid etching method and preparation of BCN-BCN and BCN-Gr samples; Figure S5: Raman spectrum of CVD grown graphene.

Author Contributions: Conceptualization, C.D.; methodology, C.D. and Y.J.; validation, X.L., L.H. and Z.Z.; formal analysis, X.L.; investigation, C.D. and X.L.; data curation, X.L. and L.H.; writing—original draft preparation, C.D.; writing—review and editing, C.D., Z.Z., J.Q. and X.L.; supervision, Z.Z. and Y.J.; project administration, J.Q.; funding acquisition, C.D. and Z.Z. All authors have read and agreed to the published version of the manuscript.

Funding: This research was funded by National Natural Science Foundation of China (No. 52273075) and the Talent project of Liaoning Petrochemical University (Nos. 1100011651, 1100011652).

Data Availability Statement: Data is contained within the article.

Acknowledgments: The authors thank the National Natural Science Foundation of China (No. 52273075) and the Talent project of Liaoning Petrochemical University (Nos. 1100011651, 1100011652) for financial support.

Conflicts of Interest: The authors declare no conflict of interest.

References

- Bohm, S. Graphene against corrosion. *Nat. Nanotechnol.* **2014**, *9*, 741–742. [CrossRef] [PubMed]
- Novoselov, K.S.; Fal'Ko, V.I.; Colombo, L.; Gellert, P.R.; Schwab, M.G.; Kim, K. A roadmap for graphene. *Nature* **2012**, *490*, 192–200. [CrossRef] [PubMed]
- Farag, A.A.; Toghan, A.; Mostafa, M.S.; Lan, C.; Ge, G.L. Environmental remediation through catalytic inhibition of steel corrosion by schiff's bases: Electrochemical and biological aspects. *Catalysts* **2022**, *12*, 838. [CrossRef]
- Wu, Q.Y.; Chen, C.Y.; Liu, L. Preparation and anticorrosion performance of TiO₂-based nanocontainers. *J. Petrochem. Univ.* **2021**, *34*, 7–12.
- Bunch, J.S.; Verbridge, S.S.; Alden, J.S.; Zande, A.M.; Parpia, J.M.; Craighead, H.G.; McEuen, P.L. Impermeable atomic membranes from graphene sheets. *Nano Lett.* **2008**, *8*, 2458–2462. [CrossRef] [PubMed]

6. Kulyk, B.; Freitas, M.A.; Santos, N.F.; Mohseni, F.; Carvalho, A.F.; Yasakau, K.; Fernandes, A.J.S.; Adriana, B.; Figueiredo, B.; Silva, R.; et al. A critical review on the production and application of graphene and graphene-based materials in anti-corrosion coatings. *Crit. Rev. Solid State* **2022**, *47*, 309–355. [CrossRef]
7. Wu, Y.M.; Zhao, W.J.; Qiang, Y.J.; Chen, Z.J.; Wang, L.P.; Gao, X.L.; Fang, Z.W. π - π interaction between fluorinated reduced graphene oxide and acridizinium ionic liquid: Synthesis and anti-corrosion application. *Carbon* **2020**, *159*, 292–302. [CrossRef]
8. Schriver, M.; Regan, W.; Gannett, W.J.; Zaniewski, A.M.; Crommie, M.F.; Zettl, A. Graphene as a long-term metal oxidation barrier: Worse than nothing. *ACS Nano* **2013**, *7*, 5763–5768. [CrossRef]
9. Ollik, K.; Lieder, M. Review of the application of graphene-based coatings as anticorrosion layers. *Coatings* **2020**, *10*, 883. [CrossRef]
10. Geim, A.K.; Novoselov, K.S. The rise of graphene. *Nat. Mater.* **2007**, *6*, 183–191. [CrossRef]
11. Nair, R.R.; Blake, P.; Grigorenko, A.N.; Novoselov, K.S.; Booth, T.J.; Stauber, T.; Peres, N.M.R.; Geim, A.K. Fine structure constant defines visual transparency of graphene. *Science* **2008**, *320*, 1308. [CrossRef] [PubMed]
12. Saeed, M.A.; Kinloch, I.A.; Derby, B. Atmospheric pressure catalytic vapor deposition of graphene on liquid In and Cu-In alloy substrates. *Catalysts* **2021**, *11*, 1318. [CrossRef]
13. Surwade, S.P.; Smirnov, S.N.; Vlasiouk, I.V.; Unocic, R.R.; Veith, G.M.; Dai, S.; Mahurin, S.M. Water desalination using nanoporous single-layer graphene. *Nat. Nanotechnol.* **2015**, *10*, 459–464. [CrossRef] [PubMed]
14. Cheng, Z.H.; Liao, J.; He, B.Z.; Zhang, F.; Zhang, F.; Huang, X.H.; Zhou, L. One-step fabrication of graphene oxide enhanced magnetic composite gel for highly efficient dye adsorption and catalysis. *ACS Sustain. Chem. Eng.* **2015**, *3*, 1677–1685. [CrossRef]
15. Stoller, M.D.; Park, S.; Zhu, Y.W.; An, J.; Ruoff, R.S. Graphene-based ultracapacitors. *Nano Lett.* **2008**, *8*, 3498–3502. [CrossRef]
16. Chen, H.; Chen, Z.; Yang, H.; Wen, L.H.; Yi, Z.; Zhou, Z.G.; Dai, B.; Zhang, J.G.; Wu, X.W.; Wu, P.H. Multi-mode surface plasmon resonance absorber based on dart-type single-layer graphene. *RSC Adv.* **2022**, *12*, 7821–7829. [CrossRef]
17. Lee, C.; Wei, X.D.; Kysar, J.W.; Hone, J. Measurement of the elastic properties and intrinsic strength of monolayer graphene. *Science* **2008**, *321*, 385–388. [CrossRef]
18. Zhang, Z.H.; Cai, R.; Long, F.; Wang, J. Development and application of tetrabromobisphenol a imprinted electrochemical sensor based on graphene/carbon nanotubes three-dimensional nanocomposites modified carbon electrode. *Talanta* **2015**, *134*, 435–442. [CrossRef]
19. Shangguan, Q.; Chen, Z.; Yang, H.; Cheng, S.B.; Yang, W.X.; Yi, Z.; Wu, X.W.; Wang, S.F.; Yi, Y.G.; Wu, P.H. Design of ultra-narrow band graphene refractive index sensor. *Sensors* **2022**, *22*, 6483. [CrossRef]
20. Luo, X.H.; Zhong, J.W.; Zhou, Q.L.; Du, S.; Yuan, S.; Liu, Y.L. Cationic reduced graphene oxide as self-aligned nanofiller in the epoxy nanocomposite coating with excellent anticorrosive performance and its high antibacterial activity. *ACS Appl. Mater. Inter.* **2018**, *10*, 18400–18415. [CrossRef]
21. Novoselov, K.S.; Geim, A.K.; Morozov, S.V.; Jiang, D.; Zhang, Y.; Dubonos, S.V.; Grigorieva, I.V.; Firsov, A.A. Electric field effect in atomically thin carbon films. *Science* **2004**, *306*, 666–669. [CrossRef] [PubMed]
22. Kaloni, T.P.; Joshi, R.P.; Adhikari, N.P.; Schwingenschlogl, U. Band gap tuning in BN-doped graphene systems with high carrier mobility. *Appl. Phys. Lett.* **2014**, *104*, 73116. [CrossRef]
23. Song, L.; Liu, Z.; Reddy, A.L.M.; Narayanan, T.; Taha-Tijerina, J.; Peng, J.; Gao, G.H.; Lou, J.; Vajtai, R.; Ajayan, P.M. Binary and ternary atomic layers built from carbon, boron, and nitrogen. *Adv. Mater.* **2012**, *24*, 4878–4895. [CrossRef] [PubMed]
24. Iyyamperumal, E.; Wang, S.Y.; Dai, L.M. Vertically aligned BCN nanotubes with high capacitance. *ACS Nano* **2012**, *6*, 5259–5265. [CrossRef]
25. Garel, J.; Zhao, C.; Popovitz-Biro, R.; Golberg, D.; Wang, W.; Joselevich, E. BCN nanotubes as highly sensitive torsional electromechanical transducers. *Nano Lett.* **2014**, *14*, 6132–6137. [CrossRef] [PubMed]
26. Puyoo, G.; Teyssandier, F.; Paillet, R.; Labrugère, C.; Chollon, G. Boron carbonitride coatings synthesized by LPCVD, structure and properties. *Carbon* **2017**, *122*, 19–46. [CrossRef]
27. Li, X.S.; Magnuson, C.W.; Venugopal, A.; Tromp, R.M.; Hannon, J.B.; Vogel, E.M.; Colombo, L.; Ruoff, R.S. Large-area graphene single crystals grown by low-pressure chemical vapor deposition of methane on copper. *J. Am. Chem. Soc.* **2011**, *133*, 2816–2819. [CrossRef]
28. Nanayakkara, T.R.; Wijewardena, U.K.; Withanage, S.M.; Kriisa, A.; Samaraweera, R.L.; Mani, R.G. Strain relaxation in different shapes of single crystal graphene grown by chemical vapor deposition on copper. *Carbon* **2020**, *168*, 684–690. [CrossRef]
29. Zhu, Y.X.; Duan, C.Y.; Liu, H.Y.; Chen, Y.F.; Wang, Y. Graphene coating for anti-corrosion and the investigation of failure mechanism. *J. Phys. D: Appl. Phys.* **2017**, *50*, 114001. [CrossRef]
30. Coleman, J.N.; Lotya, M.; Neill, A.O.; Bergin, S.D.; King, P.J.; Khan, U.; Young, K.; Gaucher, A.; De, S.; Smith, R.J.; et al. Two-dimensional nanosheets produced by liquid exfoliation of layered materials. *Science* **2011**, *331*, 568–571. [CrossRef]
31. Yan, K.A.I.; Fu, L.E.I.; Peng, H.; Liu, Z.F. Designed CVD growth of graphene via process engineering. *Acc. Chem. Res.* **2013**, *46*, 2263–2274. [CrossRef] [PubMed]
32. Duan, C.Y.; Zhu, Y.X.; Gu, W.; Li, M.Q.; Zhao, D.; Zhao, Z.H.; Chen, Y.F.; Wang, Y. Atomic coupling growth of graphene on carbon steel for exceptional anti-icing performance. *ACS Sustain. Chem. Eng.* **2018**, *6*, 17359–17367. [CrossRef]
33. Somani, P.R.; Somani, S.P.; Umeno, M. Planer nano-graphenes from camphor by CVD. *Chem. Phys. Lett.* **2006**, *430*, 56–59. [CrossRef]

34. Robertson, A.W.; Warner, J.H. Hexagonal single crystal domains of few-layer graphene on copper foils. *Nano Lett.* **2011**, *11*, 1182–1189. [CrossRef] [PubMed]
35. Ramnani, P.; Neupane, M.R.; Ge, S.; Balandin, A.A.; Lake, R.K.; Mulchandani, A. Raman spectra of twisted CVD bilayer graphene. *Carbon* **2017**, *123*, 302–306. [CrossRef]
36. Attri, R.; Roychowdhury, S.; Biswas, K.; Rao, C.N.R. Low thermal conductivity of 2D borocarbonitride nanosheets. *J. Solid State Chem.* **2020**, *282*, 121105. [CrossRef]
37. Levendorf, M.P.; Kim, C.J.; Brown, L.; Huang, P.Y.; Havener, R.W.; Muller, D.A.; Park, J. Graphene and boron nitride lateral heterostructures for atomically thin circuitry. *Nature* **2012**, *488*, 627–632. [CrossRef]
38. Linss, V.; Rodil, S.E.; Reinke, P.; Garnier, M.G.; Oelhafen, P.; Kreissig, U.; Richter, F. Bonding characteristics of DC magnetron sputtered B–C–N thin films investigated by fourier-transformed infrared spectroscopy and X-ray photoelectron spectroscopy. *Thin Solid Films* **2004**, *467*, 76–87. [CrossRef]
39. Cheng, L.K.; Meng, J.H.; Pan, X.J.; Lu, Y.; Zhang, X.W.; Gao, M.L.; Yin, Z.G.; Wang, D.G.; Wang, Y.; You, J.B.; et al. Two-dimensional hexagonal boron–carbon–nitrogen atomic layers. *Nanoscale* **2019**, *11*, 10454–10462. [CrossRef]
40. Huh, J.H.; Kim, S.H.; Chu, J.H.; Kim, S.Y.; Kim, J.H.; Kwon, S.Y. Enhancement of seawater corrosion resistance in copper using acetone-derived graphene coating. *Nanoscale* **2014**, *6*, 4379–4386. [CrossRef]
41. Zhang, J.; Yang, Y.C.; Lou, J. Investigation of hexagonal boron nitride as an atomically thin corrosion passivation coating in aqueous solution. *Nanotechnology* **2016**, *27*, 364004. [CrossRef] [PubMed]
42. Liu, R.Q.; Fan, M.; Liang, P. Effect of nitric acid passivation time on corrosion behavior of S32750 super duplex stainless steel. *J. Liaoning Petrochem. Univ.* **2020**, *40*, 78–83.
43. Das, S.; Lahiri, D.; Lee, D.; Agarwal, A.; Choi, W. Measurements of the adhesion energy of graphene to metallic substrates. *Carbon* **2013**, *59*, 121–129. [CrossRef]

Article

Copper–Cerium–Tin Oxide Catalysts for Preferential Oxidation of CO in Hydrogen: Effects of Synthesis Method and Copper Content

Igor Yu. Kaplin *, Ekaterina S. Lokteva *, Artem V. Tikhonov, Konstantin I. Maslakov , Oksana Ya. Isaikina and Elena V. Golubina 

Department of Chemistry, Lomonosov Moscow State University, Leninskie Gory, 1, bld. 3, 119991 Moscow, Russia
* Correspondence: kaplinigormsu@gmail.com (I.Y.K.); e.lokteva@rambler.ru (E.S.L.)

Abstract: Copper was incorporated into the Ce-Sn and comparative Ce-Zr oxide supports by one-pot precipitation in the presence of CTAB template and by the impregnation of templated Ce-Sn and Ce-Zr oxides. The synthesized Cu-Ce-Sn and Cu-Ce-Zr catalysts were tested in the continuous-flow preferential oxidation of CO in hydrogen excess. The one-pot synthesized tin- and zirconium-doped catalysts demonstrated better CO conversion and CO₂ selectivity than their impregnated counterparts. For the tin-modified ternary system that showed the best catalytic performance, the copper content was further optimized. The structure, reducibility, surface chemical state and textural properties of the catalysts were analyzed by SEM-EDX, XRD, H₂-TPR, Raman spectroscopy, XPS and TEM. The nonmonotonic changes in the specific surface area, Cu⁺/Cu²⁺ ratio and ratio of lattice and non-lattice oxygen with increasing the Cu content are discussed in terms of copper distribution in the catalysts. The influence of the interaction between copper oxide species and the cerium–tin/cerium–zirconium oxide support on the performance of the ternary catalysts was thoroughly analyzed and discussed.

Keywords: CO catalytic oxidation; CO preferential oxidation; template; CTAB; mixed oxides; copper oxides; ceria; tin oxides



Citation: Kaplin, I.Y.; Lokteva, E.S.; Tikhonov, A.V.; Maslakov, K.I.; Isaikina, O.Y.; Golubina, E.V.

Copper–Cerium–Tin Oxide Catalysts for Preferential Oxidation of CO in Hydrogen: Effects of Synthesis Method and Copper Content.

Catalysts **2022**, *12*, 1575. <https://doi.org/10.3390/catal12121575>

Academic Editors: Yongjun Ji, Liwen Xing and Ke Wu

Received: 31 October 2022

Accepted: 29 November 2022

Published: 3 December 2022

Publisher's Note: MDPI stays neutral with regard to jurisdictional claims in published maps and institutional affiliations.



Copyright: © 2022 by the authors. Licensee MDPI, Basel, Switzerland. This article is an open access article distributed under the terms and conditions of the Creative Commons Attribution (CC BY) license (<https://creativecommons.org/licenses/by/4.0/>).

1. Introduction

Global environmental challenges stimulate the development of the carbon-free industry, in which hydrogen is an important energy carrier. Today, H₂ is used as a clean energy source in polymer electrolyte membrane fuel cells. But the high purity of H₂ is required for the more efficient operation of such devices. Even traces of CO (less than 100 ppm) remaining in hydrogen after fuel reforming and the water gas shift reaction should be removed to prevent poisoning of the Pt anode of the fuel cell [1–3]. Preferential CO oxidation (CO-PROX) is considered as one of the simplest and most efficient methods for reducing the CO concentration in the H₂ reach stream to an acceptable level.

The catalysts used at this stage should be highly active and selective in H₂ excess. They should also tolerate large amounts of CO₂ and H₂O in the feed stream and be stable and durable in a wide operating temperature range [4].

Although noble metals are very active in CO oxidation [5,6] and show high performance in the CO-PROX [1,7], they have certain disadvantages. The most important ones are their high price, rapid deactivation under high temperature treatment and, in some cases, low selectivity. Copper oxide catalysts supported on cerium dioxide (ceria) are a promising alternative due to their affordable cost, high activity, selectivity and stability [8,9]. Varying the synthesis method, pretreatment conditions, type of promoters and other modifiers allows tuning the catalyst properties in a targeted manner [4,10,11]. Specifically, in the CO-PROX reaction, it is necessary to efficiently convert CO on the catalyst surface while minimizing undesirable hydrogen conversion. The improved performance of the catalyst is achieved via a synergistic action of a nonstoichiometric support that provides oxygen vacancies and an active component that adsorbs and activates CO [12]. The interaction of

copper and cerium oxides [13]—in particular, the extent of their contact [14]—are widely discussed in the literature. Several reasons were proposed to explain their synergistic action in oxidation catalysis. Among them are the redox interplay between $\text{Ce}^{3+}/\text{Ce}^{4+}$ and $\text{Cu}^+/\text{Cu}^{2+}$ redox pairs, ample amount of oxygen vacancies, improvement of the reduction properties of each component, ligand and geometric effects, especially on the $\text{CuO}-\text{CeO}_2$ interface [13,15].

A significant number of works have been devoted to thermally stable cerium–zirconium catalysts [16–23]. Doping with tin dioxide was recently reported as a promising way for the modification of cerium-based catalysts [24,25]. It was demonstrated that a solid solution of tin in the crystal lattice of cerium oxide was formed up to a tin oxide content of 5–10 wt.% [26,27]. Earlier, we synthesized for the first time the Cu–Ce–Sn oxide catalysts with the Ce:Sn mole ratio of 9:1 using the cetyltrimethylammonium bromide (CTAB) template and demonstrated its high catalytic activity in the total CO oxidation [28]. It was attributed to the relatively high specific surface area of the catalysts, high dispersion of CuO_x species and the presence of active copper oxide–ceria interfacial sites.

However, the effects of the copper content and strength of the interaction between copper oxide and ceria on the performance of the CTAB-templated Cu–Ce–Sn oxide catalysts in CO-PROX have not been thoroughly analyzed. Modifying the synthesis method is a promising way to control the strength of interactions between components of ternary oxide catalysts and their surface chemistry.

That is why this work compares two methods for copper incorporation into $\text{Ce}_{0.9}\text{Sn}_{0.1}\text{O}_2$ oxide (further denoted as CeSn). In the first one, CuO-modified $\text{Ce}_{0.9}\text{Sn}_{0.1}\text{O}_2$ (further denoted as CuCeSn) was prepared by the one-pot precipitation method using a sacrificial CTAB template and citric acid as a complexing agent. In the second method, copper was supported on $\text{Ce}_{0.9}\text{Sn}_{0.1}\text{O}_2$ by wet impregnation. The synthesized catalysts were compared with the CuCeZr catalysts produced by the same methods. The copper content was optimized in the CuCeSn catalyst prepared by the more efficient single-stage one-pot method. Different physicochemical methods, including the X-ray diffraction analysis, temperature-programmed reduction with hydrogen, low-temperature nitrogen physisorption, X-ray photoelectron and Raman spectroscopies and electron microscopy, were used to elucidate the influence of the preparation method and copper content on the physicochemical and catalytic properties of the synthesized catalysts in the flow-type CO-PROX.

2. Results

2.1. Catalytic Performance in CO-PROX

The temperature dependencies of the CO and O_2 conversions and CO_2 selectivity for all the synthesized catalysts (Figure 1) allowed qualitatively compared their catalytic activities, because all the catalysts were tested under the same conditions.

Firstly, we tested the catalysts synthesized by different methods but with the same copper content of 20% calculated as $(n(\text{Cu}) \cdot 100\%)/[n(\text{Ce}) + n(\text{Sn})]$ that corresponded to the copper loading of 6.1 wt.% relative to the CeSn support (Figure 1a–c). These catalysts were denoted as 20CuCeSn. Their Zr-containing counterparts (20CuCeZr) were also tested in the CO-PROX. For a better comparison, the equal Ce:Zr and Ce:Sn ratios of nine were used in the catalysts. The names of impregnated samples were ended with “-im”.

Among the samples with the same composition, the one-pot synthesized catalysts were more active than the impregnated ones. The tin-containing one-pot synthesized 20CuCeSn showed higher CO conversion than its Zr-containing 20CuCeZr counterpart (Figure 1a). However, at low temperatures of 100–150 °C, the one-pot synthesized 20CuCeZr catalyst was more efficient than the impregnated 20CuCeSn-im, while, at higher temperatures (at 250–450 °C), they showed similar CO conversions.

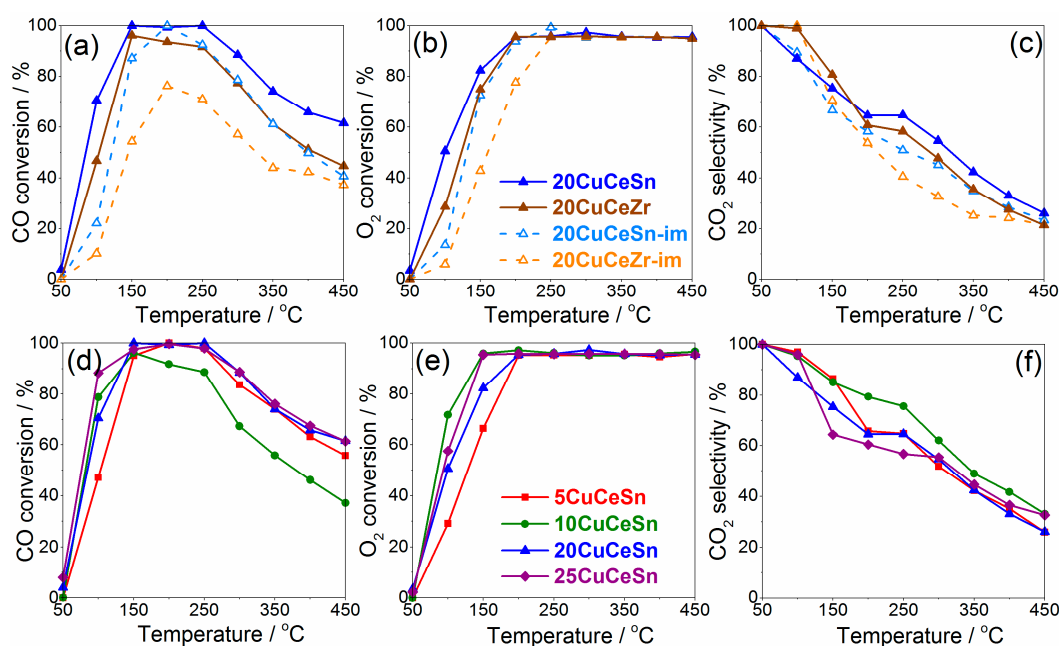


Figure 1. CO (a,d) and O₂ (b,e) conversions and CO₂ selectivity (c,f) vs. reaction temperature for CuCeSn and CuCeZr catalysts with the same (a–c) and different (d–f) copper contents.

Not only CO conversion but also carbon dioxide selectivity are very important for the cost efficiency of the catalyst in the CO-PROX process. As expected, the CO₂ selectivity decreased for all the catalysts with increasing the reaction temperature. The conversion of oxygen at higher temperatures remained close to 100%, while both the CO conversion and CO₂ selectivity decreased (Figure 1b). This fact suggests that a part of the oxygen was consumed by the hydrogen oxidation reaction that produced water. Among all the synthesized catalysts, 20CuCeSn exhibited the highest CO₂ selectivity in a wide temperature range of 200–450 °C (Figure 1c). Note that, at 200–250 °C, a high CO₂ selectivity was achieved at 100% CO conversion, which provided the target process parameters—complete removal of CO at low degree of hydrogen oxidation, which makes this catalyst cost-efficient. The Zr-containing one-pot synthesized 20CuCeZr catalyst demonstrated higher CO₂ selectivity (98–99%) at 100–150 °C than its tin-containing counterpart but at the cost of a lower CO conversion. It can be concluded that templated coprecipitation is the most efficient method for preparation of ternary 20CuCeSn and 20CuCeZr catalysts, but the former catalyst is more efficient. Therefore, it was chosen for the Cu content optimization.

The catalytic results for the one-pot synthesized samples with different copper contents are shown in Figure 1d–f. All these catalysts demonstrated a significant CO conversion even at 100 °C, but 25CuCeSn and 10CuCeSn were the most active at this temperature, showing CO conversions of 88 and 79%, respectively. At 150 °C, all the catalysts demonstrated near 100% CO conversion. Taking into account the uncertainty of the CO conversion measurement, the efficiencies of all the catalysts, except for the somewhat less efficient 10CuCeSn sample, were similar in the temperature range from 150 to 250 °C. At higher temperatures, the CO conversion decreased for all the catalysts.

10CuCeSn demonstrated the highest CO₂ selectivity at 200–400 °C (Figure 1f). Despite its lower CO conversion in this temperature range among the catalysts with different copper contents, it was still high enough (over 80%) to provide a good balance between reasonable CO and O₂ conversions and high CO₂ selectivity. At a relatively low temperature of 100 °C, the efficiencies of 10CuCeSn and 5CuCeSn were similarly high. However, the widest operating windows were observed for the 20CuCeSn and 25CuCeSn catalysts with high copper loadings.

A 65% CO conversion and 70% CO₂ selectivity at 100 °C were earlier reported for the 5wt.%CuO/CeO₂ catalyst synthesized by the precipitation method [29]. Our 10CuCeSn

catalyst with a lower copper content (3.4 wt.% of Cu according to the AAS data) exhibited at this temperature the CO conversion of about 80% and CO₂ selectivity above 90%. However, the 5wt.%CuO/CeO₂ sample prepared in the above-mentioned work by the hydrothermal method showed a higher catalytic performance than that of our catalyst. However, in addition to the higher copper loading than in our 10CuCeSn catalyst, a stoichiometric CO/O₂ reaction mixture with a lower hydrogen content (50 vs. 80 vol.% H₂ in our work) and more than eight times higher contact time (0.800 vs. 0.095 g·s/cm³ in our work) were used in [29] for catalytic tests. Under similar test conditions, the performance of our catalysts should be better.

The stability of 10CuCeSn was tested in the isothermal conditions at 200 °C for more than 10 h time-on-stream (Figure 2) at longer contact time than in short-time tests. No loss of activity was observed after more than 10 h of the test at a CO conversion of about 99.8% and CO₂ selectivity of about 92%.

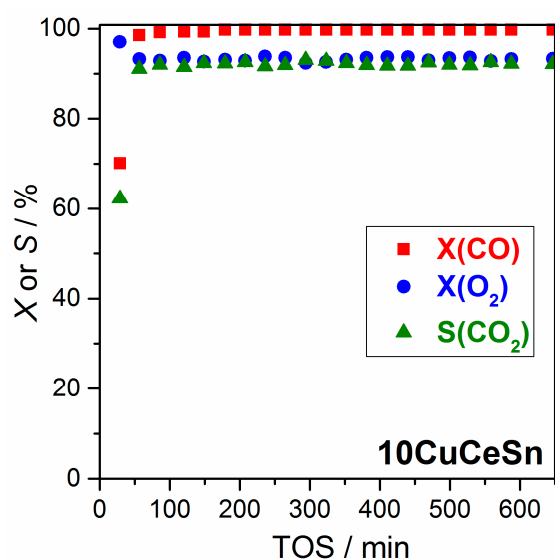


Figure 2. Results of the stability test for 10CuCeSn at 200 °C (reaction mixture: 4 vol.% CO, 3 vol.% O₂, 13 vol.% N₂ and 80 vol.% H₂).

2.2. Physicochemical Characterization of Catalysts Synthesized by Different Techniques

The physicochemical parameters of the 20Cu series catalysts prepared by the two methods were measured by N₂ physisorption, XRD, XPS and H₂-TPR, and the results are summarized in Table 1.

Table 1. Physicochemical parameters of 20CuCeSn and 20CuCeZr catalysts prepared by the one-pot and wet impregnation methods.

Sample	S _{BET} , m ² /g	Average CeO ₂ Crystallite Size, nm	XPS Atomic and Ion Ratios				H ₂ Uptake, μmol/g	
			Ce/Cu	Ce/Sn(Zr)	Ce ³⁺ /Ce ⁴⁺	Cu ⁺ /Cu ²⁺	Low T Range (80–400 °C)	Medium T Range (400–650 °C)
20CuCeSn	149 ± 15	5 ± 1	5.8	6.3	0.11	0.70	1479	100
20CuCeZr	28 ± 3	10 ± 1	4.0	9.7	0.11	0.20	1417	159
20CuCeSn-im	81 ± 8	12 ± 1	2.9	20.0	0.04	0.18	1248	85
20CuCeZr-im	27 ± 3	15 ± 1	2.2	10.3	0.07	0.39	933	136

Figure S1 (Supplementary Materials, SM) shows the SEM micrographs of these catalysts and the EDX mappings of the Sn(Zr) and Cu distributions on the catalyst surface. Rather large particles from 50 to 200 μm in size were observed in all the catalysts. The Zr-containing samples looked much less porous, which agreed with their lower specific surface areas. Copper-enriched areas were not detected on the surfaces of all the samples,

even of those synthesized by the impregnation, which can be explained by the relatively low Cu content (6.1 wt.%).

The textural parameters of the catalysts were measured by low-temperature nitrogen physisorption. Though the different synthesis methods were used for 20CuCeZr and 20CuCeZr-im, their physisorption isotherms (Figure S2 in Supplementary Materials) and specific surface areas (Table 1) were similar. The average pore sizes calculated from the NL-DFT pore size distributions were 3.1 and 5.7 nm for 20CuCeSn and 20CuCeSn-im and 7 and 12 nm for 20CuCeZr and 20CuCeZr-im, respectively.

Higher BET specific surface areas of the tin-containing catalysts (Table 1) testify to a much more developed surface of these catalysts than of their Zr-doped counterparts. The impregnated 20CuCeSn-im demonstrated a lower specific surface area than its one-pot synthesized counterpart (20CuCeSn). In contrast to the one-pot synthesized catalyst, CuO_x particles in the impregnated 20CuCeSn-im sample can block micro- and small mesopores. The specific surface areas of CuCeZr and CuCeZr-im were about the same but much lower than those of their Sn-doped counterparts, which may be the reason for the lower activity of the former catalysts in CO oxidation.

To analyze the phase composition of the catalysts, they were studied by XRD and Raman spectroscopy. The diffraction patterns of all the studied samples (Figure 3a) show only broad reflections of the fluorite phase of CeO₂. Thus, the samples did not contain well-crystallized phases of tin/zirconium and copper oxides. We may assume that copper existed in the samples both as ions incorporated into the ceria or double cerium–zirconium/cerium–tin oxide lattice and as highly dispersed X-ray amorphous copper oxide species.

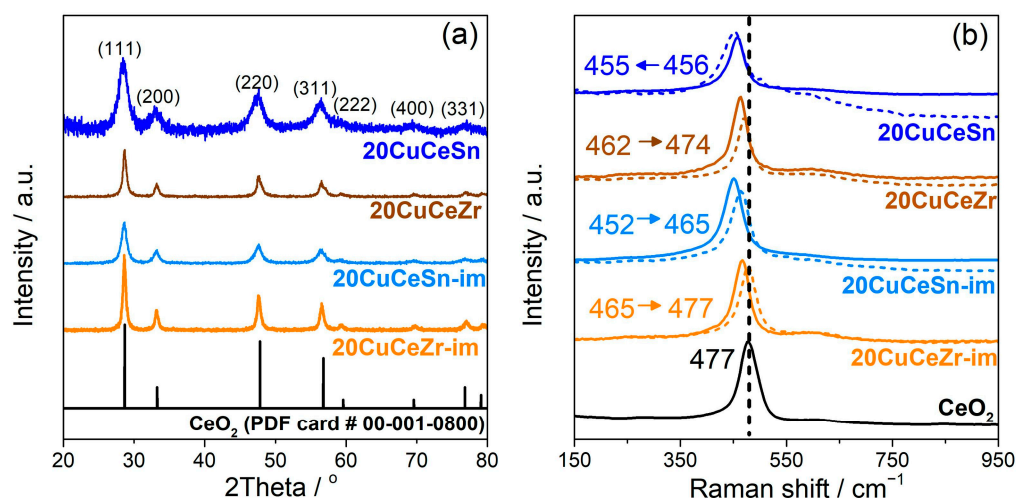


Figure 3. XRD patterns (a) and Raman spectra (b) of 20CuCeSn, 20CuCeZr, 20CuCeSn-im and 20CuCeZr-im catalysts before (solid lines) and after catalytic tests (dashed lines).

The Raman spectroscopy data testify to the inclusion of zirconium/tin and copper ions into the crystal structure of cerium oxide (Figure 3b). The main F_{2g} band in the 440–465 cm⁻¹ region confirms the cubic fluorite structure of CeO₂ [30]. This band is broader for tin-containing catalysts, especially for 20CuCeSn, which could result from the small particle size in these catalysts [30,31]. Indeed, according to the XRD data (Table 1), 20CuCeSn has the smallest crystallite size. The slight asymmetry of the F_{2g} band is clearly visible in the spectrum of 20CuCeSn, along with a red shift of the F_{2g} band that points to the presence of oxygen vacancies [30]. Both the asymmetry of the F_{2g} band and its shift for nanosized particles originate from the phonon confinement effect resulting from the high concentration of structural defects and small average crystallite size [32]. The shift of the F_{2g} band for all the Cu-containing catalysts relative to their positions in CeO₂ (Figure 3b) and CeSn double oxide (see Figure 5b below) can be caused by the change in the Ce–O vibration frequency resulting from the incorporation of Cu²⁺ ions. A similar

effect was observed in [33]. The shift of the band maximum is more pronounced for the CuCeSn samples. All spectra also contain a broad low-intensity band at 560–650 cm⁻¹ that is usually denoted as the ‘O_v band’ (where O_v means oxygen vacancies) or ‘D-band’ (D means defects) [31]. It could be attributed to the LO mode (longitudinal mode, F_{1u} symmetry) appearing due to the local asymmetry caused by the presence of Frenkel-type oxygen defects or non-stoichiometry oxygen vacancies in ceria resulting from the reduction of Ce⁴⁺ to Ce³⁺ [31,34]. Due to a rather small crystallite size in the catalysts, it is difficult to accurately determine the contribution of this component to the spectra.

The Raman spectra of the 20Cu series samples are similar before and after catalytic tests (Figure 3b). No carbon-related bands appeared in the spectra. The spectra of all the samples, excluding 20CuCeSn, showed a blue shift of the F_{2g} mode. It can be explained by the partial reduction of cerium in the surface layers under the reaction conditions and by the increase in the fraction of Ce³⁺ ions that are larger than Ce⁴⁺ ones. This shift agrees with the equation that describes the changes in the F_{2g} band frequency with varying the crystal lattice parameters of ceria-based oxide [35]:

$$\Delta\omega = -3 \gamma \omega_0 \frac{\Delta a}{a_0}$$

where γ is the dimensionless Grüneisen constant (1.44 for CeO₂), $\Delta a = (a - a_0)$ is the difference between the crystal lattice parameters of the doped and pure CeO₂ and $\Delta\omega = (\omega - \omega_0)$ is the difference between the frequencies of their F_{2g} bands.

A weak redshift of the F_{2g} band was observed in the Raman spectrum of the most active 20CuCeSn sample. This fact indicates the high stability of this system and the high mobility of oxygen, which ensures its fast transport to the surface from deeper structural layers and allows rapid reoxidation of the catalyst surface.

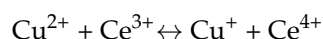
The surface composition of the catalysts was studied by XPS (Table 1). The processing of Ce3d and Cu2p XPS spectra was detailed in our previous work [36].

The survey XPS spectra are presented in Supplementary Materials (Figure S3a). All the samples contained Cu, O, Ce, Sn or Zr and a relatively high amount of carbon on the surface. The latter can be a template/precursor residue or adventitious carbon resulting from the air exposure of the catalysts.

The Ce/Zr atomic ratios on the surface of zirconium-containing samples calculated from the XPS spectra were close to the target values (Table 1). In contrast, the tin-containing 20CuCeSn and 20CuCeSn-im samples demonstrated different surface Ce/Sn ratios. The surface of 20CuCeSn-im was depleted in tin, while that of 20CuCeSn was enriched with this element. These significant differences in the surface compositions of the samples can be explained by the segregation processes and formation of mixed oxide phases with different compositions.

The copper content on the surface of the impregnated catalysts is much higher than that for the 20CuCeSn and 20CuCeZr samples (Table 1). This fact confirms the uniform distribution of copper in the one-pot synthesized catalysts and less uniformity of the impregnated catalysts, which was expected considering the nature of the synthesis methods.

The highest Cu⁺/Cu²⁺ XPS ratio over all samples was found in 20CuCeSn. This fact points to a strong interaction between ceria and CuO_x and easy electron transfer between Cu²⁺ and Ce³⁺ species [28,37]:



The ability of the cerium ion to transfer an electron is confirmed by a high surface Ce³⁺/Ce⁴⁺ ratio. The synergistic model proposed in [37,38] supposes a key role of Cu⁺ species as surface sites for CO adsorption and activation. The in situ XANES and DRIFTS study demonstrated that the CO-PROX reaction over ceria–copper catalysts mainly proceeded via adsorption of CO on Cu⁺ species rather than on Cu²⁺ and Cu⁰ ones [39]. These

Cu⁺ sites are stabilized by the interaction between copper oxide species and cerium oxide on their interface [40]. The role of cerium oxide is to create oxygen vacancies.

The reducibility of the samples was investigated by H₂-TPR. The TPR profiles are presented in Figure 4. This analysis is very important, because the CO-PROX reaction mixture contains an excess of H₂, so the reduction of the catalyst components can proceed during the catalytic test.

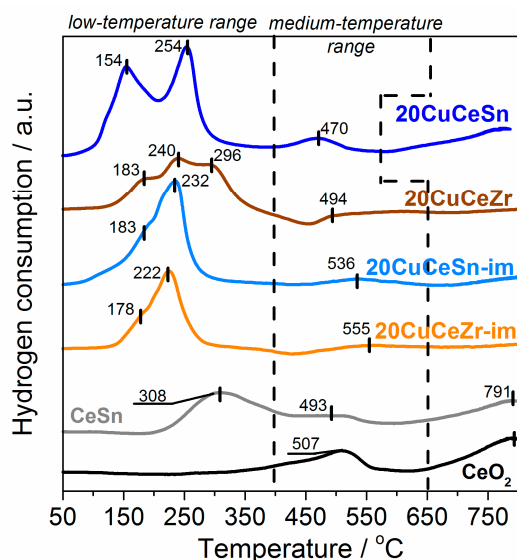


Figure 4. H₂-TPR profiles of 20CuCeSn, 20CuCeZr, 20CuCeSn-im and 20CuCeZr-im catalysts and reference CeSn and CeO₂ samples.

The main peaks in the TPR profiles can be divided into three groups: low-temperature (80–400 °C), medium-temperature (400–650 °C) and high-temperature (above 650 °C) peaks. The high-temperature peaks are probably associated with the reduction of bulk Ce⁴⁺ and Sn⁴⁺ [27,41].

At medium temperatures, a group of relatively low-intense peaks was observed in all the TPR profiles. These peaks can be associated with the reduction of surface Ce⁴⁺, Sn⁴⁺ and/or Zr⁴⁺ species. The presence of Cu⁰ species strongly affects their reducibility. The maxima of medium-temperature peaks shift to lower temperatures but to a different extent for different sample compositions. The low-temperature peaks at 50–400 °C are usually attributed to the reduction of highly dispersed and bulk Cu²⁺ oxide species and to the sequential reduction of Cu²⁺ to Cu⁰ (Cu²⁺ → Cu⁺ → Cu⁰) [11,42]. The reduction of Sn⁴⁺ on the surface of the cerium–tin binary sample proceeded at a temperature slightly above 300 °C (Figure 3), but this peak was not visible in the TPR profiles of the copper-containing catalysts. Most likely, it strongly shifted to lower temperatures and overlapped with the CuO reduction peaks, indicating the promoting effect of copper on the Sn⁴⁺ reduction. The partial reduction of a fraction of surface Ce⁴⁺ species in the low-temperature range also cannot be excluded considering that the intensity of the middle-temperature peak decreased in the TPR profiles of Cu-containing catalysts relative to those of CeSn and CeO₂.

The low-temperature peaks were quite similar in the TPR profiles of the impregnated catalysts: both profiles comprised a broad hydrogen consumption peak centered at 222–232 °C. However, a slight shift to higher temperatures and a significant increase in the hydrogen consumption (Table 1) were observed for CuCeSn-im.

The hydrogen uptake peaks in the low-temperature region differ markedly for the one-pot synthesized 20CuCeSn and 20CuCeZr samples. Several intense peaks in the reduction profile of 20CuCeZr correspond to the reduction of various forms of copper oxide on the surface and in bulk. The TPR profile of 20CuCeSn has only two intense signals with a small shoulder at 119 °C, indicating the lower diversity of copper forms in this catalyst. However, the copper reduction in this sample started at lower temperatures, and the hydrogen uptake

was higher than that for 20CuCeZr (Table 1), which may be due to the partial reduction of cerium and tin in the interfacial regions, in which ceria (or Sn-doped ceria) contacted copper oxide.

2.3. Effect of Copper Content on Physicochemical Properties of Catalysts

This section presents the results of the physicochemical study of the catalysts with different copper contents prepared by the one-pot method (Table 2).

Table 2. Textural properties and chemical compositions of one-pot synthesized CuCeSn catalysts with different Cu contents.

Sample	AAS Copper Content, wt. %	S_{BET} , m ² /g	SEM-EDX Atomic Ratio	XPS Atomic and Ion Ratios		
			Ce/Cu	Ce/Cu	Ce ³⁺ /Ce ⁴⁺	Cu ⁺ /Cu ²⁺
5CuCeSn	1.8	145 ± 15	24.0	20.6	0.27	0.72
10CuCeSn	3.4	183 ± 18	12.0	13.0	0.22	1.08
20CuCeSn	6.1	149 ± 15	5.6	5.8	0.11	0.70
25CuCeSn	7.5	155 ± 16	5.2	4.5	0.11	0.81

The EDX analysis of all the catalysts demonstrated the presence of oxygen, cerium, tin, copper and carbon. A bromine signal was also detected in the EDX spectra of all the samples, but its intensity was near the sensitivity level and similar for all the catalysts. Therefore, it was not taken into account in the sample composition calculations.

According to the EDX element mappings (Figure S4 in Supplementary Materials), all the samples comprised the areas of uniform and nonuniform tin distributions. We could assume either the presence of highly dispersed tin oxide or/and the formation of mixed cerium–tin oxide phases of various compositions. The cerium–copper atomic ratios were calculated from the SEM-EDX data (Table 2). As expected, the Ce/Cu ratio decreased with decreasing the Cu content.

The distribution of copper on the surface of the (5–20) CuCeSn samples could be considered as uniform. However, on the surface of the 25CuCeSn sample with the highest copper content, the copper-enriched areas were detected, which may indicate the presence of copper oxide phases in this sample.

10CuCeSn showed the highest BET-specific surface area. The average pore size calculated from the pore size distributions (NL-DFT method) was 3–4 nm for all the catalysts. A significant contribution of micropores was observed in all the samples, but it was the highest in 10CuCeSn.

No reflections of copper-containing phases were detected in the XRD profiles of the copper-modified samples (Figure 5a). Therefore, all the samples contained only the fluorite-type crystalline phase of cubic ceria. The particle size noticeably increased with the decreasing copper content; the average crystallite sizes were 5 ± 1 nm for 25CuCeSn and 20CuCeSn, 6 ± 1 nm for 10CuCeSn and 9 ± 1 nm for 5CuCeSn, approaching the value of 12 ± 1 nm for double oxide CeSn. Copper could exist in the samples in the form of finely dispersed oxide particles or/and as ions partially incorporated into the ceria/ceria–tin lattice.

A slight shift of the reflections in the diffraction patterns of the cerium–tin–copper samples to higher angles relative to the pattern of reference CeO₂ indicates a decrease in the crystal lattice parameter and can testify to the partial incorporation of tin or/and copper ions into the crystal lattice of cerium oxide. However, it is impossible to accurately calculate the lattice parameter for the catalysts due to the strong broadening of the reflections.

The sizes of Sn⁴⁺ (0.81 Å for a coordination number of 8) and Cu²⁺ (0.71 Å) cations are smaller than those of cerium cations (1.10 Å for Ce³⁺ and 0.97 Å for Ce⁴⁺). Therefore, they can be incorporated into the CeO₂ crystal lattice, and this incorporation will slightly decrease the lattice parameter. At the same time, the incorporation of such ions can promote the Ce⁴⁺ to Ce³⁺ reduction, which increases the crystal lattice parameter. Thus,

it is impossible to draw unambiguous conclusions about the degree of ion incorporation based only on the crystal lattice parameters calculated from the XRD data.

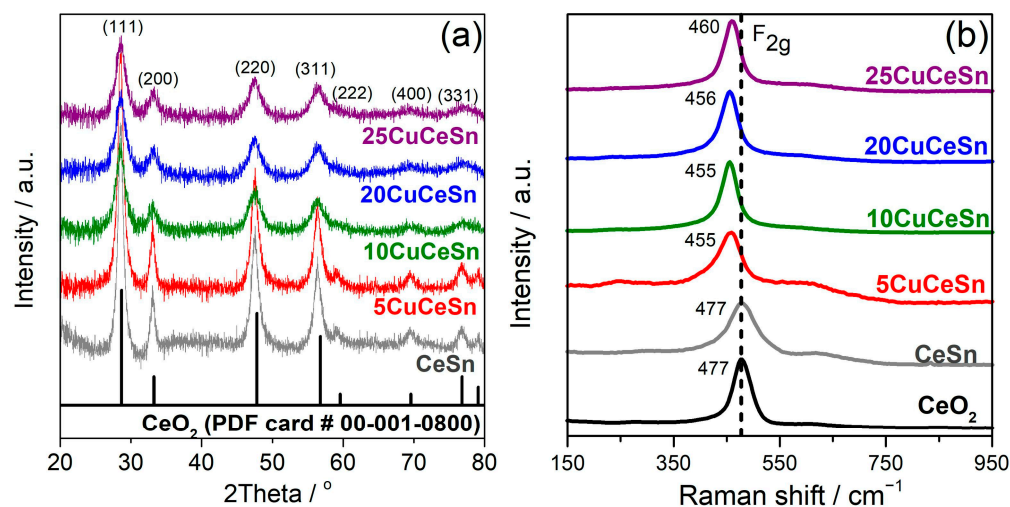


Figure 5. XRD patterns (a) and Raman spectra (b) of catalysts with different Cu contents.

The F_{2g} band in the Raman spectra of all the catalysts (Figure 5b) is broadened and shifted by about 20 cm^{-1} relative to the spectra of references CeSn and CeO_2 . As it has been already mentioned, the broadening is caused by the small crystallite size and by the defectiveness of the structure. The reason for the F_{2g} band shift is a partial incorporation of copper into the CeSn lattice.

The survey XPS spectra of the catalysts with different Cu contents (Figure S3b) in addition to the expected Ce, Sn and Cu lines showed the presence of C and Br, which agrees with the SEM-EDX results. The calculated Ce/Cu ratios (Table 2) indicated the depletion of the surface in copper, especially for 10CuCeSn, which confirms the SEM-EDX data.

The fraction of Ce^{3+} decreased with increasing the copper content. It can be assumed that the limit of copper incorporation was reached in 5CuCeSn and 10CuCeSn. At higher copper concentrations, fine copper oxide particles started to form on the surface, which explains the sharp drop in the Ce/Cu and $\text{Ce}^{3+}/\text{Ce}^{4+}$ ratios (Table 2). The possibility of partial cerium reduction in the XPS chamber during analysis should be also considered. However, because the spectra acquisition time was about the same for all the catalysts, in the case of the X-ray-induced reduction, we should have expected the same portion of Ce^{4+} reduced to Ce^{3+} on the surfaces of all the samples, which was not the case.

The surface fractions of copper in +2 and +1 oxidation states were calculated from the areas of the Cu^{2+} and Cu^+ components in the $\text{Cu}2p$ spectra (Table 2). The highest Cu^+ content was observed in 10CuCeSn. The important role of Cu^+ sites in CO-PROX was earlier reported [10,39,42].

Figure 6a shows the high resolution O1s XPS spectra fitted with several components. The interpretation of these components in the literature is ambiguous, as was shown in our previous work [28]. Many authors have distinguished two major groups of peaks: the components at lower binding energies (denoted as O_{lat}) are associated with lattice oxygen [26,43], while the peaks at higher binding energies (O_{ads} and O_{OH}) are assigned to low-coordinated highly polarized oxygen species (superoxide or peroxide species) adsorbed on the surface or to oxygen in hydroxyl groups [44,45]. These species are believed to play a significant role in catalytic oxidation.

The atomic ratio of lattice and non-lattice oxygen (the latter is the sum of oxygen in hydroxyl and other adsorbed groups) substantially changed with increasing the copper content (Figure 6b). A minimum was observed for the 10CuCeSn sample. The relative contribution of these components to the O1s spectrum correlates with the concentration of

the active surface oxygen species [4]. The opposite trend with a maximum for 10CuCeSn was observed for the S_{BET} and $\text{Cu}^+/\text{Cu}^{2+}$ ratio dependencies on Cu loading.

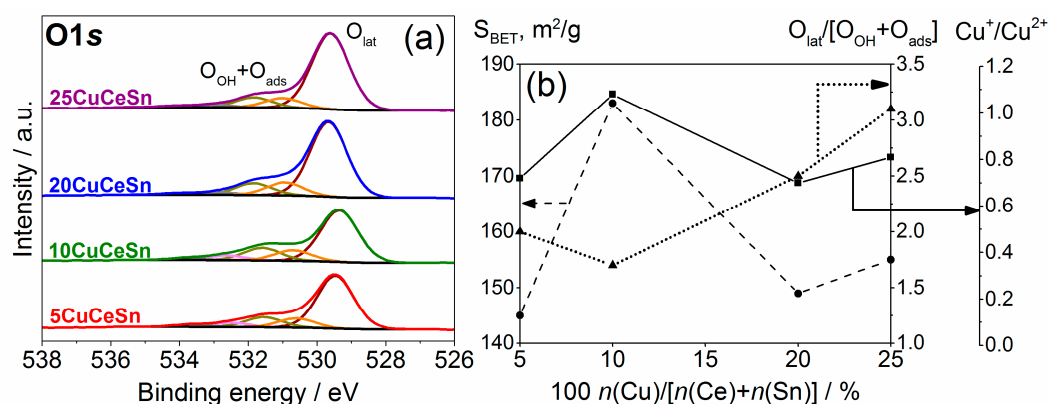


Figure 6. High-resolution O1s XPS spectra (a) and a correlation between the S_{BET} , ratio of oxygen forms, $\text{Cu}^+/\text{Cu}^{2+}$ ratio measured by XPS and Cu content in one-pot synthesized CuCeSn catalysts (b).

The H_2 -TPR experiments were performed to reveal the copper content effect on the catalyst reduction. The H_2 -TPR profiles of the catalysts with different copper loadings (Figure 7) are similar and show a broad reduction signal in the high- and medium-temperature ranges, in addition to two intense peaks (α and β) in the low-temperature region (80–400 °C). The latter peaks can be attributed to the reduction of copper species finely dispersed on ceria, while the peak at a higher temperature (β) relates to the reduction of well-formed CuO particles or mixed oxide phases (CuCeO_x or CuCeSnO_x) [26,46,47].

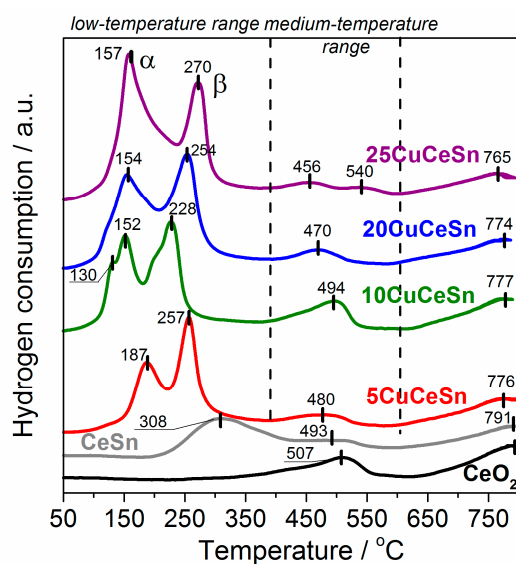


Figure 7. H_2 -TPR profiles of one-pot synthesized CuCeSn catalysts with different Cu loadings.

However, the positions of the α and β peaks in the TPR profiles of our samples strongly depended on the Cu loading. With decreasing the copper content ($n(\text{Cu}) \cdot 100\% / [n(\text{Ce}) + n(\text{M})]$) from 25 to 10%, the maxima of both peaks shifted to low temperatures, and the shift of the β peak was more pronounced than that of the α one. As a result, the difference between the positions of their maxima became smaller (Table 3). A further decrease in the copper content shifted the peaks of copper reduction to higher temperatures. One can notice a decrease in the area ratio of the α and β peaks with the decreasing copper content. This indicates

the increase in the fraction of copper particles strongly bonded to the oxide support in the catalysts with low copper contents.

Table 3. H₂-TPR results for CuCeSn catalysts with different Cu loadings.

Sample	Hydrogen Uptake, $\mu\text{mol/g}$			$\Delta T_{\alpha\beta}$ ¹ , °C	H ₂ /Cu, mol. Ratio (from AAS) ²
	Low-Temperature Range (80–400 °C)	Medium-Temperature Range (400–650 °C)	Total		
5CuCeSn	977	92	1069	70	3.7
10CuCeSn	1213	242	1455	76	2.8
20CuCeSn	1479	100	1579	100	1.9
25CuCeSn	1697	105	1802	113	1.8

¹ Temperature gap between α and β components. ² Calculated from the Cu content determined by AAS, assuming that H₂ absorbed in the low-temperature region is consumed only for the reduction of CuO to Cu⁰.

The observed copper oxide reduction peaks point to the easiest reduction of copper in 10CuCeSn, which can be associated with the fact that the copper content in this catalyst reached the limiting copper “solubility” in the cerium–tin double oxide. A further increase in the copper loading led to the growth of the fraction of CuO particles weakly interacting with the support, which complicates the reduction.

An additional shoulder with a maximum at 130 °C was detected near the main signal at 152 °C in the TPR profile of 10CuCeSn. A similar shoulder was observed in the low-temperature peak in the H₂-TPR profile of 20CuCeSn, but it strongly overlapped with the reduction signal at 154 °C. This peak can be associated with the hydrogen consumption by oxygen ions weakly bonded with surface copper species [48], probably located at interfacial positions.

The quantitative estimation of hydrogen consumption in the low-temperature region is presented in Table 3. The hydrogen uptake increased in this region with increasing the copper content. However, the experimental hydrogen uptakes for all the catalysts exceeded the calculated amounts of hydrogen required for the complete reduction of CuO, assuming that all the copper determined by AAS existed as CuO (see the H₂/Cu ratio in Table 3). The additional hydrogen was apparently consumed by the low-temperature reduction of ceria or tin oxide. This fact indicates that the reduction of these oxides is favored by the presence of dispersed surface CuO species, i.e., the larger the number of CuO–ceria or CuO–SnO_x contacts, the easier the reduction of CeO₂ and/or SnO_x proceeds. The H₂/Cu ratio decreased with increasing the copper content probably because of the decrease in the surface fraction of oxide support with Ce⁴⁺ and Sn⁴⁺ species available for low-temperature reduction.

Note that the H₂-TPR profile of double CeSn oxide showed a noticeable peak at 308 °C. Finer tin oxide particles can be reduced much easier than larger ones [49] due to the improved ability of the former particles to form active oxygen species. In contrast to large SnO₂ particles that reduce at temperatures about 677 °C, small nano-sized crystals reduce in a broad temperature range of 100–500 °C [50].

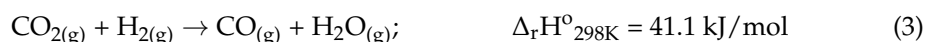
The H₂ uptake in the medium-temperature region (400–650 °C) was related to the reduction of the ceria surface, and it depended nonmonotonically on the copper loading. The highest H₂ uptake was observed for the 10CuCeSn sample. The shift of this reduction peak towards higher temperatures relative to other catalysts could deteriorate the catalyst activity at relatively high reaction temperatures.

The TEM images of all the catalysts (Figure S5) demonstrated relatively large particle aggregates and individual CeO₂ particles. The interplanar spacings of $d = 0.31$ and 0.27 in these particles can be attributed to (111) and (200) planes of cubic ceria crystals. Moiré fringes observed in nearly all images can result from the interaction of aggregates of epitaxially interfaced nanocrystallites. Neither metallic copper nor copper and tin oxide crystallites were detected by HR-TEM. TEM-EDX also points to the absence of copper-enriched areas. Therefore, the fact that copper oxide particles were not detected in the

catalysts confirms our assumption about the high dispersion or amorphous state of copper- and tin-containing phases that was made based on the XRD data.

3. Discussion

Along with the desired CO oxidation reaction (1), three side reactions (hydrogen oxidation (2), the reverse water gas shift (RWGS) (3) and CO hydrogenation (4)) are involved in the PROX process: [51]:



The latter reaction usually shows a significant rate over cobalt-containing [51] and noble metal catalysts [10], while the contributions of reactions (2) and (3) are strong for copper and cerium oxide catalysts.

Our thermodynamic calculations demonstrated that the increase in temperature above 50 °C gradually decreased the equilibrium CO conversion and CO₂ yield over the Cu/(CeO₂-SiO₂) catalysts with the simultaneous increase in the H₂ conversion and water yield [36]. In a real experiment, we should consider both kinetic and thermodynamic factors. Reduced copper species in the CuO/CeO₂ catalyst increase the mobility of lattice oxygen in CeO₂, which leads to the surface reduction of CeO₂ and decreases CO conversion in favor of the H₂ oxidation [52]. On the other hand, the presence of Cu⁺ ions can increase the activation rate of CO molecules on the catalyst surface. High oxygen mobility and electron exchange between Cu²⁺/Cu⁺ and Ce⁴⁺/Ce³⁺ redox pairs have a crucial effect on the catalytic efficiency. In this way, though CeO₂ reduction can be detrimental to the CO conversion, the improved reducibility of the surface of copper particles to form Cu⁺ may play a positive role. The high redox properties of copper species mainly result from their interaction with the cerium-containing oxide support. The template synthesis not only improves the textural properties of mixed oxide catalysts but also contributes to the uniform distribution of elements and strong interaction between components in the catalyst.

In the present work, we studied the influence of the method of copper incorporation into the CeSn and CeZr oxide catalysts and Cu content in the one-pot synthesized CuCeSn catalysts on the physicochemical properties of the catalysts and their efficiencies in CO-PROX.

Both 20CuCeSn and 20CuCeZr were active in CO-PROX. The one-pot template-assisted method of copper incorporation provided a higher performance of the ternary oxide catalysts than the post-impregnation of templated double CeSn and CeZr oxides. The tin-doped 20CuCeSn catalyst prepared by the one-pot method was more efficient than its zirconium-doped counterpart in terms of the CO conversion/CO₂ selectivity ratio; it demonstrated about 70% CO conversion and more than 50% CO₂ selectivity.

We experimentally showed that the one-pot co-precipitation of copper, tin and cerium precursors in the presence of the CTAB template led to the uniform distribution of elements in 20CuCeSn and developed micro- and mesoporosity (average pore size of 3.1 nm) with the increased fraction of micropores and the highest S_{BET} of 149 m²/g. Apparently, this method and these precursors are effective for the formation of micellar structures and complexes with citric acid during synthesis. Moreover, the easier reducibility of tin due to the reversible Sn⁴⁺ ↔ Sn²⁺ transition that can proceed at relatively low temperatures can provide an additional redox pair in contrast to zirconium, which is not prone to such transitions [53]. In addition, the one-pot method provides a high dispersion of copper oxide species on the surface and structure defectiveness, as indicated by the absence of copper oxide reflections in the diffraction pattern and a small average crystallite size (about 5 nm), respectively. The H₂-TPR analysis revealed the excellent reducibility of 20CuCeSn, which plays mainly a positive role in catalytic oxidation [4], especially at relatively high

temperatures. However, high reducibility in the low-temperature region can deteriorate the selectivity of the process. Based on the CO-PROX test and operando-DRIFTS and XANES results, some authors [42] believed that the main side process of H₂ oxidation could easily proceed immediately after the onset of Cu²⁺ reduction to Cu⁺ and Cu⁰. This process starts easily in dispersed copper oxide nanoparticles that are in loose contact with the ceria-based support. In this way lower CO₂ selectivity of tin-containing catalysts than of their zirconium-containing counterparts at 100–150 °C can be explained.

The change in the copper content in the one-pot synthesized ternary CuCeSn oxide catalyst also strongly affects its catalytic properties. It should be emphasized that, in our work, the copper content was calculated in mole fractions related to the total content of Ce + M (M = Sn or Zr) as $(n(\text{Cu}) \cdot 100) / [(n(\text{Ce}) + n(\text{M}))]$. The maximum copper loading did not exceed 7.5 wt.%, i.e., there was not too much copper in all the catalysts.

The CuCeSn samples with different Cu contents prepared by the one-pot method demonstrated the increased defectiveness (broadening and shift of the F_{2g} line in the Raman spectra) and a high S_{BET} (Table 2). For all the samples, a strong interaction between the cerium–tin oxide particles and finely dispersed copper oxide species was observed. This fact was confirmed by the shift of the F_{2g} band in the Raman spectra relative to the spectrum of CeSn and the absence of reflections of crystalline copper oxide phases in XRD and HR-TEM diffraction patterns.

On the other hand, a change in the copper content affected several physicochemical properties of the catalysts, which determined the differences in their catalytic performances. Moreover, some properties changed nonmonotonically (Figure 5b). Thus, the S_{BET} of 10CuCeSn was a bit higher than those of the catalysts with higher and lower Cu contents. The increase in the total copper content led to the growth of the surface copper concentration and improved the copper reducibility, which shifted the copper reduction peaks in the H₂-TPR profiles to lower temperatures. This fact was confirmed by SEM-EDX and XPS. However, again, for 10CuCeSn, both the α and β peaks of copper reduction are located at lower temperatures than for the other samples. Nonmonotonic dependences of the fractions of active oxygen and Cu⁺ species on the surface on the copper loading in the catalysts were observed. The extrema of these dependences were also observed for the 10CuCeSn catalyst. Therefore, the minimum O_{lat}/[O_{ads} + O_{OH}] ratio of 1.75, the highest value of the specific surface area of 183 m²/g, the maximum Cu⁺/Cu²⁺ ratio of 1.08 and a higher reduction ability at 400–650 °C (Table 3) were inherent to the 10CuCeSn sample. However, hydrogen absorption in the low-temperature region grew monotonically with increasing the Cu content (Table 3). It was lower for 10CuCeSn (1213 μmol/g) than for the samples with higher copper contents.

It is important to note that the drop in the ratio of the experimental and theoretical values of hydrogen consumption in the low-temperature region (H₂/Cu ratio) and the increase in the temperature gap between the α and β reduction components (ΔT_{αβ}) with increasing the copper content can indicate a decrease in the fraction of easily reducible copper sites. This means that there is a limit of copper “solubility” in CeSn oxide that was approached in the 5CuCeSn and 10CuCeSn samples. This limit can be characterized both by the formation of solid solutions and by high concentrations of contacts between the cerium–tin oxide and fine CuO particles.

A higher reducibility of 10CuCeSn in the medium-temperature interval (400–650 °C) is very important. It resulted from the easier reduction of surface Ce⁴⁺ ions in direct contact with copper sites in a mixed oxide phase or at interfacial positions. The authors of [42] studied the redox–catalytic correlations in copper–ceria CO-PROX catalysts and concluded that CO predominantly oxidized over interfacial positions of the partially reduced dispersed copper sites. This fact explains the high CO₂ selectivity of 10CuCeSn in the low-temperature region in which there is no noticeable phase segregation, sintering of active phase particles and formation of metallic copper. However, CO conversion over this catalyst was close to 100% only at 150 °C. At higher temperatures, it was inferior to the catalysts with lower and higher copper contents.

25CuCeSn with the highest copper content showed the best catalytic performance at 50 °C and exhibited excellent CO conversion of 79% and CO₂ selectivity of 97% at 100 °C. This catalyst demonstrated a sufficiently easy reducibility of copper, albeit at slightly higher temperatures, and only a slightly lower Cu⁺/Cu²⁺ ratio on the surface than in 10CuCeSn. However, the high content of copper in 25CuCeSn provided ample amount of adsorption sites for CO molecules. That is why this catalyst surpassed 10CuCeSn in the catalytic activity at 100 °C. However, a large copper fraction in 25CuCeSn weakly interacted with CeSn support, so, at higher temperatures, these copper species were easily reduced with hydrogen from the reaction medium, leading to a sharp drop in the CO₂ selectivity. The surface of the reduced catalyst was active in hydrogen oxidation, which led to hydrogen loss.

The same trend was found for 20CuCeSn. However, because of the lower concentration of the active adsorption sites in 20CuCeSn than in 25CuCeSn, the CO conversion and CO₂ selectivity at 100 °C were lower for the former catalyst. It was found early that the increase in the total copper content in the CuO/CeO₂ catalyst significantly improved its reducibility [39]. We can assume that only a limited fraction of copper in the 20CuCeSn catalyst was in tight contact with the CeSn support and could provide interfacial sites active in CO-PROX. The rest part of copper weakly interacted with CeSn particles. Despite their easy reducibility, these species had no influence on the ceria/tin reduction and oxygen vacancies formation, which is consistent with the H₂-TPR and XPS data.

An interesting behavior was observed for 5CuCeSn. This catalyst, comprising only a small number of copper-active centers, was inferior to other samples in terms of the CO conversion at low temperatures (only 47% at 100 °C). However, at higher temperatures, the CO conversion over this catalyst was comparable with those over 20CuCeSn and 25CuCeSn with much higher copper loadings. The reaction medium possibly affected the properties of this sample to a lesser extent than for 10 CuCeSn, which showed lower CO conversions.

It seems that achieving a high efficiency of the Cu-Ce-Sn ternary oxide catalysts requires not only the developed porosity and highly dispersed active copper oxide species but also the optimal loading of copper that increases the concentration of interfacial centers between copper oxide and cerium–tin oxide and their stability over a wide temperature range.

Thus, in this work, we demonstrated that the one-pot template method is more efficient for the synthesis of the CuCeSn and CuCeZr CO-PROX catalysts than the post-impregnation of double oxides with copper salt. Varying the copper loading in the catalysts allowed tuning the CO conversion/CO₂ selectivity ratio. Nonmonotonic changes in the physicochemical characteristics with increasing Cu loading was explained by the differences in copper distribution in the support; at low loading copper was predominantly distributed in the CeSn phase, while at higher loadings, separate copper oxide phases were formed, which increased the interfacial interactions between the copper-containing and CeSn phases. The high stability of 10CuCeSn, containing only 3.4 wt.% of copper, was demonstrated in the 10-h catalytic test.

4. Materials and Methods

4.1. Catalysts Preparation

Double CeO₂-SnO₂ (denoted as CeSn) and ternary CuO-CeO₂-SnO₂ (denoted as CuCeSn) oxide catalysts were synthesized by the template-assisted evaporation-induced self-assembly method (EISA) described in detail in our previous work [54]. Cetyltrimethylammonium bromide (CTAB, 99%, BioChemica, Billingham, UK) was used as a template. The *n*(CTAB):*Sn*(Me) ratio was 1:1. (NH₄)₂[Ce(NO₃)₆] (puriss., ReaChem, Moscow, Russia), SnCl₂·2H₂O (puriss., ReaChem, Moscow, Russia) and Cu(CH₃COO)₂·H₂O (p.a., Vecton, Saint Petersburg, Russia) were used as precursors for the synthesis. The Ce:Sn and CeZr molar ratios were 9 for all the samples. The high cerium to tin ratio in the catalysts was chosen based on the literature data.

Synthesis of CeSn. The required amounts of cerium and tin salts were dissolved in 70 mL of distilled water and added to 30 mL aqueous solution of citric acid. The resulting solution was stirred at a constant rate. Then, the mixture was added dropwise

to the solution of CTAB in 15 mL of 96% ethanol and stirred at room temperature for 4 h. After that, the excess of the solvent was slowly evaporated for 2 h. The obtained gel-like mixture was dried at 80 °C for 24 h and then heated up to 500 °C and calcined in air at this temperature for 3.5 h.

The ternary CuCeSn oxide catalyst was prepared using two different techniques. The first technique was the one-pot synthesis. The aqueous solution of all the precursors was added to the CTAB solution in ethanol, as described above. The copper molar ratios in the catalysts ($n(\text{Cu}) \cdot 100\% / [n(\text{Ce}) + n(\text{Sn})]$) were 5, 10, 20 and 25. These samples were denoted as $y\text{CuCeSn}$, where y is the copper molar ratio. In the second technique, CeSn oxide was prepared as described above and calcined at 500 °C. Then, it was impregnated with the aqueous solution of copper acetate, followed by drying at 120 °C for 2 h and calcination in the air at 500 °C for 2 h (this sample was denoted as 20CuCeSn-im).

Reference CeO₂, 20CuCeZr and 20CuCeZr-im samples with a Ce:Zr ratio of 9 were prepared by the same methods (one-pot and post-impregnation) using (NH₄)₂[Ce(NO₃)₆] (puriss., Reachem, Moscow, Russia) and ZrO(NO₃)₂·H₂O(99.5%, Acros Organics, Geel, Belgium) as cerium and zirconium precursors, respectively.

The results of the catalytic test of the unmodified cerium–tin catalyst are not presented. The maximum CO conversion was only 47% at 250 °C, which is significantly lower than that for the Cu-containing sample.

4.2. Catalysts Characterization

The copper content in the catalysts was measured by atomic absorption spectroscopy (AAS) on a Thermo Fisher Scientific series iCE 3000 spectrometer (Waltham, MA, USA) using air–acetylene flame atomization. SOLAAR Data Station software was used for the device control and data processing. The uncertainty of the copper content measurements did not exceed ± 0.2 wt.%.

XRD diffractograms of the catalysts were recorded on a Rigaku Ultima IV powder diffractometer (Rigaku Corporation, Tokyo, Japan) (CuK α radiation, 1.5418 Å) in the 2 θ range of from 5 to 90° with a step size of 0.02°. The phase composition was analyzed by comparison with the JCPDS PDF1 library data (ICDD database).

X-ray photoelectron spectroscopy (XPS) was used to reveal the composition and oxidation state of elements on the catalyst surface. The spectra were acquired on an Axis Ultra DLD spectrometer (Kratos Analytical, Manchester, UK) with a monochromatic AlK α radiation source ($h\nu = 1486.7$ eV, 150 W). The pass energies of the analyzer were 160 eV for the survey spectra and 40 eV for the high-resolution scans. The binding energy scale of the spectrometer was preliminarily calibrated using the position of the peaks for the Au 4f_{7/2} (83.96 eV), Ag 3d_{5/2} (368.21 eV) and Cu 2p_{3/2} (932.62 eV) core levels of pure metallic gold, silver, and copper. The powder samples were mounted on a holder using double-sided nonconductive adhesive tape. The spectra were fitted into CasaXPS software. The Kratos charge neutralizer was used, and the spectra were charge-referenced to the high energy component of the Ce3d spectrum set to 916.5 eV.

Raman spectra were recorded on a Horiba Jobin Yvon Lab RAM HR 800 UV instrument (Horiba ABX S.A., Montpellier, France). An argon ion laser with a wavelength of 514 nm was used for the excitation, and the power on the sample did not exceed 7 mW. For each sample, the spectra were accumulated for 200 s.

Scanning electron microscopy (SEM) of the catalysts was performed on a JCM–6000 Neoscope microscope (JEOL, Tokyo, Japan). The high-resolution transmission electron microscopic images (HR-TEM) were registered using a JEM 2100A instrument (JEOL, Japan) at an accelerating voltage of 200 kV. Both microscopes were equipped with an energy dispersive X-ray spectroscopy (EDX) accessory.

Nitrogen physisorption isotherms were recorded on an Autosorb–1 analyzer (Quantachrome, Boynton Beach, FL, USA). Before measurements, the samples were outgassed for 3 h at 200 °C. The specific surface area was calculated by the BET method with an accuracy

of 10%. Desorption branches of the isotherms were used for the calculation of pore size distributions by the NL-DFT method.

Temperature-programmed reduction with hydrogen (H₂-TPR) was carried out on a USGA-101 chemisorption analyzer (UNISIT, Moscow, Russia). A 5% H₂/Ar mixture was fed to a quartz reactor at a flow rate of 30 mL/min. The sample weight was approximately 50 mg. Before analysis, a catalyst was preliminarily kept at 300 °C for 30 min in an argon flow and then cooled to 30 °C. The H₂-TPR profiles were recorded under heating the sample from 30 to 900 °C at a rate of 10 °C/min. Hydrogen consumption during analysis was registered with a thermal conductivity detector preliminarily calibrated by NiO (99.99%, Sigma-Aldrich, St. Lois, MO, USA) reduction.

4.3. Catalytic Tests

The catalysts were tested in CO-PROX on a ULCat-1 catalytic unit (UNISIT, Moscow, Russia) equipped with a fixed-bed continuous-flow stainless steel reactor (length—32 cm, inner diameter—12 mm and outer diameter—16 mm) in the temperature range from 50 to 450 °C using 150 mg of the catalyst. The reaction mixture comprising 4 vol.% CO, 3 vol.% O₂, 13 vol.% N₂ and 80 vol.% H₂ was fed into the reactor at a flow rate of 95 mL·min⁻¹ (contact time of 0.095 g·s·cm⁻³). The composition of the effluent was analyzed by a Chromatec-Crystal 5000.2 (Chromatec, Yoshkar-Ola, Mari El, Russia) gas chromatograph (GC) equipped with a Carboxen-1010 PLOT column (Supelco Inc., Bellefonte, Pennsylvania, USA). Air was supplied by an air compressor. He (40 L, grade “A”), N₂ (40 L, high purity grade), CO (40 L, grade 3.0) and H₂ (40 L, grade 3.8) were supplied by the PGS-service company (Moscow, Russia) and used without additional purification. The gases were fed to the reactor using mass flow controllers (Bronkhorst Nederland B.V., Bronkhorst, the Netherlands).

The main catalytic parameters were calculated from the areas of chromatographic peaks (*A*) of each component using the following equations:

$$\text{CO conversion : } X_{\text{CO}}, \% = \frac{[A(\text{CO})_{\text{in}} - A(\text{CO})_{\text{out}}] \Delta \frac{A(\text{N}_2)_{\text{in}}}{A(\text{N}_2)_{\text{out}}}}{A(\text{CO})_{\text{in}}} \times 100 \quad (5)$$

$$\text{O}_2 \text{ conversion : } X_{\text{O}_2}, \% = \frac{[A(\text{O}_2)_{\text{in}} - A(\text{O}_2)_{\text{out}}] \Delta \frac{A(\text{N}_2)_{\text{in}}}{A(\text{N}_2)_{\text{out}}}}{A(\text{O}_2)_{\text{in}}} \times 100 \quad (6)$$

$$\text{CO}_2 \text{ selectivity : } S_{\text{CO}_2}, \% = \frac{0.5 \Delta f(\text{CO}) \Delta [A(\text{CO})_{\text{in}} - A(\text{CO})_{\text{out}}] \Delta \frac{A(\text{N}_2)_{\text{in}}}{A(\text{N}_2)_{\text{out}}}}{f(\text{O}_2) \Delta [A(\text{O}_2)_{\text{in}} - A(\text{O}_2)_{\text{out}}] \Delta \frac{A(\text{N}_2)_{\text{in}}}{A(\text{N}_2)_{\text{out}}}} \times 100 \quad (7)$$

The subscripts “in” and “out” denote the concentrations of components in the feed and effluent of the reactor; *f*(CO) and *f*(O₂) are the calibration factors for CO and O₂, respectively. The calibration factors were calculated based on the chromatographic analysis of two calibration mixtures (PGS-service, Moscow, Russia): (i) CH₄ (30.20 vol.%), H₂ (4.81 vol.%), CO (4.87 vol.%) and balance N₂ and (ii) O₂ (14.90 vol.%), CO₂ (29.18 vol.%) and balance N₂.

The stability of the 10CuCeSn catalyst was tested in the isothermal experiment at 200 °C for more than 10 h using the same reaction mixture as in the non-isothermal experiments. However, the increased catalyst loading of 300 mg and a total flow rate of 30 mL·min⁻¹ were used (contact time of 0.600 g·s·cm⁻³).

The uncertainties of the calculated conversion and selectivity values did not exceed ±4%.

5. Conclusions

Thus, in this work, we demonstrated that the one-pot template method allows synthesizing more efficient CuCeSn and CuCeZr catalysts for CO-PROX than the post-impregnation of double CeSn/CeZr oxides with copper salt. A small amount of tin dopant more strongly improves the reducibility of cerium-based catalysts than the same amount of

zirconium. Moreover, the transformation of Sn^{4+} to Sn^{2+} can provide an additional redox pair in the catalyst, which positively affects its activity. The one-pot technique promotes the uniform distribution of elements in the 20CuCeSn catalyst and develops its micro- and mesoporosity. Varying the copper loading allows tuning the CO conversion/ CO_2 selectivity ratio. Nonmonotonic changes in the physicochemical characteristics of the CuCeSn catalyst with increasing the copper loading can be explained by differences in the copper distribution in the support. At low loading, copper is predominantly distributed in the CeSn phase, while, at higher loadings, separate copper oxide phases are formed, which increases the interfacial interaction between copper and CeSn oxides.

Supplementary Materials: The following supporting information can be downloaded at: <https://www.mdpi.com/article/10.3390/catal12121575/s1>: Figure S1: SEM images and SEM-EDX elemental mappings of CuCeSn and CuCeZr catalysts. Figure S2: N_2 physisorption isotherms of 20CuCeSn and 20CuCeZr catalysts synthesized by the one-pot method and post-impregnation method. Figure S3: Survey XPS spectra of 20CuCeSn and 20CuCeZr catalysts prepared by different methods (a), and one-pot synthesized CuCeSn catalysts with different copper loadings (b). Figure S4: SEM images and SEM-EDX mappings of one-pot synthesized CuCeSn catalysts with different copper loadings. Figure S5: HR-TEM images of one-pot synthesized CuCeSn catalysts with different copper loadings.

Author Contributions: Conceptualization, I.Y.K. and E.S.L.; methodology, I.Y.K.; formal analysis, I.Y.K. and E.S.L.; investigation, I.Y.K., A.V.T., K.I.M. and O.Y.I.; writing—original draft preparation, I.Y.K. and E.S.L.; writing—review and editing, I.Y.K., E.S.L., E.V.G. and K.I.M.; visualization, I.Y.K. and A.V.T. and supervision, E.S.L. All authors have read and agreed to the published version of the manuscript.

Funding: This work was supported by the Russian State assignment “Physical Chemistry of Surface, Adsorption, and Catalysis”, registration number AAAA-A21-121011990019-4.

Institutional Review Board Statement: Not applicable.

Informed Consent Statement: Not applicable.

Data Availability Statement: Not applicable.

Acknowledgments: The authors acknowledge support from the Lomonosov Moscow State University Program of Development for providing access to XPS and TEM instruments.

Conflicts of Interest: The authors declare no conflict of interest.

Sample Availability: Samples of the catalysts are not available from the authors.

References

- Jing, P.; Gong, X.; Liu, B.; Zhang, J. Recent Advances in Synergistic Effect Promoted Catalysts for Preferential Oxidation of Carbon Monoxide. *Catal. Sci. Technol.* **2020**, *10*, 919–934. [CrossRef]
- Sahebdelfar, S.; Ravanchi, M.T. Carbon Monoxide Clean-up of the Reformate Gas for PEM Fuel Cell Applications: A Conceptual Review. *Int. J. Hydrogen Energy* **2022**, *in press*. [CrossRef]
- Gu, D.; Jia, C.J.; Bongard, H.; Spliethoff, B.; Weidenthaler, C.; Schmidt, W.; Schüth, F. Ordered Mesoporous Cu–Ce–O Catalysts for CO Preferential Oxidation in H_2 -Rich Gases: Influence of Copper Content and Pretreatment Conditions. *Appl. Catal. B Environ.* **2014**, *152–153*, 11–18. [CrossRef]
- Ayastuy, J.L.; Gurbani, A.; González-Marcos, M.P.; Gutiérrez-Ortiz, M.A. Selective CO Oxidation in H_2 Streams on $\text{CuO/Ce}_x\text{Zr}_{1-x}\text{O}_2$ Catalysts: Correlation between Activity and Low Temperature Reducibility. *Int. J. Hydrogen Energy* **2012**, *37*, 1993–2006. [CrossRef]
- Chee, S.W.; Arce-Ramos, J.M.; Li, W.; Genest, A.; Mirsaidov, U. Structural Changes in Noble Metal Nanoparticles during CO Oxidation and Their Impact on Catalyst Activity. *Nat. Commun.* **2020**, *11*, 1–9. [CrossRef] [PubMed]
- Altass, H.M.; Ahmed, S.A.; Salama, R.S.; Moussa, Z.; Jassas, R.S.; Alsantali, R.I.; Al-Rooqi, M.M.; Ibrahim, A.A.; Khder, M.A.; Morad, M.; et al. Low Temperature CO Oxidation Over Highly Active Gold Nanoparticles Supported on Reduced Graphene Oxide@Mg-BTC Nanocomposite. *Catal. Letters* **2022**, *1*, 1–11.
- Kim, Y.H.; Park, E.D.; Lee, H.C.; Lee, D.; Lee, K.H. Preferential CO Oxidation over Supported Noble Metal Catalysts. *Catal. Today* **2009**, *146*, 253–259. [CrossRef]
- Martínez-Munuera, J.C.; Giménez-Mañogil, J.; Yeste, M.P.; Hungría, A.B.; Cauqui, M.A.; García-García, A.; Calvino, J.J. New Findings Regarding the Role of Copper Entity Particle Size on the Performance of Cu/Ceria-Based Catalysts in the CO-PROX Reaction. *Appl. Surf. Sci.* **2022**, *575*, 151717. [CrossRef]

9. Wu, Z.; Zhu, H.; Qin, Z.; Wang, H.; Ding, J.; Huang, L.; Wang, J. CO Preferential Oxidation in H₂-Rich Stream over a CuO/CeO₂ Catalyst with High H₂O and CO₂ Tolerance. *Fuel* **2013**, *104*, 41–45. [CrossRef]
10. Chagas, C.A.; Schmal, M. The Effect of Copper Oxide on the CuO–NiO/CeO₂ Structure and Its Influence on the CO-PROX Reaction. *Int. J. Hydrogen Energy* **2022**, *47*, 8858–8866. [CrossRef]
11. Araújo, V.D.; Bellido, J.D.A.; Bernardi, M.I.B.; Assaf, J.M.; Assaf, E.M. CuO–CeO₂ Catalysts Synthesized in One-Step: Characterization and PROX Performance. *Int. J. Hydrogen Energy* **2012**, *37*, 5498–5507. [CrossRef]
12. Silva, R.B.M.; de Oliveira, C.S.; Teixeira-Neto, É.; Sigoli, F.A.; Mazali, I.O. Improvement of PROX-CO Catalytic Performance by Modulation of the Pore Structure of CeO₂ Nanorods Decorated with Au Nanoparticles. *Microporous Mesoporous Mater.* **2022**, *330*, 111574. [CrossRef]
13. Konsolakis, M. The Role of Copper–Ceria Interactions in Catalysis Science: Recent Theoretical and Experimental Advances. *Appl. Catal. B Environ.* **2016**, *198*, 49–66. [CrossRef]
14. Martínez-Arias, A.; Hungria, A.B.; Fernández-García, M.; Conesa, J.C.; Munuera, G. Preferential Oxidation of CO in a H₂-Rich Stream over CuO/CeO₂ and CuO/(Ce,M)O_x (M = Zr, Tb) Catalysts. *J. Power Sources* **2005**, *151*, 32–42. [CrossRef]
15. Hermes, E.D.; Jenness, G.R.; Schmidt, J.R. Decoupling the Electronic, Geometric and Interfacial Contributions to Support Effects in Heterogeneous Catalysis. *Mol. Simul.* **2015**, *41*, 123–133. [CrossRef]
16. Colón, G.; Valdivieso, F.; Pijolat, M.; Baker, R.T.; Calvino, J.J.; Bernal, S. Textural and Phase Stability of Ce_xZr_{1-x}O₂ Mixed Oxides under High Temperature Oxidising Conditions. *Catal. Today* **1999**, *50*, 271–284. [CrossRef]
17. Janvier, C.; Pijolat, M.; Valdivieso, F.; Soustelle, M.; Zing, C. Thermal Stability of Ce_{1-x}Zr_xO₂ Solid Solution Powders. *J. Eur. Ceram. Soc.* **1998**, *18*, 1331–1337. [CrossRef]
18. Fornasiero, P.; Balducci, G.; Di Monte, R.; Kašpar, J.; Sergo, V.; Gubitosa, G.; Ferrero, A.; Graziani, M. Modification of the Redox Behaviour of CeO₂ Induced by Structural Doping with ZrO₂. *J. Catal.* **1996**, *164*, 173–183. [CrossRef]
19. Di Monte, R.; Fornasiero, P.; Kaspar, J.; Graziani, M.; Gatica, J.M.; Bernal, S.; Gomez-Herrero, A. Stabilisation of Nanostructured Ce_{0.2}Zr_{0.8}O₂ Solid Solution by Impregnation on Al₂O₃: A Suitable Method for the Production of Thermally Stable Oxygen Storage/Release Promoters for Three-Way Catalysts. *Chem. Commun.* **2000**, *21*, 2167–2168. [CrossRef]
20. Ozawa, M.; Kimura, M.; Isogai, A. The Application of Ce-Zr Oxide Solid Solution to Oxygen Storage Promoters in Automotive Catalysts. *J. Alloys Compd.* **1993**, *193*, 1–2. [CrossRef]
21. Kozlov, A.I.; Do, H.K.; Yezerets, A.; Andersen, P.; Kung, H.H.; Kung, M.C. Effect of Preparation Method and Redox Treatment on the Reducibility and Structure of Supported Ceria–Zirconia Mixed Oxide. *J. Catal.* **2002**, *209*, 417–426. [CrossRef]
22. Qiu, Z.; Guo, X.; Mao, J.; Zhou, R. Elucidating the Structure, Redox Properties and Active Entities of High-Temperature Thermally Aged CuO_x–CeO₂ Catalysts for CO-PROX. *Phys. Chem. Chem. Phys.* **2021**, *23*, 15582–15590. [CrossRef] [PubMed]
23. Qiu, Z.; Guo, X.; Mao, J.; Zhou, R. Insights into the Structure-Performance Relationship of CuO_x–CeO₂ Catalysts for Preferential Oxidation of CO: Investigation on Thermally Induced Copper Migration Process. *Appl. Surf. Sci.* **2022**, *600*, 154100. [CrossRef]
24. Chen, Y.-Z.; Liaw, B.-J.; Chen, H.-C. Selective Oxidation of CO in Excess Hydrogen over CuO/Ce_xZr_{1-x}O₂ Catalysts. *Int. J. Hydrogen Energy* **2006**, *31*, 427–435. [CrossRef]
25. Chen, Y.Z.; Liaw, B.J.; Huang, C.W. Selective Oxidation of CO in Excess Hydrogen over CuO/Ce_xSn_{1-x}O₂ Catalysts. *Appl. Catal. A Gen.* **2006**, *302*, 168–176. [CrossRef]
26. Iglesias-González, A.; Ayastuy, J.L.; González-Marcos, M.P.; Gutiérrez-Ortiz, M.A. CuO/Ce_xSn_{1-x}O₂ Catalysts with Low Tin Content for CO Removal from H₂-Rich Streams. *Int. J. Hydrogen Energy* **2014**, *39*, 5213–5224. [CrossRef]
27. Ayastuy, J.L.; Iglesias-González, A.; Gutiérrez-Ortiz, M.A. Synthesis and Characterization of Low Amount Tin-Doped Ceria (Ce_xSn_{1-x}O_{2-δ}) for Catalytic CO Oxidation. *Chem. Eng. J.* **2014**, *244*, 372–381. [CrossRef]
28. Kaplin, I.Y.; Lokteva, E.S.; Tikhonov, A.V.; Zhilyaev, K.A.; Golubina, E.V.; Maslakov, K.I.; Kamaev, A.O.; Isaikina, O.Y. Templated Synthesis of Copper Modified Tin-Doped Ceria for Catalytic CO Oxidation. *Top. Catal.* **2020**, *63*, 86–98. [CrossRef]
29. Maciel, C.G.; Silva, T.D.F.; Hirooka, M.I.; Belgacem, M.N.; Assaf, J.M. Effect of Nature of Ceria Support in CuO/CeO₂ Catalyst for PROX-CO Reaction. *Fuel* **2012**, *97*, 245–252. [CrossRef]
30. Jayakumar, G.; Albert Irudayaraj, A.; Dhayal Raj, A. A Comprehensive Investigation on the Properties of Nanostructured Cerium Oxide. *Opt. Quantum Electron.* **2019**, *51*, 1–15. [CrossRef]
31. Loidant, S. Raman Spectroscopy as a Powerful Tool to Characterize Ceria-Based Catalysts. *Catal. Today* **2021**, *373*, 98–111. [CrossRef]
32. Gouadec, G.; Colombari, P. Raman Spectroscopy of Nanomaterials: How Spectra Relate to Disorder, Particle Size and Mechanical Properties. *Prog. Cryst. Growth Charact. Mater.* **2007**, *53*, 1–56. [CrossRef]
33. Sudarsanam, P.; Hillary, B.; Amin, M.H.; Rockstroh, N.; Bentrup, U.; Brückner, A.; Bhargava, S.K. Heterostructured Copper-Ceria and Iron-Ceria Nanorods: Role of Morphology, Redox, and Acid Properties in Catalytic Diesel Soot Combustion. *Langmuir* **2018**, *34*, 2663–2673. [CrossRef] [PubMed]
34. Wu, Z.; Li, M.; Howe, J.; Meyer, H.M.; Overbury, S.H. Probing Defect Sites on CeO₂ Nanocrystals with Well-Defined Surface Planes by Raman Spectroscopy and O₂ Adsorption. *Langmuir* **2010**, *26*, 16595–16606. [CrossRef]
35. Choudhury, B.; Choudhury, A. Ce³⁺ and Oxygen Vacancy Mediated Tuning of Structural and Optical Properties of CeO₂ Nanoparticles. *Mater. Chem. Phys.* **2012**, *131*, 666–671. [CrossRef]

36. Kaplin, I.Y.; Lokteva, E.S.; Maslakov, K.I.; Tikhonov, A.V.; Kharlanov, A.N.; Fionov, A.V.; Kamaev, A.O.; Isaikina, O.Y.; Maksimov, S.V.; Golubina, E.V. Ceria-Silica Mesoporous Catalysts for CO Preferential Oxidation in H₂-Rich Stream: The Effect of Ce:Si Ratio and Copper Modification. *Appl. Surf. Sci.* **2022**, *594*, 153473. [CrossRef]
37. Sedmak, G.; Hočevár, S.; Levec, J. Transient Kinetic Model of CO Oxidation over a Nanostructured Cu_{0.1}Ce_{0.9}O_{2-y} Catalyst. *J. Catal.* **2004**, *222*, 87–99. [CrossRef]
38. Liu, W.; Flytzani-Stephanopoulos, M. Total Oxidation of Carbon-Monoxide and Methane over Transition Metal Fluorite Oxide Composite Catalysts. II. Catalyst Characterization and Reaction-Kinetics. *J. Catal.* **1995**, *153*, 317–332. [CrossRef]
39. Miranda Cruz, A.R.; Assaf, E.M.; Gomes, J.F.; Assaf, J.M. Active Copper Species of Co-Precipitated Copper-Ceria Catalysts in the CO-PROX Reaction: An in Situ XANES and DRIFTS Study. *Catal. Today* **2020**, *381*, 42–49. [CrossRef]
40. Wang, W.-W.; Du, P.-P.; Zou, S.-H.; He, H.-Y.; Wang, R.-X.; Jin, Z.; Shi, S.; Huang, Y.-Y.; Si, R.; Song, Q.-S.; et al. Highly Dispersed Copper Oxide Clusters as Active Species in Copper-Ceria Catalyst for Preferential Oxidation of Carbon Monoxide. *ACS Catal.* **2015**, *5*, 2088–2099. [CrossRef]
41. Wang, J.; Chen, H.; Hu, Z.; Yao, M.; Li, Y. A Review on the Pd-Based Three-Way Catalyst. *Catal. Rev.-Sci. Eng.* **2015**, *57*, 79–144. [CrossRef]
42. Martínez-Arias, A.; Gamarra, D.; Fernández-García, M.; Hornés, A.; Bera, P.; Koppány, Z.; Schay, Z. Redox-Catalytic Correlations in Oxidised Copper-Ceria CO-PROX Catalysts. *Catal. Today* **2009**, *143*, 211–217. [CrossRef]
43. Wang, W.W.; Yu, W.Z.; Du, P.P.; Xu, H.; Jin, Z.; Si, R.; Ma, C.; Shi, S.; Jia, C.J.; Yan, C.H. Crystal Plane Effect of Ceria on Supported Copper Oxide Cluster Catalyst for CO Oxidation: Importance of Metal-Support Interaction. *ACS Catal.* **2017**, *7*, 1313–1329. [CrossRef]
44. Tang, X.; Zhang, B.; Li, Y.; Xu, Y.; Xin, Q.; Shen, W. Carbon Monoxide Oxidation over CuO/CeO₂ Catalysts. *Catal. Today* **2004**, *93–95*, 191–198. [CrossRef]
45. Holgado, J.P.; Munuera, G.; Espinós, J.P.; González-Elipe, A.R. XPS Study of Oxidation Processes of CeO_x Defective Layers. *Appl. Surf. Sci.* **2000**, *158*, 164–171. [CrossRef]
46. Liu, W.; Sarofim, A.F.; Flytzani-Stephanopoulos, M. Complete Oxidation of Carbon Monoxide and Methane over Metal-Promoted Fluorite Oxide Catalysts. *Chem. Eng. Sci.* **1994**, *49*, 4871–4888. [CrossRef]
47. He, D.; Liu, L.S.; Ren, J.; Hu, T.P. Catalytic Combustion of Volatile Organic Compounds over CuO-CeO₂ Supported on SiO₂-Al₂O₃ Modified Glass-Fiber Honeycomb. *J. Fuel Chem. Technol.* **2017**, *45*, 354–361. [CrossRef]
48. Yu, Q.; Liu, L.; Dong, L.; Li, D.; Liu, B.; Gao, F.; Sun, K.; Dong, L.; Chen, Y. Effects of Ce/Zr Ratio on the Reducibility, Adsorption and Catalytic Activity of CuO/Ce_xZr_{1-x}O₂/Al₂O₃ Catalysts for NO Reduction by CO. *Appl. Catal. B Environ.* **2010**, *96*, 350–360. [CrossRef]
49. Lan, F.; Wang, X.; Xu, X.; Zhang, R.; Zhang, N. Preparation and Characterization of SnO₂ Catalysts for CO and CH₄ Oxidation. *React. Kinet. Mech. Catal.* **2012**, *106*, 113–125. [CrossRef]
50. Wang, H.; Wang, H.; Li, X.; Li, C. Nature of Active Tin Species and Promoting Effect of Nickle in Silica Supported Tin Oxide for Dehydrogenation of Propane. *Appl. Surf. Sci.* **2017**, *407*, 456–462. [CrossRef]
51. Nyathi, T.M.; Fischer, N.; York, A.P.E.; Claeys, M. Environment-Dependent Catalytic Performance and Phase Stability of Co₃O₄ in the Preferential Oxidation of Carbon Monoxide Studied in-situ. *ACS Catal.* **2020**, *10*, 11892–11911. [CrossRef]
52. Davó-Quiñero, A.; Bailón-García, E.; López-Rodríguez, S.; Juan-Juan, J.; Lozano-Castelló, D.; García-Melchor, M.; Herrera, F.C.; Pellegrin, E.; Escudero, C.; Bueno-López, A. Insights into the Oxygen Vacancy Filling Mechanism in CuO/CeO₂ Catalysts: A Key Step toward High Selectivity in Preferential CO Oxidation. *ACS Catal.* **2020**, *10*, 6532–6545. [CrossRef]
53. Slavinskaya, E.M.; Zadesenets, A.V.; Stonkus, O.A.; Stadnichenko, A.I.; Shchukarev, A.V.; Shubin, Y.V.; Korenev, S.V.; Boronin, A.I. Thermal Activation of Pd/CeO₂-SnO₂ Catalysts for Low-Temperature CO Oxidation. *Appl. Catal. B Environ.* **2020**, *277*, 119275. [CrossRef]
54. Kaplin, I.Y.; Lokteva, E.S.; Golubina, E.V.; Shishova, V.V.; Maslakov, K.I.; Fionov, A.V.; Isaikina, O.Y.; Lunin, V.V. Efficiency of Manganese Modified CTAB-Templated Ceria-Zirconia Catalysts in Total CO Oxidation. *Appl. Surf. Sci.* **2019**, *485*, 432–440. [CrossRef]

Article

Ab Initio Investigation of the Adsorption and Dissociation of O₂ on Cu-Skin Cu₃Au(111) Surface

Yanlin Yu¹, Zhiming Liu¹, Wenxian Huang², Shan Zhou¹, Zuofu Hu¹ and Ligen Wang^{3,*}¹ School of Mathematics and Physics, Jinggangshan University, Ji'an 343009, China² School of Architectural Engineering, Jinggangshan University, Ji'an 343009, China³ General Research Institute for Nonferrous Metals, Beijing 100088, China

* Correspondence: lg_wang1@yahoo.com; Tel.: +86-135-2113-4375; Fax: +86-10-82-240-096

Abstract: Surface adsorption and dissociation processes can have a decisive impact on the catalytic properties of metal alloys. We have used density functional theory to investigate the adsorption and dissociation of O₂ on Cu-skin Cu₃Au(111) surface. The calculated results show that the b-f(h)-b adsorption configuration is the most energetically favorable on the Cu-skin Cu₃Au(111) surface. For O₂ dissociation, there are two thermodynamically favorable dissociation paths. One path is from b-f-b to two O atoms in hcp sites, and the other path is from b-h-b to two O atoms in fcc sites. Moreover, the stability of O₂ adsorption is higher and the dissociation energy barrier of the adsorbed O₂ is lower as compared to those on the Cu(111) surface. This theoretical work provides valuable guidance for the practical application of Cu-Au alloys as highly efficient CO oxidation catalysts.

Keywords: adsorption; dissociation; density-functional theory calculations; Cu-skin Cu₃Au(111) surface



Citation: Yu, Y.; Liu, Z.; Huang, W.; Zhou, S.; Hu, Z.; Wang, L. Ab Initio Investigation of the Adsorption and Dissociation of O₂ on Cu-Skin Cu₃Au(111) Surface. *Catalysts* **2022**, *12*, 1407. <https://doi.org/10.3390/catal12111407>

Academic Editors: Yongjun Ji, Liwen Xing and Ke Wu

Received: 29 September 2022

Accepted: 1 November 2022

Published: 10 November 2022

Publisher's Note: MDPI stays neutral with regard to jurisdictional claims in published maps and institutional affiliations.



Copyright: © 2022 by the authors. Licensee MDPI, Basel, Switzerland. This article is an open access article distributed under the terms and conditions of the Creative Commons Attribution (CC BY) license (<https://creativecommons.org/licenses/by/4.0/>).

1. Introduction

Bimetal alloys exhibit promising applications in various technologies related to surface science and heterogeneous catalysis [1–3]. In particular, they are significant in dominating catalytic reactions, such as selective hydrogenation [4], oxygen reduction [5], synthesis gas reaction [6], and synthesis of vinyl acetate [7]. This is attributed to their specific surface electronic properties affecting the surface adsorption and dissociation processes. Many theoretical studies have shown that the reaction process can have a decisive impact on catalytic performance. For example, Feng et al. [8] surveyed the electronic structures of cobalt-molybdenum bimetallic, arguing that H₂ adsorption/dissociation on the alloy surface was a key process determining the catalytic activity. Shin et al. [9] investigated the catalytic properties of Ag-Cu binary alloy in oxygen reduction reactions, and further confirmed that the activation energy of O₂ dissociation was a rate-determining process in the catalytic reaction. The study by Liu et al. [10] demonstrated that O₂ adsorption and dissociation on the surface of Cu-Au alloys were considered to be key processes to limit the rate of CO oxidation. Therefore, studying the reaction process will provide a significant support for understanding the catalytic reaction mechanism of binary catalysts.

Among the bimetallic systems, copper alloys have received much attention because of their wide application in a large number of chemical reactions including heterogeneous methanol reforming [11], methanol synthesis [12], the synthesis of diamond [13], and the reduction of 4-nitrophenol [14]. In the context of the CO oxidation reaction, the experiments have demonstrated that the Cu alloying with Au element could improve the efficiency of the CO oxidation reaction and promote the reaction toward desired products [15]. This is attributed to the synergistic interaction between Cu and Au, which improves the catalytic performance of the alloy. Although some studies [10,16,17] have indicated that the adsorption and dissociation of O₂ were the key processes to limit the rate of CO oxidation on the surface of noble metal catalysts, few studies have been carried out on the adsorption and

dissociation of O₂ on the surface of Cu-Au catalysts. Obviously, the theoretical calculations can provide necessary help for understanding the reaction processes.

In this work, we perform first-principles calculations to investigate the adsorption and dissociation of O₂ on the Cu-skin Cu₃Au(111) surface. The calculated results show that the b-f(h)-b adsorption configuration is the most energetically favorable on the Cu-skin Cu₃Au(111) surface. For O₂ dissociation, there are two thermodynamically favorable dissociation paths. One path is from b-f-b to two O atoms in hcp sites, and the other path is from b-h-b to two O atoms in fcc sites. Moreover, the stability of O₂ adsorption is higher and the dissociation energy barrier of the adsorbed O₂ is lower as compared to those on the Cu(111) surface. The remainder of the paper is organized as follows. In Section 2, the computational details are described. Section 3 presents the calculated results and discussion. A brief summary is given in Section 4.

2. Computational Methods

The spin-polarized DFT calculations were performed employing the Vienna Ab-initio Simulation Program (VASP) [18–20]. We used the projector augmented-wave method (PAW) [21,22] and the Perdew–Burke–Ernzerhof formulation of the generalized-gradient approximation (GGA-PBE) for the exchange correlation functional [23]. The plane-wave cutoff energy was set at 400 eV. The convergence criterion for the electronic self-consistent cycle was fixed to 10^{−5} eV per supercell and the ionic relaxation loop were set to 0.02 eV/Å. The electric dipole was neglected, and the Brillouin zone was sampled with a 5 × 5 × 1 Monkhorst-Pack [24] k-point mesh for the slab calculations.

In this work, we chose low index (111) surface to simulate the surfaces of pure Cu and CuAu alloy system, mainly because the (111) surface may be the dominant facet [25]. The previous studies have shown that Cu₃Au alloys with L1₂ crystal structure can be widely used in various chemical reactions [26–28]. In addition, the catalyst inevitably contacts with air in the process of preparation and practical application, which will lead to oxygen adsorption-induced segregation, forming a copper segregation structure with 100% copper in the topmost surface layer and 50% copper in the second surface layer, which is the so-called Cu-skin structure [28]. Therefore, we employed the Cu-skin Cu₃Au(111) alloys to investigate the adsorption and dissociation of O₂ on the surface of Cu-Au catalysts. The DFT-lattice constants for Cu₃Au and pure Cu were 3.79 and 3.63 Å, respectively, which are consistent with previously reported results [26,29]. Figure 1 shows the slab models for pure Cu(111) and Cu₃Au(111) surfaces. We employed a 2 × 2 (111) unit cell for both slab models, which consisted of four atomic layers and six equivalent layers of vacuum. In all slab models, atoms in the top two layers were allowed to relax to the most stable configuration, while atoms in the bottom two layers were fixed to their bulk positions. Adsorbates were adsorbed on the surface of the model.

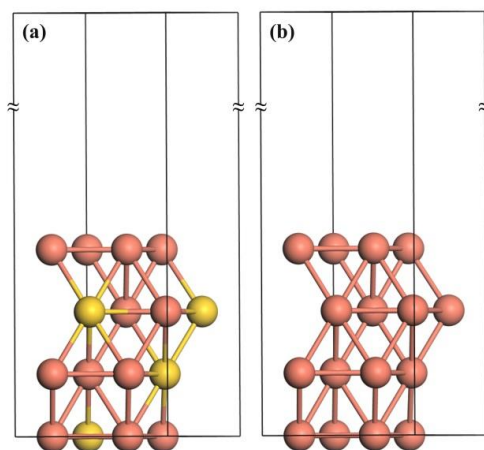


Figure 1. The slab models consist of (a) Cu-skin Cu₃Au(111) surface, (b) pure Cu(111) surface. In the figure, brick-red and gold balls represent Cu and Au atoms, respectively.

The adsorption energies (E_{ads}) of molecular O_2 adsorbed on the pure Cu(111) and Cu-skin $Cu_3Au(111)$ surfaces were calculated as following:

$$E_{ads,O_2} = E_{O_2-slab} - E_{slab} - E_{O_2} \quad (1)$$

In the equation, the first and second terms on the right-hand side correspond to the energies of substrates with and without O_2 adsorption, respectively, and the remaining term corresponds to the energy of the O_2 molecule. A negative value of E_{ads} indicates that it favors the adsorption of O_2 on the metal surface.

The transition states and minimum energy path (MEP) for O_2 dissociation on the Cu(111) and Cu-skin $Cu_3Au(111)$ surfaces was studied by using the climbing-image nudged elastic band (CI-NEB) method [30,31]. The CI-NEB is a small modification of the NEB method, where the highest energy image is driven to the saddle point (transition state) in an attempt to maximize its energy along the band and minimize it in all other directions. When the algorithm converges, the highest energy images will be at an exact saddle point, so the CI-NEB method is currently the predominant method for finding the transition state and the minimum energy path between known reactants and products. Once a minimum energy path is determined, the transition state is located and the activation energy will be calculated as following:

$$E_a = E_b^{TS} - E_b^{PS} \quad (2)$$

In the equation, the E_b^{TS} corresponds to the total energy of the transition state and the E_b^{PS} corresponds to the total energy of the precursor state. The basis set superposition errors correction for the precursor state in our calculation was ignored because it had little effect on the calculated results.

3. Theoretical Results

3.1. The Adsorption of O_2

For Cu-skin $Cu_3Au(111)$ surface, there are two kinds of nonequivalent Cu atoms in the topmost layer of the alloy because of the uneven distribution of Cu and Au atoms in the second layer. These two Cu atoms are denoted as Cu_1 and Cu_2 , respectively, as shown in Figure 2a. For the Cu_1 atom, it is located at the center of one Au atom and two Cu atoms in the second layer of the surface; while for the Cu_2 atom, it is located at the center of one Cu atom and two Au atoms in the second layer of the surface. We can find that the Cu_1 atom is about 0.082 Å lower than the Cu_2 atom in the vertical position after the surface structure is relaxed. In addition, the Bader [32] analysis shows that Au in the alloy obtains fewer electrons from Cu_1 than from Cu_2 , and the number of electrons is 0.04 and 0.07, respectively. This may be because the amount of Au close to Cu_1 is smaller than that of Au close to Cu_2 . The similar phenomena can also be found in the Pt-skin Pt_3Fe [33] and Pt-skin Pt_3Cr [34] systems.

Many studies have shown that five types of stable adsorption sites for O_2 existed on the low-index (111) surface of transition metals, namely, b-f-b, t-f-b, b-h-b, t-h-b, and t-b-t sites [35]. For Cu-skin $CuAu(111)$ surface, due to the presence of two nonequivalent Cu atoms in the topmost layer of the alloy, there are mainly two different adsorption configurations for each type of adsorption site. We calculated the adsorption energies of O_2 on these adsorption sites of Cu(111) and Cu-skin $Cu_3Au(111)$, and the stable adsorption configurations and calculated results are shown in Figure 2 and Table 1, respectively. For the Cu(111) surface, we can find that the adsorption energies of O_2 on the b-h-b and b-f-b sites are the highest, both of which are -0.76 eV. When O_2 is adsorbed at the t-h-b, t-f-b, and t-b-t sites, their adsorption energies are -0.71 , -0.71 , and -0.50 eV, respectively. This calculation result is consistent with the previous theoretical calculation result [25]. For the Cu-skin $Cu_3Au(111)$ surface, the adsorption energies at each adsorption site are very close, and they range from -1.07 to -1.15 eV. Similar to the Cu(111) surface, b-f-b1 and b-h-b1 are the two most stable adsorption configurations with values of -1.14 and -1.15 eV, respectively. In contrast to the Cu(111) surface, the t-b-t adsorption configuration is not

stable on the Cu-skin $\text{Cu}_3\text{Au}(111)$ surface. This may be due to the weak interaction between O_2 and the substrate [36]. The Bader analysis shows that the adsorption of O_2 will cause the Cu on the surface to lose more electrons. A part of these electrons is acquired by Au atoms in the second layer, and the other part is acquired by O_2 adsorbed on the surface. Furthermore, O_2 gains more electrons from the Cu-skin $\text{Cu}_3\text{Au}(111)$ surface than from the $\text{Cu}(111)$ surface, suggesting that the modification of the surface electronic structure by alloying promotes the formation of strong adsorption bonds between O_2 and Cu atoms on the alloy surface.

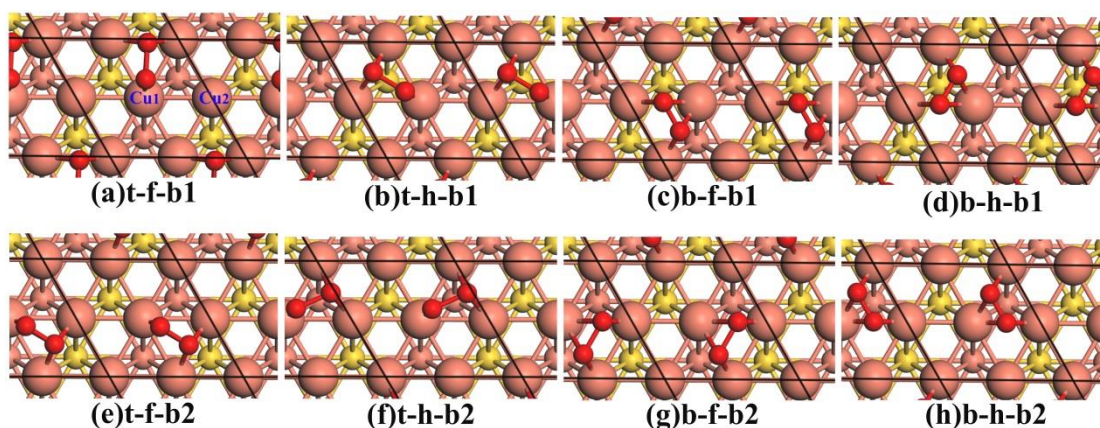


Figure 2. The top view for optimized configurations of O_2 adsorption on Cu-skin $\text{Cu}_3\text{Au}(111)$ surface. The two kinds of nonequivalent Cu atoms (Cu_1 and Cu_2) are marked in Figure 2a. The brick-red, gold, and red balls represent copper, gold, and oxygen atoms, respectively. For clarity, the topmost atoms on the surface are displayed with the biggest balls and only the top two layers are displayed.

Table 1. The adsorption energy of O_2 (E_{ads} in eV) and the number of electrons obtained by O_2 from the surfaces of Cu-skin $\text{Cu}_3\text{Au}(111)$ and $\text{Cu}(111)$.

$\text{Cu}_3\text{Au}(111)$			$\text{Cu}(111)$		
Site	E_{ads}	N_{chg}	Site	E_{ads}	N_{chg}
t-f-b1	−1.08	0.92	t-f-b	−0.71	0.87
t-f-b2	−1.08	0.93	t-h-b	−0.71	0.87
t-h-b1	−1.09	0.91	t-b-t	−0.50	0.70
t-h-b2	−1.07	0.92	b-f-b	−0.76	0.94
b-f-b1	−1.14	1.01	b-h-b	−0.76	0.94
b-f-b2	−1.12	1.00			
b-h-b1	−1.15	1.01			
b-h-b2	−1.11	1.00			

3.2. The Electronic Structure of Cu-Skin Cu_3Au Surface

The density of states (DOS) can provide key information for understanding the electronic structure and bonding properties of alloy compounds, especially when it comes to investigating the adsorption properties of metal alloy surfaces, the d-band DOS is an extremely significant reference [37,38]. Figure 3 shows the d-band DOS of the Cu atoms in the outermost layer of alloys and pure metals in the absence of adsorption. From the figure, we can find that compared with the d-band center for Cu on the $\text{Cu}(111)$ surface, the d-band center for Cu on the Cu-skin $\text{Cu}_3\text{Au}(111)$ alloy surface is closer to the Fermi level. This similar phenomenon can also be seen in Pt and Pd alloys [39,40]. This phenomenon is attributed to the overlapping of the d-electron density of states for Cu and Au atoms in the alloy, which leads to the re-hybridization of the d-band DOS for Cu, thus promoting the d-band center of copper in the alloy to move closer to the Fermi level [41]. On the basis of the adsorption model established by Hammer and Nørskov [37,38], it is shown that the adsorption strength of the adsorbate on the metal surface is closely related to the d-band

center. When the center of the d-band moves to the high-energy region, the adsorption strength is larger. Therefore, the adsorption strength of O_2 on the Cu-skin $Cu_3Au(111)$ surface should be greater than that on the $Cu(111)$ surface. This result is consistent with our calculation above.

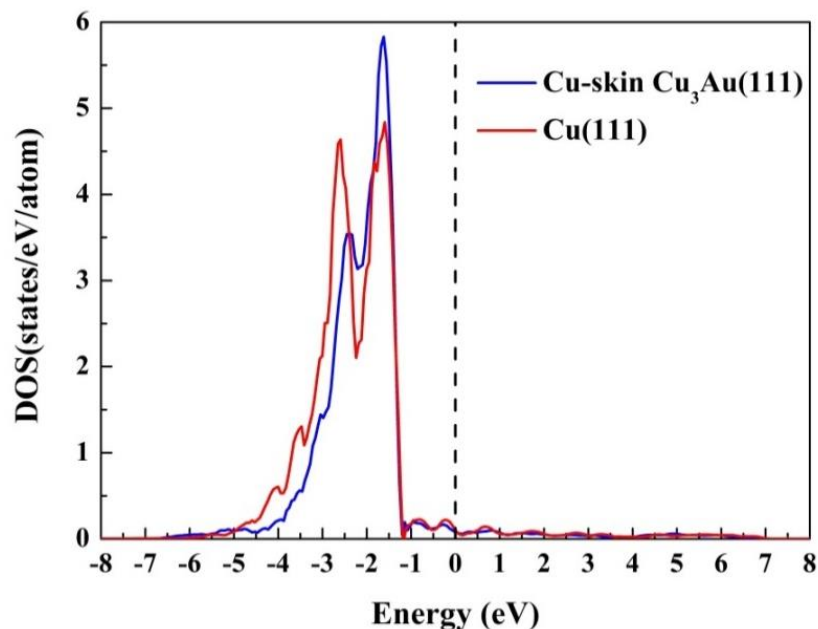


Figure 3. The calculated densities of states (DOS) of the Cu atoms in the Cu-skin $Cu_3Au(111)$ and $Cu(111)$ surfaces. The d-band DOS of surface Cu atoms on $Cu(111)$ is presented for comparison.

3.3. The Dissociation of O_2

Many studies have shown that studying the dissociation process of the adsorbate on the catalyst surface by using DFT calculations required knowledge of the initial and final states of the reaction [35,36,42–44]. According to the above calculation results, the oxygen molecule tends to be adsorbed on the b-f(h)-b sites. Therefore, we chose the b-f(h)-b adsorption configuration as the initial state of the reaction. Many studies [35,36,42,43] have also shown that it is impossible for two O atoms to simultaneously adsorb on a set of adjacent hcp and fcc sites after the O-O bond of the precursor is broken; this is because they will be very strongly repulsed, and the two O atoms are more inclined to adsorb on two adjacent hcp or two adjacent fcc sites. Therefore, there are two thermodynamically favorable dissociation paths for O_2 dissociation. One path is from b-f-b to $2 \times$ hcp (two O atoms adsorb on a set of adjacent hcp sites), and the other path is from b-h-b to $2 \times$ fcc (two O atoms adsorb on a set of adjacent fcc sites). For the $O_2/Cu_3Au(111)$ system, we only studied the dissociation process of the adsorption configurations of b-f-b1 and b-h-b1 with higher adsorption strength, and their dissociation processes are shown in Figure 4a,b, respectively. From the figure, we can find that the dissociation process of the adsorption configuration of b-f-b1 and b-h-b1 is very similar. Early in the dissociation process, they both form a transition state with a low energy barrier (less than 0.1 eV) by stretching the O-O bond. When the O-O bond is stretched to break, the two separated O atoms will be adsorbed on two adjacent stable adsorption sites. This shows that O_2 easily dissociates on the Cu-skin $Cu_3Au(111)$ surface and forms a stable adsorption structure, which is consistent with other theoretical studies [28,45].

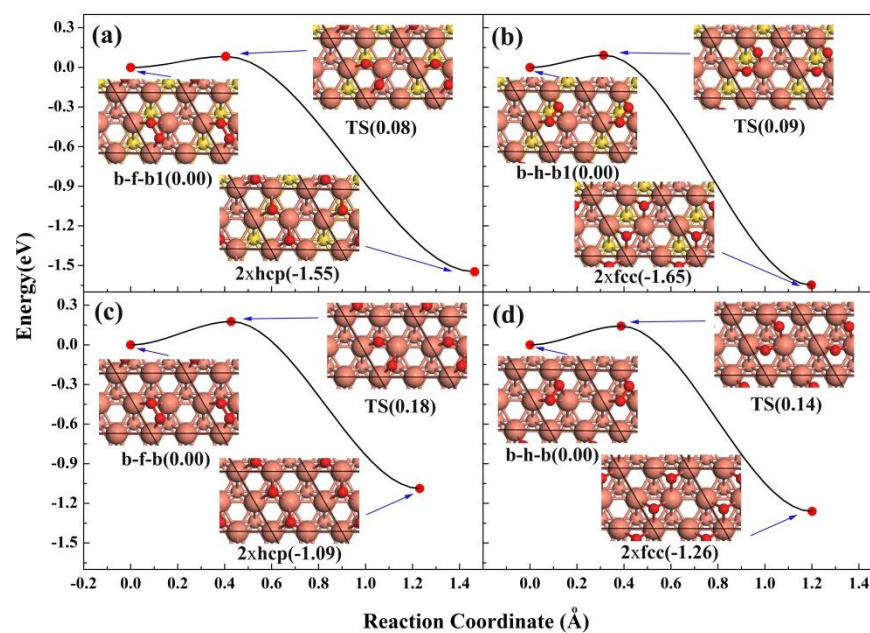


Figure 4. The minimum energy path (MEP) of the dissociation process for: (a) b-f-b1 adsorption state on Cu-skin $\text{Cu}_3\text{Au}(111)$ surface, (b) b-h-b1 adsorption state on Cu-skin $\text{Cu}_3\text{Au}(111)$ surface, (c) b-f-b adsorption state on Cu(111) surface, (d) b-h-b adsorption state on Cu(111) surface. The $2 \times \text{fcc}$ (two O occupying a set of neighboring fcc sites) and $2 \times \text{hcp}$ (two O occupying a set of neighboring hcp sites) are designated as the dissociation state of b-h-b and b-f-b adsorption configuration, respectively. TS represents the transitions state and the numbers in the brackets represent the energy of each state relative to initial state.

To further understand the dissociation process of O_2 on the Cu-skin $\text{Cu}_3\text{Au}(111)$ surface, we also investigated the dissociation process of the $\text{O}_2/\text{Cu}(111)$ system, and the results are shown in Figure 4c,d. It can be seen from the figure that although the dissociation process of the $\text{O}_2/\text{Cu}(111)$ system is very similar to that of the $\text{O}_2/\text{Cu}_3\text{Au}(111)$ system, the dissociation energy barrier of the $\text{O}_2/\text{Cu}(111)$ system is higher. For example, for the b-h-b and b-f-b states, their dissociation energy barriers are 0.14 and 0.18 eV, respectively, which are consistent with the estimate of 0.08–0.18 eV/ O_2 by Habraken et al. [46]. This also explains why Cu alloying with the Au element can improve the efficiency of the CO oxidation reaction and promote the reaction toward desired products [15,47].

4. Conclusions

We have used density functional theory to investigate the adsorption and dissociation of O_2 on the Cu-skin $\text{Cu}_3\text{Au}(111)$ surface. The calculated results show that the b-f(h)-b adsorption configuration is the most energetically favorable on the Cu-skin $\text{Cu}_3\text{Au}(111)$ surface. For the Cu-skin $\text{Cu}_3\text{Au}(111)$ surface, the adsorption energies at each adsorption site are very close, and they range from -1.07 to -1.15 eV. In contrast to the Cu(111) surface, the t-b-t adsorption configuration is not stable on the Cu-skin $\text{Cu}_3\text{Au}(111)$ surface. This may be due to the weak interaction between O_2 and the substrate. The Bader analysis shows that O_2 gains more electrons from the Cu-skin $\text{Cu}_3\text{Au}(111)$ surface than from the Cu(111) surface, suggesting that the modification of the surface electronic structure by alloying promotes the formation of strong adsorption bonds between O_2 and Cu atoms on the alloy surface. For O_2 dissociation, there are two thermodynamically favorable dissociation paths. One path is from b-f-b to $2 \times \text{hcp}$ (two O atoms adsorb on a set of adjacent hcp sites), and the other path is from b-h-b to $2 \times \text{fcc}$ (two O atoms adsorb on a set of adjacent fcc sites). The dissociation energy barrier of O_2 on the Cu-skin $\text{Cu}_3\text{Au}(111)$ surface is lower as compared to those on the Cu(111) surface. This theoretical work provides valuable guidance for the practical application of Cu-Au alloys as highly efficient CO oxidation catalysts.

Author Contributions: Conceptualization, Y.Y. and L.W.; methodology, Y.Y.; software, Z.L.; validation, Z.L., S.Z. and Z.H.; formal analysis, S.Z.; investigation, W.H.; resources, Z.H.; data curation, W.H.; writing—original draft preparation, Y.Y.; writing—review and editing, Y.Y.; visualization, Z.L.; supervision, L.W.; project administration, L.W.; funding acquisition, Y.Y. All authors have read and agreed to the published version of the manuscript.

Funding: This research was funded by the Science and technology planning project of Jiangxi Provincial Department of Education, grant numbers GJJ180572 and GJJ160733, and the doctoral research project of Jinggangshan university, grant number JZB1815.

Data Availability Statement: Not applicable.

Conflicts of Interest: The authors declare no conflict of interest.

References

1. Stamenkovic, V.R.; Mun, B.S.; Arenz, M.; Mayrhofer, K.J.; Lucas, C.A.; Wang, G.; Ross, P.N.; Markovic, N.M. Trends in electrocatalysis on extended and nanoscale Pt-bimetallic alloy surfaces. *Nat. Mater.* **2007**, *6*, 241–247. [CrossRef] [PubMed]
2. Dong, Z.; Zhao, J.; Tian, Y.; Zhang, B.; Wu, Y. Preparation and performances of ZIF-67-derived FeCo bimetallic catalysts for CO₂ hydrogenation to light olefins. *Catalysts* **2020**, *10*, 455. [CrossRef]
3. Montemore, M.M.; van Spronsen, M.A.; Madix, R.J.; Friend, C.M. O₂ activation by metal surfaces: Implications for bonding and reactivity on heterogeneous catalysts. *Chem. Rev.* **2017**, *118*, 2816–2862. [CrossRef] [PubMed]
4. Murillo, L.E.; Goda, A.M.; Chen, J.G. Selective hydrogenation of the CO bond in acrolein through the architecture of bimetallic surface structures. *J. Am. Chem. Soc.* **2007**, *129*, 7101–7105. [CrossRef] [PubMed]
5. Tripkovic, V.; Hansen, H.A.; Rossmeisl, J.; Vegge, T. First principles investigation of the activity of thin film Pt, Pd and Au surface alloys for oxygen reduction. *Phys. Chem. Chem. Phys.* **2015**, *17*, 11647–11657. [CrossRef]
6. Pompeo, F.; Nichio, N.N.; Ferretti, O.A.; Resasco, D. Study of Ni catalysts on different supports to obtain synthesis gas. *Int. J. Hydrog. Energy* **2005**, *30*, 1399–1405. [CrossRef]
7. Chen, M.; Kumar, D.; Yi, C.-W.; Goodman, D.W. The promotional effect of gold in catalysis by palladium-gold. *Science* **2005**, *310*, 291–293. [CrossRef]
8. Feng, M.; Huang, J.; Peng, Y.; Huang, C.; Yue, X.; Huang, S. Tuning the electronic structures of cobalt-molybdenum bimetallic carbides to boost the hydrogen oxidation reaction in alkaline medium. *Chem. Eng. J.* **2022**, *428*, 131206. [CrossRef]
9. Shin, K.; Kim, D.H.; Lee, H.M. Catalytic characteristics of AgCu bimetallic nanoparticles in the oxygen reduction reaction. *ChemSusChem* **2013**, *6*, 1044–1049. [CrossRef]
10. Liu, X.; Wang, A.; Wang, X.; Mou, C.-Y.; Zhang, T. Au–Cu alloy nanoparticles confined in SBA-15 as a highly efficient catalyst for CO oxidation. *Chem. Commun.* **2008**, *27*, 3187–3189. [CrossRef]
11. Yong, S.T.; Ooi, C.W.; Chai, S.-P.; Wu, X. Review of methanol reforming-Cu-based catalysts, surface reaction mechanisms, and reaction schemes. *Int. J. Hydrog. Energy* **2013**, *38*, 9541–9552. [CrossRef]
12. Graciani, J.; Mudiyansele, K.; Xu, F.; Baber, A.E.; Evans, J.; Senanayake, S.D.; Stacchiola, D.J.; Liu, P.; Hrbek, J.; Sanz, J.F. Highly active copper-ceria and copper-ceria-titania catalysts for methanol synthesis from CO₂. *Science* **2014**, *345*, 546–550. [CrossRef] [PubMed]
13. Chen, L.; Zhu, P.; Ma, H.; Jia, X.; Wakatsuki, M.; Zou, G. Effects of copper-based alloy on the synthesis of single-crystal diamond. *J. Phys. Condens. Matter* **2002**, *141*, 10957–10961. [CrossRef]
14. Menumerov, E.; Gilroy, K.D.; Hajfathalian, M.; Murphy, C.J.; Neretina, S. Plastically deformed Cu-based alloys as high-performance catalysts for the reduction of 4-nitrophenol. *Catal. Sci. Technol.* **2016**, *6*, 5737–5745. [CrossRef]
15. Bauer, J.C.; Mullins, D.; Li, M.; Wu, Z.; Payzant, E.A.; Overbury, S.H.; Dai, S. Synthesis of silica supported AuCu nanoparticle catalysts and the effects of pretreatment conditions for the CO oxidation reaction. *Phys. Chem. Chem. Phys.* **2011**, *13*, 2571–2581. [CrossRef]
16. Hashmi, A.S.K.; Hutchings, G.J. Gold catalysis. *Angew. Chem. Int. Ed.* **2006**, *45*, 7896–7936. [CrossRef]
17. Bond, G.C.; Thompson, D.T. Catalysis by gold. *Catal. Rev.-Sci. Eng.* **1999**, *41*, 319–388. [CrossRef]
18. Kresse, G.; Furthmüller, J. Efficiency of ab-initio total energy calculations for metals and semiconductors using a plane-wave basis set. *Comput. Mater. Sci.* **1996**, *6*, 15–50. [CrossRef]
19. Kresse, G.; Furthmüller, J. Efficient iterative schemes for ab initio total-energy calculations using a plane-wave basis set. *Phys. Rev. B Condens. Matter* **1996**, *54*, 11169–11186. [CrossRef]
20. Kresse, G.; Hafner, J. Ab initio molecular-dynamics simulation of the liquid-metal-amorphous-semiconductor transition in germanium. *Phys. Rev. B* **1993**, *49*, 14251–14269. [CrossRef]
21. Blöchl, P.E. Projector augmented-wave method. *Phys. Rev. B Condens. Matter* **1994**, *50*, 2665–2668. [CrossRef] [PubMed]
22. Kresse, G.; Joubert, D. From ultrasoft pseudopotentials to the projector augmented-wave method. *Phys. Rev. B* **1999**, *59*, 1758–1775. [CrossRef]
23. Perdew, J.P.; Burke, K.; Ernzerhof, M. Generalized Gradient Approximation Made Simple. *Phys. Rev. Lett.* **1996**, *77*, 3865–3868. [CrossRef] [PubMed]

24. Monkhorst, H.J.; Hendrik, J.; James, D. Special points for Brillouin-zone integrations. *Phys. Rev. B* **1976**, *13*, 5188–5192. [CrossRef]
25. Dhifallah, M.; Dhouib, A.; Aldulaijan, S.; Di Renzo, F.; Guesmi, H. First-principles study of Au–Cu alloy surface changes induced by gas adsorption of CO, NO, or O₂. *J. Chem. Phys.* **2016**, *145*, 024701. [CrossRef]
26. Hirunsit, P.; Soodsawang, W.; Limtrakul, J. CO₂ Electrochemical Reduction to Methane and Methanol on Copper-Based Alloys: Theoretical Insight. *J. Phys. Chem. C* **2015**, *119*, 8238–8249. [CrossRef]
27. Hirunsit, P. Electroreduction of Carbon Dioxide to Methane on Copper, Copper–Silver, and Copper–Gold Catalysts: A DFT Study. *J. Phys. Chem. C* **2013**, *117*, 8262–8268. [CrossRef]
28. Oka, K.; Tsuda, Y.; Makino, T.; Okada, M.; Hashinokuchi, M.; Yoshigoe, A.; Teraoka, Y.; Kasai, H. The effects of alloying and segregation for the reactivity and diffusion of oxygen on Cu₃Au (111). *Phys. Chem. Chem. Phys.* **2014**, *16*, 19702–19711. [CrossRef]
29. Yu, Y.; Huang, W.; Liu, Z.; Hu, Z.; Wang, L. First-principles study of surface segregation in bimetallic Cu₃M (1 1 1)(M = Au, Ag, and Zn) alloys in presence of adsorbed CO. *Comput. Mater. Sci.* **2022**, *212*, 111550. [CrossRef]
30. Henkelman, G.; Jónsson, H. Improved tangent estimate in the nudged elastic band method for finding minimum energy paths and saddle points. *J. Chem. Phys.* **2000**, *113*, 9978–9985. [CrossRef]
31. Henkelman, G.; Uberuaga, B.P.; Jónsson, H. A climbing image nudged elastic band method for finding saddle points and minimum energy paths. *J. Chem. Phys.* **2000**, *113*, 9901–9904. [CrossRef]
32. Henkelman, G.; Arnaldsson, A.; Jónsson, H. A fast and robust algorithm for Bader decomposition of charge density. *Comput. Mater. Sci.* **2006**, *36*, 354–360. [CrossRef]
33. Hirschl, R.; Delbecq, F.; Sautet, P.; Hafner, J. Pt₈₀Fe₂₀ surface from first principles: Electronic structure and adsorption of CO and atomic H. *Phys. Rev. B* **2002**, *66*, 155438. [CrossRef]
34. Anderson, A.B. Theory for the Potential Shift for OH ads Formation on the Pt Skin on Pt₃Cr (111) in Acid. *J. Electrochem. Soc.* **2004**, *151*, E85.
35. Xu, Y.; Mavrikakis, M. Adsorption and dissociation of O₂ on Cu (111): Thermochemistry, reaction barrier and the effect of strain. *Surf. Sci.* **2001**, *494*, 131–144. [CrossRef]
36. Yang, Z.; Wang, J.; Yu, X. The adsorption, diffusion and dissociation of O₂ on Pt-skin Pt₃Ni (111): A density functional theory study. *Chem. Phys. Lett.* **2010**, *499*, 83–88. [CrossRef]
37. Hammer, B.; Nørskov, J.K. Why gold is the noblest of all the metals. *Nature* **1995**, *376*, 238–240. [CrossRef]
38. Hammer, B.; Nørskov, J.K. Electronic factors determining the reactivity of metal surfaces. *Surf. Sci.* **1995**, *343*, 211–220. [CrossRef]
39. Kitchin, J.; Nørskov, J.K.; Barteau, M.; Chen, J. Modification of the surface electronic and chemical properties of Pt (111) by subsurface 3d transition metals. *J. Chem. Phys.* **2004**, *120*, 10240–10246. [CrossRef]
40. Hensley, A.J.R.; Zhang, R.; Wang, Y.; Mcewen, J.S. Tailoring the Adsorption of Benzene on PdFe Surfaces: A Density Functional Theory Study. *J. Phys. Chem. C* **2013**, *117*, 24317–24328. [CrossRef]
41. Schweitzer, N.; Xin, H.; Nikolla, E.; Miller, J.T.; Linic, S. Establishing relationships between the geometric structure and chemical reactivity of alloy catalysts based on their measured electronic structure. *Top. Catal.* **2010**, *53*, 348–356. [CrossRef]
42. Yang, Z.; Wang, J.; Yu, X. Density functional theory studies on the adsorption, diffusion and dissociation of O₂ on Pt(111). *Phys. Lett. A* **2010**, *374*, 4713–4717. [CrossRef]
43. Xu, Y.; Ruban, A.V.; Mavrikakis, M. Adsorption and dissociation of O₂ on Pt–Co and Pt–Fe alloys. *J. Am. Chem. Soc.* **2004**, *126*, 4717–4725. [CrossRef] [PubMed]
44. Diao, Z.Y.; Han, L.L.; Wang, Z.X.; Dong, C.C. The adsorption and dissociation of O₂ on Cu low-index surfaces. *J. Phys. Chem. B* **2005**, *109*, 5739–5745. [CrossRef] [PubMed]
45. Okada, M.; Hashinokuchi, M.; Fukuoka, M.; Kasai, T.; Moritani, K.; Teraoka, Y. Protective layer formation during oxidation of Cu₃Au(100) using hyperthermal O₂ molecular beam. *Appl. Phys. Lett.* **2006**, *89*, 201912. [CrossRef]
46. Habraken, F.; Kieffer, E.P.; Bootsma, G. A study of the kinetics of the interactions of O₂ and N₂O with a Cu(111) surface and of the reaction of CO with adsorbed oxygen using AES, LEED and ellipsometry. *Surf. Sci.* **1979**, *83*, 45–59. [CrossRef]
47. Liu, Y.; Xu, C.; Cen, W.; Li, H. Design strategy of bifunctional catalysts for CO oxidation. *Fuel* **2022**, *320*, 123909. [CrossRef]

Article

Hydride Generation on the Cu-Doped CeO₂(111) Surface and Its Role in CO₂ Hydrogenation Reactions

Zhi-Qiang Wang^{1,†}, Hui-Hui Liu^{1,†}, Xin-Ping Wu^{1,*}, Peijun Hu^{1,2} and Xue-Qing Gong^{1,*}

¹ Key Laboratory for Advanced Materials and Joint International Research Laboratory for Precision Chemistry and Molecular Engineering, Feringa Nobel Prize Scientist Joint Research Center, Centre for Computational Chemistry and Research Institute of Industrial Catalysis, School of Chemistry and Molecular Engineering, East China University of Science and Technology, 130 Meilong Road, Shanghai 200237, China

² School of Chemistry and Chemical Engineering, The Queen's University of Belfast, Belfast BT9 5AG, UK

* Correspondence: xpwu@ecust.edu.cn (X.-P.W.); xgong@ecust.edu.cn (X.-Q.G.)

† These authors contributed equally to this work.

Abstract: Ceria-based catalysts exhibit great activity in catalyzing selective hydrogenation of CO₂ to methanol. However, the underlying mechanism of this reaction, especially the generation of active H species, remains unclear. In this work, we performed extensive density functional theory calculations corrected by on-site Coulomb interaction (DFT + U) to investigate the H₂ dissociation and the reaction between the active H species and CO₂ on the pristine and Cu-doped CeO₂(111) (denoted as Cu/CeO₂(111)) surfaces. Our calculations evidenced that the heterolytic H₂ dissociation for hydride generation can more readily occur on the Cu/CeO₂(111) surface than on the pristine CeO₂(111) surface. We also found that the Cu dopant can facilitate the formation of surface oxygen vacancies, further promoting the generation of hydride species. Moreover, the adsorption of CO₂ and the hydrogenation of CO₂ to HCOO* can be greatly promoted on the Cu/CeO₂(111) surface with hydride species, which can lead to the high activity and selectivity toward CO₂ hydrogenation to methanol.

Keywords: ceria; hydride; CO₂ hydrogenation; single Cu doping; density functional theory



Citation: Wang, Z.-Q.; Liu, H.-H.; Wu, X.-P.; Hu, P.; Gong, X.-Q. Hydride Generation on the Cu-Doped CeO₂(111) Surface and Its Role in CO₂ Hydrogenation Reactions. *Catalysts* **2022**, *12*, 963. <https://doi.org/10.3390/catal12090963>

Academic Editor: Albert Poater

Received: 14 July 2022

Accepted: 26 August 2022

Published: 29 August 2022

Publisher's Note: MDPI stays neutral with regard to jurisdictional claims in published maps and institutional affiliations.



Copyright: © 2022 by the authors. Licensee MDPI, Basel, Switzerland. This article is an open access article distributed under the terms and conditions of the Creative Commons Attribution (CC BY) license (<https://creativecommons.org/licenses/by/4.0/>).

1. Introduction

Oxide-based materials are increasingly recognized as highly efficient and selective catalysts for hydrogenation reactions [1–6]. Among numerous metal oxides, ceria (CeO₂), which usually contains abundant oxygen vacancies (O_V) on the surface and in the bulk, has attracted great attention for its excellent performance in catalyzing reactions such as hydrogenation of CO₂ to methanol [7–12]. The combined experimental and density functional theory (DFT) study of Liu et al. [9] reported that the morphology control of CeO₂ nano-catalysts is important for methanol synthesis. They also proposed that methanol was likely generated via the so-called formate (HCOO) pathway where the adsorbed CO₂ is firstly hydrogenated to the HCOO* species. Cheng et al. [10] investigated the conversion of CO₂ to methanol on the reduced CeO₂(110) surface by performing DFT calculations corrected by on-site Coulomb interaction (DFT + U) and microkinetic analysis. They also found that the HCOO route is the dominant pathway for methanol formation on the reduced CeO₂(110). Kumari et al. [11] performed DFT calculations to study the mechanisms of CO₂ reduction to CO and the hydrogenation of CO₂ to methanol on both the stoichiometric and reduced CeO₂(110) surfaces. It was found that CO₂ dissociates to CO through the interaction with the oxygen vacancy on the reduced ceria surface, and the produced CO can be further hydrogenated to methanol. Li et al. [12] investigated the mechanism of thermal catalytic hydrogenation of CO₂ to methanol on the reduced CeO₂(100) by using DFT calculations, and they found that CO₂ was hydrogenated via

the HCOO route rather than the COOH route. These results then indicate that oxygen vacancies on the reduced CeO₂ surface are crucial to the conversion of CO₂ to CH₃OH.

Cu-based catalysts are particularly active for CO₂ hydrogenation and have been commercially utilized for CO/CO₂ hydrogenation to methanol [13–16]. Xu et al. [17,18] reported the synergetic effect of Cu and ZnO on the catalytic activity and selectivity in the direct hydrogenation of CO₂ to C₂₊ alcohols. This synergetic effect can regulate the CO₂ and H₂ activation processes to achieve the optimal concentrations of surface CH_x^{*}, CO^{*} and H^{*} species for C₂₊ alcohols synthesis via CH_x^{*}–CO^{*} coupling and hydrogenation reactions. Jia et al. [19] found that abundant surface oxygen vacancies were in situ generated and consumed during the CO₂ reduction reaction on the Cu/CeO₂ catalyst with a Cu loading of 15 wt.%, and such vacancy sites can be combined with the adjacent copper clusters to promote the activation of CO₂ and increase the catalytic efficiency. Wang et al. [20] proposed that sub-nano Cu cubes supported on the thermally reduced CeO₂ nanorods through strong metal-support interaction (SMSI) can significantly enhance the formation and activity of hydrides species on both Cu and ceria, as compared with the Cu nanoparticles supported at stoichiometric CeO₂ nanorods. Xia et al. [21] performed DFT calculations and illustrated that the formation of oxygen vacancies was suppressed at the interface of the Cu cluster and CeO₂(111), while H₂ oxidation can be facilitated and the catalytic activity can be enhanced, in comparison with the pristine CeO₂(111). At the same time, single-atom catalysts were often reported to have catalytic properties that surpass those of nanoparticles [22,23]. Huang et al. [24] demonstrated that the C₃N₄-supported Cu single-atom catalysts with tailored coordination structures can serve as highly active and selective catalysts for CO₂ hydrogenation to methanol at low temperature, though the role of the Cu single atom in such catalytic process is still vague.

The study of the interaction between H₂ and ceria is crucial to understanding the mechanism of ceria catalyzed selective hydrogenation reactions [25–29]. Many studies have found that the homolytic dissociation of H₂ to form two hydroxyl (OH) groups is thermodynamically favored on the stoichiometric surface of ceria [6,30]. On the other hand, a few recent studies suggested that oxygen vacancies can facilitate the formation of active hydrides (H[−]) species through heterolytic dissociation of H₂ on the reduced surface of ceria [6,31–37]. This agrees with the previous studies that reduced ceria surface is more active than the stoichiometric one in CO₂ hydrogenation reactions [10,11]. Moreover, our recent studies proposed that low-coordinated Ce sites can promote the formation of H[−] species even on the stoichiometric CeO₂ stepped surfaces [38], which is consistent with the finding by García-Melchor et al. [27], and suggests that oxygen vacancy may not be essential for the formation of hydrides on the CeO₂ surfaces. To better drive the hydrogenation reactions such as the CO₂ reduction reaction (CO₂-RR) under moderate conditions, the activity and stability of the hydride species would need to be further enhanced on the surfaces of the ceria-based catalysts.

In this work, we investigated the role of the Cu dopant on the CeO₂(111) surface in the catalytic dissociation of H₂ to produce hydride species. Specifically, DFT + U calculations have been performed to illustrate the reactivity of H₂ dissociation on the pristine and Cu-doped CeO₂(111) (denoted as Cu/CeO₂(111)) surfaces. Our results showed that the doping of a single Cu atom is accompanied by the formation of an oxygen vacancy on the CeO₂(111) surface, and the formed oxygen vacancy can play a key role in the formation of H[−] species through heterolytic H₂ dissociation. In addition, the single Cu site can also enhance the adsorption of CO₂, which is favorable for improving the catalytic activity. Our calculations further indicated that the Cu/CeO₂(111) surface with H[−] species exhibits high activity and selectivity in the hydrogenation of CO₂ to methanol.

2. Calculation Methods

In this work, all spin-polarized DFT calculations were carried out using the Vienna Ab-initio Simulation Package (VASP) [39]. The projector augmented wave (PAW) method [40] and the Perdew–Burke–Ernzerhof (PBE) [41] functional under the generalized gradient

approximation (GGA) [42] were applied in the calculations. The kinetic energy cut-off was set as 400 eV (Table S1), and the force threshold for structure optimizations was 0.05 eV/Å. A large vacuum gap of 15 Å was used to eliminate the interaction between neighboring slabs. Different k -point meshes have been tested during the optimization of the unit cell of bulk ceria. It was shown that the k -point mesh of $(5 \times 5 \times 5)$ can give the converged result (Table S2), and the calculated lattice parameter ($a = b = c = 5.456$ Å) is in good agreement with the experimental value (5.411 Å), which was then used for the subsequent study [43].

We then built a $p(3 \times 3)$ surface slab containing three O–Ce–O layers to model the CeO₂(111) surface. To model the Cu-doped CeO₂(111), one surface Ce atom was replaced by a Cu atom and one surface oxygen nearby was removed accordingly to ensure charge conservation. The top two layers of the slabs were allowed to fully relax, while the bottom layer was kept fixed to mimic the bulk region. Due to the relatively large surface cell (11.56 Å × 11.56 Å), the k -point mesh of $(2 \times 2 \times 1)$ suggested by previous studies was used for Brillouin-zone integrations [44]. Note that the on-site Coulomb interaction correction is necessary for the appropriate description of the localized Ce 4*f* electrons [45–47], and therefore we used an effective U value of 5 eV, as suggested by previous studies [45,46].

The transition states (TSs) of surface reactions were located using a constrained optimization scheme and were verified when (i) all forces on the relaxed atoms vanish and (ii) the total energy is a maximum along the reaction coordination but a minimum with respect to the rest of the degrees of freedom [48–50]. For example, when using this approach to calculate the transition states of H₂ dissociation, we fixed the H–H distance at preselected values and then optimized the whole system with respect to all the remaining degrees of freedom.

The adsorption energy of species X on the surface, $E_{\text{ads}}(X)$, was calculated with

$$E_{\text{ads}}(X) = -(E_{X/\text{slab}} - E_{\text{slab}} - E_X) \quad (1)$$

where $E_{X/\text{slab}}$ is the calculated total energy of the adsorption system, while E_{slab} and E_X are the calculated energies of the clean surface and the gas phase molecule X , respectively. Accordingly, a positive $E_{\text{ads}}(X)$ value indicates an energetically favorable adsorption process, and the more positive the $E_{\text{ads}}(X)$ is, the more strongly the adsorbate X binds to the surface, and this definition was also proposed by Somorjai and Li [51].

The neutral oxygen vacancy formation energy (E_{OV}) was calculated according to

$$E_{\text{OV}} = E_{\text{slab-vac}} + 1/2E_{\text{O}_2} - E_{\text{slab}} \quad (2)$$

where $E_{\text{slab-vac}}$ is the total energy of the surface with a neutral oxygen vacancy and E_{O_2} is the energy of a gas-phase O₂ molecule.

3. Results and Discussion

3.1. Structural and Electronic Properties

The CeO₂(111) surface is known as the most stable termination of ceria [26,27]. From Figure 1a, one can see that there are two types of lattice oxygen on the CeO₂(111) surface, namely, the three-fold coordinated O (denoted as O_{3c}) on the top layer and four-fold coordinated O (denoted as O_{4c}) on the subsurface. The calculated bond lengths of Ce–O_{3c} (2.36 Å) and Ce–O_{4c} (2.37 Å) are nearly identical. Figure 1b shows the optimized structure of the Cu-doped CeO₂(111) (Cu/CeO₂(111)). As we have explained, the doping of one Cu atom onto the CeO₂(111) surface is accompanied by the spontaneous formation of an oxygen vacancy ($E_{\text{OV}} = -0.94$ eV) to ensure charge conservation [52,53]. The calculated bond lengths of Ce–O_{3c} (2.35 Å) and Ce–O_{4c} (2.36 Å) on the doped Cu/CeO₂(111) are nearly identical to those of the pristine CeO₂(111). Moreover, the calculated bond lengths of Cu–O_{3c} and Cu–O_{4c} on the Cu/CeO₂(111) surface are 3.13 and 1.96 Å, respectively, and these results are consistent with previous studies [52–54]. The elongation of the Cu–O_{3c} bond also indicates that the top surface O atoms bonding to Cu are activated.

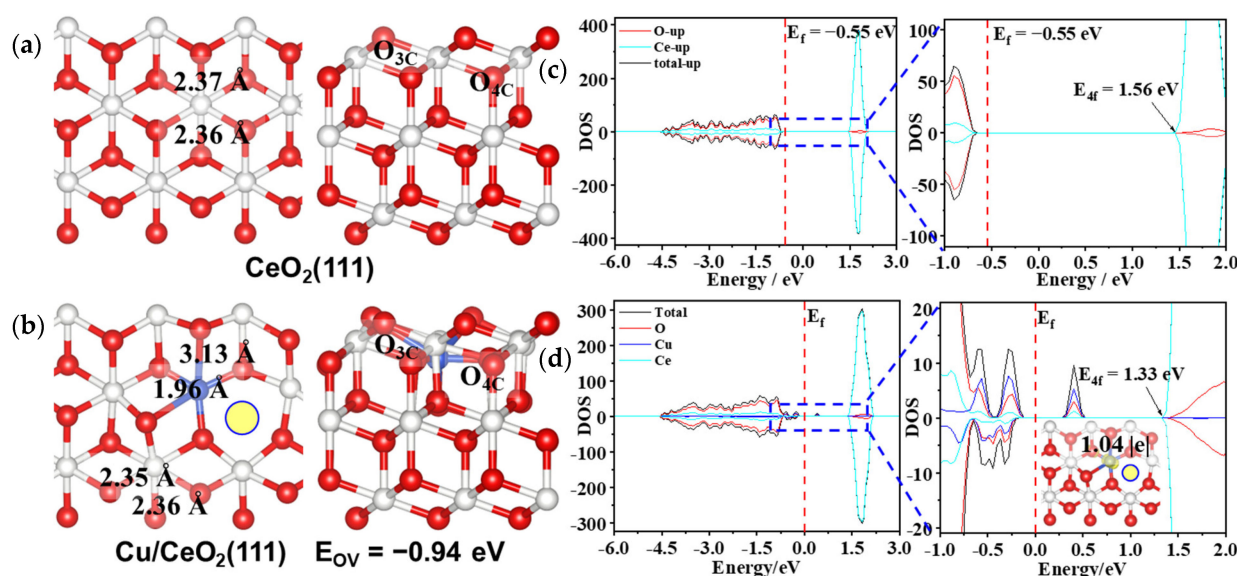


Figure 1. Calculated structures (left: top view; right: side view) of the (a) $\text{CeO}_2(111)$ and (b) $\text{Cu}/\text{CeO}_2(111)$ surfaces, and calculated density of states (DOS) of the (c) $\text{CeO}_2(111)$ and (d) $\text{Cu}/\text{CeO}_2(111)$ surfaces. The blue circles filled with yellow represent the inherent surface oxygen vacancy on the $\text{Cu}/\text{CeO}_2(111)$. Red: O atoms; ivory: Ce atoms; blue: Cu atoms. These notations are used throughout the paper. All DOS were aligned with respect to the O 2s orbital of a fixed bottom O atom of the surface slabs.

To better understand the doped $\text{Cu}/\text{CeO}_2(111)$, we first calculated the density of states (DOS) and spin density distribution of this surface (Figure 1d). The lowest unoccupied states are mainly composed of Cu 3d and O 2p. This indicates that the local CuO structure is capable of receiving extra electrons and may act as the catalytically active site. The calculated Bader charge of the Cu dopant is +1.04 |e|, which is close to that of the Cu^{2+} on the CuO surface (+0.97 |e|, see Table S3), indicating that the oxidation state of the Cu dopant on the $\text{CeO}_2(111)$ is indeed +2 [52,55]. This is also consistent with the calculated spin density distribution on the Cu site (Figure 1d). In addition, we also found that after Cu doping the energy level of the lowest unoccupied Ce 4f orbital decreases by 0.23 eV from 1.56 eV to 1.33 eV (Figure 1c,d), indicating that the electron accepting capacity of Ce 4f is also enhanced accordingly.

3.2. H Adsorption

Previous studies suggested that hydride is the key species for selective hydrogenation of CO_2 over ceria surfaces [10,11]. To verify the nature of various H species including proton, hydride and hydrogen radical ($\text{H}\bullet$), one needs to calculate their Bader charges as well as the spin density distributions. For the hydride species, there is no (net) spin density localized on it, and the calculated Bader charges are usually negative, while for the hydrogen radical, there are spin densities localized on it and the calculated Bader charge is usually close to 0 |e|. Bearing the above in mind, we thus studied the adsorption of one H atom at different sites on the $\text{Cu}/\text{CeO}_2(111)$ surface. The calculated results show that two types of H species can be formed after H adsorption at the Cu site (Figure 2a,b). Electronic structure analyses confirmed that one adsorbed H species is a radical-like species since it has net spin densities (Figure 2a), and the other one has a Bader charge that is close to zero (Figure 2b). For the calculated adsorption energies, they are negative for both cases, though the second type gives higher value (−1.61 vs. −0.45 eV, Figure 2a,b). Moreover, the calculated density of states of the system shown in Figure S1 also indicates that a relatively stronger Cu-H bond is formed for the second adsorption structure (Figure 2b) [53,54]. In addition, we also investigated H adsorption at the surface O site. In this case, a proton (H^+)

is formed, and the surface is clearly reduced, with either the Cu or Ce taking the electron from the H (Figure 2c,d). However, it needs to be mentioned that for the reduction of Cu^{2+} to Cu^{1+} (Bader charge = 0.66 |e|), the corresponding adsorption process is exothermic by 1.99 eV (Figure 2c), and for the reduction of Ce^{4+} to Ce^{3+} , it is exothermic by 2.36 eV (Figure 2d).

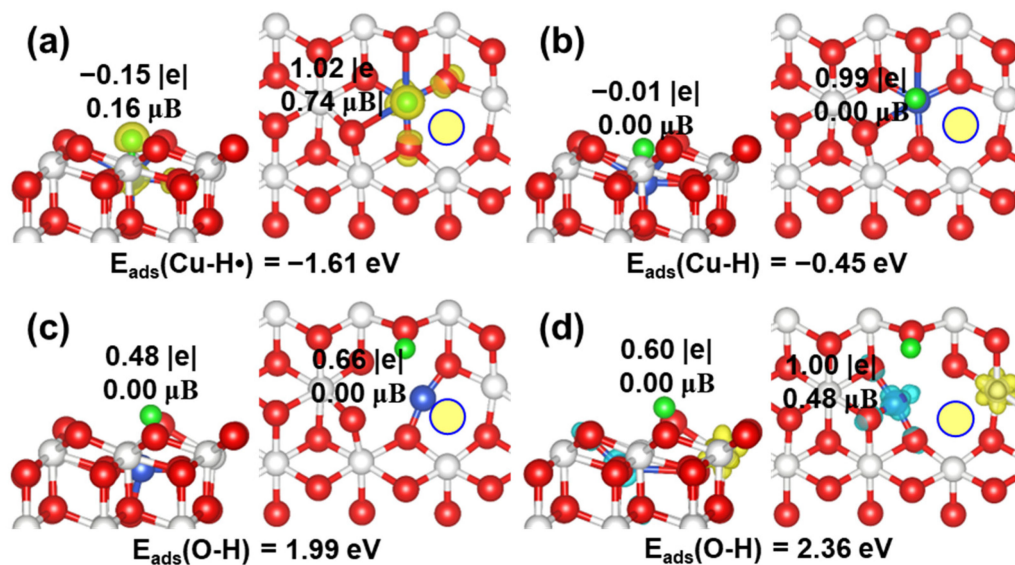


Figure 2. Calculated structures (left: side view; right: top view) of H adsorption at (a,b) Cu and (c,d) O sites of the Cu/CeO₂(111) surface. The calculated adsorption energies of H, Bader charges and the magnetic moments of H (left) and Cu (right), and spin density distributions (in yellow) are also shown.

Hermansson and Fernandez-Gacia and their co-workers [52,55] have shown that the four coordinated planar Cu^{2+} is relatively stable within the Cu/CeO₂(111) structure. It is interesting for us to find that with the hydrogen species being adsorbed at the O site on the Cu/CeO₂(111) surface, the coordinate number of Cu maintains four when the extra electron is localized at the Ce site. On the other hand, when the extra electron is localized at the Cu, it induces the change of the coordinate number of Cu to three (Figure S2 and Table S4). In fact, we have also estimated and compared the electrostatic interaction energies at such Ce^{3+} and Cu^{1+} sites, which are -134.05 eV and -130.40 eV, respectively (see Figure S2 and Table S4). These results clearly show that the Cu/CeO₂(111) surface can be more stable with the extra electron being localized at the Ce site than the Cu due to the more favorable electrostatic interaction. Moreover, the calculated density of states of the corresponding systems further showed that the newly occupied Cu *3d* orbital is 0.15 eV higher in energy than the occupied Ce *4f* orbital (Figure S3). These results can indeed support that the excess electron prefers to be localized in the Ce *4f*, even though the empty Cu(*3d*)-O(*2p*) state is lower (Figure 1d).

3.3. H₂ Dissociation and H[•] Formation

Recent studies have shown that ceria has the capability of catalyzing partial hydrogenation of alkynes and CO₂ reduction reactions [2,4,10,11]. The formation of hydride through heterolytic dissociation of H₂ on the CeO₂ surface was found to be one of the vital processes in these reactions [7–12,38]. Then, we systematically studied the dissociative adsorption of H₂ on both the pristine and Cu-doped CeO₂(111) surfaces.

The calculated energy profiles of H₂ adsorption and dissociation on the CeO₂(111) and Cu/CeO₂(111) surfaces are shown in Figure 3. As one can see, the adsorption energy of H₂ on the Cu/CeO₂(111) surface (0.30 eV) is 0.26 eV higher than that on the pristine CeO₂(111) surface (0.04 eV), indicating that the H₂ molecule has a stronger interaction with the Cu/CeO₂(111) surface. We further considered the homolytic and heterolytic

pathways of H₂ dissociation on the CeO₂(111) and Cu/CeO₂(111) surfaces. The homolytic dissociation produces two surface hydroxyls, while the heterolytic dissociation produces a surface hydroxyl and a hydride species [27,38]. According to our calculations, the homolytic dissociation of H₂ on the CeO₂(111) (gray dotted line) and Cu/CeO₂(111) surfaces (black dotted line) needs to overcome the energy barriers of 1.34 and 1.08 eV, respectively (see Figures 3, S4 and S5). In each transition state of the homolytic H₂ dissociation, one OH species and one hydrogen radical are formed on the surface firstly (Figures S4b and S5b), giving rise to rather high barrier for this process. The as-formed H radical will then migrate to the neighboring O site to form the second OH species. Moreover, on the CeO₂(111) and Cu/CeO₂(111) surfaces, the homolytic H₂ dissociation process was calculated to be exothermic by 2.41 and 3.25 eV, respectively.

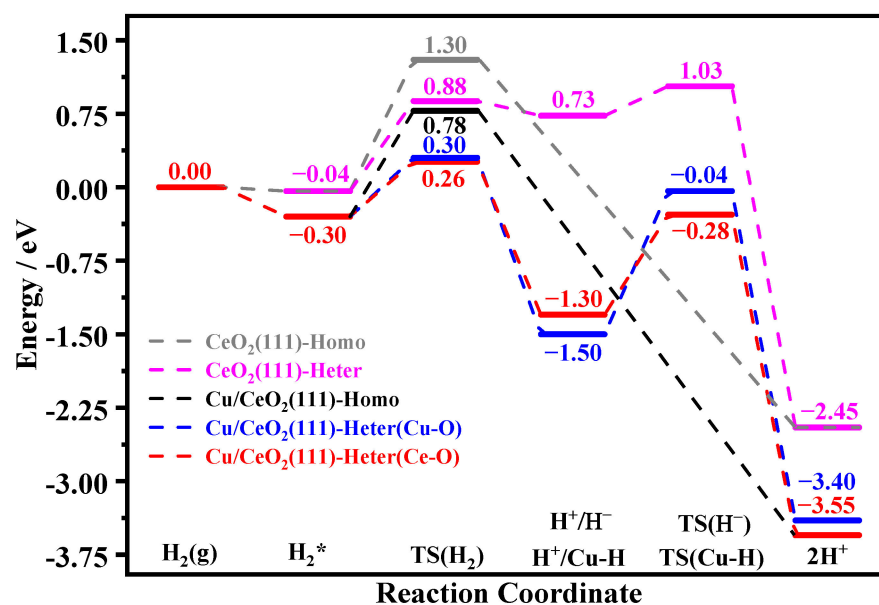


Figure 3. Calculated energy profiles of homolytic (Homo) and heterolytic (Heter) H₂ dissociation on the CeO₂(111) and Cu/CeO₂(111) surfaces. “*” is defined as the surface free site, and this notation is used throughout the paper.

Interestingly, our calculated results (Figures 3, S4 and S5) showed that the energy barrier for the heterolytic dissociation of H₂ at the Ce-O site on the Cu/CeO₂(111) (red dotted line, 0.56 eV) is lower than that on the pristine CeO₂(111) (pink dotted line, 0.92 eV) and they are both significantly lower than those of the homolytic dissociation. Following the transition state (Figures S4c and S5c), one OH and one hydride species are formed, and this process is endothermic by 0.77 eV at CeO₂(111) and exothermic by 1 eV at Cu/CeO₂(111). Notably, we found that the obvious stability of H[−] species on the Cu/CeO₂(111) surface (Figure S5d) can be attributed to the low coordination number of Ce at the oxygen vacancy. These results clearly indicate that the Cu doping promotes the formation of oxygen vacancies, which is critical for the stabilization of hydride species. We also calculated the heterolytic dissociation of H₂ at the Cu-O site on the Cu/CeO₂(111) surface to produce H⁺ and Cu-H species (blue dotted line). This process needs to overcome a barrier of 0.60 eV and is exothermic by 1.20 eV.

Furthermore, we also considered the migration of hydride species to the neighboring O site to form another hydroxyl species on the two surfaces. The calculated energy barriers of the migration process on the CeO₂(111) and Cu/CeO₂(111) surfaces are 0.30 and 1.02 eV, respectively. The high energy barrier of the migration on the Cu/CeO₂(111) surface indicates that the hydride species can be kinetically stable on this surface. In addition, we calculated the migration of the hydrogen species (Cu-H) to the neighboring O site to form

another hydroxyl species on the Cu/CeO₂(111) surface, and it needs to overcome an energy barrier of 1.46 eV and is exothermic by 1.90 eV (Figure 3).

It should be noted that the CeO₂ surface accepts two extra electrons after the hydride migration. For the Cu/CeO₂(111), we found that the two electrons prefer to be localized in the 4*f* orbitals of two Ce atoms rather than in one Ce 4*f* orbital and one Cu 3*d* orbital as the former case is 0.15 eV more stable than the latter one (Figure S5h,j). This again indicates the significant role of Ce 4*f* as the “electron reservoir” [56].

To gain deeper insights into the effect of Cu doping on the formation of hydride species on the Cu/CeO₂(111) surface, we calculated the partial density of states of the Ce³⁺ species on the two CeO₂ surfaces with one H being adsorbed at the O site. Note that this H can be regarded as the “co-adsorbate” of the other H in dissociative H₂ adsorption (Figure 4). The calculated results show that the occupied 4*f* state of the Cu/CeO₂(111) with one hydroxyl lies in the higher energy than that of the CeO₂(111) with one hydroxyl. So, one may expect that the Ce³⁺ species on the Cu/CeO₂(111) with one hydroxyl can donate this electron to the second H to form a hydride species more readily than the Ce³⁺ species on the CeO₂(111) with one hydroxyl.

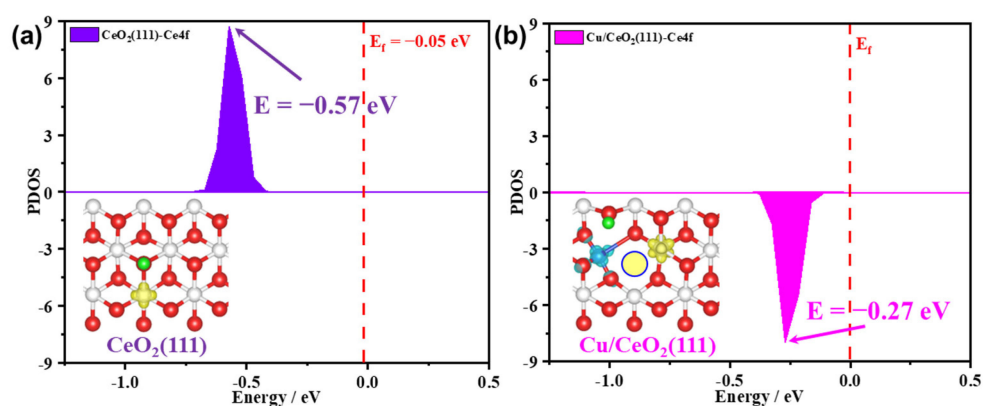


Figure 4. Calculated partial density of states (PDOS) of the Ce³⁺ on the (a) CeO₂(111) and (b) Cu/CeO₂(111) surfaces with one H being adsorbed on O. The Fermi energy level (E_f) is labeled with a red dashed line. All DOS are aligned with respect to the O 2*s* orbital of a fixed bottom O atom of the surface slabs.

Previous studies reported that surface oxygen vacancies can stabilize hydride species [33,37,38]. We then calculated the formation of an extra surface oxygen vacancy on the CeO₂(111) and Cu/CeO₂(111) (Figure 5). It was found that the Cu/CeO₂(111) gives a much smaller surface oxygen vacancy formation energy (0.59 eV) than the CeO₂(111) surface (2.41 eV), suggesting that the Cu dopant can further promote the formation of the surface oxygen vacancy. The newly formed surface oxygen vacancy can reduce two Ce⁴⁺ into Ce³⁺ cations. This is mainly due to the fact that the calculated crystal reduction potential (V_r) [57] for Cu²⁺ → Cu⁺ (−1.43 V) is higher than that for Ce⁴⁺ → Ce³⁺ (−1.77 V), and the coordination number of Ce around the new O_v site is also reduced (Figure 5b). We also found that it is more favorable to form hydride species on such reduced Cu/CeO₂(111) surface (i.e., Cu/CeO₂(111)-O_v) than the Cu/CeO₂(111) surface (Figure 5c,d). We calculated the dissociation of H₂ on the Cu/CeO₂(111)-O_v surface (Figures 5e and S6) and found that the heterolytic dissociation of H₂ at the Ce-O site to produce hydride species is kinetically the most favorable one. The energy barrier of this process is 0.47 eV, which is even lower than the corresponding energy barrier on the Cu/CeO₂ surface (0.56 eV). This result further indicates the great ability of the Cu/CeO₂(111) in generating surface hydride species.

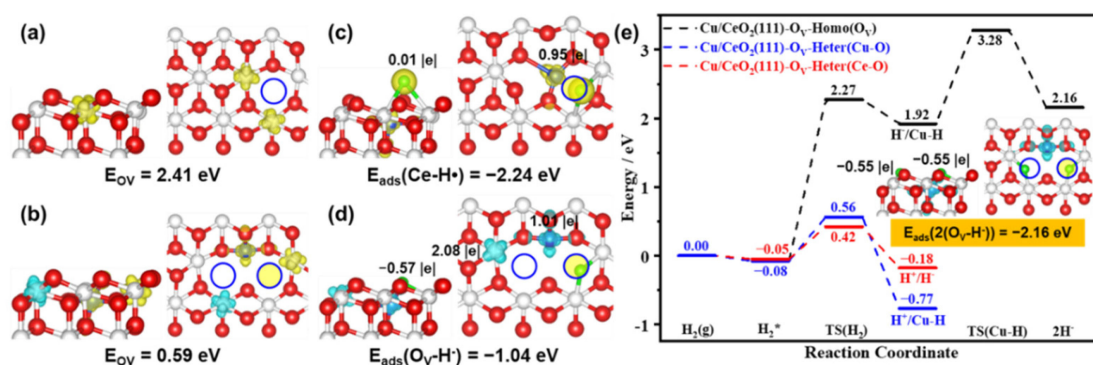


Figure 5. Calculated structures (left: side view; right: top view) of the (a) reduced $\text{CeO}_2(111)$ with one surface oxygen vacancy and (b) reduced $\text{Cu}/\text{CeO}_2(111)$ with one inherent surface oxygen vacancy and an extra surface oxygen vacancy. Calculated structures (left: side view; right: top view) of a single H at the oxygen vacancy sites of the (c) $\text{Cu}/\text{CeO}_2(111)$ and (d) reduced $\text{Cu}/\text{CeO}_2(111)\text{-O}_V$ surfaces. (e) Calculated energy profiles of homolytic (Homo) and heterolytic (Heter) H_2 dissociation on the $\text{Cu}/\text{CeO}_2(111)\text{-O}_V$ surface. The unfilled blue circle represents the surface oxygen vacancy, and the blue circle filled with yellow represents the inherent surface oxygen vacancy on the $\text{Cu}/\text{CeO}_2(111)$. The spin density distributions are illustrated in yellow and blue, and the surface oxygen vacancy formation energies are also given.

3.4. Selective Hydrogenation of CO_2

To unveil the catalytic activities of the various surfaces, we then continued to study the main reaction steps of the CO_2RR at $\text{CeO}_2(111)$ and $\text{Cu}/\text{CeO}_2(111)$ (Figures 6, S7 and S8). It is generally accepted that the adsorption and activation of CO_2 and the generation of hydride species are the key steps of the whole CO_2RR [10,11,38]. As shown in Figure 6, the adsorption of CO_2 on the $\text{Cu}/\text{CeO}_2(111)$ surface is exothermic by 1.06 eV. In comparison, the adsorption of CO_2 on the $\text{CeO}_2(111)$ surface is much weaker, with an exothermic adsorption energy of 0.32 eV only. Therefore, the Cu dopant can indeed promote CO_2 adsorption. This is mainly attributed to the relatively high energy level of the occupied Cu $3d$ orbital which can donate its electron to the CO_2 molecule (Figure 1d). This is also consistent with some previous experimental observation [13]. Then we calculated the adsorption of H_2 and found that the adsorption of H_2 is weak on both the $\text{CeO}_2(111)$ and $\text{Cu}/\text{CeO}_2(111)$ surfaces with pre-adsorbed CO_2 , and the corresponding adsorption energies are 0.01 and 0.12 eV, respectively, which are largely close to those on the clean surfaces (Figure 3). Nevertheless, since the adsorption of CO_2 is stronger than that of H_2 on both the $\text{CeO}_2(111)$ and $\text{Cu}/\text{CeO}_2(111)$ surfaces, it is reasonable to consider the dissociative adsorption of H_2 on the CO_2 pre-covered surfaces.

Since our calculated results presented above already showed that the hydride species are kinetically and thermodynamically unstable at $\text{CeO}_2(111)$, we only considered the formation of two hydroxyl species on the CO_2 pre-adsorbed $\text{CeO}_2(111)$ through H_2 dissociation. This process needs to overcome a barrier of 0.83 eV and is exothermic by 2.67 eV (Figure 6). We found that the produced proton species has rather low activities in the hydrogenation of CO_2 to HCOO^* or COOH^* , with the calculated barriers being higher than 3 eV. Moreover, the COOH pathway is both thermodynamically and kinetically more favorable than the HCOO pathway on this surface.

By contrast, on the $\text{Cu}/\text{CeO}_2(111)$ surface, hydride species can be stable, and H_2 can readily dissociate into one hydride and one OH^- species. This process needs to overcome a barrier of 0.79 eV and is exothermic by 0.55 eV. We found that the produced hydride species is quite active for CO_2 hydrogenation. In the HCOO pathway, the calculated barrier and reaction energy are 1.20 and 0.18 eV, respectively, while in the COOH pathway, the corresponding values are 1.34 and -1.59 eV, respectively. Although the generated COOH^* species is more stable than the HCOO^* species, the HCOO pathway is kinetically more favorable than the COOH pathway. We also studied the reaction of CO_2 hydrogenation by

H⁺ to form COOH* on the Cu/CeO₂(111) surface, and the calculated barrier is extremely high (4.47 eV). These results indicate that the as-formed hydride species is crucial to the activity and selectivity of the Cu/CeO₂(111) in the CO₂ reduction reaction.

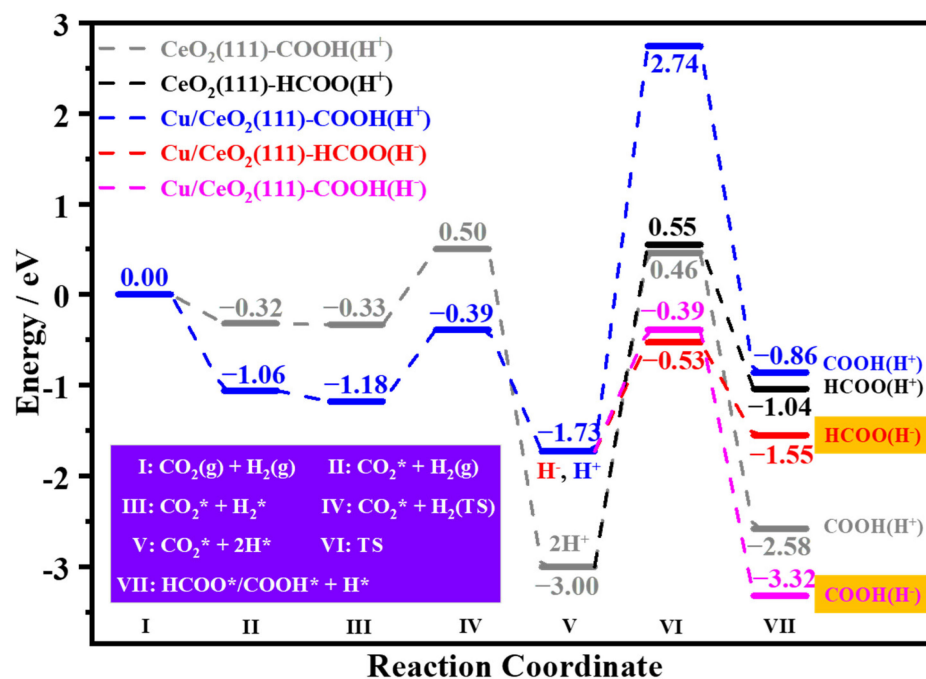


Figure 6. Calculated energy profiles of the first few key steps of the CO₂ hydrogenation reaction on the CeO₂(111) and Cu/CeO₂(111) surfaces.

4. Conclusions

In conclusion, we systematically studied the hydride formation and its reaction with CO₂ on the pristine and Cu-doped CeO₂(111) surfaces. The calculated results showed that the hydride species are thermodynamically and kinetically unstable on the pristine CeO₂(111) surface, and the adsorption of CO₂ on this surface is rather weak. In contrast, kinetically stable hydride species can be effectively produced by heterolytic H₂ dissociation on the Cu/CeO₂(111) surface with inherent oxygen vacancies. We also found that the Cu dopant promotes the formation of oxygen vacancies, which is favorable for the generation of hydride species. Moreover, the Cu dopant also promotes the adsorption of CO₂, and the hydrogenation of CO₂ to HCOO* can be significantly facilitated by the hydride species on the Cu/CeO₂(111) surface, showing that the doping of Cu significantly improves the activity and selectivity of the CeO₂(111) toward the hydrogenation of CO₂ to methanol. Our findings may guide the rational design of efficient ceria and Cu based catalysts for CO₂ reduction reactions.

Supplementary Materials: The following are available online at <https://www.mdpi.com/article/10.3390/catal12090963/s1>, Tables S1 and S2: Calculated lattice constants of bulk ceria by using different plane wave kinetic energy cutoff and different *k*-point mesh densities. Table S3: Calculated Bader charges of the Cu²⁺ of CuO and the Cu¹⁺ of Cu₂O. Table S4: Calculated Bader charges of the Cu and Ce species and their nearby O; calculated Cu-O and Ce-O bond distances, and the electrostatic interaction energies (E_{Cu+Ce}) between the Cu and Ce and their nearby species on the Cu/CeO₂(111) and the Cu/CeO₂(111) surface with H being adsorbed at the O site; calculated Cu coordinate numbers on the Cu/CeO₂(111) and the Cu/CeO₂(111) surface with H being adsorbed at the O site. Figure S1: Calculated density of states (DOS) of the Cu/CeO₂(111) surface with H being adsorbed at the Cu site. Figure S2: Calculated structures of Cu/CeO₂(111) and Cu/CeO₂(111) with adsorbed H which gives to the localized electron at different site. Figure S3: Calculated density of states (DOS) of the Cu/CeO₂(111) surface with H being adsorbed at the O site. Figure S4: Calculated structures

of H₂ adsorption and dissociation on the CeO₂(111) surface. Figure S5: Calculated structures of H₂ adsorption and dissociation on the Cu/CeO₂(111) surface. Figure S6: Calculated structures of H₂ adsorption and dissociation on the Cu/CeO₂(111)-O_V surface. Crystal Reduction Potential (Vr). Figure S7: Calculated structures of CO₂ hydrogenation on the CeO₂(111) surface. Figure S8: Calculated structures of CO₂ hydrogenation on the Cu/CeO₂(111) surface. References [27,38,57] are cited in the Supplementary Materials.

Author Contributions: Conceptualization, X.-P.W. and X.-Q.G.; methodology, H.-H.L. and Z.-Q.W.; software, H.-H.L. and Z.-Q.W.; validation, Z.-Q.W.; formal analysis, Z.-Q.W., X.-P.W. and X.-Q.G.; investigation, Z.-Q.W.; resources, X.-Q.G.; data curation, H.-H.L. and Z.-Q.W.; writing—original draft preparation, Z.-Q.W.; writing—review and editing, X.-P.W. and X.-Q.G.; visualization, Z.-Q.W.; supervision, X.-P.W., P.H. and X.-Q.G.; project administration, X.-Q.G.; funding acquisition, X.-P.W., P.H. and X.-Q.G. All authors have read and agreed to the published version of the manuscript.

Funding: This research was funded by National Key R&D Program of China (2018YFA0208602) and National Nature Science Foundation of China (21825301, 22003016, 92045303, 92145302) and Shanghai Sailing Program (21YF1409400) and China Postdoctoral Science Foundation (2020M671020).

Data Availability Statement: Not applicable.

Conflicts of Interest: The authors declare no conflict of interest.

References

- Gianvito, V.; Patrick, D.; Julia, V.; Miguel, B.; Sebastián, C.; Mónica, C.; Adrian, B.; Javier, P.-R. Promoted Ceria Catalysts for Alkyne Semi-hydrogenation. *J. Catal.* **2015**, *324*, 69–78.
- Esrafilzadeh, D.; Zavabeti, A.; Jalili, R.; Atkin, P.; Choi, J.; Carey, B.J.; Brkljača, R.; O'Mullane, A.P.; Dickey, M.D.; Officer, D.L.; et al. Room Temperature CO₂ Reduction to Solid Carbon Species on Liquid Metals Featuring Atomically Thin Ceria Interfaces. *Nat. Commun.* **2019**, *10*, 865. [CrossRef]
- Rodríguez, J.A.; Grinter, D.C.; Liu, Z.; Palomino, R.M.; Senanayake, S.D. Ceria-based Model Catalysts: Fundamental Studies on the Importance of the Metal—Ceria Interface in CO Oxidation, the Water—Gas Shift, CO₂ Hydrogenation, and Methane and Alcohol Reforming. *Chem. Soc. Rev.* **2017**, *46*, 1824–1841. [CrossRef] [PubMed]
- Vilé, G.; Bridier, B.; Wichert, J.; Pérez-Ramírez, J. Ceria in Hydrogenation Catalysis: High Selectivity in the Conversion of Alkynes to Olefins. *Angew. Chem. Int. Ed.* **2012**, *51*, 8620–8623. [CrossRef] [PubMed]
- Riley, C.; Zhou, S.; Kunwar, D.; Riva, A.D.L.; Peterson, E.; Payne, R.; Gao, L.; Lin, S.; Guo, H.; Datye, A. Design of Effective Catalysts for Selective Alkyne Hydrogenation by Doping of Ceria with a Single-atom Promotor. *J. Am. Chem. Soc.* **2018**, *140*, 12964–12973. [CrossRef]
- James, K.; Jisue, M.; Wu, Z.L. A Review of the Interactions between Ceria and H₂ and the Applications to Selective Hydrogenation of Alkynes. *Chin. J. Catal.* **2020**, *41*, 901–914.
- Wang, F.; Wei, M.; Evans, D.G.; Duan, X. CeO₂-based Heterogeneous Catalysts toward Catalytic Conversion of CO₂. *J. Mater. Chem. A* **2016**, *4*, 5773–5783. [CrossRef]
- Chang, K.; Zhang, H.C.; Cheng, M.-J.; Lu, Q. Application of Ceria in CO₂ Conversion Catalysis. *ACS Catal.* **2020**, *10*, 613–631. [CrossRef]
- Jiang, F.; Wang, S.S.; Liu, B.; Liu, J.; Wang, L.; Xiao, Y.; Xu, Y.B.; Liu, X.H. Insights into the Influence of CeO₂ Crystal Facet on CO₂ Hydrogenation to Methanol over Pd/CeO₂ Catalysts. *ACS Catal.* **2020**, *10*, 11493–11509. [CrossRef]
- Cheng, Z.; Lo, C.S. Mechanistic and Microkinetic Analysis of CO₂ Hydrogenation on Ceria. *Phys. Chem. Chem. Phys.* **2016**, *18*, 7987–7996. [CrossRef] [PubMed]
- Kumari, N.; Haider, M.A.; Agarwal, M.; Sinha, N.; Basu, S. Role of Reduced CeO₂ Surface for CO₂ Reduction to CO and Methanol. *J. Phys. Chem. C* **2016**, *120*, 16626–16635. [CrossRef]
- Zhang, W.; Ma, X.-L.; Xiao, H.; Lei, M.; Li, J. Mechanistic Investigations on Thermal Hydrogenation of CO₂ to Methanol by Nanostructured CeO₂: The Crystal-Plane Effect on Catalytic Reactivity. *J. Phys. Chem. C* **2019**, *123*, 11763–11771. [CrossRef]
- Zhao, Y.-F.; Yang, Y.; Mims, C.; Peden, C.H.F.; Li, J.; Mei, D.H. Insight into Methanol Synthesis from CO₂ Hydrogenation on Cu(111): Complex Reaction Network and the Effects of H₂O. *J. Catal.* **2011**, *281*, 199–211. [CrossRef]
- Kuld, S.; Thorhauge, M.; Falsig, H.; Elkjær, C.F.; Helveg, S.; Chorkendorff, I.; Sehested, J. Quantifying the Promotion of Cu Catalysts by ZnO for Methanol Synthesis. *Science* **2016**, *352*, 969–974. [CrossRef] [PubMed]
- Kattel, S.; Ramirez, P.J.; Chen, J.G.; Rodriguez, J.A.; Liu, P. Active Sites for CO₂ Hydrogenation to Methanol on Cu/ZnO Catalysts. *Science* **2017**, *355*, 1296–1299. [CrossRef]
- Liu, S.P.; Zhao, M.; Gao, W.; Jiang, Q.; Jacob, T. Theoretical Studies on the CO₂ Reduction to CH₃OH on Cu(211). *Electrocatalysis* **2017**, *8*, 647–656. [CrossRef]
- Xu, D.; Ding, M.Y.; Hong, X.L.; Liu, G.L. Mechanistic Aspects of the Role of K Promotion on Cu–Fe-based Catalysts for Higher Alcohol Synthesis from CO₂ Hydrogenation. *ACS Catal.* **2020**, *10*, 14516–14526. [CrossRef]

18. Xu, D.; Wang, Y.Q.; Ding, M.Y.; Hong, X.L.; Liu, G.L.; Tsang, S.C.E. Advances in Higher Alcohol Synthesis from CO₂ Hydrogenation. *Chem* **2020**, *7*, 849–881. [CrossRef]
19. Liu, H.X.; Li, S.Q.; Wang, W.W.; Yu, W.-Z.; Zhang, W.-J.; Ma, C.; Jia, C.-J. Partially Sintered Copper–Ceria as Excellent Catalyst for the High-Temperature Reverse Water Gas Shift Reaction. *Nat. Commun.* **2022**, *13*, 867. [CrossRef] [PubMed]
20. Wang, B.B.; Zhang, L.J.; Cai, J.; Peng, Z.; Cheng, P.H.; Li, X.B.; Zhang, H.; Yang, F.; Liu, Z. Formation and Activity Enhancement of Surface Hydrides by the Metal–Oxide Interface. *Adv. Mater. Interfaces* **2021**, *8*, 2002169. [CrossRef]
21. Wang, S.; Zheng, M.H.; Li, M.; Wu, X.J.; Xia, C.R. Synergistic Effects towards H₂ Oxidation on the Cu–CeO₂ Electrode: A Combination Study with DFT Calculations and Experiments. *J. Mater. Chem. A* **2016**, *4*, 5745–5754. [CrossRef]
22. Wan, Q.; Wei, F.F.; Wang, Y.Q.; Wang, F.T.; Zhou, L.S.; Lin, S.; Xie, D.Q.; Guo, H. Single Atom Detachment from Cu Clusters, and Diffusion and Trapping on CeO₂: Implications in Ostwald Ripening and Atomic Redispersion. *Nanoscale* **2018**, *10*, 17893–17901. [CrossRef] [PubMed]
23. Wang, Y.F.; Chen, Z.; Han, P.; Du, Y.H.; Gu, Z.X.; Xu, X.; Zheng, Z.F. Single-Atomic Cu with Multiple Oxygen Vacancies on Ceria for Electrocatalytic CO₂ Reduction to CH₄. *ACS Catal.* **2018**, *8*, 7113–7119. [CrossRef]
24. Yang, T.; Mao, X.N.; Zhang, Y.; Wu, X.P.; Wang, L.; Chu, M.Y.; Pao, C.-W.; Yang, S.Z.; Xu, Y.; Huang, X.Q. Coordination Tailoring of Cu Single Sites on C₃N₄ Realizes Selective CO₂ Hydrogenation at Low Temperature. *Nat. Commun.* **2021**, *12*, 6022. [CrossRef] [PubMed]
25. Schweke, D.; Shelly, L.; David, R.B.; Danon, A.; Kostirya, N.; Hayun, S. Comprehensive Study of the Ceria H₂ System: Effect of the Reaction Conditions on the Reduction Extent and Intermediates. *J. Phys. Chem. C* **2020**, *124*, 6180–6187. [CrossRef]
26. Fernandez-Torre, D.; Carrasco, J.; Ganduglia-Pirovano, M.V.; Perez, R. Hydrogen Activation, Diffusion, and Clustering on CeO₂: A DFT + U Study. *J. Chem. Phys.* **2014**, *141*, 014703. [CrossRef] [PubMed]
27. García-Melchor, M.; López, N. Homolytic Products from Heterolytic Paths in H₂ Dissociation on Metal Oxides: The Example of CeO₂. *J. Phys. Chem. C* **2014**, *118*, 10921–10926. [CrossRef]
28. Duchoň, T.; Hackl, J.; Mueller, D.N.; Kullgren, J.; Du, D.; Senanayake, S.D.; Mous, C.; Gottlob, D.; Khan, M.M.I.; Cramm, S.; et al. Establishing Structure-sensitivity of Ceria Reducibility: Real-time Observations of Surface-hydrogen Interactions. *J. Mater. Chem. A* **2020**, *8*, 5501–5507. [CrossRef]
29. Vilé, G.; Colussi, S.; Krumeich, F.; Trovarelli, A.; Pérez-Ramírez, J. Opposite Face Sensitivity of CeO₂ in Hydrogenation and Oxidation Catalysis. *Angew. Chem. Int. Ed.* **2014**, *53*, 12069–12072. [CrossRef] [PubMed]
30. Wu, X.-P.; Gong, X.-Q.; Lu, G. Role of Oxygen Vacancies in the Surface Evolution of H at CeO₂: A Charge Modification Effect. *Phys. Chem. Chem. Phys.* **2015**, *17*, 3544–3549. [CrossRef]
31. Li, Z.; Werner, K.; Qian, K.; You, R.; Plucienik, A.; Jia, A.; Wu, L.; Zhang, L.; Pan, H.; Kühlenbeck, H.; et al. Oxidation of Reduced Ceria by Incorporation of Hydrogen. *Angew. Chem. Int. Ed.* **2019**, *131*, 14828–14835. [CrossRef]
32. Wu, Z.; Cheng, Y.; Tao, F.; Daemen, L.; Foo, G.S.; Nguyen, L.; Zhang, X.; Beste, A.; Ramirez-Cuesta, A.J. Direct Neutron Spectroscopy Observation of Cerium Hydride Species on a Cerium Oxide Catalyst. *J. Am. Chem. Soc.* **2017**, *139*, 9721–9727. [CrossRef] [PubMed]
33. Werner, K.; Weng, X.; Calaza, F.; Sterrer, M.; Kropp, T.; Paier, J.; Sauer, J.; Wilde, M.; Fukutani, K.; Shaikhtudinov, S.; et al. Toward an Understanding of Selective Alkyne Hydrogenation on Ceria: On the Impact of O Vacancies on H₂ Interaction with CeO₂. *J. Am. Chem. Soc.* **2017**, *139*, 17608–17616. [CrossRef] [PubMed]
34. Coperet, C.; Estes, D.P.; Larmier, K.; Searles, K. Isolated Surface Hydrides: Formation, Structure, and Reactivity. *Chem. Rev.* **2016**, *116*, 8463–8505. [CrossRef]
35. Moon, J.; Cheng, Y.; Daemen, L.L.; Li, M.; Polo-Garzon, F.; Ramirez-Cuesta, A.J.; Wu, Z. Discriminating the Role of Surface Hydride and Hydroxyl for Acetylene Semi-Hydrogenation over Ceria through in Situ Neutron and Infrared Spectroscopy. *ACS Catal.* **2020**, *10*, 5278–5287. [CrossRef]
36. Wang, Q.R.; Guo, J.P.; Chen, P. The Power of Hydrides. *Joule* **2020**, *4*, 705–709. [CrossRef]
37. Li, Z.R.; Kristin, W.; Chen, L.; Jia, A.P.; Qian, K.; Zhong, J.Q.; You, R.; Wu, L.H.; Zhang, L.Y.; Pan, H.B.; et al. Interaction of Hydrogen with Ceria: Hydroxylation, Reduction, and Hydride Formation on the Surface and in the Bulk. *Chem. Eur. J.* **2021**, *27*, 5268–5276. [CrossRef]
38. Wang, Z.-Q.; Chu, D.-R.; Zhou, H.; Wu, X.-P.; Gong, X.-Q. Role of Low-Coordinated Ce in Hydride Formation and Selective Hydrogenation Reactions on CeO₂ Surfaces. *ACS Catal.* **2022**, *12*, 624–632. [CrossRef]
39. Kresse, G.; Furthmüller, J. Efficient Iterative Schemes for Ab Initio Total-Energy Calculations Using a Plane-Wave Basis Set. *Phys. Rev. B* **1996**, *54*, 11169–11186. [CrossRef]
40. Blöchl, P.E. Projector Augmented-wave Method. *Phys. Rev. B* **1994**, *50*, 17953–17979. [CrossRef]
41. Perdew, J.P.; Burke, J.; Ernzerhof, M. Generalized Gradient Approximation Made Simple. *Phys. Rev. Lett.* **1996**, *77*, 3865–3868. [CrossRef] [PubMed]
42. Teter, M.P.; Payne, M.C.; Allan, D.C. Solution of Schrodinger’s Equation for Large Systems. *Phys. Rev. B* **1989**, *40*, 12255–12263. [CrossRef] [PubMed]
43. Kümmerle, E.; Heger, G. The Structures of C–Ce₂O_{3+δ}, Ce₇O₁₂, and Ce₁₁O₂₀. *J. Solid State Chem.* **1999**, *147*, 485–500. [CrossRef]
44. Jerratsch, J.-F.; Shao, X.; Nilius, N.; Freund, H.-J.; Popa, C.; Ganduglia-Pirovano, M.V.; Burow, A.M.; Sauer, J. Electron Localization in Defective Ceria Films: A Study with Scanning-Tunneling Microscopy and Density-Functional Theory. *Phys. Rev. Lett.* **2011**, *106*, 246801. [CrossRef] [PubMed]

45. Nolan, M.; Parker, S.C.; Watson, G.W. The Electronic Structure of Oxygen Vacancy Defects at the Low Index Surfaces of Ceria. *Surf. Sci.* **2005**, *595*, 223–232. [CrossRef]
46. Nolan, M.; Grigoleit, S.; Sayle, D.C.; Parker, S.C.; Watson, G.W. Density Functional Theory Studies of the Structure and Electronic Structure of Pure and Defective Low Index Surfaces of Ceria. *Surf. Sci.* **2005**, *576*, 217–229. [CrossRef]
47. Vicario, G.; Balducci, G.; Fabris, S.; Gironcoli, S.D.; Baroni, S. Interaction of Hydrogen with Cerium Oxide Surfaces: A Quantum Mechanical Computational Study. *J. Phys. Chem. B* **2006**, *110*, 19380–19385. [CrossRef]
48. Michaelides, A.; Liu, Z.P.; Zhang, C.J.; Alavi, A.; King, D.A.; Hu, P. Identification of General Linear Relationships between Activation Energies and Enthalpy Changes for Dissociation Reactions at Surfaces. *J. Am. Chem. Soc.* **2003**, *125*, 3704–3705. [CrossRef]
49. Alavi, A.; Hu, P.; Deutsch, T.; Silvestrelli, P.L.; Hutter, J. CO Oxidation on Pt(111): An Ab Initio Density Functional Theory Study. *Phys. Rev. Lett.* **1998**, *80*, 3650–3653. [CrossRef]
50. Liu, Z.P.; Hu, P. General Rules for Predicting Where a Catalytic Reaction Should Occur on Metal Surfaces: A Density Functional Theory Study of C–H and C–O Bond Breaking/making on Flat, Stepped, and Kinked Metal Surfaces. *J. Am. Chem. Soc.* **2003**, *125*, 1958–1967. [CrossRef]
51. Somorjai, G.A.; Li, Y.M. *Introduction to Surface Chemistry and Catalysis*; Wiley-VCH: Berkeley, CA, USA, 2010.
52. Yang, Z.X.; He, B.L.; Lu, Z.S.; Hermansson, K. Physisorbed, Chemisorbed, and Oxidized CO on Highly Active Cu–CeO₂. *J. Phys. Chem. C* **2010**, *114*, 4486–4494. [CrossRef]
53. Zhou, S.L.; Wan, Q.; Lin, S. Cu/O Frustrated Lewis Pairs on Cu Doped CeO₂ for Acetylene Hydrogenation: A First-Principles Study. *Catalysts* **2022**, *12*, 74. [CrossRef]
54. Guo, C.; Wei, S.; Zhou, S.; Zhang, T.; Wang, Z.; Ng, S.-P.; Lu, X.; Wu, C.-M.L.; Guo, W. Initial Reduction of CO₂ on Pd-, Ru-, and Cu-Doped CeO₂ Surfaces: Effects of Surface Modification on Catalytic Activity and Selectivity. *ACS Appl. Mater. Interfaces* **2017**, *9*, 26107–26117. [CrossRef] [PubMed]
55. Wang, X.Q.; Rodriguez, J.A.; Hanson, J.C.; Gamarra, D.; Martínez-Arias, A.; Fernández-García, A. Unusual Physical and Chemical Properties of Cu in Ce_{1-x}Cu_xO₂ Oxides. *J. Phys. Chem. B* **2005**, *109*, 19595–19603. [CrossRef]
56. Wang, Z.-Q.; Wang, D.; Gong, X.-Q. Strategies to Improve the Activity while Maintaining the Selectivity of Oxidative Coupling of Methane at La₂O₃: A Density Functional Theory Study. *ACS Catal.* **2020**, *10*, 586–594. [CrossRef]
57. Wexler, R.B.; Gautam, G.S.; Stechel, E.B.; Carter, E.A. Factors Governing Oxygen Vacancy Formation in Oxide Perovskites. *J. Am. Chem. Soc.* **2021**, *143*, 13212–13227. [CrossRef]

Article

Synthesis of Self-Supported Cu/Cu₃P Nanoarrays as an Efficient Electrocatalyst for the Hydrogen Evolution Reaction

Rui Dang ^{1,*} , Xiufeng Xu ², Mengmeng Xie ² and Jian Liu ^{2,*}¹ Northwest Institute for Nonferrous Metal Research, 96 Weiyang Road, Weiyang District, Xi'an 710016, China² Faculty of Printing, Packaging Engineering and Digital Media Technology, Xi'an University of Technology, Xi'an 710054, China; xfengalone@163.com (X.X.); xiemeng1216@163.com (M.X.)

* Correspondence: dr0501@163.com (R.D.); liujian@xaut.edu.cn (J.L.)

Abstract: Owing to the energy crisis and environmental pollution, it is essential to develop cheap, environmentally friendly and sustainable energy to replace noble metal electrocatalysts for use in the hydrogen evolution reaction (HER). We report herein that a Cu/Cu₃P nanoarray catalyst was directly grown on the surfaces of Cu nanosheets from its Cu/CuO nanoarray precursor by a low-temperature phosphidation process. In particular, the effects of phosphating distance, mass ratio and temperature on the morphology of Cu/Cu₃P nanoarrays were studied in detail. This nanoarray, as an electrocatalyst, displays excellent catalytic performance and long-term stability in an acid solution for electrochemical hydrogen generation. Specifically, the Cu/Cu₃P nanoarray-270 exhibits a low onset overpotential (96 mV) and a small Tafel slope (131 mV dec⁻¹).

Keywords: Cu/Cu₃P nanoarrays; Cu nano-substrates; electrocatalyst; HER



Citation: Dang, R.; Xu, X.; Xie, M.; Liu, J. Synthesis of Self-Supported Cu/Cu₃P Nanoarrays as an Efficient Electrocatalyst for the Hydrogen Evolution Reaction. *Catalysts* **2022**, *12*, 762. <https://doi.org/10.3390/catal12070762>

Academic Editors: Yongjun Ji, Liwen Xing and Ke Wu

Received: 27 May 2022

Accepted: 7 July 2022

Published: 9 July 2022

Publisher's Note: MDPI stays neutral with regard to jurisdictional claims in published maps and institutional affiliations.



Copyright: © 2022 by the authors. Licensee MDPI, Basel, Switzerland. This article is an open access article distributed under the terms and conditions of the Creative Commons Attribution (CC BY) license (<https://creativecommons.org/licenses/by/4.0/>).

1. Introduction

Due to the excessive consumption of fossil fuels, the resulting environmental pollution and global energy crisis have aroused widespread concern. It is essential to develop clean, environmental friendly and renewable energy sources to reduce our dependence on fossil fuels and benefit the environment by reducing greenhouse gas emissions [1–7]. Among variable alternatives, hydrogen has been considered as an ideal energy carrier due to its environmental friendliness and high energy density. Electrochemical water splitting is one of the most simple and promising strategies to create high-purity hydrogen in an economic way [8–14]. However, the production efficiency is low without the use of electrocatalysts, which can significantly reduce the large overpotential for the hydrogen evolution reaction (HER). It is well known that Pt, Ru-based and Ir-based catalysts are regarded as the most promising electrocatalysts for the HER and OER, because of their high electrocatalytic performance [15–23], whereas their widespread application is restricted by their high costs and low abundance on Earth. Therefore, the major challenge in hydrogen production is to reduce the use of noble metals or replace them with inexpensive non-precious metal catalysts.

In recent years, a lot of effort in the field of highly active, Earth-abundant catalysts has been dedicated to various types of alternative materials, such as transition metal sulfides [24–26], metal carbides [27–29], metal nitrides [30–32], metal phosphides [33–36] and even metal-free materials [37,38]. Transition-metal phosphides (TMPs) are an important class of compounds with metalloid characteristics and good electrical conductivity. In the structure of metal phosphides, negatively charged P atoms can act as ideal active centers for proton adsorption, bringing about the dynamical optimization of the HER [39–41]. To date, various metal phosphides have been adopted for electrochemical hydrogen evolution, such as cobalt phosphide nanoparticles (CoP NPs [42]), nickel phosphide nanoparticles (Ni₂P NPs [43]), molybdenum phosphide nanoparticles (MoP NPs [44]) and Ni-Fe phosphide nanohybrids [45], which have attracted attention for their excellent electrocatalytic activities

for the HER. However, the relatively low electrical conductivity of most phosphide catalysts remains a problem, leading to limited charge transfer and passivated electrocatalytic activity. Furthermore, these electrocatalysts are prone to agglomeration under high current density or long-term tests in practical application in the HER.

To overcome the above-mentioned issues, alternative architectural arrays grown on conductive substrates have been explored due to the large surface area, abundant active sites, and synergistic effects between the electrocatalysts and the conductive substrates. Recently, Sun and co-workers [46] reported on porous urchin-like Ni_2P microsphere superstructures anchored on nickel foam, which afforded a current density of 10 mA cm^{-2} at a low overpotential of only -98 mV for the HER. Tan and co-workers [47] reported on flower-like structures consisting of NiCoP-CoP nanowires grown directly on porous nickel frameworks to achieve a highly efficient HER in an alkaline solution. For the HER, a binder-free NiCoP-CoP/Ni/NF electrode can reach 10 mA cm^{-2} current density at a quite low overpotential of 49 mV . Despite extensive progress in nanoarray architectures, self-supporting nanoarray structures on conductive materials are still a key challenge.

Over the past decade, Fe, Co and Ni as electrocatalysts have exhibited excellent catalytic performance for the HER. Nevertheless, as an Earth-abundant transition metal, Cu-based catalysts have been relatively less studied in terms of the HER. Therefore, it is significant to design Cu-based materials with special structures for developing high-efficiency electrocatalysts. Recent studies have shown that Cu_3P is an excellent electrocatalyst for use in the HER [48,49]. Herein, self-supported Cu/ Cu_3P nanoarrays were successfully grown on the surfaces of Cu nanosheets from Cu/ CuO nanoarrays precursor by a low-temperature phosphidation process. The Cu/ Cu_3P nanoarray-270, as an electrocatalyst, displays excellent catalytic performance and durability for electrochemical hydrogen generation, and exhibits a low onset overpotential (96 mV) and a small Tafel slope (131 mV dec^{-1}). The morphology and nanostructure of the self-supported Cu/ Cu_3P nanoarray catalyst affect the electrocatalytic efficiency significantly. The nanoarrays possess large surface areas and a great number of active sites, which is immensely beneficial for electrocatalysis capacity enhancement. At the same time, copper-based catalysts can also be used in other types of organic reactions [50]. It is expected that this innovative approach will become a new concept to synthesize highly efficient catalysts.

2. Results

The typical procedure for the synthesis of Cu/ Cu_3P nanoarrays is summarized in Figure 1. In brief, Cu nanosheets are firstly synthesized according to hydrothermal method. Then, Cu nanosheets, as both a self-template and nano-conductive substrate, are immersed in a solution of $\text{NaOH}/\text{H}_2\text{O}_2$ for the formation of Cu/ CuO nanoarrays. Cu/ CuO nanoarrays and NaH_2PO_2 are calcinated under an Ar gas flow; the original black color of the Cu/ CuO turns gray after the phosphorization process, thus suggesting that the copper oxides on the surfaces of Cu nanosheets are converted into cuprous phosphide.

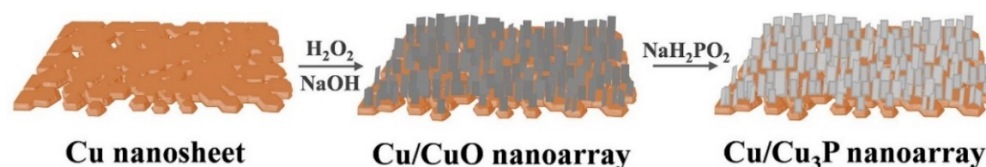


Figure 1. Illustration of the preparation of Cu/ Cu_3P nanoarrays.

The X-ray diffraction (XRD) patterns of the Cu/ CuO nanoarrays before and after phosphidation are shown in Supplementary Figures S1c and 2a. The precursor shows diffraction peaks characteristic of CuO (JCPDS No. 04-1548). In contrast, only peaks corresponding to Cu_3P can be observed for the resulting copper phosphide. Figure 2a shows that all diffraction peaks are in accordance with the hexagonal structure of Cu_3P (JCPDS No. 02-1623), and the strong peaks at 43.4° , 50.4° and 74.1° originate from the Cu nanosheets (JCPDS No. 04-0836), indicating that all copper oxides are completely trans-

formed into cuprous phosphides in the phosphating process, while the copper nanosheets, as a conductive template, have not been completely consumed.

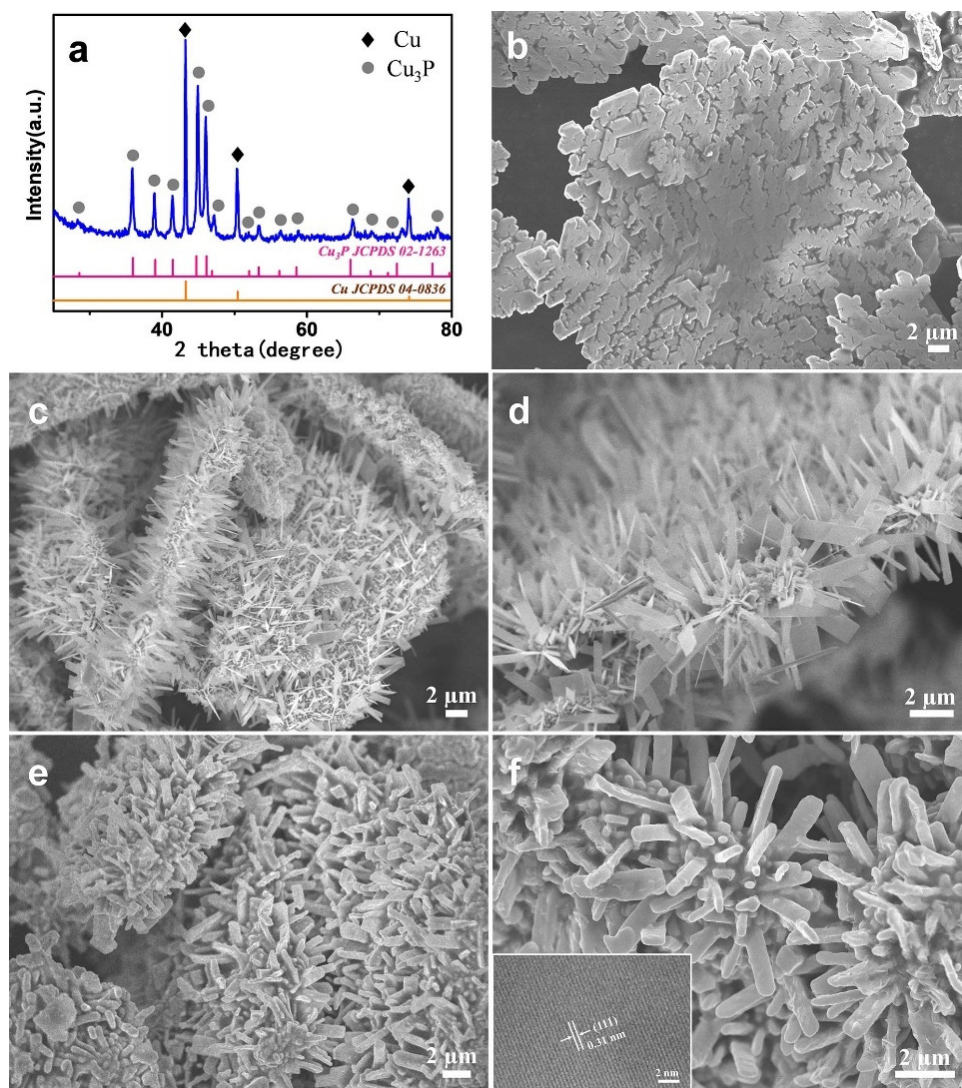


Figure 2. Characterization of the morphology and structure of sample: (a) XRD pattern of Cu/Cu₃P nanoarrays. (b) SEM image of Cu nanosheets. (c,d) SEM images of Cu/CuO nanoarrays. (e,f) SEM images of Cu/Cu₃P nanoarrays; inset shows the HRTEM of Cu₃P.

The morphologies of products were characterized by scanning electron microscopy (SEM). Figures 2b and S1a show the SEM images of Cu nanosheets as the self-template and conductive substrate, which had a large area of 30–100 μm in diameter with smooth surface. The SEM images of the Cu/CuO nanoarrays at different magnification are shown in Figures 2c,d and S2. The CuO nanoarrays are uniformly distributed on the surface of the Cu nanosheet, consisting of uniform nanoplates with a width ranging from 30 nm to 80 nm and are 3–5 μm in length. After phosphidation, the nanoarray morphology is still preserved, as shown in Figure 2e,f. The plate Cu₃P nanoarrays grown on the Cu nanosheet substrate and the surfaces of the nanoarrays become rough. The high-magnification SEM image of the Cu₃P nanoplate is shown in Figure S3, and close observation reveals that the thickness of an individual Cu₃P nanoplate increases from 60 nm to 120 nm in the phosphating process. The nanoarray structure helps to expose more active sites in the catalytic reaction, and the interspace between the nanoarrays can favor the diffusion of electrolytes. The high-resolution transmission electron microscopy (HRTEM) image (inset f) shows clear lattice fringes with an interplane distance of 0.31 nm, corresponding to the

(111) of the Cu_3P . All these results clearly confirm the successful synthesis of $\text{Cu}/\text{Cu}_3\text{P}$ nanoarrays by low-temperature phosphidation from the Cu/CuO nanoarray precursor.

The detailed elemental compositions and valence states of as-synthesized $\text{Cu}/\text{Cu}_3\text{P}$ were characterized by X-ray photoelectron spectroscopy (XPS), as shown in Figure 3. The full survey XPS spectrum (Figure S4) shows that the $\text{Cu}/\text{Cu}_3\text{P}$ comprises Cu, P, O and C elements. As shown in Figure 3a, two main peaks of Cu 2p are located at 934.6 eV and 954.4 eV, which represent the Cu $2p_{3/2}$ and Cu $2p_{1/2}$ peaks, respectively. The peaks at 933.1 eV and 935.1 eV are assigned to the $\text{Cu}^{\delta+}$ in the Cu_3P and oxidized Cu for the Cu $2p_{3/2}$ energy level, while the peaks at 940.8 and 944.1 eV belong to the satellite peaks of Cu $2p_{3/2}$. The three peaks appearing at 952.8, 955.2 and 962.9 eV are indexed to the $\text{Cu}^{\delta+}$ in the Cu_3P , oxidized Cu and the satellite for Cu $2p_{1/2}$, respectively [51,52]. In Figure 3b, the peak at 133.6 eV could be indexed to oxidized phosphate species, resulting from the exposure of the sample to air. The lower binding energy peaks situated at around 129.1 eV and 129.9 eV correspond to P $2p_{3/2}$ and P $2p_{1/2}$ of $\text{Cu}/\text{Cu}_3\text{P}$ nanoarrays, respectively [53,54]. Note that the binding energy of P 2p (129.9 eV) shows a negative shift from elemental P (130.2 eV), indicating that P carries a negative charge (δ^-). The results suggest that charge transfer occurs between Cu and P, in which Cu may serve as the hydride-acceptor center and P may act as the proton-acceptor center [55].

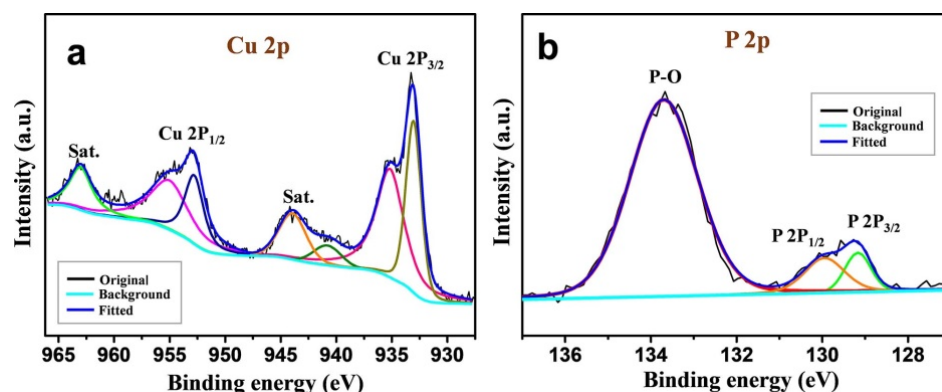


Figure 3. Cu 2p (a) and P 2p (b) core-level spectra of $\text{Cu}/\text{Cu}_3\text{P}$ nanoarrays.

The fabrication process of the $\text{Cu}/\text{Cu}_3\text{P}$ nanoarray is illustrated in Figure 4a. The morphology of the products was found to strongly depend on the distance between Cu/CuO nanoarrays and sodium hypophosphite in the phosphating process. When the distance between the two precursors is less than 5 cm, the nanoarray structure on the surface of the Cu nanosheets disappears and its surface becomes rough, as shown in Figure 4b,c. Further increasing the phosphating distance to 16 cm, part of the array structure on the surface can be observed, as shown in Figure 4d. The nanoarrays are obviously thicker than the original CuO nanoplate, and agglomeration between the nanoarrays is more serious. When the phosphating distance was extended to 24 cm (in Figure 4e), the nanoarray structure composed of Cu_3P nanoplates with a width of around 300–800 nm and lengths of up to several micrometers was vertically grown on the surface of the Cu nanosheets. The topotactic conversion of the Cu/CuO nanoarrays into the $\text{Cu}/\text{Cu}_3\text{P}$ nanoarray could be explained as follows: first, the thermal decomposition of NaH_2PO_2 generates PH_3 , and the CuO nanoarrays are reduced to Cu nanoarrays by PH_3 . Then, the resulting Cu subsequently catalyzes the decomposition of PH_3 into elemental P. Finally, the elemental P further reacts with Cu to form Cu_3P nanoarrays.

The influence of different mass ratios of phosphorus precursor and the Cu/CuO nanoarrays on the morphology and crystal structure was investigated, as shown in Figure 5. When the mass ratio of NaH_2PO_2 to CuO is 1, the morphology of $\text{Cu}/\text{Cu}_3\text{P}$ nanoarrays does not change significantly (Figure 5a), and the corresponding XRD pattern shows that only a small amount of Cu_3P is formed in the product (Figure 5b), indicating that the CuO cannot be converted into Cu_3P at this ratio. When the mass ratio of $\text{NaH}_2\text{PO}_2/\text{CuO}$ increases to

2, the obtained array structure is thicker than that of the precursor (Figure 5c), and the corresponding XRD pattern reveals that CuO has been converted into Cu₃P completely, but the amount of Cu₃P in the product is small (Figure 5d). When the mass ratio of NaH₂PO₂/CuO further increases to 2.5, the morphology of the product still maintains the nanoarray structure (Figure 5e), and the corresponding XRD pattern shows that Cu₃P is generated, while the peak intensity of the copper substrate does not change significantly (Figure 5f), indicating that the Cu nanosheet has not been converted. Until the mass ratio of NaH₂PO₂/CuO reached 3, the corresponding SEM image of this sample reveals that the Cu₃P nanoarrays thickened and agglomerated together (Figure 5g). The intensity of the XRD pattern of Cu in the product is significantly weakened (Figure 5h), indicating that the Cu nanosheet substrate is partially converted into Cu₃P during the phosphating reaction.

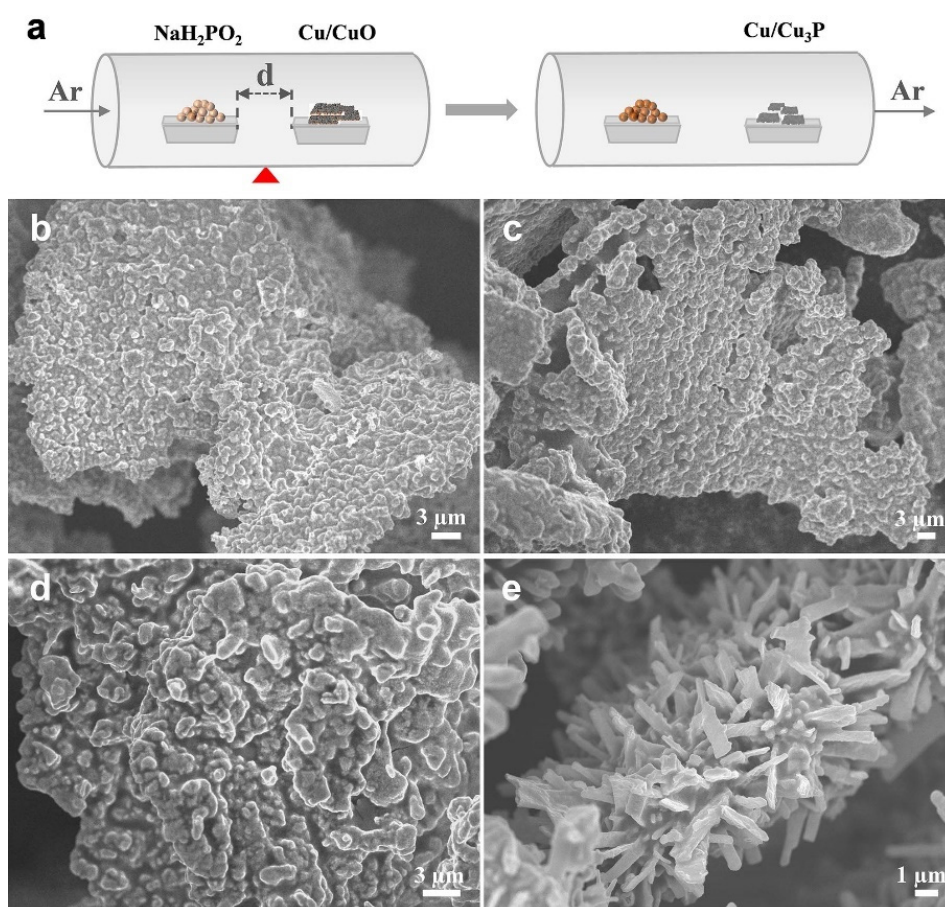


Figure 4. (a) Schematic of the preparation process of the Cu₃P nanoarrays via the phosphorization of Cu/CuO. (b–e) SEM images of products at different distances between Cu/CuO and NaH₂PO₂: (b) $d = 0$ cm, (c) $d = 5$ cm, (d) $d = 16$ cm and (e) $d = 24$ cm.

The influence of the phosphating temperature on the nanostructures formed was investigated, as shown in Figure 6. Figure 6a,b show that CuO and Cu₃P were simultaneously observed on the Cu nanosheets at 260 °C. With the increase in temperature, the thickness of nanoarrays composed of nanoplates was increased, while the CuO nanoarrays were completely converted to Cu₃P nanoarrays at 290 °C, as shown in Figure 6c,d. Until the temperature reached 310 °C, the nanoarray structures grown on the surfaces of Cu nanosheets experienced obvious agglomeration and collapse, and the corresponding XRD pattern revealed that a part of the Cu nanosheets was converted to Cu₃P in the phosphating reaction (Figure 6e,f). The effects of phosphating time on the morphology and phase of as-prepared nanostructures were likewise studied, as shown in Figure S5. When the calcination time was increased to 1.5 h, the morphology of the product obtained was as shown

in Figure S5c. The nanoarray structure composed of nanoplates is significantly thicker than that obtained at 1 h (Figure S5a). Moreover, the weak diffraction peak of Cu indicated that most of the Cu nanosheet substrates were transformed into Cu_3P (Figure S5d). The above results reveal that the phosphating temperature and time had a great impact on the formation of the resultant Cu/ Cu_3P nanoarrays in the present study.

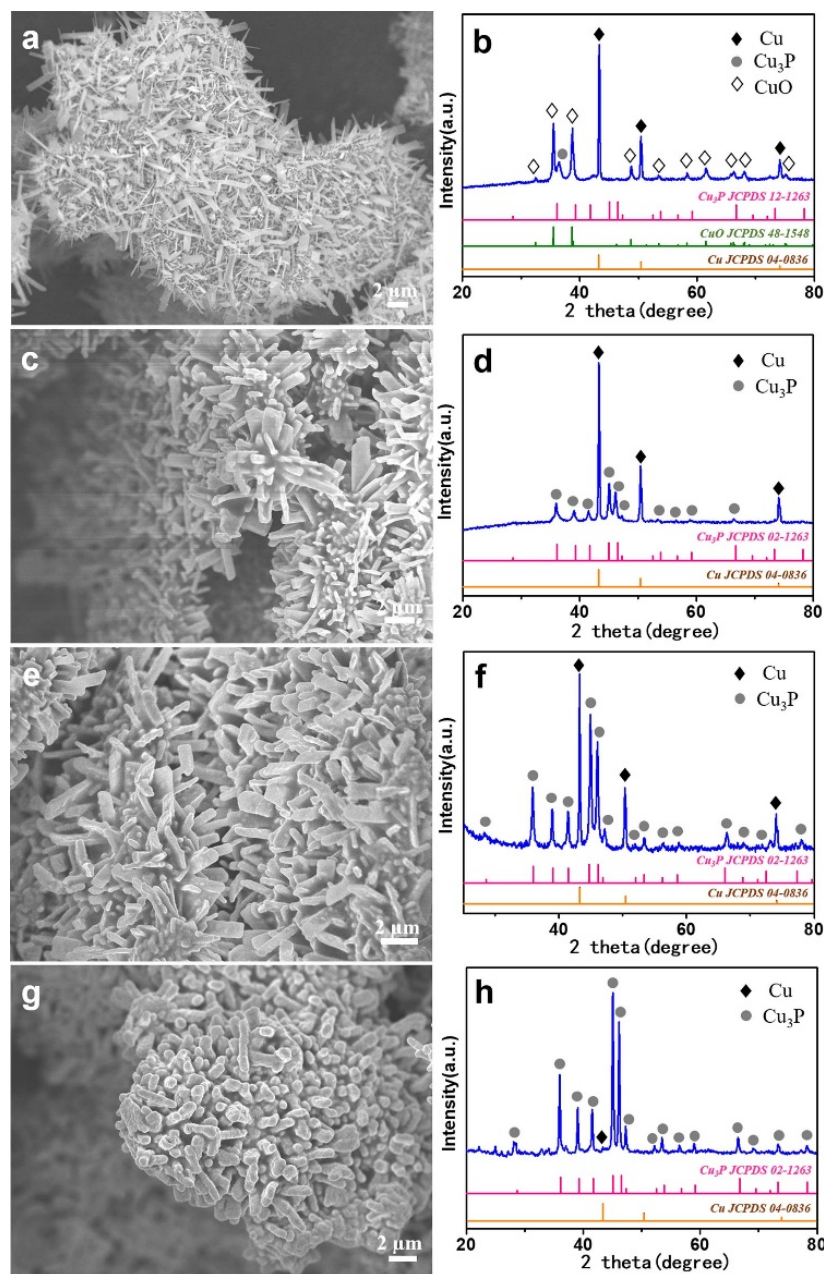


Figure 5. SEM images and XRD patterns of products at different mass ratios of $\text{NaH}_2\text{PO}_2/\text{CuO}$: (a,b) 1, (c,d) 2, (e,f) 2.5, (g,h) 3.

As a comparison, the pure Cu nanosheet was directly phosphated and calcined under the same conditions, while the morphology and crystal structure of the products were characterized. As shown in Figure S6a, the 2D nanosheet morphology was still preserved, and the smooth surface of the Cu nanosheets became rough after phosphating. At the same time, the corresponding XRD pattern confirmed that Cu_3P was indeed generated (Figure S6b). The results indicate that the CuO nanoarray on the surface of the Cu nanosheet plays a very significant role in maintaining the morphology of Cu/ Cu_3P nanoarrays.

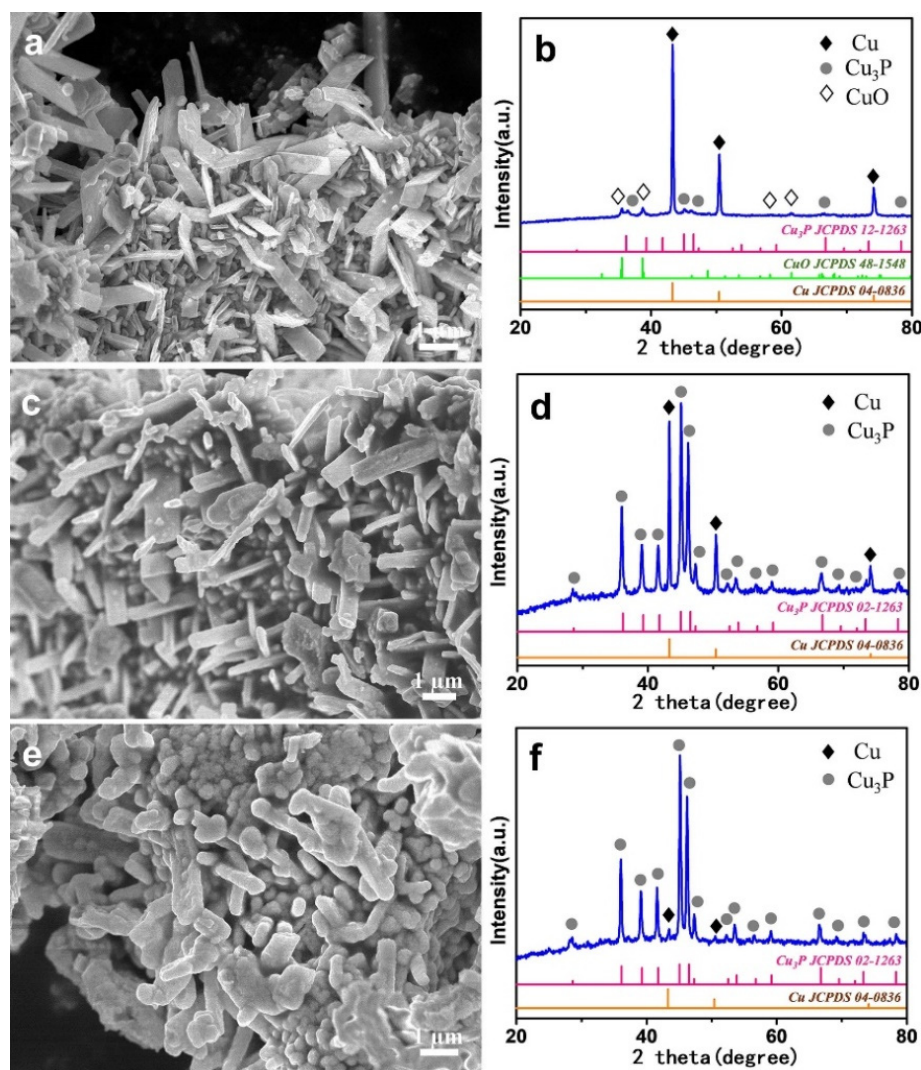


Figure 6. SEM images and XRD patterns of products at different phosphating temperatures: (a,b) 260 °C, (c,d) 290 °C, (e,f) 310 °C.

The electrocatalytic activity of the Cu/Cu₃P nanoarray for the HER was tested by using a standard three-electrode device in 0.5 M H₂SO₄ solution. Figure 7 shows the polarization curves of these electrodes obtained at different temperatures without iR correction. The catalytic behavior of Cu/Cu₃P NS obtained by the direct phosphating of the Cu nanosheet was also investigated for comparison. Obviously, the Cu/Cu₃P NS showed poor electrocatalytic activity, with an onset overpotential value of 347 mV. In sharp contrast, Cu/Cu₃P nanoarray-270 was significantly active for the HER, with an onset overpotential as low as 96 mV, and additional negative potential leads to a rapid rise in the cathodic current. It requires 253 mV of overpotential (η_{10}) to reach a current density (j) of 10 mA cm⁻², which is lower than that of Cu/Cu₃P nanoarray-290 (η_{10} = 342 mV) and Cu/Cu₃P nanoarray-310 (η_{10} = 395 mV). Moreover, an overpotential of 424 mV is required for Cu/Cu₃P nanoarray-270 to reach the current density of 100 mA cm⁻², which is much lower than that of Cu/Cu₃P nanoarray-290 (η_{100} = 589 mV) and Cu/Cu₃P nanoarray-310 (η_{100} = 635 mV).

The Tafel slope is an effective means to assess the advantages of electrocatalysts. The Tafel plots in Figure 7b were obtained from the linear portion that conformed to the Tafel equation ($\eta = a + b \log j$, where b is the Tafel slope and j is the current density). It can be seen that the Tafel slope for Cu/Cu₃P nanoarray-270 is 131 mV dec⁻¹, much lower than that of Cu/Cu₃P nanoarray-290 (145 mV dec⁻¹) and Cu/Cu₃P nanoarray-310 (156 mV dec⁻¹).

These results indicate that Cu/Cu₃P nanoarray-270 exhibits high electrocatalytic efficiency. A detailed comparison of Cu/Cu₃P nanoarray-270 with other electrocatalysts is shown in Table S1, indicating its superior or comparable performance [56–59].

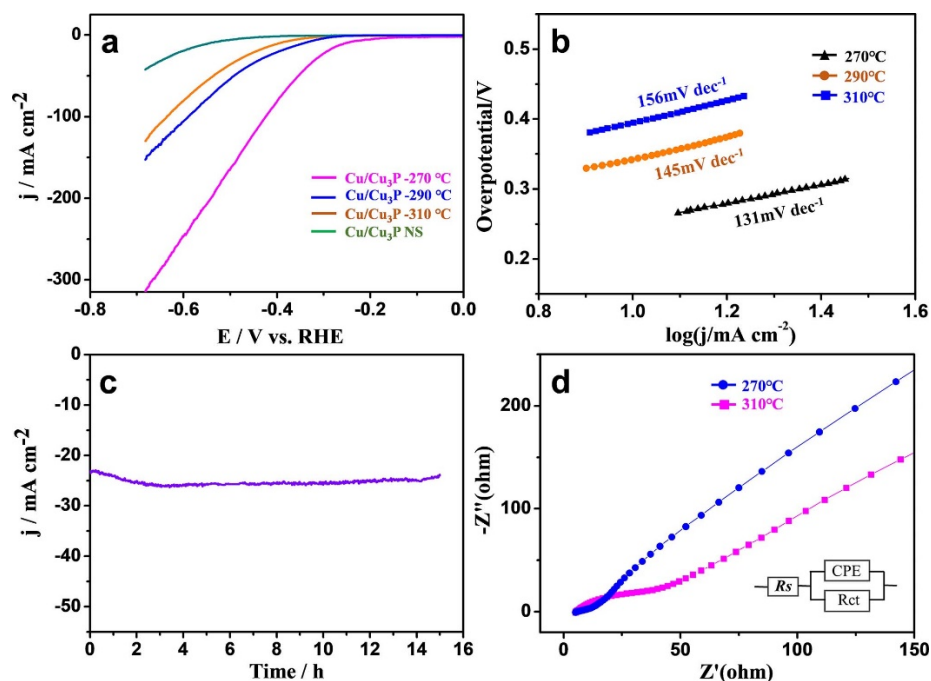


Figure 7. Electrocatalytic activity of the as-prepared Cu/Cu₃P nanoarray electrode for HER in 0.5 M H₂SO₄. (a) Polarization curves, (b) Tafel plots, (c) EIS Nyquist plots (inset: the equivalent circuit), (d) current density curve related to time at 23 mA cm⁻².

The long-term stability of an electrode is another important issue to consider for practical applications. The durability of Cu/Cu₃P nanoarray-270 was examined at 23 mA cm⁻² in H₂SO₄ solution, as shown in Figure 7c. The current density curve related to time reveals a minor increase after 15 h, indicating the high electrochemical stability of the Cu/Cu₃P nanoarray catalysts for the HER in an acidic solution. Electrochemical impedance spectroscopy (EIS) was performed to identify the interfacial properties and catalytic kinetics of the as-synthesized Cu/Cu₃P nanoarray catalyst in the HER process. As shown in Figure 7d (inset: the equivalent circuit), the series resistance values (R_s) were obtained in the high-frequency zone, and the semicircle in the low-frequency range reflects the charge transfer resistance at the interface between the Cu/Cu₃P and the electrolyte (R_{ct}). The Nyquist plots reveal that Cu/Cu₃P nanoarray-270 (4.1 Ω) exhibits a much smaller semicircle than Cu/Cu₃P nanoarray-310 (49.6 Ω), suggesting that it has fast charge transfer kinetics for the HER. This result validates that the introduced Cu nanosheet, as a conductive substrate and nano-template, can improve the charge transport and electrochemical activity of the Cu/Cu₃P nanoarray electrode.

3. Materials and Methods

3.1. Chemicals and Materials

Copper(II) sulfate (CuSO₄·5H₂O), glucose (C₆H₁₂O₆), polyvinylpyrrolidone (PVP, $M_w = 30,000$), hydrogen peroxide (H₂O₂, wt% = 30%), Nafion solution and sodium hypophosphite (NaH₂PO₂) were purchased from Sigma-Aldrich. All chemicals were used without further purification.

3.2. Synthesis of Cu Nanosheets

All chemicals in the experiment were analytical grade and used without purification. The well-defined Cu nanosheets were prepared according to the procedures in our previous

report [60]. In brief, 1.0 g $C_6H_{12}O_6 \cdot H_2O$, 0.5 g polyvinyl pyrrolidone (PVP) and $CuSO_4$ were dissolved in 25 mL of deionized water with vigorous magnetic stirring, and then the mixture was transferred into a Teflon-lined autoclave and heated at 180 °C for 3 h. The brown-red products were collected, washed three times with deionized water and ethanol, respectively, and then dried in a vacuum at 60 °C.

3.3. Synthesis of Cu/CuO Nanoarrays

The hierarchical Cu nanosheet@CuO nanorods were synthesized by a simple hydrothermal process. In a typical synthesis procedure, an amount of Cu nanosheets and 22 mL of NaOH (0.55 mol/L) were added into a Teflon-lined vessel with vigorous magnetic stirring, and then 2 mL H_2O_2 (30%) was injected rapidly into the mixture solution under stirring. Afterward, the vessel was sealed and then hydrothermally heated at 130 °C for 9 h; the as-prepared products were collected and washed three times with deionized water, and then dried in a vacuum at 60 °C.

3.4. Synthesis of Cu/Cu₃P Nanoarrays

To prepare Cu/Cu₃P nanoarrays, NaH_2PO_2 was placed at the center of the tube furnace and the Cu/CuO nanoarray was placed at the downstream side of the furnace at carefully adjusted locations to set the temperature, and the distance between them was measured to be approximately 24 cm. After flushing with Ar, the center of the furnace was elevated to 270 °C with a heating rate of 2 °C/min and held at this temperature for 60 min. For comparison, samples at different phosphating temperatures were synthesized by the same process.

3.5. Material Characterization

XRD patterns were collected using an M21X diffractometer (MAC Science Co. Ltd., Japan) with high-intensity Cu K α radiation ($\lambda = 1.541 \text{ \AA}$). The morphology of the products was characterized via scanning electron microscopy (SEM, ZEISS SUPRA55). The HRTEM images were collected on a FEI Tecnai F20 electron microscope operated at 200 kV. The elemental compositions and valence states of the samples were determined by XPS. XPS measurements were performed using a Thermo Fisher Scientific, Escalab-250Xi spectrometer with an Al K α X-ray resource. The C 1s contamination peak was used for charge correction (284.8 eV).

3.6. Electrochemical Measurements

The electrochemical performances of Cu/Cu₃P nanoarrays were evaluated with the CHI 660D electrochemical workstation. All the electrochemical measurements were conducted in a typical three-electrode setup with an electrolyte solution of 0.5 M H_2SO_4 using Cu/Cu₃P nanoarrays as the working electrode, a graphite plate as the counter electrode and Ag/AgCl as the reference electrode. In all measurements, the Ag/AgCl reference electrode was calibrated with respect to a reversible hydrogen electrode (RHE). Linear sweep voltammetry (LSV) measurements were conducted in 0.5 M H_2SO_4 with a scan rate of 2 mV s⁻¹. All the potentials reported in our work were versus the RHE according to $E_{vs. RHE} = E_{vs. Ag/AgCl} + E^0_{vs. Ag/AgCl} + 0.059 \text{ pH}$. Impedance measurements were carried out with a frequency range from 0.1 Hz to 10 kHz at the open-circuit potentials.

4. Conclusions

In summary, we have successfully prepared Cu/Cu₃P nanoarrays via a facile two-step synthetic strategy, including the hydrothermal synthesis of a Cu/CuO nanoarray precursor and a low-temperature phosphorization process in an Ar atmosphere. The as-prepared Cu/Cu₃P nanoarrays, as electrocatalysts, display excellent catalytic performance and durability for electrochemical hydrogen generation. Specifically, the Cu/Cu₃P nanoarray-270 exhibits a low onset overpotential (96 mV) and a small Tafel slope (131 mV dec⁻¹). The excellent electrocatalytic efficiency of the Cu/Cu₃P nanoarray catalyst for the HER

can be attributed to its unique architecture. The nanoarray structure provides more active sites and contributes to the diffusion of the products. The Cu/Cu₃P nanoarrays show good electrical conductivity, which is favorable to a faster transfer rate of electrons. This strategy provides an efficient technique that can be extended to other metal phosphides and metal-based nanostructures, thus creating a new opportunity in hydrogen production.

Supplementary Materials: The following supporting information can be downloaded at: <https://www.mdpi.com/article/10.3390/catal12070762/s1>, Figure S1: Characterization of the morphology and structure of samples: (a) SEM image of Cu nanosheet, (b) XRD patterns of Cu nanosheets, and (c) XRD patterns of Cu/CuO nanoarrays; Figure S2: The high-magnification SEM images of samples: (a,b) SEM image of Cu/CuO nanoarrays; Figure S3: The high-magnification SEM images of (a) CuO nanoplate, (b) Cu₃P nanoplate; Figure S4: XPS survey spectrum of Cu /Cu₃P nanoarrays; Figure S5: The SEM images and XRD patterns of samples at different phosphating time: (a,b) 1 h; (c,d) 1.5 h; Figure S6: The pure Cu nanosheet was directly phosphated and calcined: (a) SEM image; (b) XRD pattern; Table S1: Comparison of HER catalytic performance of Cu/Cu₃P nanoarray-270 and other non-noble-metal electrocatalysts in acidic media.

Author Contributions: The manuscript was written with contributions from all authors. Conceptualization, R.D. and J.L.; methodology and investigation, R.D. and X.X.; data curation, M.X.; formal analysis, R.D. and X.X.; writing—original draft preparation, R.D.; writing—review and editing, R.D. and J.L.; visualization, M.X.; project administration, R.D. All authors have read and agreed to the published version of the manuscript.

Funding: This research was funded by the National Natural Science Foundation of China (Program No. 21905232) and Natural Science Basic Research Plan in Shaanxi Province of China (Program No. 2022JM-236).

Data Availability Statement: The data are available upon request from the corresponding author.

Acknowledgments: The authors thank G. Wang and H.Y. Gao (University of Science and Technology Beijing, Beijing 100083, China) and X.W. Zhang and M.Y. Han (Beijing Normal University, 100088, China) for their help.

Conflicts of Interest: The authors declare no conflict of interest.

References


- Zhang, Y.; Li, W.; Lu, L.; Song, W. Tuning active sites on cobalt/nitrogen doped graphene for electrocatalytic hydrogen and oxygen evolution. *Electrochim. Acta* **2018**, *265*, 497–506. [CrossRef]
- Jebaslinhepybai, B.T.; Prabu, N.; Sasidharan, M. Facile galvanic replacement method for porous nanoparticles as an efficient HER electrocatalyst. *Int. J. Hydrog. Energy* **2020**, *45*, 11127–11137. [CrossRef]
- Jiang, H.; Gu, J.; Zheng, X.; Liu, M.; Qiu, X.; Wang, L.; Li, W.; Chen, Z.; Ji, X.; Li, J. Defect-rich and ultrathin N doped carbon nanosheets as advanced trifunctional metal-free electrocatalysts for the ORR, OER and HER. *Energy Environ. Sci.* **2019**, *12*, 322–333. [CrossRef]
- Li, Y.; Liu, J.; Chen, C.; Zhang, X.; Chen, J. Preparation of NiCoP Hollow Quasi-Polyhedra and Their Electrocatalytic Properties for Hydrogen Evolution in Alkaline Solution. *ACS Appl. Mater. Interfaces* **2017**, *9*, 5982–5991. [CrossRef]
- Martini, B.K.; Maia, G. Using a combination of Co, Mo, and Pt oxides along with graphene nanoribbon and MoSe₂ as efficient catalysts for OER and HER. *Electrochim. Acta* **2021**, *391*, 138907. [CrossRef]
- Yu, J.; Dai, Y.; He, Q.; Cheng, C.; Ni, M. Robust non-Pt noble metal-based nanomaterials for electrocatalytic hydrogen generation. *Appl. Phys. Rev.* **2020**, *7*, 041304. [CrossRef]
- El-Hallag, I.; Elsharkawy, S.; Hammad, S. The effect of electrodeposition potential on catalytic properties of Ni nanoparticles for hydrogen evolution reaction (HER) in alkaline media. *J. Appl. Electrochem.* **2022**, *52*, 907–918. [CrossRef]
- Li, Y.; Wang, H.; Xie, L.; Liang, Y.; Hong, G.; Dai, H. MoS₂ Nanoparticles Grown on Graphene: An Advanced Catalyst for Hydrogen Evolution Reaction. *J. Am. Chem. Soc.* **2011**, *133*, 7296–7299. [CrossRef]
- Popczun, E.J.; Mckone, J.R.; Read, C.G.; Biacchi, A.J.; Wiltrout, A.M.; Lewis, N.S.; Schaak, R.E. Nanostructured nickel phosphide as an electrocatalyst for the hydrogen evolution reaction. *J. Am. Chem. Soc.* **2013**, *135*, 9267–9270. [CrossRef]
- Li, S.; Wang, Y.; Wang, H.; Zhang, Q.; Zhang, Z.; Liu, H. Correction to: Heterostructures of MXenes and CoNx-Graphene as highly active electrocatalysts for hydrogen evolution reaction in alkaline media. *J. Appl. Electrochem.* **2021**, *51*, 1109. [CrossRef]
- Pu, M.; Wang, D.; Zhang, Z.; Guo, Y.; Guo, W. Flexoelectricity enhanced water splitting and hydrogen evolution reaction on grain boundaries of monolayer transition metal dichalcogenides. *Nano Res.* **2022**, *15*, 978–984. [CrossRef]

12. Pak, S.; Lim, J.; Hong, J.; Cha, S.N. Enhanced Hydrogen Evolution Reaction in Surface Functionalized MoS₂ Monolayers. *Catalysts* **2021**, *11*, 70. [CrossRef]
13. Yan, X.; Huang, S.; Yang, F.; Sun, S.; Li, Y. Enhanced Catalytic Hydrogen Evolution Reaction Performance of Highly Dispersed Ni₂P Nanoparticles Supported by P-Doped Porous Carbon. *Colloids Surf. A Physicochem. Eng. Asp.* **2021**, *616*, 126308. [CrossRef]
14. Kluge, R.M.; Haid, R.W.; Stephens, I.; Callevallejo, F.; Bandarenka, A.S. Monitoring the active sites for the hydrogen evolution reaction at model carbon surfaces. *Phys. Chem. Chem. Phys.* **2021**, *23*, 10051–10058. [CrossRef]
15. Kita, H.; Shen, Y.; Gao, Y. Mass transfer effect in hydrogen evolution reaction on Pt single-crystal electrodes in acid solution. *J. Electroanal. Chem.* **1992**, *334*, 351–357. [CrossRef]
16. Yang, B.; Xu, J.; Duan, B.; Wang, J.; Liu, B. Amorphous phosphatized ruthenium-iron bimetallic nanoclusters with Pt-like activity for hydrogen evolution reaction. *Appl. Catal. B Environ.* **2021**, *283*, 119583. [CrossRef]
17. Lai, Y.; Zhang, Z.; Tan, Y.; Yu, L.; Wu, W.; Wang, Z.; Jiang, T.; Gao, S.; Cheng, N. Electronic modulation of Pt nanoclusters through tuning the interface of Pt-SnO₂ clusters for enhanced hydrogen evolution catalysis. *Chem. Eng. J.* **2022**, *435*, 135102. [CrossRef]
18. Chen, J.; Chen, C.; Chen, Y.; Wang, H.; Wang, Y. Improving alkaline hydrogen evolution reaction kinetics on molybdenum carbide: Introducing Ru dopant. *J. Catal.* **2020**, *392*, 313–321. [CrossRef]
19. Cai, J.; Liao, X.; Li, P.; Wang, Q.; Huang, H.; Lyu, Z.; Lin, J.; Xie, S. Penta-Twinned Rh@Pt Core-Shell nanobranches with engineered shell thickness for reversible and active hydrogen redox electrocatalysis. *Chem. Eng. J.* **2022**, *429*, 132414. [CrossRef]
20. Yang, Q.; Li, G.; Manna, K.; Fan, F.; Sun, Y. Topological Engineering of Pt-Group-Metal-Based Chiral Crystals toward High-Efficiency Hydrogen Evolution Catalysts. *Adv. Mater.* **2020**, *32*, 1908518. [CrossRef]
21. Jy, A.; Dan, W.B.; Zhe, Z.B.; Wy, A.; Hs, A.; Yq, A.; Sw, B.; Yukc, D.; Yz, C. Facile synthesis of Nafion-supported Pt nanoparticles with ultra-low loading as a high-performance electrocatalyst for hydrogen evolution reaction. *J. Colloid Interface Sci.* **2020**, *566*, 505–512.
22. Tiwari, J.N.; Dang, N.K.; Sultan, S.; Thangavel, P.; Jeong, H.Y.; Kim, K.S. Multi-heteroatom-doped carbon from waste-yeast biomass for sustained water splitting. *Nat. Sustain.* **2020**, *3*, 556–563. [CrossRef]
23. Bae, S.Y.; Mahmood, J.; Jeon, I.Y.; Baek, J.B. Recent advances in ruthenium-based electrocatalysts for the hydrogen evolution reaction. *Nanoscale Horiz.* **2020**, *5*, 43–56. [CrossRef]
24. Bonde, J.; Moses, P.G.; Jaramillo, T.F.; Nørskov, J.K.; Chorkendorff, I. Hydrogen evolution on nano-particulate transition metal sulfides. *Faraday Discuss.* **2008**, *140*, 219–231. [CrossRef]
25. Reeve, R.W.; Christensen, P.A.; Dickinson, A.J.; Hamnett, A.; Scott, K. Methanol-tolerant oxygen reduction catalysts based on transition metal sulfides and their application to the study of methanol permeation. *Electrochim. Acta* **2000**, *45*, 4237–4250. [CrossRef]
26. Ys, A.; Ch, B.; Js, A.; Yz, A.; Jn, C.; Yong, H.A. One-step construction of a transition-metal surface decorated with metal sulfide nanoparticles: A high-efficiency electrocatalyst for hydrogen generation. *J. Colloid Interface Sci.* **2020**, *558*, 1–8.
27. Dolmatov, V.S.; Kuznetsov, S.A. Synthesis of Refractory Metal Carbides on Carbon Fibers in Molten Salts and Their Electrocatalytic Properties. *J. Electrochem. Soc.* **2021**, *168*, 122501. [CrossRef]
28. Diaz-Coello, S.; Afonso, M.M.; Palenzuela, J.A.; Pastor, E.; García, G. Composite materials from transition metal carbides and ionic liquids as electrocatalyst for hydrogen evolution in alkaline media. *J. Electroanal. Chem.* **2021**, *898*, 115620. [CrossRef]
29. Ihsanullah, I. MXenes (two-dimensional metal carbides) as emerging nanomaterials for water purification: Progress, challenges and prospects. *Chem. Eng. J.* **2020**, *388*, 124340. [CrossRef]
30. Yu, F.; Zhang, X.; Yang, Z.; Yang, P.; Ma, J. Environmental applications of two-dimensional transition metal carbides and nitrides for water purification: A review. *Environ. Chem. Lett.* **2022**, *20*, 633–660. [CrossRef]
31. Yan-Juan, L.I.; Wang, M.; Liu, S.; Gao, J.X.; Yan, X. Preparation and properties of transition metal nitrides caged in N-doped hollow porous carbon sphere for oxygen reduction reaction. *Trans. Nonferrous Met. Soc. China* **2021**, *31*, 1427–1438.
32. Sun, H.; Yan, Z.; Liu, F.; Xu, W.; Cheng, F.; Chen, J. Self-Supported Transition-Metal-Based Electrocatalysts for Hydrogen and Oxygen Evolution. *Adv. Mater.* **2020**, *32*, 1806326.1–1806326.18. [CrossRef]
33. Li, A.; Zhang, L.; Wang, F.; Li, L.; Chen, H.; Wei, Z. Rational design of porous Ni-Co-Fe ternary metal phosphides nanobricks as bifunctional electrocatalysts for efficient overall water splitting. *Appl. Catal. B Environ.* **2022**, *310*, 121353. [CrossRef]
34. Han, P.; Li, B.; Dang, Y.; Zhou, Y. A Novel Trimetal Phosphide with Amorphous Porous Structure for the Enhanced Electrocatalysis of Oxygen Evolution Reaction. *J. Electrochem. Soc.* **2021**, *168*, 116510.
35. Wy, A.; Yg, A.; Zhi, C.A.; Ying, Z.A.; Zw, A.; Lei, W. Strategies on improving the electrocatalytic hydrogen evolution performances of metal phosphides. *Chin. J. Catal.* **2021**, *42*, 1876–1902.
36. Liu, L.; Li, N.; Han, J.; Yao, K.; Liang, H. Multicomponent transition metal phosphide for oxygen evolution. *Int. J. Miner. Metall. Mater.* **2022**, *29*, 503–512. [CrossRef]
37. Jian, L.; Gao, X.; Liu, B.; Feng, Q.; Li, X.B.; Huang, M.Y.; Liu, Z.; Zhang, J.; Tung, C.H.; Wu, L.Z. Graphdiyne: A Metal-Free Material as Hole Transfer Layer to Fabricate Quantum Dot-Sensitized Photocathodes for Hydrogen Production. *J. Am. Chem. Soc.* **2016**, *138*, 3954.
38. Cao, R.; Hu, F.; Zhang, T.; Shao, W.; Jian, X. Bottom-up fabrication of triazine-based frameworks as metal-free materials for supercapacitors and oxygen reduction reaction. *RSC Adv.* **2021**, *11*, 8384–8393. [CrossRef]
39. Wei, S.; Qi, K.; Jin, Z.; Cao, J.; Zheng, W.; Chen, H.; Cui, X. One-Step Synthesis of a Self-Supported Copper Phosphide Nanobush for Overall Water Splitting. *ACS Omega* **2016**, *1*, 1367–1373. [CrossRef]

40. Ping, L.; Rodriguez, J.A. Catalysts for hydrogen evolution from the [NiFe] hydrogenase to the Ni₂P (001) surface: The importance of ensemble effect. *J. Am. Chem. Soc.* **2005**, *127*, 14871–14878.
41. Zhang, W.; Hong, J.; Zheng, J.; Huang, Z.; Zhou, J.; Xu, R. Nickel-thiolate complex catalyst assembled in one step in water for solar H₂ production. *J. Am. Chem. Soc.* **2011**, *133*, 20680–20683. [CrossRef]
42. Li, Q.; Xing, Z.; Asiri, A.M.; Ping, J.; Sun, X. Cobalt phosphide nanoparticles film growth on carbon cloth: A high-performance cathode for electrochemical hydrogen evolution. *Int. J. Hydrog. Energy* **2014**, *39*, 16806–16811. [CrossRef]
43. Cao, S.; Yong, C.; Wang, C.J.; He, P.; Fu, W.F. Highly efficient photocatalytic hydrogen evolution by nickel phosphide nanoparticles from aqueous solution. *Chem. Commun.* **2014**, *50*, 10427–10429. [CrossRef]
44. Mccanney, J.M.; Crompton, J.C.; Callejas, J.F.; Popczun, E.J.; Biacchi, A.J.; Lewis, N.S.; Schaak, R.E. Amorphous Molybdenum Phosphide Nanoparticles for Electrocatalytic Hydrogen Evolution. *Chem. Mater.* **2014**, *26*, 4826–4831. [CrossRef]
45. Wu, Y.; Li, Y.; Yuan, M.; Zhe, L.; Wei, B. Direct growth of Ni-Fe phosphides nanohybrids on NiFe foam for highly efficient water oxidation. *J. Alloys Compd.* **2020**, *847*, 156363. [CrossRef]
46. You, B.; Jiang, N.; Sheng, M.; Bhushan, M.W.; Sun, Y. Hierarchically Porous Urchin-Like Ni₂P Superstructures Supported on Nickel Foam as Efficient Bifunctional Electrocatalysts for Overall Water Splitting. *ACS Catal.* **2016**, *6*, 714–721. [CrossRef]
47. Gao, X.; Lu, K.; Chen, J.; Min, J.; Tan, M. NiCoP–CoP heterostructural nanowires grown on hierarchical Ni foam as a novel electrocatalyst for efficient hydrogen evolution reaction. *Int. J. Hydrog. Energy* **2021**, *46*, 23205–23213. [CrossRef]
48. Yang, Z.; Tuo, Y.; Lu, Q.; Chen, C.; Liu, M.; Liu, B.; Duan, X.; Zhou, Y.; Zhang, J. Hierarchical Cu₃P-based nanoarrays on nickel foam as efficient electrocatalysts for overall water splitting. *Green Energy Environ.* **2020**, *2*, 236–245. [CrossRef]
49. Hou, C.C.; Chen, Q.Q.; Wang, C.J.; Liang, F.; Lin, Z.; Fu, W.F.; Chen, Y. Self-Supported Cedarlike Semimetallic Cu₃P Nanoarrays as a 3D High-Performance Janus Electrode for Both Oxygen and Hydrogen Evolution under Basic Conditions. *ACS Appl. Mater. Interfaces* **2016**, *8*, 23037–23048. [CrossRef]
50. Shiri, P. An overview on the copper-promoted synthesis of five-membered heterocyclic systems. *Appl. Organomet. Chem.* **2020**, *34*, 5600–5622. [CrossRef]
51. Zheng, H.; Huang, X.; Gao, H.; Lu, G.; Dong, W.; Wang, G. Cu@Cu₃P core-shell nanowires attached on Ni foam as high-performance electrocatalyst for hydrogen evolution reaction. *Chemistry* **2018**, *25*, 1083–1089. [PubMed]
52. Fedorov, A.; Saraev, A.; Kremneva, A.; Selivanova, A.; Vorokhta, M.; Šmíd, B.; Bulavchenko, O.; Yakovlev, V.; Kaichev, V. Kinetic and mechanistic study of CO oxidation over nanocomposite CuFeAl oxide catalysts. *ChemCatChem* **2020**, *19*, 4911–4921. [CrossRef]
53. Rong, J.; Xu, J.; Qiu, F.; Zhu, Y.; Fang, Y.; Xu, J.; Zhang, T. Sea Urchin-Like MOF-Derived Formation of Porous Cu₃P@C as an Efficient and Stable Electrocatalyst for Oxygen Evolution and Hydrogen Evolution Reactions. *Adv. Mater. Interfaces* **2019**, *6*, 1900502. [CrossRef]
54. Zhou, X.; Zhou, X.; Liu, L.; Chen, H.; Hu, X.; Qian, J.; Huang, D.; Zhang, B.; Tang, J. Self-supported Cu₃P nanowire electrode as an efficient electrocatalyst for the oxygen evolution reaction. *RSC Adv.* **2021**, *11*, 34137–34143. [CrossRef] [PubMed]
55. Kou, Y.; Wang, K.; Wumaer, M.; Guo, C.; Tian, B.; Zhang, L.; Akram, N.; Wang, J. Synthesis of hollow Cu@Cu₃-xP core-shell nanostructure as dual-functional catalyst with copper vacancy for enhancing chemical reduction and photocatalytic performance. *Appl. Surf. Sci.* **2022**, *589*, 153031. [CrossRef]
56. Ma, L.; Shen, X.; Zhou, H.; Zhu, J.; Xi, C.; Ji, Z.; Kong, L. Synthesis of Cu₃P nanocubes and their excellent electrocatalytic efficiency for the hydrogen evolution reaction in acidic solution. *RSC Adv.* **2016**, *6*, 9672–9677. [CrossRef]
57. Tian, J.; Liu, Q.; Cheng, N.; Asiri, A.M.; Sun, X. Self-supported Cu₃P nanowire arrays as an integrated high-performance three-dimensional cathode for generating hydrogen from water. *Angew. Chem.* **2015**, *126*, 9731–9735. [CrossRef]
58. Tian, T.; Ai, L.; Jiang, J. Metal-organic framework-derived nickel phosphides as efficient electrocatalysts toward sustainable hydrogen generation from water splitting. *RSC Adv.* **2015**, *5*, 10290–10295. [CrossRef]
59. Xu, Y.; Wu, R.; Zhang, J.; Shi, Y.; Zhang, B. Anion-exchange synthesis of nanoporous FeP nanosheets as electrocatalysts for hydrogen evolution reaction. *Chem. Commun.* **2013**, *49*, 6656–6658. [CrossRef]
60. Dang, R.; Song, L.L.; Dong, W.J.; Li, C.R.; Zhang, X.B. Synthesis and self-assembly of large-area Cu nanosheets and their application as an aqueous conductive ink on flexible electronics. *ACS Appl. Mater. Interfaces* **2014**, *6*, 622–629. [CrossRef]

Article

Low-Temperature Selective NO Reduction by CO over Copper-Manganese Oxide Spinel

Fenglan Fan ¹, Lingjuan Wang ¹, Lei Wang ¹, Jinyu Liu ^{1,*}  and Minghui Wang ^{2,*}

¹ School of Chemistry and Chemical Engineering, Hebei Normal University for Nationalities, Chengde 067000, China; ffl619@163.com (F.F.); lingjuan1992@163.com (L.W.); lanlan19870619@163.com (L.W.)

² School of Chemical Engineering, Changchun University of Technology, Changchun 130012, China

* Correspondence: llhliulu@163.com (J.L.); whm0932@ccut.edu.cn (M.W.)

Abstract: Selective catalytic reduction of NO with CO (CO-SCR) has been suggested as an attractive and promising technology for removing NO and CO simultaneously from flue gas. Manganese-copper spinels are a promising CO-SCR material because of the high stability and redox properties of the spinel structure. Here, we synthesized $\text{Cu}_x\text{Mn}_{3-x}\text{O}_4$ spinel by a citrate-based modified pechini method combining CuO and MnO_x , controlling the molar Cu/Mn concentrations. All the samples were characterized by SEM, EDX, XRD, TEM, H_2 -TPR, XPS and nitrogen adsorption measurements. The $\text{Cu}_{1.5}\text{Mn}_{1.5}\text{O}_4$ catalyst exhibits 100% NO conversion and 53.3% CO conversion at 200 °C. The $\text{Cu}_x\text{Mn}_{3-x}\text{O}_4$ catalyst with Cu-O-Mn structure has a high content of high valence Mn, and the high mass transfer characteristics of the foam-like structure together promoted the reaction performance. The CO-SCR catalytic performance of Cu was related to the spinel structure with the high ratio of Mn^{4+}/Mn , the synergistic effect between the two kinds of metal oxides and the multistage porous structure.

Keywords: low-temperature; CO-SCR; Cu-Mn oxide spinels



Citation: Fan, F.; Wang, L.; Wang, L.; Liu, J.; Wang, M. Low-Temperature Selective NO Reduction by CO over Copper-Manganese Oxide Spinel. *Catalysts* **2022**, *12*, 591. <https://doi.org/10.3390/catal12060591>

Academic Editor: Sónia Carabineiro

Received: 22 April 2022

Accepted: 27 May 2022

Published: 29 May 2022

Publisher's Note: MDPI stays neutral with regard to jurisdictional claims in published maps and institutional affiliations.



Copyright: © 2022 by the authors. Licensee MDPI, Basel, Switzerland. This article is an open access article distributed under the terms and conditions of the Creative Commons Attribution (CC BY) license (<https://creativecommons.org/licenses/by/4.0/>).

1. Introduction

Currently, environmental protection is more stringent than ever before. The large quantities of nitrogen oxides (NO_x) produced by the burning of fossil fuels are a major cause of atmospheric pollutants. Carbon monoxide (CO) is another atmospheric pollutant in flue gases. Thus, the reduction of NO by the CO produced by incomplete combustion in the flue gas can remove toxic CO and NO simultaneously and economically (CO-SCR) [1–3]. However, the high price and low catalytic activity at low temperature (more than 50% NO conversion below 250 °C) of efficient noble metal catalysts seriously limit their further application. Therefore, it is necessary to develop catalysts with low temperature, high performance, low cost and that are green [4].

For the CO-SCR reaction, the ideal catalyst should not only be economical, easy to prepare, long-term stable and so on. In addition, a low reaction temperature [5,6], high selectivity [7,8] and NO conversion rate [9] are required. Noble metals are frequently used in CO-SCR reactions to prepare noble-metal catalysts. However, the scarce resources, high price and high temperature instability limit its large-scale application. As a result, many studies have focused on the development of nonprecious metals. NO reduction occurs through a redox reaction mechanism. Therefore, the reducibility and oxygen migration ability of the catalyst are two key factors that determine the catalytic performance of the catalyst for NO removal. At present, metal oxides have become a hotspot of heterogeneous catalysis research because of their low price and large reserves, such as CoO_x [10,11], CuO_x [12–14], MnO_x [15,16] and CeO_2 [17]. Among them, copper oxides and manganese oxides have attracted much attention due to their good redox properties. Manganese oxides show a variety of valences (Mn^{2+} , Mn^{3+} , Mn^{4+}) and abundant reactive oxygen species

(vacancy oxygen and adsorbed oxygen), which imply their potential in low-temperature CO-SCR catalysis [18–20].

In related reports, the reducibility and oxygen migration ability of MnO_x could be improved by proper cation doping. These include MnCe [21], MnCu [22–24], MnCo [25], MnNi [26,27] and MnFe [28]. Because of its excellent oxidation–reduction performance and strong synergistic effect between binary metal oxides, doping copper into the catalyst can effectively improve the removal rate of the catalyst. Wan et al. [29] found that the Mn_2O_3 -modified $\text{CuO}/\gamma\text{-Al}_2\text{O}_3$ catalyst showed significant catalytic efficiency, and they attributed the increase in activity to the establishment of a $\text{Cu}^{2+} + \text{Mn}^{3+} \rightleftharpoons \text{Cu}^+ + \text{Mn}^{4+}$ oxidation–reduction cycle. In addition, the addition of Cu to Mn-based catalysts is beneficial to the dispersion of MnO_x . The performance of copper oxides is affected by many factors in the $\text{NO} + \text{CO}$ reaction. Ivanka Spassova [24] reported that CuCo_2O_4 and $\text{Cu}_{1.5}\text{Mn}_{1.5}\text{O}_4$ mixed oxides supported on DFS were responsible for enhancing activity. The results showed that Liu [30] suggested that copper-modified manganites had higher catalytic activity for CO oxidation and selective catalytic reduction of NO than pure MnO_x . Therefore, it is further expected that CuO and MnO_x form a strong coupling at the nanointerface, which will lead to a change in the Mn^{4+} octahedral environment, thereby further improving the CO–SCR performance of MnO_x .

This article reports that foam-like $\text{Cu}_x\text{Mn}_{3-x}\text{O}_4$ spinels were prepared by using a citrate-based modified pechini method and applied to the CO-SCR reaction in the temperature range of 100–400 °C. It was characterized by scanning electron microscopy (SEM), transmission electron microscopy (TEM), X-ray diffraction (XRD), BET surface area (BET), H_2 temperature programmed reduction (H_2 –TPR) and X-ray photoelectron spectroscopy (XPS). The structure–activity relationship between the physical chemistry properties and the catalytic performance of the $\text{Cu}_x\text{Mn}_{3-x}\text{O}_4$ catalyst with different concentrations of Mn^{4+} was studied. The purpose of this work is to investigate the relationship between the active phase of spinel and the bulk properties of $\text{Cu}_x\text{Mn}_{3-x}\text{O}_4$ ($x = 0, 1, 1.5, 2, 3$) catalysts prepared with different CuO/ MnO_x contents.

2. Results and Discussion

2.1. XRD Analysis of Catalysts

XRD patterns were tested to identify the crystal structure of Mn_2O_3 , CuO and synthesized $\text{Cu}_x\text{Mn}_{3-x}\text{O}_4$ spinels. As shown in Figure 1a, for the Mn_2O_3 sample, (200), (211), (222), (123), and (440) planes of Mn_2O_3 (JCPDS#01-076-0150) could be observed at 18.5°, 23.1°, 33.0°, 35.7° and 55.0°, respectively. The diffraction peaks of 32.5°, 35.5°, 38.6°, 48.9°, 53.4°, 58.2°, 61.5°, 66.3°, 67.7°, 68.0°, 72.3° and 82.6° were assigned to the (110), (−111), (111), (−202), (020), (202), (−113), (−311), (113), (220), (311) and (−313) planes of cubic phase CuO (JCPDS#01-080-0076). A $\text{Cu}_x\text{Mn}_{3-x}\text{O}_4$ mixed oxide with a spinel structure was found in the $\text{Cu}_1\text{Mn}_2\text{O}_4$ (JCPDS#01-074-2422), $\text{Cu}_{1.5}\text{Mn}_{1.5}\text{O}_4$ (JCPDS#01-070-0260) and $\text{Cu}_2\text{Mn}_1\text{O}_4$ catalysts. XRD patterns show that the diffraction peak (I peak) can match spinel $\text{Cu}_{1.5}\text{Mn}_{1.5}\text{O}_4$ (Figure 1b). Compared with other samples, the intensity of the “I” diffraction peak of the $\text{Cu}_{1.5}\text{Mn}_{1.5}\text{O}_4$ sample is the strongest, indicating that the $\text{Cu}_{1.5}\text{Mn}_{1.5}\text{O}_4$ sample contains a spinel active structure (Cu–O–Mn) [30,31]. As for $\text{Cu}_1\text{Mn}_2\text{O}_4$ and $\text{Cu}_{1.5}\text{Mn}_{1.5}\text{O}_4$, they showed identical diffraction patterns to Mn_2O_3 but only with a slight shift in the peak position of Mn_2O_3 toward high values, implying the insertion of Cu atoms with smaller radius than Mn atoms into the lattice of Mn_2O_3 . It is also noticed that the crystallinity of $\text{Cu}_{1.5}\text{Mn}_{1.5}\text{O}_4$ becomes higher in comparison with that of $\text{Cu}_1\text{Mn}_2\text{O}_4$ and $\text{Cu}_2\text{Mn}_1\text{O}_4$, implying that excessive Cu doping is not conducive to the formation of Cu–O–Mn structure (Table 1). The lattice parameters of the synthesized $\text{Cu}_x\text{Mn}_{3-x}\text{O}_4$ catalyst were calculated by XRD, as shown in Table 1. Compared to $\text{Cu}_x\text{Mn}_{3-x}\text{O}_4$ spinels, the lattice parameters of $\text{Cu}_x\text{Mn}_{3-x}\text{O}_4$ spinels became smaller after doping with increased copper contents. The results also prove the above conclusions.

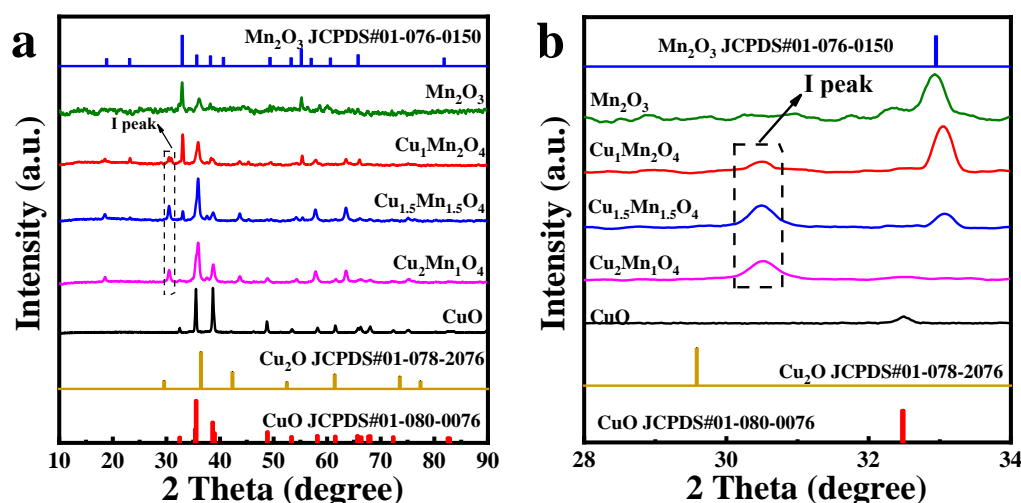


Figure 1. XRD patterns (a), local enlargement of (I) in XRD (b) of the as-synthesized $\text{Cu}_x\text{Mn}_{3-x}\text{O}_4$ samples.

Table 1. Crystal sizes, lattice parameters, actual molar ratios of Cu to Mn and BET surface areas of $\text{Cu}_x\text{Mn}_{3-x}\text{O}_4$.

Sample	Crystal Size nm	Lattice Parameter ^a nm	Actual Molar Ratios of Cu:Mn ^b	BET Surface Area $\text{m}^2 \text{g}^{-1}$ ^c
Mn_2O_3	63.07	$a = b = c = 0.9423$	-	18.2
$\text{Cu}_1\text{Mn}_2\text{O}_4$	42.69	$a = b = c = 0.8290$	0.93:2.05	18.9
$\text{Cu}_{1.5}\text{Mn}_{1.5}\text{O}_4$	31.79	$a = b = c = 0.8284$	1.46:1.54	19.7
$\text{Cu}_2\text{Mn}_1\text{O}_4$	31.76	$a = b = c = 0.8282$	1.97:1.02	18.7
CuO	42.43	$a = 0.4687, b = 0.3427,$ $c = 0.5135$	-	28.9

^a Calculated $2\theta = 33.0^\circ$ by the XRD patterns using the Debye–Scherrer equation. ^b Obtained by the ICP results. ^c Surface area derived from the BET equation.

2.2. N_2 Sorption Analysis of Catalysts

Figure 2 illustrates the obtained N_2 adsorption-desorption isotherm and pore size distribution of all the catalysts. The $\text{Cu}_x\text{Mn}_{3-x}\text{O}_4$ samples have type IV isotherms, which also proves that the samples possess a mesopores and significant macropores structure, and that the results of mesopores or macroporous foamy network structure are consistent with that of SEM. The low-pressure part of the near-linear middle part of the isotherm curve can be attributed to the unsaturated adsorption of single or multilayers, which also proves the existence of a macroporous structure. However, the hysteresis loops in the high p/p_0 range are related to capillary condensation in the mesopores, indicating that there are mesopores on the wall of the macropores. In addition, the corresponding Barrett–Joyner–Halenda (BJH) pore-size distribution curves in Figure 2b show that the $\text{Cu}_x\text{Mn}_{3-x}\text{O}_4$ samples have mesoporous and macroporous structures with a large distribution range of pore [32]. It should be pointed out that of the $\text{Cu}_{1.5}\text{Mn}_{1.5}\text{O}_4$ catalyst own the largest BET surface area and most mesoporous among the $\text{Cu}_x\text{Mn}_{3-x}\text{O}_4$ catalysts, Cu doping leads to the formation of more $\text{Cu}_{1.5}\text{Mn}_{1.5}\text{O}_4$ spinel structures, resulting in irregular changes in grain size. The specific surface areas of Cu–Mn spinel oxides with different Cu/Mn ratios are recorded in Table 1. The corresponding results conform to the XRD analysis of the catalysts.

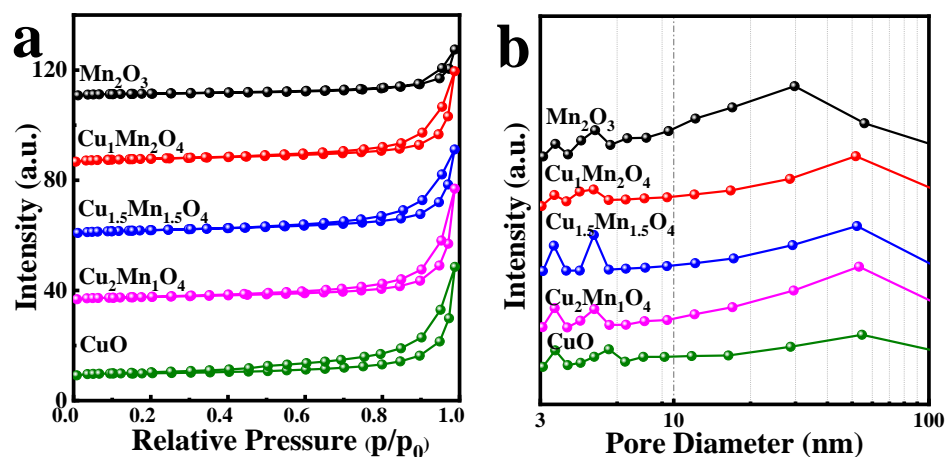


Figure 2. N_2 adsorption-desorption isotherms (a) and pore size distributions (b) of the as-synthesized $Cu_xMn_{3-x}O_4$ samples.

2.3. SEM and TEM Observation

The morphology and structural characteristics of the as-prepared catalysts at different molar ratios of Cu/Mn were characterized, as shown in Figure 3. Figure 3a,b show SEM images of pure Mn_2O_3 at different magnifications. The Mn_2O_3 sample is mainly composed of a foam structure with a diameter of 5–20 μm . The magnified SEM image further revealed that the surface of these particles had a hierarchical porous structure. In addition, with increasing Cu doping content, the surface of $Cu_xMn_{3-x}O_4$ catalyst particles becomes irregular, and the foam-like particles are broken into a uniform particle structure with a smaller particle size in Figure 3c–j. The mapping of $Cu_xMn_{3-x}O_4$ sample images is displayed in Figure 3k₁–k₄. It can be clearly observed that copper and manganese elements are uniformly dispersed on the entire catalyst surface.

Figure 4 shows the morphologies and microstructures of the $Cu_{1.5}Mn_{1.5}O_4$ catalyst at different magnifications. Combined with the SEM results, spherical nanoparticles with particle sizes ranging from 20 to 40 nm were formed in the $Cu_{1.5}Mn_{1.5}O_4$ sample. According to the equipped $Cu_{1.5}Mn_{1.5}O_4$ standard card (JCPDS#01-070-0260), the 0.48 and 0.25 nm lattice fringes can be matched to the (111) and (311) crystal planes of the $Cu_{1.5}Mn_{1.5}O_4$ spinel structure, respectively. It is worth noting that there was a strong synergistic interaction between Cu and Mn oxides in the active components of the spinel structure. Compared with $Cu_2Mn_1O_4$ spinel, $Cu_{1.5}Mn_{1.5}O_4$ has low crystallinity and can provide more oxygen vacancies, which may improve the catalytic performance of Cu-Mn catalysts in CO-SCR [30].

2.4. H_2 -TPR Analysis

The H_2 -TPR data of $Cu_xMn_{3-x}O_4$ samples are exhibited in Figure 5. Four peaks were observed on the Mn_2O_3 sample at 385, 466, 524 and 651 $^{\circ}C$, respectively. The relatively weak reduction peak at low temperature is due to the existence of surface species that can be easily reduced, that is, Mn_2O_3 is reduced to Mn_3O_4 . The strong reduction peak at high temperature can be attributed to the reduction of Mn_3O_4 to MnO , which is attributed to the manganese in the spinel phase. Mn_3O_4 is generally considered to consist of Mn^{2+} and Mn^{3+} . However, Mn^{4+} appears in the samples due to the equilibrium state of $2Mn^{3+} \rightleftharpoons Mn^{4+} + Mn^{2+}$. This phenomenon shows that the valence state of the Mn cation was complex in the Mn_3O_4 spinel, which may be of significance and be responsible for the completion of the catalytic cycle. For the $Cu_1Mn_2O_4$ spinel in Figure 5, there are only two well-defined reduction peaks at 298 and 351 $^{\circ}C$. The first reduction peak at 298 $^{\circ}C$ was attributed to the reduction of Cu^{2+} to Cu^+ , and the second reduction peak at 351 $^{\circ}C$ corresponded to the three reduction processes: the reduction of $Mn^{4+} \rightarrow Mn^{3+}$, $Mn^{3+} \rightarrow Mn^{2+}$ and $Cu^+ \rightarrow Cu^0$. The changes in the reduction peak number, reduction temperature and

peak intensity showed that there is electron transfer between Cu ions and Mn ions in the spinel lattice ($\text{Mn}^{3+} + \text{Cu}^{2+} \rightleftharpoons \text{Mn}^{4+} + \text{Cu}^+$), and the presence of the strong interaction between Cu and Mn could play a synergistic role in the reducibility of the catalysts, leading to the enhancement of the catalytic cycle in CO-SCR [29].

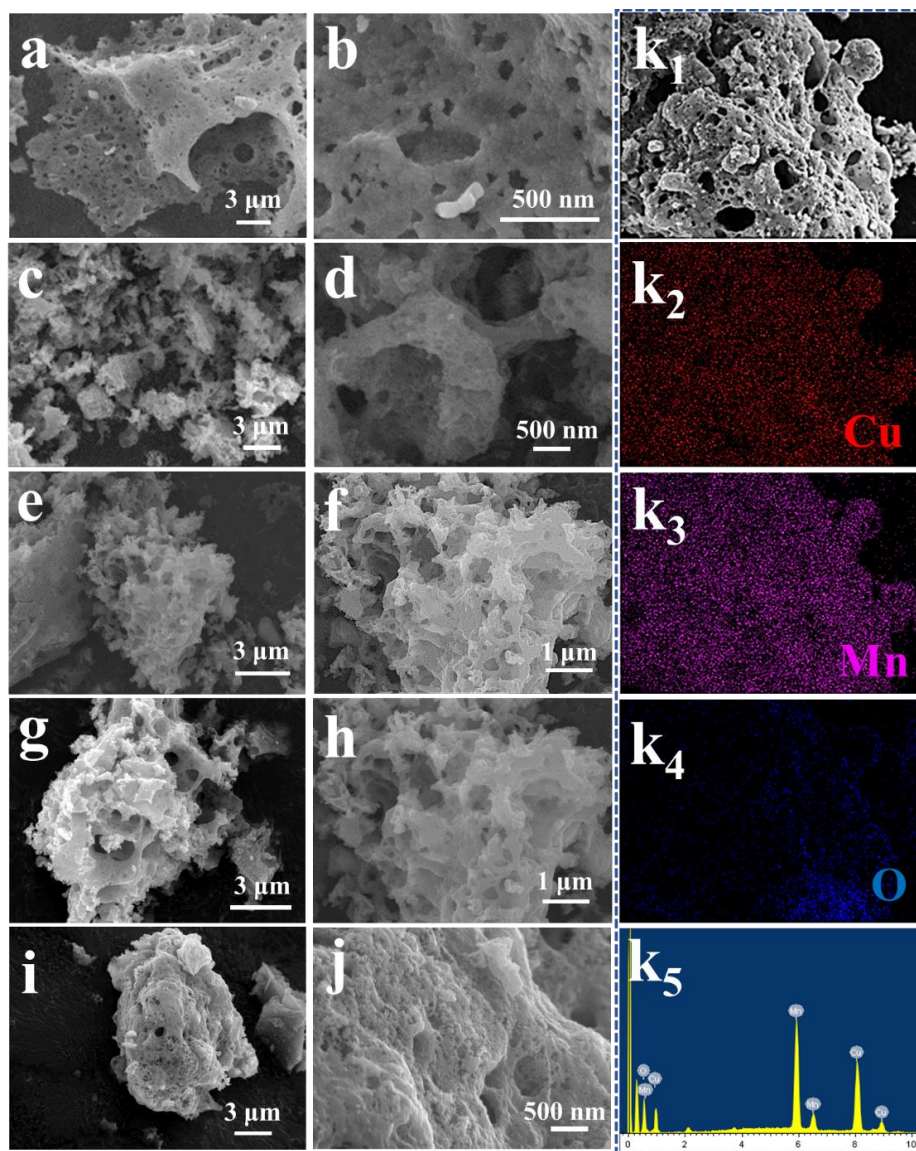


Figure 3. SEM images of Mn_2O_3 (a,b), $\text{Cu}_1\text{Mn}_2\text{O}_4$ (c,d), $\text{Cu}_{1.5}\text{Mn}_{1.5}\text{O}_4$ (e,f), $\text{Cu}_2\text{Mn}_1\text{O}_4$ (g,h) and CuO (i,j). Cu, Mn and O elemental mapping recordings from $\text{Cu}_{1.5}\text{Mn}_{1.5}\text{O}_4$ (k₁–k₄) and the EDS result (k₅).

For the $\text{Cu}_{1.5}\text{Mn}_{1.5}\text{O}_4$ sample, the low-temperature reduction peak reaches the same temperature (298 °C), and the high-temperature reduction peak moves to a lower temperature (342 °C). This phenomenon can be explained by the reduction in lattice distortion and the strong interaction between copper and manganese. Compared with $\text{Cu}_2\text{Mn}_1\text{O}_4$, the two reduction peaks of $\text{Cu}_2\text{Mn}_1\text{O}_4$ (at 299 and 328 °C) have shifted to lower values. It is noteworthy that as the Cu doping content increased, the low-temperature reduction peaks of all catalysts became stronger. These results indicate that the interaction between Cu and Mn is enhanced, and that the redox property is improved with an increasing Cu doping amount.

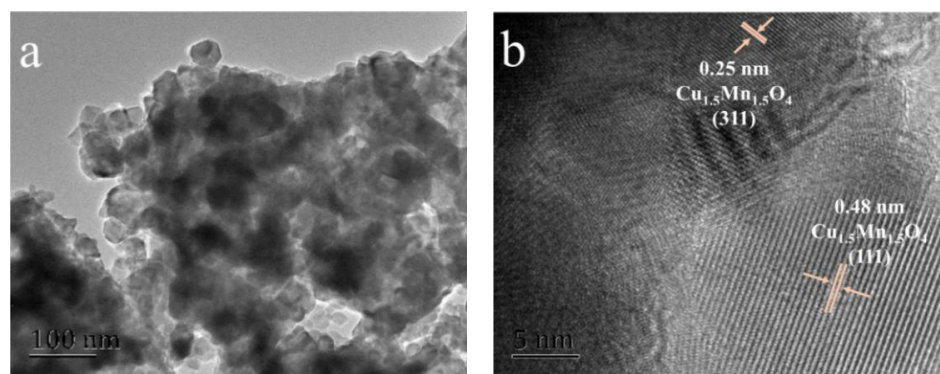


Figure 4. TEM image (a) and HRTEM image (b) of the $\text{Cu}_{1.5}\text{Mn}_{1.5}\text{O}_4$ sample.

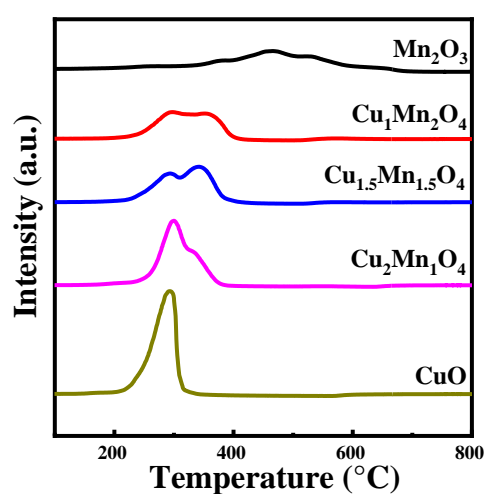


Figure 5. H_2 -TPR curves of the as-synthesized $\text{Cu}_x\text{Mn}_{3-x}\text{O}_4$ samples.

2.5. XPS Analysis

XPS was obtained on the $\text{Cu}_x\text{Mn}_{3-x}\text{O}_4$ sample, and the spectra of Cu 2p, Mn 2p and O 1s scans, as well as C from the reference, are shown in Figure 6a. The Cu 2p 3/2 spectra could be divided into two characteristic peaks attributed to Cu^+ (931.0 eV) and Cu^{2+} (934.1 eV) by performing peak-fitting deconvolutions, we can also see that accompanied by two distinct satellite peaks (marked by Sat.) at 938.2–945.9 and 959.7–964.7 eV in Figure 6b, which confirms the presence of Cu^{2+} . The content of $\text{Cu}^{+/0}$ of $\text{Cu}_{1.5}\text{Mn}_{1.5}\text{O}_4$ is the highest among the $\text{Cu}_x\text{Mn}_{3-x}\text{O}_4$. This result validated the existence of electron transfer between Cu ions and Mn ions ($\text{Mn}^{3+} + \text{Cu}^{2+} \rightleftharpoons \text{Mn}^{4+} + \text{Cu}^+$) in the $\text{Cu}_{1.5}\text{Mn}_{1.5}\text{O}_4$ spinel (Table 2). The spectra recorded from the $\text{Cu}_{1.5}\text{Mn}_{1.5}\text{O}_4$ sample consist of a broad spin-orbit double peak, indicating the presence of more than one Mn contribution. An obvious feature of this spectrum is that the high binding energy side of the main peaks 2p3/2 and 2p1/2 are obviously the Mn 2p3/2 spectra, and could be divided into three characteristic peaks attributed to Mn^{2+} (640.7 eV), Mn^{3+} (641.8 eV), and Mn^{4+} (643.9 eV), respectively (Figure 6c). The results show that the $\text{Cu}_{1.5}\text{Mn}_{1.5}\text{O}_4$ sample contains the highest content of Mn^{4+} ions (54.4%), which indicates that Cu replaces the low valence Mn cations and significantly promotes the formation of high valence Mn cations. This result support the TPR results. In other words, due to the strong interaction between manganese and copper oxide (Cu), there are some electronic interactions between Mn^{4+} and Cu^+ (Cu–O–Mn bridge). To study the different O species on the surface of the $\text{Cu}_x\text{Mn}_{3-x}\text{O}_4$ samples, the O 1s photoelectron spectra were obtained, as shown in Figure 6d. The deconvoluted peaks indicate that there are two different kinds of O species on the surface of the catalyst. The split peak at a lower binding energy of approximately 531.4 eV corresponds to lattice oxygen (denoted as O_α), and the other peak at approximately 529.5 eV is assigned to surface chemisorbed oxygen,

potentially including the chemisorbed oxygen O_2^{2-} or defective O^- (denoted as O_β). The doping of Cu leads to the partial substitution of Cu atoms for Mn atoms in the $-O-Mn-$ structure ($O-Cu$), which enhances the instability of O species and forms more active O species. This result is similar to the conclusion in the reported literature [30].

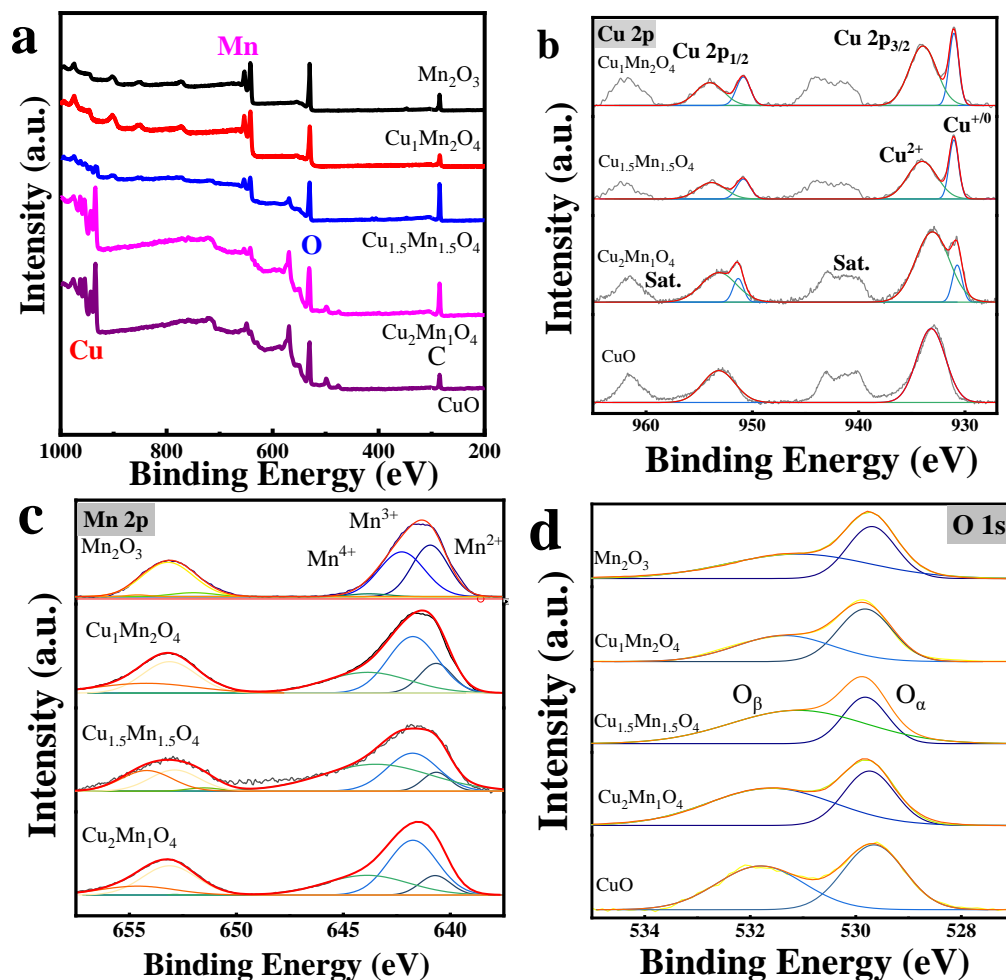


Figure 6. Survey spectra (a), Cu 2p (b), Mn 2p (c) and O 1s, (d) XPS spectra of $Cu_xMn_{3-x}O_4$ catalysts.

Table 2. XPS results of all the catalysts.

Sample	Mn ⁴⁺ /Mn	Mn ³⁺ /Mn	Mn ²⁺ /Mn	Cu ²⁺ /Cu	O _α /O	O _β /O
Mn ₂ O ₃	2.7	50.7	46.6	-	55.4	44.6
Cu ₁ Mn ₂ O ₄	31.6	50.8	17.6	70.1	53.1	46.9
Cu _{1.5} Mn _{1.5} O ₄	54.4	36.0	9.6	66.2	32.3	67.7
Cu ₂ Mn ₁ O ₄	33.4	54.4	12.2	86.7	37.5	62.5
CuO	-	-	-	100	51.1	48.9

3. Catalytic Performances of the Catalysts

3.1. Catalytic Reduction of NO with CO

In the temperature range 100–400 °C, the catalytic performance of the synthesized materials for the reduction of NO by CO is shown in Figure 7. It can be seen that pure Mn₂O₃ has CO-SCR catalytic activity, the NO conversion rate can reach 100% at a temperature of approximately 350 °C, and the CO conversion rate is the worst. It can be clearly found that the catalytic activity of all Cu-doped catalysts is significantly higher than that of manganese oxide catalysts in the test temperature range. The CO-SCR activities of the Cu_{1.5}Mn_{1.5}O₄ catalyst exhibited the best NO conversion when the temperature was below

200 °C. High-valence state spinel is the active component of the CO-SCR reaction, which is more conducive to showing better low-temperature activity, as reported in the literature. The CO conversion of the Cu-doped catalyst has a similar trend with the increase of temperature, and the CO conversion data are inconsistent with the NO conversion data above 200 °C, implying that CO reduced partial metal oxides in Figures 7c and S1 (consistent with the H₂-TPR result). From the CO catalytic activity results, it can be seen that the Cu-doped catalyst shows better catalytic activity than the pure Mn₂O₃ sample. The Cu₂Mn₁O₄ sample shows a higher CO catalytic oxidation activity, which suggests that excessive copper doping causes the adsorption of CO to be stronger than that of NO. This also implies that the Cu–O–Mn structure in spinel is the active site of CO-SCR (corresponding to the XRD results). The reaction of CO-SCR under O₂-rich conditions was performed to investigate the effect of O₂ on the catalytic performance. As shown in Figure S2, the NO conversion of the catalyst significantly decreased, and CO conversion increased with the increase of temperature. It can be found that the main reason affecting the NO conversion is the competitive reaction between CO and NO with O₂, resulting in the decline of performance. Improving the low-temperature catalytic performance of the catalyst under oxygen conditions will be the focus of our future research.

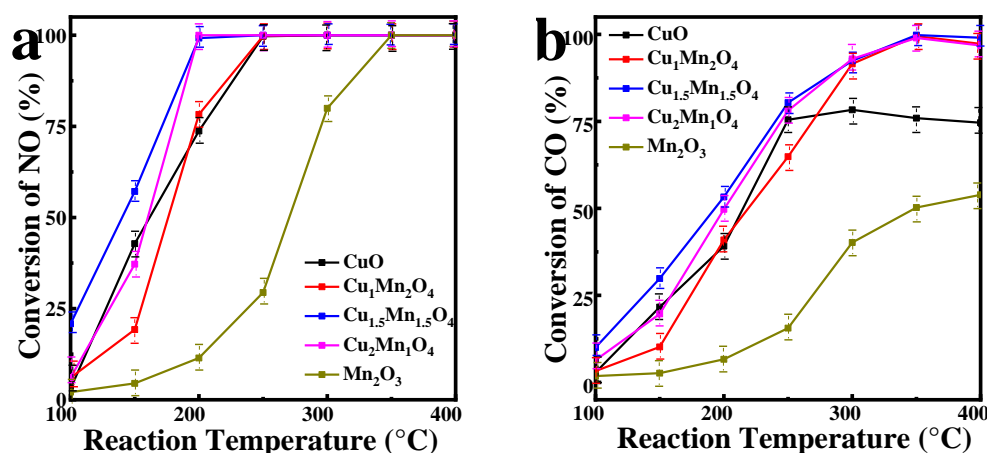


Figure 7. (a) NO conversion and (b) CO conversion of all the catalysts in the CO-SCR.

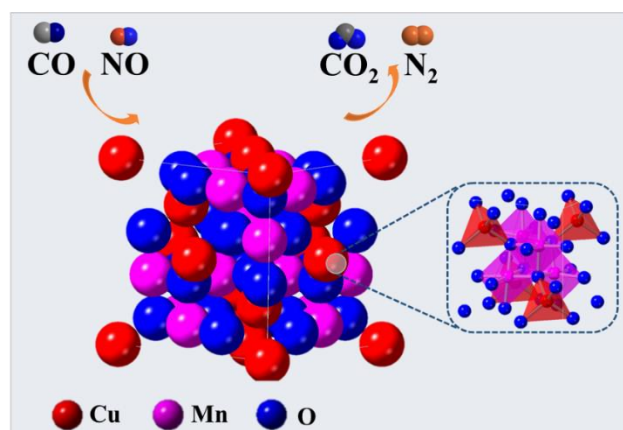
Therefore, Cu doping is conducive to the performance improvement of the Cu_xMn_{3-x}O₄ catalyst because there is a strong synergistic effect between the binary metal oxides. It is accepted that the active phase of spinel is the highly reactive center in the catalytic reaction process. The active phase of Cu_{1.5}Mn_{1.5}O₄ spinel plays an important role in the CO-SCR reaction, and the catalytic performance of the spinel structure catalyst is better than that of the other catalysts. The stability of this catalyst was further confirmed by the XRD (Figure S3a) and TEM analyses (Figure S3b,c), which showed no obvious change in the structure after the reaction at 400 °C.

3.2. Structure Activity Relationship and Catalytic Reaction Mechanism

According to reports, the active phase of Cu_xMn_{3-x}O₄ in the redox reaction is the Mn⁴⁺ concentration on the catalyst surface [30]. On Cu-Mn spinels, the number of surface-active sites and bulk concentration of Mn⁴⁺/Mn are critical to the reaction. At the same time, Cu²⁺ is transformed into Cu⁺, and Mn³⁺ is transformed into Mn⁴⁺. Mn⁴⁺ is considered to be a manganese species that has a passivation effect on the redox reaction. With the doping of copper ions in Mn₂O₃, the spinel structure with rich lattice defects and oxygen vacancies increases the concentration of Mn⁴⁺, which can adsorb reactant molecules and improve its redox performance, enhance the mobility of active oxygen species and enhance its catalytic activity. Therefore, compared with CuO and Mn₂O₃, the spinel-type copper-manganese composite oxide rich in Cu⁺ and Mn⁴⁺ will have a significantly improved activity. In

other words, due to the strong synergy between the binary metal oxides, copper doping is beneficial to the stability and catalytic performance of the $\text{Cu}_x\text{Mn}_{3-x}\text{O}_4$ catalyst.

Based on the above analysis, important information on the catalytic route was obtained, and a reasonable mechanism of the CO-SCR reaction on a $\text{Cu}_x\text{Mn}_{3-x}\text{O}_4$ catalyst was initially proposed. A proposed mechanism of the two processes is shown in Scheme 1: (i) CO and NO molecules are the first adsorbed oxygen vacancies, Mn^{4+} and Cu^{+} on the catalyst surface. In this process, the reactant molecules CO and NO are adsorbed as CO (ads) and NO (ads). Subsequently, CO (ads) reacts with the active oxygen on the catalyst to produce CO_2 . (ii) NO molecules are adsorbed on the catalyst surface oxygen vacancy, the oxygen O of NO reacts with the oxygen vacancy, and nitrogen gas is generated. Herein, the redox cycle occurs between bimetallic oxide components ($\text{Cu}^{2+} + \text{Mn}^{3+} \rightleftharpoons \text{Cu}^{+} + \text{Mn}^{4+}$) in the $\text{Cu}_x\text{Mn}_{3-x}\text{O}_4$ spinels, and the Cu^{+} and Mn^{4+} formed by this interaction distorts the spinel structure and promotes the generation of more surface vacancies; that is, it is conducive to the activation of reactants CO and NO and forms more active species and improves the catalytic performance for CO-SCR of the catalysts.



Scheme 1. Schematic illustration of the proposed mechanism for the catalytic CO-SCR over $\text{Cu}_x\text{Mn}_{3-x}\text{O}_4$ catalysts.

4. Experimental

4.1. Material Synthesis

Specifically, $\text{Cu}_x\text{Mn}_{3-x}\text{O}_4$ ($x = 0, 1, 1.5, 2, 3$) spinels were prepared by a citrate-based modified pechini method [33–35]. $\text{Cu}(\text{NO}_3)_2 \cdot 3\text{H}_2\text{O}$ (Sinopharm Chemical Reagent Co., Ltd., Beijing, China, $\geq 99.0\%$) and $\text{Mn}(\text{NO}_3)_2$ solution (Macklin, 50% in H_2O) were dissolved in deionized water. In the calculated amount of copper nitrate trihydrate and 50% manganenitrate solution (Table 3), citric acid monohydrate (Xilong Chemical Co., Ltd., Guangzhou, China, $\geq 99.5\%$) was added at a molar ratio of 1:1 (Cu+Mn/citric acid). The solution was stirred for 2 h at room temperature to obtain a homogeneous mixture and then evaporated to obtain a sticky gel. The gel was dried in a 120 °C oven for 6 h, forming a foam metal citrate complex. Finally, the samples were calcined in 600 °C air for 8 h to form spinel oxides.

Table 3. The chemicals and their amounts used for preparing samples.

Sample	$\text{Cu}(\text{NO}_3)_2 \cdot 3\text{H}_2\text{O}$ (g)	50% $\text{Mn}(\text{NO}_3)_2$ Solution (g)	Citric Acid Monohydrate (g)
Mn_2O_3	-	23.4	11.7
$\text{Cu}_1\text{Mn}_2\text{O}_4$	5.1	15.0	11.7
$\text{Cu}_{1.5}\text{Mn}_{1.5}\text{O}_4$	7.5	11.1	11.7
$\text{Cu}_2\text{Mn}_{1.5}\text{O}_4$	9.8	7.3	11.7
CuO	15.1	-	11.7

4.2. Characterization

The powder samples were characterized by XRD with the use of a PANalytica X'Pert PRO MPD diffractometer using Cu K α radiation ($\lambda = 0.154$ nm, 40 kV, 40 mA). The crystallite sizes of all samples were calculated using the Debye–Scherrer equation. The morphology of the particles was analyzed with a JSM-7001F field-emission SEM with energy-dispersive spectroscopy (EDS) (INCA X-MAX, JEOL, Oxford, UK) and TEM (JEM-2010F, JEOL, Tokyo, Japan). The reducibility of the catalysts was examined by H₂-TPR using a Quantachrome automated chemisorption analyzer (Chem BET pulsar TPR/TPD). Briefly, 50 mg of sample was loaded into a quartz U-tube and heated from room temperature to 150 °C at 10 °C min⁻¹ under helium flow to remove moisture and impurities. Then, the sample was cooled to room temperature, followed by heating to 800 °C at a heating rate of 10 °C min⁻¹ under a binary gas mixture (10 vol.% H₂/Ar) with a gas flow rate of 30 mL min⁻¹. H₂ consumption was detected continuously as a function of increasing temperature using a thermal conductivity detector (TCD). The BETs were determined using N₂ physisorption at -196 °C using Quantachrome NOVA 3200e equipment. Prior to N₂ adsorption, each catalyst was degassed for 2 h under vacuum at 200 °C. The surface chemical composition was determined by XPS (Model VG ESCALAB 250 spectrometer, Thermo Electron, London, UK) using non-monochromatized Al K α X-ray radiation ($h\nu = 1486.6$ eV).

4.3. Measurement

The evaluation of the catalyst was carried out with a typical fixed-bed reactor with a quartz tube (8 mm inner diameter). Two grams of the catalysts (particle size was 20–40 mesh) were used in quartz tubes between glass wool. The catalytic activity was measured using feed gas compositions of 1000 ppm NO, 2000 ppm CO and N₂ (the balance) at different temperatures at a rate of 30,000 h⁻¹. First, the catalysts were treated using a CO/N₂ gas flow at 200 °C for 1 h before each test. After the catalysts were cooled to room temperature under a N₂ flow, they were allowed to react with the mixed gas. The CO, NO and NO₂ concentrations were monitored using a Testo 350 flue gas analyzer. The catalytic activity was calculated using the following formula:

$$\text{NO conversion (\%)} = \frac{\text{NO}_{\text{in}} - \text{NO}_{\text{out}}}{\text{NO}_{\text{in}}} \times 100\% \quad (1)$$

$$\text{CO conversion (\%)} = \frac{\text{CO}_{\text{in}} - \text{CO}_{\text{out}}}{\text{CO}_{\text{in}}} \times 100\% \quad (2)$$

where the “in” and “out” subscripts indicate the inlet and outlet concentrations of NO and CO in the steady state, respectively. The selectivity of N₂ was not calculated here due to NO₂ being detected at the outlet.

5. Conclusions

In this work, a series of Cu_xMn_{3-x}O₄ spinels were synthesized by the citrate-based modified pechini method. The results show that controlling the doping amount of Cu can improve the low-temperature activity of the Mn₂O₃ catalyst. Doping Cu species could shift the redox balance in the catalyst system (Cu²⁺ + Mn³⁺ \rightleftharpoons Mn⁴⁺ + Cu⁺), improve the redox performance and catalytic activity of manganese oxide catalyst, and promote the grain formation and growth of the Cu_{1.5}Mn_{1.5}O₄ spinel structure instead of manganese oxides to increase the surface area and particle size. The surface of Cu_{1.5}Mn_{1.5}O₄ spinels retained a high ratio of Mn⁴⁺/Mn, more reactive oxygen species were formed than pure Mn₂O₃ on the surface to promote the adsorption of oxygen molecules, and it enhanced the adsorption capacity of CO and NO. In general, the doping of low valence state Cu significantly enhanced the CO–SCR activity of Cu_xMn_{3-x}O₄ spinels at low temperature, which could be an effective way to design and synthesize highly active Mn–based CO-SCR catalysts.

Supplementary Materials: The following supporting information can be downloaded at: <https://www.mdpi.com/article/10.3390/catal12060591/s1>, Figure S1: CO conversion of Cu_{1.5}Mn_{1.5}O₄ catalyst in the CO-SCR (Reaction conditions: [CO] = 2000 ppm and N₂ as balance gas, GHSV = 30,000 h⁻¹); Figure S2: (a) NO conversion; (b) N₂ selectivity in CO-SCR reaction (Reaction conditions: [NO] = 1000 ppm, [CO] = 2000 ppm, [O₂] = 0 or 1%, and N₂ as balance gas, GHSV = 30,000 h⁻¹); Figure S3: (a) XRD patterns, and (b,c) TEM images of the catalyst of Cu_{1.5}Mn_{1.5}O₄ after reaction.

Author Contributions: Conceptualization, F.F.; data curation, F.F. and L.W. (Lingjuan Wang); formal analysis, F.F., L.W. (Lingjuan Wang) and L.W. (Lei Wang); methodology, F.F. and M.W.; project administration, J.L.; writing—original draft, F.F. and M.W.; writing—review and editing, F.F., M.W. and J.L.; funding acquisition, F.F. and J.L. All authors have read and agreed to the published version of the manuscript.

Funding: This research was funded by the Chengde Science and Technology Research and Development Project (202006A117), School-level Youth Fund Project (QN2021001), the Scientific Research Project of the Higher Education Institutions of Hebei Province (ZD2021413) and the School-level teaching reform project (JG-202021571).

Data Availability Statement: Data are available from the corresponding author on request.

Conflicts of Interest: The authors declare no conflict of interest.


References

- Liu, K.; Yu, Q.; Liu, J.; Wang, K.; Han, Z.; Xuan, Y.; Qin, Q. Selection of catalytically active elements for removing NO and CO from flue gas at low temperatures. *New J. Chem.* **2017**, *41*, 13993–13999. [CrossRef]
- Qin, Y.; Fan, S.; Li, X.; Gan, G.; Wang, L.; Yin, Z.; Guo, X.; Tadé, M.O.; Liu, S. Peanut-shaped Cu–Mn nano-hollow spinel with oxygen vacancies as catalysts for low-temperature NO reduction by CO. *ACS Appl. Nano Mater.* **2021**, *4*, 11969–11979. [CrossRef]
- Li, S.; Chen, X.; Wang, F.; Xie, Z.; Hao, Z.; Liu, L.; Shen, B. Promotion effect of Ni doping on the oxygen resistance property of Fe/CeO₂ catalyst for CO-SCR reaction: Activity test and mechanism investigation. *J. Hazard. Mater.* **2022**, *431*, 128622. [CrossRef] [PubMed]
- Roy, S.; Hegde, M.; Madras, G. Catalysis for NO_x abatement. *Appl. Energy* **2009**, *86*, 2283–2297. [CrossRef]
- Fernandez, E.; Liu, L.; Boronat, M.; Arenal, R.; Concepcion, P.; Corma, A. Low-temperature catalytic NO reduction with CO by subnanometric Pt clusters. *ACS Catal.* **2019**, *9*, 11530–11541. [CrossRef]
- Hu, Y.; Dong, L.; Shen, M.; Liu, D.; Wang, J.; Ding, W.; Chen, Y. Influence of supports on the activities of copper oxide species in the low-temperature NO+CO reaction. *Appl. Catal. B* **2001**, *31*, 61–69. [CrossRef]
- Ilieva, L.; Pantaleo, G.; Velinov, N.; Tabakova, T.; Petrova, P.; Ivanov, L.; Avdeev, G.; Paneva, D.; Venezia, A. NO reduction by CO over gold catalysts supported on Fe-loaded ceria. *Appl. Catal. B* **2015**, *174*, 176–184. [CrossRef]
- Zhang, S.; Shan, J.; Zhu, Y.; Nguyen, L.; Huang, W.; Yoshida, H.; Takeda, S.; Tao, F. Restructuring transition metal oxide nanorods for 100% selectivity in reduction of nitric oxide with carbon monoxide. *Nano Lett.* **2013**, *13*, 3310–3314. [CrossRef]
- Wang, X.; Li, X.; Mu, J.; Fan, S.; Chen, X.; Wang, L.; Yin, Z.; Tade, M.; Liu, S. Oxygen vacancy-rich porous Co₃O₄ nanosheets toward boosted NO reduction by CO and CO oxidation: Insights into the structure-activity relationship and performance enhancement mechanism. *ACS Appl. Mater. Interfaces* **2019**, *11*, 41988–41999. [CrossRef]
- Lima, T.; Pereira, C.; Castelblanco, W.; Santos, B.; Silva, S.; Santana, R.; González, U.; Sartoratto, C. Zirconia-supported cobalt catalysts: Activity and selectivity in NO reduction by CO. *Chem. Select* **2017**, *2*, 11565–11573.
- Salker, A.; Desai, M. Catalytic activity and mechanistic approach of NO reduction by CO over M_{0.05}Co_{2.95}O₄ (M = Rh, Pd & Ru) spinel system. *Appl. Surf. Sci.* **2016**, *389*, 344–353.
- Liu, L.; Yao, Z.; Deng, Y.; Gao, F.; Liu, B.; Dong, L. Morphology and crystal-plane effects of nanoscale ceria on the activity of CuO/CeO₂ for NO reduction by CO. *ChemCatChem* **2011**, *3*, 978–989. [CrossRef]
- Wang, Y.; Zhang, L.; Li, R.; He, H.; Huang, L. MOFs-based coating derived Me-ZIF-67@CuO_x materials as low-temperature NO-CO catalysts. *Chem. Eng. J.* **2019**, *381*, 122757. [CrossRef]
- Xiaoyuan, J.; Guanghui, D.; Liping, L.; Yingxu, C.; Xiaoming, Z. Catalytic activities of CuO/TiO₂ and CuO-ZrO₂/TiO₂ in NO+CO reaction. *J. Mol. Catal. A Chem.* **2004**, *218*, 187–195. [CrossRef]
- Boningari, T.; Pavani, S.; Ettireddy, P.; Chuang, S.; Smirniotis, P. Mechanistic investigations on NO reduction with CO over Mn/TiO₂ catalyst at low temperatures. *Mol. Catal.* **2017**, *451*, 33–42. [CrossRef]
- Shan, J.; Zhu, Y.; Zhang, S.; Zhu, T.; Rouvimov, S.; Tao, F. Catalytic Performance and in Situ Surface Chemistry of Pure α-MnO₂ Nanorods in Selective Reduction of NO and N₂O with CO. *J. Phys. Chem. C* **2013**, *117*, 8329–8335. [CrossRef]
- Deng, C.; Li, B.; Dong, L.; Zhang, F.; Fan, M.; Jin, G.; Gao, J.; Gao, L.; Zhang, F. NO reduction by CO over CuO supported on CeO₂-doped TiO₂: The effect of the amount of a few CeO₂. *Phys. Chem.* **2015**, *17*, 16092–16109. [CrossRef]
- Li, Y.; Wan, Y.; Li, Y.; Zhan, S.; Guan, Q.; Tian, Y. Low-temperature selective catalytic reduction of NO with NH₃ over Mn_{(2)O₍₃₎}-Doped Fe_{(2)O₍₃₎} hexagonal microsheets. *ACS Appl. Mater. Interfaces* **2016**, *8*, 5224–5233. [CrossRef]

19. Liu, J.; Wei, Y.; Li, P.; Zhang, P.; Su, W.; Sun, Y.; Zou, R.; Zhao, Y. Experimental and theoretical investigation of mesoporous MnO₂ nanosheets with oxygen vacancies for high-efficiency catalytic deNO_x. *ACS Catal.* **2018**, *8*, 3865–3874. [CrossRef]
20. Pan, K.; Young, C.; Pan, G.; Chang, M. Catalytic reduction of NO by CO with Cu-based and Mn-based catalysts. *Catal. Today* **2020**, *348*, 15–25. [CrossRef]
21. Yao, X.; Xiong, Y.; Sun, J.; Gao, F.; Deng, Y.; Tang, C.; Dong, L. Influence of MnO₂ modification methods on the catalytic performance of CuO/CeO₂ for NO reduction by CO. *J. Rare Earths* **2014**, *32*, 131–138. [CrossRef]
22. Li, D.; Yu, Q.; Li, S.; Wan, H.; Liu, L.; Qi, J.; Liu, L.; Gao, F.; Dong, L.; Chen, Y. The remarkable enhancement of CO-pretreated CuO-Mn₂O₃/gamma-Al₂O₃ supported catalyst for the reduction of NO with CO: The formation of surface synergetic oxygen vacancy. *Chem. A Eur. J.* **2011**, *17*, 5668–5679. [CrossRef] [PubMed]
23. Wang, X.; Lu, Y.; Tan, W.; Liu, A.; Ji, J.; Wan, H.; Sun, C.; Tang, C.; Dong, L. Insights into the precursor effect on the surface structure of gamma-Al₂O₃ and NO+CO catalytic performance of CO-pretreated CuO/MnO_x/gamma-Al₂O₃ catalysts. *J. Colloid Interface Sci.* **2019**, *554*, 611–618. [CrossRef] [PubMed]
24. Spassova, I.; Khristova, M.; Panayotov, D.; Mehandjiev, D. Coprecipitated CuO–MnO_x catalysts for low-temperature CO–NO and CO–NO–O₂ reactions. *J. Catal.* **1999**, *185*, 43–57. [CrossRef]
25. Li, L.; Wang, Y.; Zhang, L.; Yu, Y.; He, H. Low-temperature selective catalytic reduction of NO_x on MnO₂ octahedral molecular sieves (OMS-2) doped with Co. *Catalysts* **2020**, *10*, 396. [CrossRef]
26. Shi, Y.; Chu, Q.; Xiong, W.; Gao, J.; Ding, Y. A new type bimetallic NiMn-MOF-74 as an efficient low-temperatures catalyst for selective catalytic reduction of NO by CO. *Chem. Eng. Process.* **2020**, *159*, 108232. [CrossRef]
27. Yi, Y.; Liu, H.; Chu, B.; Qin, Z.; Dong, L.; He, H.; Tang, C.; Fan, M.; Bin, L. Catalytic removal NO by CO over LaNi_{0.5}M_{0.5}O₃ (M = Co, Mn, Cu) perovskite oxide catalysts: Tune surface chemical composition to improve N₂ selectivity. *Chem. Eng. J.* **2019**, *369*, 511–521. [CrossRef]
28. Shi, X.; Chu, B.; Wang, F.; Wei, X.; Teng, L.; Fan, M.; Li, B.; Dong, L. Mn-Modified CuO, CuFe₂O₄, and γ-Fe₂O₃ Three-phase strong synergistic coexistence catalyst system for NO reduction by CO with a wider active window. *ACS Appl. Mater. Interfaces* **2018**, *10*, 40509–40522. [CrossRef]
29. Wan, H.; Li, D.; Dai, Y.; Hu, Y.; Liu, B.; Dong, L. Catalytic behaviors of CuO supported on Mn₂O₃ modified γ-Al₂O₃ for NO reduction by CO. *J. Mol. Catal. A Chem.* **2010**, *332*, 32–44. [CrossRef]
30. Liu, T.; Yao, Y.; Wei, L.; Shi, Z.; Han, L.; Yuan, H.; Li, B.; Dong, L.; Wang, F.; Sun, C. Preparation and evaluation of copper-manganese oxide as a high-efficiency catalyst for CO oxidation and NO reduction by CO. *J. Phys. Chem. C.* **2017**, *121*, 12757–12770. [CrossRef]
31. Li, J.; Zhang, W.; Li, C.; He, C. Efficient catalytic degradation of toluene at a readily prepared Mn-Cu catalyst: Catalytic performance and reaction pathway. *J. Colloid Interface Sci.* **2021**, *591*, 396–408. [CrossRef] [PubMed]
32. Zhang, L.; Shi, L.; Huang, L.; Zhang, J.; Gao, R.; Zhang, D. Rational design of high-performance seNO_x catalysts based on Mn_xCo_{3-x}O₄ nanocages derived from metal-organic frameworks. *ACS Catal.* **2014**, *4*, 1753–1763. [CrossRef]
33. Salker, A.V.; Desai, M. CO-NO/O₂ redox reactions over Cu substituted cobalt oxide spinels. *Catal. Commun.* **2016**, *87*, 116–119. [CrossRef]
34. Salker, A.; Desai, M. Low-temperature nitric oxide reduction over silver-substituted cobalt oxide spinels. *Catal. Sci. Technol.* **2016**, *6*, 430–433. [CrossRef]
35. Liu, S.; Ji, Y.; Xu, W.; Zhang, J.; Jiang, R.; Li, L.; Jia, L.; Zhong, Z.; Xu, G.; Zhu, T.; et al. Hierarchically interconnected porous Mn_xCo_{3-x}O₄ spinels for low-temperature catalytic reduction of NO by CO. *J. Catal.* **2022**, *406*, 72–86. [CrossRef]

Article

Metal-Organic Frameworks Decorated Cu₂O Heterogeneous Catalysts for Selective Oxidation of Styrene

Mengyi Han ^{1,2,†}, Xue Tang ^{1,2,†}, Peng Wang ^{1,2}, Zhiyong Zhao ^{1,2}, Xiaohua Ba ¹, Yu Jiang ¹ and Xiaowei Zhang ^{1,*} 

¹ Institute of Advanced Materials, Beijing Normal University, Beijing 100875, China; myhan0310@163.com (M.H.); 201921220017@mail.bnu.edu.cn (X.T.); wang_peng0119@163.com (P.W.); zhiyongbnu@163.com (Z.Z.); 201821150005@mail.bnu.edu.cn (X.B.); 11112018029@bnu.edu.cn (Y.J.)

² College of Nuclear Science and Technology, Beijing Normal University, Beijing 100875, China

* Correspondence: xiaoweizhang@bnu.edu.cn; Tel.: +86-10-5880-6227

† These authors contributed equally to this work.

Abstract: The selective oxidation of styrene with highly efficient, environmentally benign, and cost-effective catalysts are of great importance for sustainable chemical processes. Here, we develop an in situ self-assembly strategy to decorate Cu-based metal-organic framework (MOF) Cu-BDC-NH₂ nanocrystals on Cu₂O octahedra to construct a series of Cu₂O@Cu-BDC-NH₂ catalysts for selective oxidation of styrene. Using H₂O₂ as green oxidants, the optimized sample of Cu₂O@Cu-BDC-NH₂-8h could achieve 85% styrene conversion with 76% selectivity of benzaldehyde under a mild condition of 40 °C. The high performance of the as-prepared heterogeneous catalysts was attributed to the well-designed Cu⁺/Cu²⁺ interface between Cu₂O and Cu-BDC-NH₂ as well as the porous MOF shells composed of the uniformly dispersed Cu-BDC-NH₂ nanocrystals. The alkaline properties of Cu₂O and the -NH₂ modification of MOFs enable the reaction to be carried out in a base-free condition, which simplifies the separation process and makes the catalytic system more environmentally friendly. Besides the Cu₂O octahedra (od-Cu₂O), the Cu₂O cuboctahedrons (cod-Cu₂O) were synthesized by adjusting the added polyvinyl pyrrolidone, and the obtained cod-Cu₂O@Cu-BDC-NH₂ composite also showed good catalytic performance. This work provides a useful strategy for developing highly efficient and environmentally benign heterogeneous catalysts for the selective oxidation of styrene.

Keywords: metal-organic frameworks; Cu₂O; styrene oxidation; H₂O₂; base free



Citation: Han, M.; Tang, X.; Wang, P.; Zhao, Z.; Ba, X.; Jiang, Y.; Zhang, X. Metal-Organic Frameworks Decorated Cu₂O Heterogeneous Catalysts for Selective Oxidation of Styrene. *Catalysts* **2022**, *12*, 487. <https://doi.org/10.3390/catal12050487>

Academic Editors: Carolina Belver and Jorge Bedia

Received: 27 March 2022

Accepted: 25 April 2022

Published: 26 April 2022

Publisher's Note: MDPI stays neutral with regard to jurisdictional claims in published maps and institutional affiliations.



Copyright: © 2022 by the authors. Licensee MDPI, Basel, Switzerland. This article is an open access article distributed under the terms and conditions of the Creative Commons Attribution (CC BY) license (<https://creativecommons.org/licenses/by/4.0/>).

1. Introduction

Benzaldehyde, as a vital intermediate and starting material, has been widely used in fine chemical industries such as pharmaceuticals, dyes, spices, and pesticides [1,2]. Conventional techniques for benzaldehyde production (e.g., oxidation of toluene) usually involve harsh conditions and complex synthesis processes, which leads to great energy consumption and serious environmental pollution [3–5]. Considering the sustainable development of the chemical industry, the selective oxidation of styrene to benzaldehyde by using environmentally benign catalysts and green oxidants becomes an ideal choice [6,7]. Hydrogen peroxide (H₂O₂) has been widely studied as one of the green oxidants due to its low price and environmentally-friendly property [8]. The H₂O₂ catalytic system usually generates benzaldehyde, accompanied with styrene oxide, and the acidity of H₂O₂ easily leads to the isomerization of styrene oxide into phenylacetaldehyde, which further decreases the selectivity of benzaldehyde [9–11]. Some basic additives (e.g., NaOH, NaHCO₃) are often introduced into the reaction system to function as a buffer to improve the selectivity of the target product [10–12]. However, the added alkaline species have difficulties in separation from the reaction system, which is not beneficial for a sustainable chemical process. Thus, it is of great significance to develop highly efficient and environmentally benign heterogeneous catalysts with suitable alkalinity for the selective oxidation of styrene under base-free conditions.

Recently, transition metal-based materials such as Mg/CTAB [13], SO_4^{2-} -Fe-V/ ZrO_2 [14], CuCr-MMO [12], NiCo_2O_4 [15], and $\text{CoFe}_2\text{O}_4/\text{TiO}_2$ [3] have been explored as novel heterogeneous catalysts for styrene oxidation under a base-free catalytic system. However, the relatively low specific surface area, low porosity, and weak alkalinity of these catalysts is not conducive to the adsorption of oxidants as well as the diffusion of the substrates and products, thus limiting the improvement in their catalytic performance. As types of environmentally-friendly and Earth-abundant materials with easy availability and low costs, Cu_2O and/or CuO with high alkalinity and easily controlled morphology have attracted great interest and show efficient catalytic activity in several chemical reaction processes [16–18]. However, the insufficient stability of $\text{Cu}_2\text{O}/\text{CuO}$ severely limits its practical application. In order to overcome this obstacle, many methods have been proposed to encapsulate $\text{Cu}_2\text{O}/\text{CuO}$ into porous materials or construct core-shell structures [19,20]. In particular, metal-organic frameworks (MOFs) have attracted immense attention due to their tunable structures, high porosity, and highly accessible active sites [21–26]. Among them, Cu-based MOFs such as Cu-BDC (BDC = 1,4-benzenedicarboxylate) have been widely investigated and shown excellent performance in a variety of catalytic reactions [27–30].

In this study, an in situ self-assembly strategy was developed to decorate Cu-based MOF (Cu-BDC- NH_2) nanocrystals on Cu_2O octahedra and cuboctahedrons for selective oxidation of styrene to benzaldehyde. The obtained $\text{Cu}_2\text{O}@$ Cu-BDC- NH_2 catalysts exhibited a highly catalytic performance with H_2O_2 as green oxidants. The basicity of Cu_2O and the introduction of the $-\text{NH}_2$ group can effectively inhibit the excessive oxidation of reaction products and enable the reaction to be carried out under a base-free condition. The Cu-BDC- NH_2 MOFs nanocrystals coated outside of Cu_2O can effectively enrich the specific surface area and porosity of the catalyst, which is conducive to the adsorption of oxidants and accelerate the reaction process. The well-designed $\text{Cu}^+/\text{Cu}^{2+}$ interface and the synergistic effects between Cu_2O and Cu-BDC- NH_2 have contributed to the enhancement of styrene conversion and benzaldehyde selectivity. In addition, a series of $\text{Cu}_2\text{O}@$ Cu-BDC- NH_2 with different MOF loadings and different Cu_2O crystal phases were prepared, and the relationship between their morphology, composition, and structure and the catalytic performance was systematically investigated. Our work provides new perspectives for the development of a cost-effective, highly-efficient, and environmentally benign heterogeneous catalyst for the selective oxidation of styrene under mild conditions.

2. Results and Discussion

2.1. Synthesis and Structural Characterization

The synthetic process of $\text{Cu}_2\text{O}@$ Cu-BDC- NH_2 is illustrated in Scheme 1. First, Cu_2O was prepared via a facile wet chemical method, in which the ascorbic acid acts as a reducing agent for the reduction of Cu^{2+} to Cu^+ in the presence of NaOH [31,32]. The added PVP in the formation process of Cu_2O serves as the stabilizing and capping agent, which can enable the uniform distribution of Cu^{2+} ions and preferentially adsorb on the {111} plane of Cu_2O through the interaction between the O atoms in PVP and the Cu ions on Cu_2O [33,34]. The morphology of Cu_2O can be precisely controlled by adjusting the amount and the molecular weight of the added PVP [33–35]. The $\text{Cu}_2\text{O}@$ Cu-BDC- NH_2 composite was prepared by an in situ assembly method, in which the as-prepared Cu_2O serves as the substrate and Cu resource to interact with the added ligands of $\text{H}_2\text{BDC-}\text{NH}_2$ for the in situ growth of Cu-BDC- NH_2 on the surface of Cu_2O . It is worth noting that only ligands, but no additional copper salts, are needed in the preparation process. In addition, the morphology and structure of the $\text{Cu}_2\text{O}@$ Cu-BDC- NH_2 composites can be adjusted by controlling the reaction time of in situ assembly.



Scheme 1. The illustration of the synthetic process from Cu₂O toward Cu₂O@Cu-BDC-NH₂ for the selective oxidation of styrene with H₂O₂ as green oxidants.

The morphological and structural properties of the as-prepared materials were demonstrated by scanning electron microscopy (SEM) and X-ray diffraction (XRD). As shown in Figure 1a, when PVP with a molecular weight of 58,000 was used as the raw material, the as-prepared Cu₂O showed an octahedral morphology with a very smooth surface and an average particle size of about 1–2 μm. The XRD patterns of the as-prepared octahedron microcrystals (Figure 2a, red curve) confirmed the Cu₂O structure, and the (111) diffraction peak of Cu₂O showed a much stronger intensity over other peaks, indicating that the octahedron Cu₂O exclusively exposes {111} planes, agreeing with previous reports [16–18,33–35]. The in situ growth of Cu-BDC-NH₂ on Cu₂O was systematically investigated by SEM (Figure 1b–f) and XRD (Figure 2a) to reveal the morphology–structure relationship of the Cu₂O@Cu-BDC-NH₂ composites. As shown in Figure 1b, when Cu₂O reacted with H₂BDC-NH₂ ligands for 4 h, the obtained Cu₂O@Cu-BDC-NH₂-4h sample exhibited a rougher surface covered with lots of nanoparticles, but no obvious change was observed in its XRD patterns (Figure 2a, blue curve). As the growth time was extended to 8 h, a much rougher surface of Cu₂O@Cu-BDC-NH₂-8h was observed (Figure 1c), indicating an increase in the number and size of nanoparticles covered on the surface of Cu₂O. The XRD patterns of Cu₂O@Cu-BDC-NH₂-8h (Figure 2a, yellow curves) showed newly emerged characteristic peaks at 10°, 17°, and 25°, which were assigned to the diffraction peaks of (110), (20-1), and (131) planes of Cu-BDC-NH₂ [33], indicating the gradual formation of the Cu-BDC-NH₂. After the in situ growth of Cu-BDC-NH₂ on Cu₂O for 12 h, 20 h, and 32 h, as shown in Figure 1d–f, the Cu₂O@Cu-BDC-NH₂ composites exhibited a smaller Cu₂O octahedron around with assembled nanosheets, and the corresponding XRD patterns presented enhanced peak intensity of Cu-BDC-NH₂ (Figure 2a). The morphological and structural changes during the in situ growth process of Cu₂O@Cu-BDC-NH₂ indicate that Cu₂O serves as the substrate and source of the Cu ions in the following growth of Cu-BDC-NH₂ nanocrystals. The growth mechanism is similar to the previous reports [36]: initially, the Cu⁺ ions of Cu₂O were gradually released into the solution, which was then oxidized to Cu²⁺ by dissolved O₂, and the Cu²⁺ ions coordinated with the added H₂BDC-NH₂ to construct Cu-BDC-NH₂. However, it should be noted that Cu-BDC-NH₂ is mainly in the shape of nanoparticles during the initial growth stage (less than 8 h), which may be limited by the release rate of Cu⁺ from Cu₂O. With the extension of in situ growth time, the internal Cu₂O core was gradually consumed, and the external MOF components were gradually increased. When the reaction time increased over 12 h, the secondary growth of Cu-BDC-NH₂ took place, which caused a structure with the assembled Cu-BDC-NH₂ nanosheets on the surface of Cu₂O.

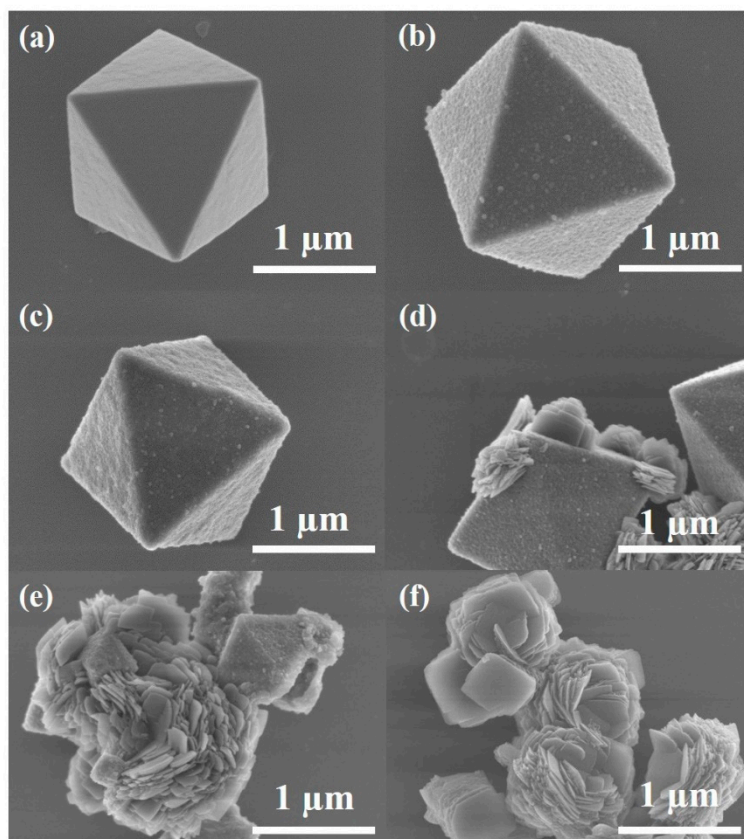


Figure 1. SEM images of (a) Cu₂O, (b) Cu₂O@Cu-BDC-NH₂-4h, (c) Cu₂O@Cu-BDC-NH₂-8h, (d) Cu₂O@Cu-BDC-NH₂-12h, (e) Cu₂O@Cu-BDC-NH₂-20h, and (f) Cu₂O@Cu-BDC-NH₂-32h.

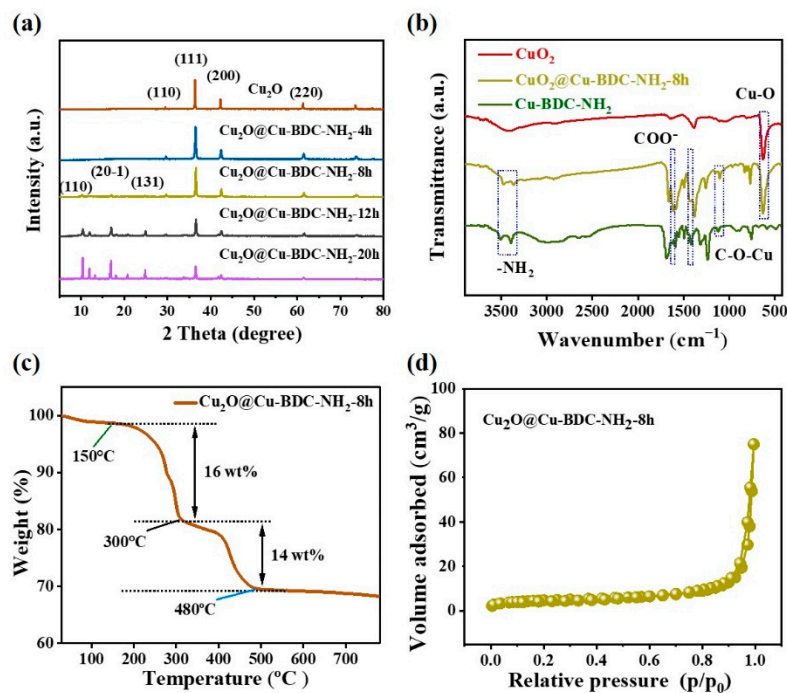


Figure 2. (a) XRD patterns of Cu₂O, Cu₂O@Cu-BDC-NH₂-4h, Cu₂O@Cu-BDC-NH₂-8h, Cu₂O@Cu-BDC-NH₂-12h, and Cu₂O@Cu-BDC-NH₂-20h. (b) FTIR spectra of Cu₂O, Cu₂O@Cu-BDC-NH₂-8h, and Cu-BDC-NH₂. (c) The TGA curves and (d) N₂ adsorption-desorption isotherms of Cu₂O@Cu-BDC-NH₂-8h.

To further identify the structural evolution during the formation of the $\text{Cu}_2\text{O}@$ Cu-BDC-NH₂ composites, Fourier transform infrared (FTIR) spectra of the as-prepared Cu_2O , $\text{Cu}_2\text{O}@$ Cu-BDC-NH₂, and Cu-BDC-NH₂ were obtained and the results are presented in Figure 2b. Compared to the FTIR spectrum of Cu_2O , $\text{Cu}_2\text{O}@$ Cu-BDC-NH₂ presented newly emerging peaks at 3480 and 3367 cm^{-1} , which were attributed to the asymmetric stretching and symmetric stretching modes of the -NH₂ group [21]. The bands at 1433 and 1617 cm^{-1} in $\text{Cu}_2\text{O}@$ Cu-BDC-NH₂ were contributed by the symmetric stretching and asymmetric stretching modes of the COO⁻ group, which originated from the H₂BDC-NH₂ ligand. The bands at 1105 and 630 cm^{-1} in $\text{Cu}_2\text{O}@$ Cu-BDC-NH₂ were assigned to the bond of C-O-Cu and Cu-O, which is consistent with the band in Cu-BDC and Cu_2O , respectively. The FTIR data confirmed the successful combination of Cu_2O and Cu-BDC-NH₂, which is consistent with the above XRD and SEM results.

The thermal stability of $\text{Cu}_2\text{O}@$ Cu-BDC-NH₂ was investigated by thermogravimetric analysis (TGA) under a N₂ atmosphere. As shown in Figure 2c, the weight loss in the temperature range of 150–300 °C was determined to be 16%, which can be attributed to the liberation of the coordinated DMF molecules, while the weight loss (14%) in the temperature of 300–480 °C corresponds to decomposition of the BDC²⁻ ligand of Cu-BDC [36]. The results of the TGA indicate that the $\text{Cu}_2\text{O}@$ Cu-BDC-NH₂-8h presented excellent thermal stability before 300 °C. Furthermore, the remaining solid with 68 wt.% was mainly attributed to Cu_2O and other copper containing components. The N₂ absorption-desorption isotherms of $\text{Cu}_2\text{O}@$ Cu-BDC-NH₂-8h were identified as type II with a Brunauer-Emmett-Teller (BET) specific surface area of 16.6 $\text{m}^2 \text{g}^{-1}$ (Figure 2d), which was just a little larger than that of Cu_2O (13.0 $\text{m}^2 \text{g}^{-1}$). This result indicates that the amount of the generated Cu-BDC-NH₂ nanoparticles in $\text{Cu}_2\text{O}@$ Cu-BDC-NH₂-8h was too small to contribute much to the higher specific surface area and porosity.

The XPS spectra were obtained to better understand the oxidation valence of Cu in $\text{Cu}_2\text{O}@$ Cu-BDC-NH₂. The typical peaks of C, N, O, and Cu were identified in the full XPS spectrum (Figure 3a) of Cu in $\text{Cu}_2\text{O}@$ Cu-BDC-NH₂-8h and the Cu 2p, C 1s, and O 1s spectra were investigated to trace the change in elemental states (Figure 3b–d). As shown in Figure 3b, the peaks at binding energy of 932.7 and 952.8 eV can be ascribed to Cu⁺ of Cu 2p_{3/2} and 2p_{1/2}, indicating the existence of Cu_2O in the surface of $\text{Cu}_2\text{O}@$ Cu-BDC-NH₂-8h. The Cu 2p_{3/2} peak at the binding energy of 935.0 eV and the Cu 2p_{1/2} peak at binding energy of 955.2 eV in the Cu 2p spectra can be attributed to the Cu²⁺, which was contributed from the partial oxidation from Cu⁺ to Cu²⁺ during the in situ growth of the Cu-BDC-NH₂ on the surface of Cu_2O [36], suggesting the formation of the Cu⁺/Cu²⁺ interface in the $\text{Cu}_2\text{O}@$ Cu-BDC-NH₂-8h composite. Besides, the comparison of the relative intensity of the Cu 2p spectrum indicate that the amount of Cu⁺ was more than that of Cu²⁺, and the relative elemental ratio of Cu²⁺/Cu⁺ was determined to be 0.699 with the area integration method. The C 1s spectra were also obtained and the groups of -C=O, C-O, and C-C were investigated at the binding energies of 288.3, 285.6, and 284.6 eV (Figure 3c). The O 1s of $\text{Cu}_2\text{O}@$ Cu-BDC-NH₂-8h (Figure 3d) represents the peaks at 531.9 and 531.2 eV, which can be attributed to the existence of C=O and C-O/O-H in the absorbed carbonate and hydroxyl species, while the peak at the binding energy of 530.4 eV indicates the Cu-O bond in Cu_2O or CuO. To further reveal the electronic change in the Cu ion in the formation of Cu-BDC-NH₂ on Cu_2O , the Cu 2p spectra of Cu_2O , $\text{Cu}_2\text{O}@$ Cu-BDC-NH₂-8h, and $\text{Cu}_2\text{O}@$ Cu-BDC-NH₂-20h are compared in Figure 3e. The enhanced intensity of Cu²⁺ from Cu_2O to $\text{Cu}_2\text{O}@$ Cu-BDC-NH₂ indicates the increasing amount of Cu²⁺ with the formation of $\text{Cu}_2\text{O}@$ Cu-BDC-NH₂ on the surface of the Cu_2O , and the 0.15 eV positive shift in the Cu⁺ 2p_{3/2} spectra indicates the anti-oxidation of Cu_2O and the stability of the $\text{Cu}_2\text{O}@$ Cu-BDC-NH₂, which is consistent with the result in the Cu-LMM spectrum (Figure 3f). The XPS results confirmed the formation and evolution of the Cu⁺/Cu²⁺ interface between Cu_2O and Cu-BDC-NH₂ during the in situ growth of $\text{Cu}_2\text{O}@$ Cu-BDC-NH₂ as well as the protective effect of the outer MOF shell on the Cu_2O core. This is consistent with the above SEM, XRD, and FTIR results.

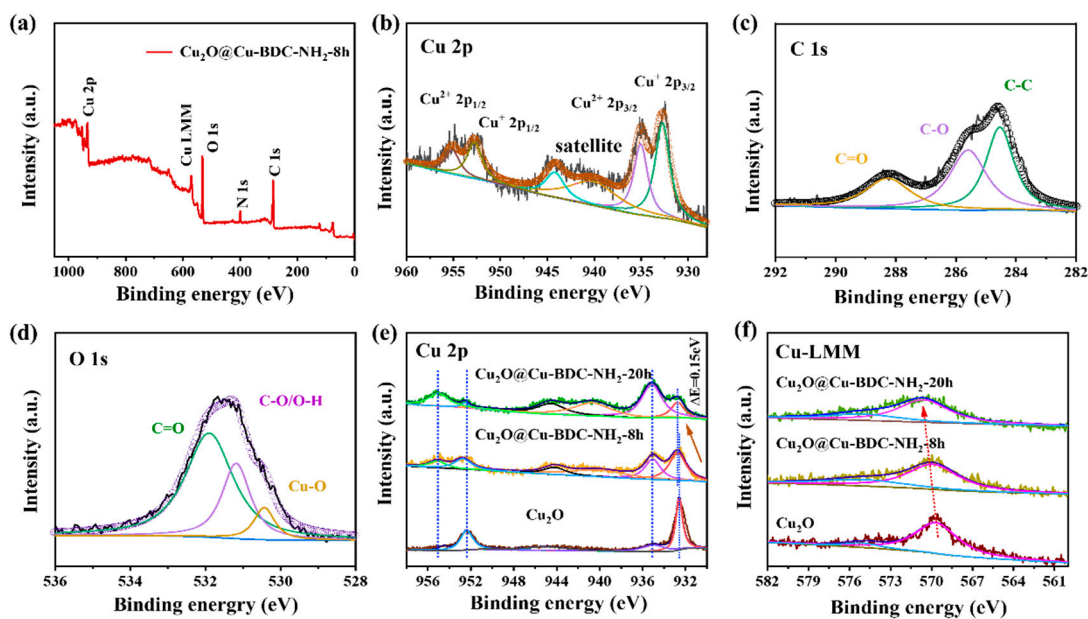


Figure 3. (a) XPS survey, (b) Cu 2p, (c) C 1s, (d) O 1s spectra of $\text{Cu}_2\text{O}@Cu\text{-BDC-NH}_2\text{-8h}$. (e) Cu 2p and (f) Cu-LMM XPS spectra of Cu_2O , $\text{Cu}_2\text{O}@Cu\text{-BDC-NH}_2\text{-8h}$, and $\text{Cu}_2\text{O}@Cu\text{-BDC-NH}_2\text{-20h}$.

2.2. Catalytic Properties

The catalytic properties for the selective oxidation of styrene over the as-prepared catalysts under a base-free condition were investigated. The catalytic tests were carried out by using 10 mg of the catalysts at a mild temperature of 40 °C with 30 wt.% H_2O_2 as the green oxidant and acetonitrile as the solvent. First, the selective oxidation of styrene to benzaldehyde over the $\text{Cu}_2\text{O}@Cu\text{-BDC-NH}_2\text{-8h}$ sample was chosen as a model reaction. The catalytic performance *versus* reaction time over $\text{Cu}_2\text{O}@Cu\text{-BDC-NH}_2\text{-8h}$ was tested and the results are presented in Figure 4. As shown in Figure 4, initially, the yield of benzaldehyde gradually increased with the increase in reaction time, which began to decline after reaction for 10 h. During this process, a continuous decrease in benzaldehyde selectivity could be observed, which was mainly due to the formation of styrene oxide according to the GC-MS analysis. It is worth noting that an increase in other by-products such as benzoic acid and phenylacetaldehyde were tested with the extension of the reaction time to over 8 h, which was mainly due to the further oxidation of benzaldehyde and styrene oxide [12,37], resulting in a further decrease in the selectivity of benzaldehyde. The highest catalytic performance was archived at 10 h with 85% styrene conversion and 76% benzaldehyde selectivity. As shown in Table 1, the catalytic performance of the as-prepared $\text{Cu}_2\text{O}@Cu\text{-BDC-NH}_2\text{-8h}$ sample was superior to most of the previously reported transition metal/metal oxide-based catalysts, and even comparable to some noble metal-based catalysts.

To explore the influence of the morphologies and structures of materials on the catalytic performance, a series of controlled experiments were conducted. First, the catalytic properties of the as-prepared Cu_2O , $\text{Cu}_2\text{O}@Cu\text{-BDC-NH}_2\text{-xh}$, and Cu-BDC-NH_2 were studied to investigate the active components of the $\text{Cu}_2\text{O}@Cu\text{-BDC-NH}_2$ composite, and the results are shown in Table 2. By comparing the catalytic performance of CuO (entry 2, Table 2), CuBDC-NH_2 (entry 7, Table 2), and the blank experiment without any catalyst (entry 1, Table 2), it can be seen that both Cu_2O and CuBDC-NH_2 have active components for styrene oxidation, and Cu_2O is beneficial to the high selectivity (82%) of benzaldehyde, while CuBDC-NH_2 contributes to the high conversion rate of styrene (92%). The above result indicates that it is possible to obtain catalysts with excellent performance by appropriately adjusting the contents of Cu_2O and CuBDC-NH_2 in the $\text{Cu}_2\text{O}@Cu\text{-BDC-NH}_2$ composite. After the in situ growth of Cu-BDC-NH_2 on Cu_2O for 4 h, there was no obvious increase in

the yield of benzaldehyde (entry 3, Table 2) than that of Cu_2O , which may be attributed to the small amount of CuBDC-NH_2 . With the increase in Cu-BDC-NH_2 loading, the sample of $\text{Cu}_2\text{O@Cu-BDC-NH}_2\text{-8h}$ (entry 4, Table 2) showed a sharp increase in styrene conversion from 38% to 85% with a relatively high benzaldehyde selectivity (76%). However, the sample of $\text{Cu}_2\text{O@Cu-BDC-NH}_2\text{-12h}$ (entry 5, Table 2), $\text{Cu}_2\text{O@Cu-BDC-NH}_2\text{-20h}$ (entry 6, Table 2) with more Cu-BDC-NH_2 loading did not exhibit higher benzaldehyde yield. These results indicate that the excellent performance of $\text{Cu}_2\text{O@Cu-BDC-NH}_2\text{-8h}$ may be attributed to the $\text{Cu}^{2+}/\text{Cu}^+$ interface between Cu_2O and Cu-BDC-NH_2 nanoparticles, while excessive loading of CuBDC-NH_2 nanosheets tends to obscure the active interface, limiting the performance of the $\text{Cu}_2\text{O@Cu-BDC-NH}_2\text{-12h}$ and $\text{Cu}_2\text{O@Cu-BDC-NH}_2\text{-20h}$ composite. Combined with the results of the XPS analysis, the sample of $\text{Cu}_2\text{O@Cu-BDC-NH}_2\text{-20h}$ had a higher ratio of $\text{Cu}^{2+}/\text{Cu}^+$ than $\text{Cu}_2\text{O@Cu-BDC-NH}_2\text{-8h}$, therefore the construction of a well-designed $\text{Cu}^{2+}/\text{Cu}^+$ active interface with suitable ratio of $\text{Cu}^{2+}/\text{Cu}^+$ [38,39] is key to achieving a high-efficient catalyst of $\text{Cu}_2\text{O@Cu-BDC-NH}_2$.

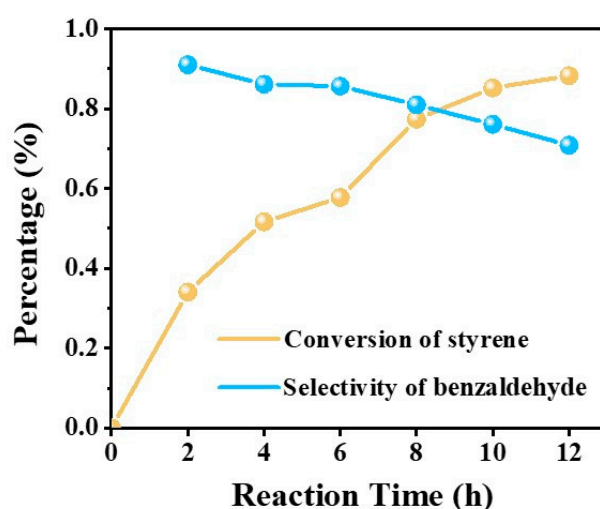


Figure 4. The catalytic performance versus reaction time over $\text{Cu}_2\text{O@Cu-BDC-NH}_2\text{-8h}$.

Table 1. Compared catalytic performance of styrene oxidation with H_2O_2 as the oxidants and a base-free condition over different catalysts.

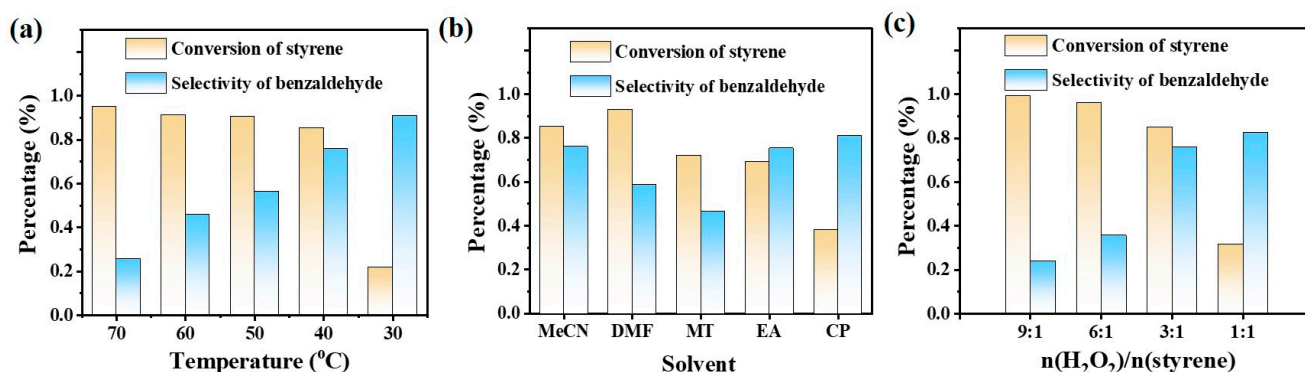
Year	Catalysts	Conversion (%)	Selectivity (%)		Temp. (°C)	Time (h)	Ref.
			Benzaldehyde	Styrene Oxide			
2022	$\text{Cu}_2\text{O@Cu-BDC-NH}_2$	85	76		40	10	This work
2022	DCP-CTF@Pd-MC	95	95		65	8	[5]
2021	$\text{Al}_2\text{O}_3\text{-FeOx}$	80	-	80	60–85	6	[37]
2020	Ti-MCM-48	78.9	85.2		60	12	[7]
2020	$\text{CoFe}_2\text{O}_4/\text{TiO}_2$	96.3	46.6		90	12	[3]
2020	$\text{SO}_4^{2-}\text{-Fe-V/ZrO}_2$	62.3	74		80	4	[14]
2019	CuCr-MMO	82.8	-	79.7	60	5	[12]
2019	NiCo_2O_4	78	30	67	70	10	[15]

Table 2. Catalytic performance of Cu₂O and Cu₂O@Cu-BDC-NH₂ in selective oxidation of styrene to benzaldehyde ^a.

Entry	Catalyst	Reaction Time (h)	Conversion (%)	Selectivity (%)
1	—	10	19	72
2	Cu ₂ O	10	31	82
3	Cu ₂ O@Cu-BDC-NH ₂ -4h	10	38	78
4	Cu ₂ O@Cu-BDC-NH ₂ -8h	10	85	76
5	Cu ₂ O@Cu-BDC-NH ₂ -12h	10	88	65
6	Cu ₂ O@Cu-BDC-NH ₂ -20h	10	91	56
7	Cu-BDC-NH ₂	10	92	43

^a Reaction conditions: 10 mg of catalysts, 2 mmol of styrene, 6 mmol of H₂O₂, 5 mL of acetonitrile, temperature 40 °C.

Additional control experiments were conducted to investigate the effects of reaction conditions (temperature, the solvent, and the amount of H₂O₂) on catalytic performance. Besides catalysts, the reaction temperature also plays an important role in the reaction process. Therefore, we explored the effect of reaction temperature (30~70 °C) on the styrene oxidation reaction. As shown in Figure 5a, the conversion of styrene over the catalyst of Cu₂O@Cu-BDC-NH₂-20h at 30 °C was only about 20%, which may be attributed to the difficulty in the activation of H₂O₂ below 30 °C. A significant increase in the conversion of styrene was observed within 30~40 °C, while no more obvious increase could be found within 40~70 °C. This phenomenon indicates that Cu₂O@Cu-BDC-NH₂-8h became active at 40 °C, but the intermediate species were more easily decomposed into different products through the cleavage of C = C and CO bands at higher temperature [40–42], which resulted in the formation of benzoic acid and phenylacetaldehyde.

**Figure 5.** The effects of (a) temperature, (b) solvent, and (c) the amount of oxidant on the catalytic performance over Cu₂O@Cu-BDC-NH₂-8h for the selective oxidation of styrene.

Then, the solvent effect was also explored at the reaction temperature of 40 °C. As shown in Figure 5b and Table 3, the conversion of styrene followed the order DMF > CH₃CN > MeOH > EtOH > acetone, while the selectivity for benzaldehyde followed the order CH₃CN > acetone > EtOH > DMF > MeOH. Among these solvents, CH₃CN is more active in catalyzing styrene, with the highest selectivity (76%) for benzaldehyde and higher conversion of styrene (85%), which can be attributed to its high permittivity and lower boiling point [43,44]. Besides, CH₃CN has been proven to be able to be miscible for styrene (oil phase) with H₂O₂ (aqueous phase), thus ensuring a large contact area for efficient styrene oxidation [12].

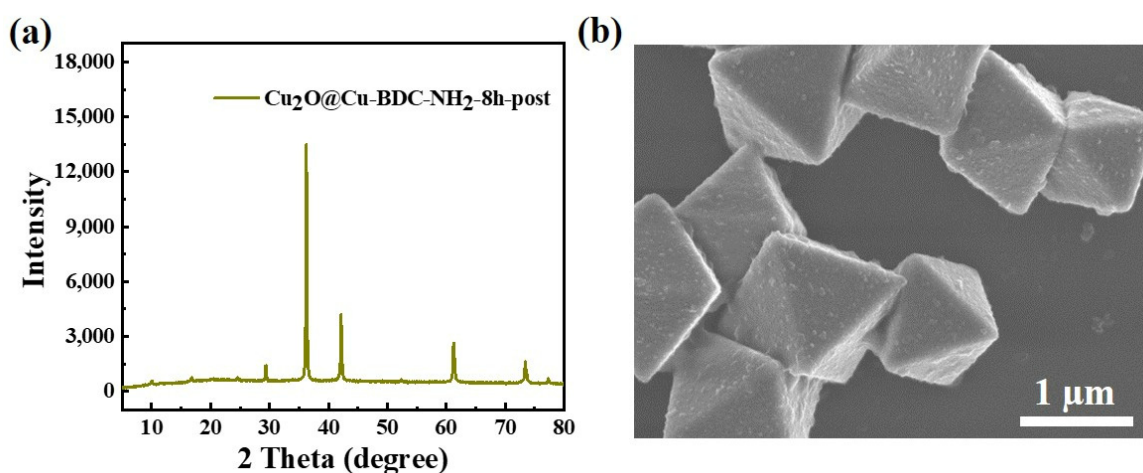
Table 3. Catalytic performance of Cu₂O@Cu-BDC-NH₂-8h for selective oxidation of styrene with different solvents ^a.

Entry	Solvent	Dielectric Constant	Boiling Point (°C)	Conversion (%)	Selectivity (%)
1	CH ₃ CN	37.5	82	85	76
2	DMF	37.6	153	93	58
3	Methanol	33.6	64	72	46
4	Ethanol	24.3	78	69	75
5	Acetone	20.7	56	38	81

^a Reaction conditions: 10 mg of catalysts, 2 mmol of styrene, 6 mmol of H₂O₂, 5 mL of acetonitrile, temperature 40 °C.

We also compared the catalytic activities with different amounts of H₂O₂: styrene (1:1, 3:1, 6:1, and 9:1) at 40 °C with CH₃CN as the solvent. As shown in Figure 5c, it can be found that both insufficient and excessive H₂O₂ are not conducive to the high efficiency of the styrene oxidation to benzaldehyde. The low yield of benzaldehyde with the H₂O₂/styrene molar ratio of 1:1 can be attributed to the lack of oxidants. The decreased selectivity with higher H₂O₂/styrene molar ratio of 6:1 and 9:1 is due to the formation of by-products such as benzoic acid catalyzed by hydroxyl radicals generated by the decomposition of excess H₂O₂ [45,46]. Therefore, the H₂O₂/styrene molar ratio of 3:1 was selected as the optimum reaction condition.

The metal leaching tests were conducted to investigate the stability of the as-prepared Cu₂O@Cu-BDC-NH₂-8h catalysts. In a typical catalytic process, the solid catalyst of Cu₂O@Cu-BDC-NH₂-8h was removed from the reaction mixture by centrifugation after 4 h while the reaction continued for another 6 h. Results showed that the yield of benzaldehyde was 43.9% (styrene conversion: 50.9%, benzaldehyde selectivity 86.3%) in the first 4 h, and no increase in benzaldehyde yields (styrene conversion: 51.6%, benzaldehyde selectivity 84.7%) could be tested when the reaction continued for another 6 h without the solid catalyst, suggesting the superior stability and environmentally-benign properties of the as-prepared Cu₂O@Cu-BDC-NH₂-8h composite without metal leaching. The powder XRD patterns (Figure 6a) and SEM image (Figure 6b) of the Cu₂O@Cu-BDC-NH₂-8h catalyst after the catalytic reaction showed that the morphology and structure of the composite were well remained, which further confirmed the above results.

**Figure 6.** (a) XRD patterns and (b) SEM image of Cu₂O@Cu-BDC-NH₂-8h after the catalytic reaction.

Aside from the Cu₂O octahedra (od-Cu₂O), the Cu₂O cuboctahedrons (cod-Cu₂O) were synthesized by adjusting the molecular weight of the added PVP. The morphology of od-Cu₂O, cod-Cu₂O, and their derived od-Cu₂O@Cu-BDC-NH₂ and cod-Cu₂O@Cu-BDC-NH₂ was investigated by SEM. As shown in Figure 7a,c, when using PVP with

the molecular weight of 130,000 instead of 58,000, a morphology change in Cu_2O from octahedron to cuboctahedron was observed, and the size of cod- Cu_2O was similar to that of od- Cu_2O , ranging from 1 μm to 2 μm with no obvious agglomeration between the particles. The XRD patterns (Figure 7e) of the two types of Cu_2O presented the same diffraction peaks but different relative intensities, indicating the different advantageous crystal planes. Specifically, the intensity of the diffraction peaks at 42.2° in cod- Cu_2O was more enhanced than that in od- Cu_2O , which corresponded to the shrinkage of {111} facets and the enlargement of {100} facets. The morphology variation can be attributed to the selected absorption of PVP on the {111} facets of Cu_2O [34]. After the in situ growth of the Cu-BDC- NH_2 , both the od- $\text{Cu}_2\text{O}@$ Cu-BDC- NH_2 and cod- $\text{Cu}_2\text{O}@$ Cu-BDC- NH_2 (Figure 7b,d) showed a rougher surface, indicating the successful growth of Cu-BDC- NH_2 nanocrystals on the Cu_2O .

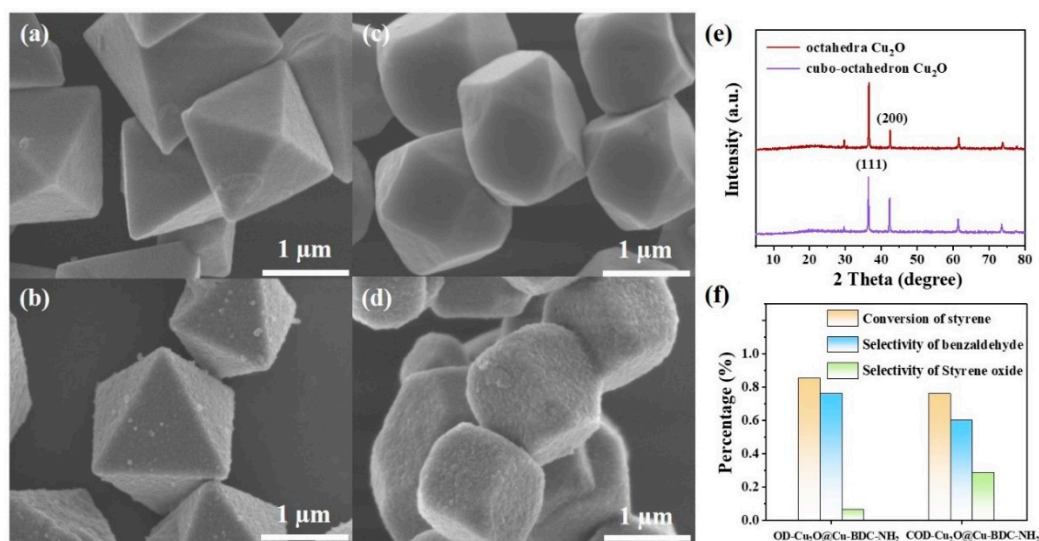


Figure 7. SEM images of (a) od- Cu_2O , (b) od- $\text{Cu}_2\text{O}@$ Cu-BDC- NH_2 , (c) cod- Cu_2O , and (d) cod- $\text{Cu}_2\text{O}@$ Cu-BDC- NH_2 . (e) XRD patterns of od- Cu_2O and cod- Cu_2O . (f) The catalytic performance of od- $\text{Cu}_2\text{O}@$ Cu-BDC- NH_2 and cod- $\text{Cu}_2\text{O}@$ Cu-BDC- NH_2 in the selective oxidation of styrene to benzaldehyde.

The catalytic performance of selective oxidation of styrene on od- $\text{Cu}_2\text{O}@$ Cu-BDC- NH_2 and cod- $\text{Cu}_2\text{O}@$ Cu-BDC- NH_2 were conducted to investigate the effects of the morphology and structure of Cu_2O on their catalytic properties. As shown in Table 4, od- $\text{Cu}_2\text{O}@$ Cu-BDC- NH_2 exhibited higher selectivity for benzaldehyde (64% \rightarrow 76%) than that of cod- $\text{Cu}_2\text{O}@$ Cu-BDC- NH_2 , while no significant difference in the conversion of styrene was observed. This can be attributed to the fact that the one-coordinated copper sites on the exposed (111) crystal plane are favorable for double bond oxidation to aldehyde groups [35]. In contrast, a small amount of styrene oxide (11%) appeared in the reaction catalyzed by cod- $\text{Cu}_2\text{O}@$ Cu-BDC- NH_2 that probably originated from the oxygen sites in the exposed (100) crystalline plane, which can promote the formation of olefin epoxide. This phenomenon suggests that the selectivity of different products can be further regulated by controlling the exposed crystal planes of Cu_2O .

Table 4. Catalytic performance of od-Cu₂O@Cu-BDC-NH₂ and cod-Cu₂O@Cu-BDC-NH₂ in the selective oxidation of styrene ^a.

Entry	Catalyst	Conversion (%)	Selectivity (%)	
			Benzaldehyde	Styrene Oxide
1	od-Cu ₂ O@Cu-BDC-NH ₂	85	76	7
2	cod-Cu ₂ O@Cu-BDC-NH ₂	83	64	11

^a Reaction conditions: 10 mg of catalysts, 2 mmol of styrene, 6 mmol of H₂O₂, 5 mL of acetonitrile, temperature 40 °C.

3. Materials and Methods

3.1. Materials

N,N-dimethylformamide (DMF, AR), acetone (AR), benzaldehyde (AR), epoxy ethane (AR), and methanol (AR) was purchased from Beijing Tong Guang Fine Chemicals Company, Beijing, China. Ethanol (AR), sodium hydroxide (NaOH, AR), ascorbic acid (AR), acetonitrile (AR), sodium thiosulfate (AR), H₂O₂ (30 wt.%), polyvinylpyrrolidone (PVP, molecular weight: 58,000 and 130,000) were purchased from Shanghai Aladdin Bio-Chem Technology Co. Ltd., Shanghai, China. Copper chloride (CuCl₂, AR), copper nitrate trihydrate (Cu(NO₃)₂, AR), phenylacetaldehyde (>99.5%), and 2-aminoterephthalic acid (H₂BDC-NH₂, AR) were purchased from Shanghai Macklin Biochemical Co. Ltd., Shanghai, China.

3.2. Synthesis of Cu₂O

The octahedron Cu₂O (denoted as od-Cu₂O) was prepared based on a previously reported method [31] with some modifications. In a typical process, 100 mL of 0.01 mol L⁻¹ CuCl₂ aqueous solution and 10 mL of 2 mol L⁻¹ NaOH aqueous solution and 0.6 mol L⁻¹ of ascorbic acid aqueous solution was first prepared. A total of 5 g of PVP (molecular weight: 58,000) was added into 100 mL of 0.01 mol L⁻¹ CuCl₂ aqueous solution under constant stirring over two hours. Then, the prepared 2M NaOH aqueous solution was slowly dropped into the above mixed solution until the color of the solution gradually changed from mild milk blue to sky-blue and then to dark brown. After the above mixed solution was immersed in a constant temperature bath for 30 min, the 0.6 mol L⁻¹ ascorbic acid aqueous solution was slowly dropped into the above solution until the color of the solution was changed to brick-red. The turbid solution was obtained by continuing the bath at 55 °C for 2.5 h. The resulting product was washed with deionized water and ethanol several times, collected by centrifugation, and finally dried at room temperature under vacuum condition overnight.

The cuboctahedron Cu₂O (denoted as cod-Cu₂O): The preparation process of the cod-Cu₂O was the same as that of the od-Cu₂O, except that the PVP with molecular weight of 58,000 was replaced by the PVP with molecular weight of 130,000.

3.3. Synthesis of Cu₂O@Cu-BDC-NH₂

od-Cu₂O@Cu-BDC-NH₂: The od-Cu₂O@Cu-BDC-NH₂ was prepared by an in situ assembly method. First, the as-prepared od-Cu₂O (80 mg) was uniformly dissolved in 20 mL ethanol, and 181.1 mg of 2-aminoterephthalic acid was added into 20 mL of a mixed solution of ethanol and DMF (1:1 vol) under continuous stirring. After stirring well, the two separate solutions were mixed at room temperature with magnetic stirring for different periods (4 h–32 h) to control the growth of MOFs on od-Cu₂O. The resulting products of od-Cu₂O@Cu-BDC-NH₂-xh (x = 4, 8, 12, 20 and 32) were washed by deionized water and ethanol several times, collected by centrifugation, and finally dried at room temperature under vacuum condition overnight.

cod-Cu₂O@Cu-BDC-NH₂: The preparation process of the cod-Cu₂O@Cu-BDC-NH₂ was the same as that of the od-Cu₂O@Cu-BDC-NH₂, except that the precursor was changed from od-Cu₂O to cod-Cu₂O, and the resulting product of cod-Cu₂O@Cu-BDC-NH₂-8h was obtained after reaction for 8 h under magnetic stirring.

3.4. Synthesis of Cu-BDC-NH₂ Nanosheets

The metal solution (named as M1) was prepared by dissolving 30 mg of Cu(NO₃)₂ into a mixed solution of 3 mL of DMF and 1 mL of CH₃CN. The ligand solution (named as L1) was synthesized by dissolving 30 mg of H₂BDC-NH₂ into 4 mL of the mixed solution of DMF and CH₃CN (1:3 vol). Then, the above solution M1 was added into L1, and the mixture was left to stand under an ambient environment for 24 h. Finally, the resulting product of Cu-BDC-NH₂ was collected by centrifugation, washed with DMF three times, and then stored in DMF.

3.5. Characterization

The morphology of the as-prepared nanomaterials was characterized using a scanning electron microscope (SEM, Regulus 8100, Hitachi, Japan) with an accelerating voltage of 5 kV. The crystallinity and structural details of materials were obtained through X-ray diffraction (XRD, Bruker D8 Advance, Bruker, Germany) using a Cu K α radiation ($\lambda = 1.541 \text{ \AA}$). Fourier-transform infrared (FT-IR) spectra were conducted on a Nicolet 6700 spectrometer (Thermo Scientific, Waltham, MA, USA) using the potassium bromide (KBr) pellet technique over a range of 400–4000 cm⁻¹. X-ray photoelectron spectroscopy (XPS) data were analyzed using a Thermo ESCALAB 250Xi spectrometer (Thermo Scientific, USA). The nitrogen adsorption–desorption isotherm was collected by using a Micromeritics ASAP2460 instrument (Micromeritics, Norcross, GA, USA) at 77 K. The thermal property was measured using thermogravimetric analysis (TGA, METTLER TOLEDO TGA/DSC3+, Mettler Toledo, Switzerland) in the range of 25–800 °C at a heating–cooling rate of $\pm 10 \text{ }^\circ\text{C min}^{-1}$ under a nitrogen gas flow rate of 20 mL min⁻¹.

3.6. Catalytic Tests for Selective Oxidation of Styrene

The catalytic tests for the selective oxidation of styrene were carried out as follows: the as-prepared catalyst (10 mg), styrene (2 mmol), and acetonitrile (5 mL) were added into three-neck round-bottom flask (25 mL) equipped with a reflux condenser. The device was immersed into an oil bath and heated to the desired temperature under magnetic stirring. Then, 6 mmol of 30 wt.% H₂O₂ aqueous solution was added into the mixture to initiate the reaction. After a desired time, the reaction mixture was centrifuged, and the liquid layer was analyzed by a gas chromatography-mass spectrometer (GC-MS, Agilent 7890/5975C, Agilent, Santa Clara, CA, USA) using the external standard method for quantitative analysis.

The stability of the as-prepared catalyst was investigated by a metal leaching test. In a typical process, the catalytic reaction was stopped after 4 h and the solid catalyst of Cu₂O@Cu-BDC-NH₂ was separated and removed by centrifugation. The reaction solution without the Cu₂O@Cu-BDC-NH₂ catalyst was then stirred for a further 6 h, and the catalytic performance was analyzed by GC-MS.

4. Conclusions

In summary, a novel core-shell structured Cu₂O@Cu-BDC-NH₂ heterogeneous catalyst with tunable Cu⁺/Cu²⁺ interface, variable composition, and structure was synthesized by a facile in situ self-assembly method. With H₂O₂ as green oxidants, the resultant Cu₂O@Cu-BDC-NH₂ catalysts exhibited significant catalytic performance for the selective oxidation of styrene at 40 °C under base-free conditions, and the optimized conversion of styrene and selectivity of benzaldehyde could reach 85% and 76%, respectively. The delicate combination of Cu₂O and Cu-BDC-NH₂ not only provides a well-designed Cu⁺/Cu²⁺ active interface and porous MOF shells for mass transfer and protection of the active Cu₂O component, but also provides appropriate acid–base regulation methods to improve the selectivity of the target product, thus suggesting a new perspective and simple strategies for the construction of a highly efficient and green catalytic system for the selective oxidation of styrene.

Author Contributions: Conceptualization, Methodology, X.Z.; Formal analysis, data curation, X.Z., M.H. and X.T.; Investigation, Data curation, P.W., Z.Z., X.B. and Y.J.; Writing-Original Draft Preparation, Review and Editing, X.Z., M.H. and X.T.; Writing-Review and Editing, X.T. and P.W.; Funding acquisition, X.Z. All authors have read and agreed to the published version of the manuscript.

Funding: This work was financially supported by the National Natural Science Foundation of China (No. 52002029).

Conflicts of Interest: The authors declare no conflict of interest.

References

- Andrade, M.A.; Martins, L.M.D.R. Selective Styrene Oxidation to Benzaldehyde over Recently Developed Heterogeneous Catalysts. *Molecules* **2021**, *26*, 1680. [CrossRef] [PubMed]
- Bhanushali, J.T.; Kainthla, I.; Keri, R.S.; Nagaraja, B.M. Catalytic Hydrogenation of Benzaldehyde for Selective Synthesis of Benzyl Alcohol: A Review. *Chemistryselect* **2016**, *1*, 3839–3853. [CrossRef]
- Liu, L.; He, W.; Fang, Z.; Yang, Z.; Guo, K.; Wang, Z. From Core-Shell to Yolk-Shell: Improved Catalytic Performance toward CoFe₂O₄@ Hollow@ Mesoporous TiO₂ toward Selective Oxidation of Styrene. *Ind. Eng. Chem. Res.* **2020**, *59*, 19938–19951. [CrossRef]
- Sheng, J.; Li, W.; Wang, Y.; Lu, W.; Yan, B.; Qiu, B.; Gao, X.; Cheng, S.; He, L.; Lu, A. Coproduction of Styrene and Benzaldehyde over a Boron Nitride-Supported Monomeric MoOx Catalyst. *J. Catal.* **2021**, *400*, 265–273. [CrossRef]
- Li, Z.; Di, M.; Zhang, Y.; Zhang, B.; Zhang, Z.; Zhang, Z.; Li, A.; Qiao, S. Covalent Triazine Frameworks with Palladium Nanoclusters as Highly Efficient Heterogeneous Catalysts for Styrene Oxidation. *ACS Appl. Polym. Mater.* **2022**, *4*, 1047–1054. [CrossRef]
- Yang, R.A.; Sarazen, M.L. Reaction Pathways and Deactivation Mechanisms of Isostructural Cr and Fe MIL-101 During Liquid-Phase Styrene Oxidation by Hydrogen Peroxide. *Catal. Sci. Technol.* **2021**, *11*, 5282–5296. [CrossRef]
- Das, D.R.; Kalita, P.; Talukdar, A.K. Ti/Cr Incorporated Mesoporous MCM-48 for Oxidation of Styrene to Benzaldehyde. *J. Porous. Mat.* **2020**, *27*, 893–903. [CrossRef]
- Escande, V.; Petit, E.; Garoux, L.; Boulanger, C.; Grison, C. Switchable Alkene Epoxidation/Oxidative Cleavage with H₂O₂/NaHCO₃: Efficient Heterogeneous Catalysis Derived from Biosourced Eco-Mn. *ACS Sustain. Chem. Eng.* **2015**, *3*, 2704–2715. [CrossRef]
- Gao, Y.; Xing, C.; Hu, S.; Zhang, S. In Situ Exsolved Au Nanoparticles from Perovskite Oxide for Efficient Epoxidation of Styrene. *J. Mater. Chem. A* **2021**, *9*, 10374–10384. [CrossRef]
- Bregante, D.T.; Flaherty, D.W. Periodic Trends in Olefin Epoxidation over Group IV and V Framework-Substituted Zeolite Catalysts: A Kinetic and Spectroscopic Study. *J. Am. Chem. Soc.* **2017**, *139*, 6888–6898. [CrossRef]
- Yuan, K.; Song, T.; Wang, D.; Zou, Y.; Li, J.; Zhang, X.; Tang, Z.; Hu, W. Bimetal-Organic Frameworks for Functionality Optimization: MnFe-MOF-74 as a Stable and Efficient Catalyst for the Epoxidation of Alkenes with H₂O₂. *Nanoscale* **2018**, *10*, 1591–1597. [CrossRef] [PubMed]
- Wang, Q.; Liang, X.; Bi, R.; Liu, Y.; He, Y.; Feng, J.; Li, D. Highly Efficient CuCr-MMO Catalyst for a Base-Free Styrene Epoxidation with H₂O₂ as the Oxidant: Synergistic Effect Between Cu and Cr. *Dalton Trans.* **2019**, *48*, 16402–16411. [CrossRef]
- Tan, K.; Iqbal, A.; Adam, F.; Abu Bakar, N.H.H.; Ahmad, M.N.; Yusop, R.M.; Pauzi, H. Influence of Mg/CTAB Ratio on the Structural, Physicochemical Properties and Catalytic Activity of Amorphous Mesoporous Magnesium Silicate Catalysts. *RSC Adv.* **2019**, *9*, 38760–38771. [CrossRef]
- Jin, W.; Wang, H.; Lu, B.; Zhao, J.; Cai, Q. SO₄²⁻-Fe-V/ZrO₂ Composite for Selective Oxidation of Styrene to Benzaldehyde in H₂O₂ Aqueous Solution. *Ind. Eng. Chem. Res.* **2020**, *59*, 4411–4418. [CrossRef]
- Paul, B.; Sharma, S.K.; Khatun, R.; Adak, S.; Singh, G.; Joshi, V.; Poddar, M.K.; Bordoloi, A.; Sasaki, T.; Bal, R. Development of Highly Efficient and Durable Three-Dimensional Octahedron NiCo₂O₄ Spinel Nanoparticles toward the Selective Oxidation of Styrene. *Ind. Eng. Chem. Res.* **2019**, *58*, 18168–18177. [CrossRef]
- Jurca, B.; Tirsoaga, A.; Granger, P.; Parvulescu, V.I. Impact of Deactivation Phenomena on Kinetics of the C-N Coupling Reaction over Supported Cu₂O Catalysts in Continuous-Flow Conditions. *J. Phys. Chem. C* **2015**, *119*, 18422–18433. [CrossRef]
- Cheng, W.; Zhang, H.; Luan, D.; Lou, X. Exposing Unsaturated Cu₁-O₂ Sites in Nanoscale Cu-MOF for Efficient Electrocatalytic Hydrogen Evolution. *Sci. Adv.* **2021**, *7*, eabg2580. [CrossRef] [PubMed]
- Zhang, X.; Wang, G.; Yang, M.; Luan, Y.; Dong, W.; Dang, R.; Gao, H.; Yu, J. Synthesis of a Fe₃O₄-CuO@ meso-SiO₂ Nanostructure as a Magnetically Recyclable and Efficient Catalyst for Styrene Epoxidation. *Catal. Sci. Technol.* **2014**, *4*, 3082–3089. [CrossRef]
- Wu, H.; Kong, X.Y.; Wen, X.; Chai, S.P.; Lovell, E.C.; Tang, J.; Ng, Y.H. Metal-Organic Framework Decorated Cuprous Oxide Nanowires for Long-lived Charges Applied in Selective Photocatalytic CO₂ Reduction to CH₄. *Angew. Chem. Int. Edit.* **2021**, *60*, 8455–8459. [CrossRef]
- Wang, S.; Zhang, X.; Dao, X.; Cheng, X.; Sun, W. Cu₂O@Cu@UiO-66-NH₂ Ternary Nanocubes for Photocatalytic CO₂ Reduction. *ACS Appl. Nano Mater.* **2020**, *3*, 10437–10445. [CrossRef]
- Tombesi, A.; Pettinari, C. Metal Organic Frameworks as Heterogeneous Catalysts in Olefin Epoxidation and Carbon Dioxide Cycloaddition. *Inorganics* **2021**, *9*, 81. [CrossRef]

22. Bavykina, A.; Kolobov, N.; Khan, I.S.; Bau, J.A.; Ramirez, A.; Gascon, J. Metal-Organic Frameworks in Heterogeneous Catalysis: Recent Progress, New Trends, and Future Perspectives. *Chem. Rev.* **2020**, *120*, 8468–8535. [CrossRef] [PubMed]
23. Allendorf, M.D.; Stavila, V.; Witman, M.; Brozek, C.K.; Hendon, C.H. What Lies beneath a Metal-Organic Framework Crystal Structure? New Design Principles from Unexpected Behaviors. *J. Am. Chem. Soc.* **2021**, *143*, 6705–6723. [CrossRef] [PubMed]
24. Cirujano, F.G.; Martin, N.; Wee, L.H. Design of Hierarchical Architectures in Metal-Organic Frameworks for Catalysis and Adsorption. *Chem. Mater.* **2020**, *32*, 10268–10295. [CrossRef]
25. Wang, Q.; Astruc, D. State of the Art and Prospects in Metal-Organic Framework (MOF)-Based and MOF-Derived Nanocatalysis. *Chem. Rev.* **2020**, *120*, 1438–1511. [CrossRef]
26. Zhang, X.; Dong, W.; Luan, Y.; Yang, M.; Tan, L.; Guo, Y.; Gao, H.; Tang, Y.; Dang, R.; Li, J.; et al. Highly Efficient Sulfonated-Polystyrene-Cu(II)@Cu₃(BTC)₂ Core-Shell Microsphere Catalysts for Base-free Aerobic Oxidation of Alcohols. *J. Mater. Chem. A* **2015**, *3*, 4266–4273. [CrossRef]
27. Jatoi, Y.F.; Fiaz, M.; Athar, M. Synthesis of Efficient TiO₂/Al₂O₃@Cu(BDC) Composite for Water Splitting and Photodegradation of Methylene Blue. *J. Aust. Ceram. Soc.* **2021**, *57*, 489–496. [CrossRef]
28. Alamgholiloo, H.; Zhang, S.; Ahadi, A.; Rostamnia, S.; Banaei, R.; Li, Z.; Liu, X.; Shokouhimehr, M. Synthesis of Bimetallic 4-PySI-Pd@Cu(BDC) via Open Metal Site Cu-MOF: Effect of Metal and Support of Pd@Cu-MOFs in H₂ Generation from Formic Acid. *Mol. Catal.* **2019**, *467*, 30–37. [CrossRef]
29. Huang, K.; Xu, Y.; Wang, L.; Wu, D. Heterogeneous Catalytic Wet Peroxide Oxidation of Simulated Phenol Wastewater by Copper Metal-Organic Frameworks. *RSC Adv.* **2015**, *5*, 32795–33283. [CrossRef]
30. Silva, B.C.E.; Irikura, K.; Frem, R.C.G.; Zandoni, M.V.B. Effect of Cu(BDC-NH₂) MOF Deposited on Cu/Cu₂O Electrode and Its Better Performance in Photoelectrocatalytic Reduction of CO₂. *J. Electroanal. Chem.* **2021**, *880*, 114856. [CrossRef]
31. Jiang, D.; Xue, J.; Wu, L.; Zhou, W.; Zhang, Y.; Li, X. Photocatalytic Performance Enhancement of CuO/Cu₂O Heterostructures for Photodegradation of Organic Dyes: Effects of CuO Morphology. *Appl. Catal. B Environ.* **2017**, *211*, 199–204. [CrossRef]
32. Gou, L.; Murphy, C.J. Solution-Phase Synthesis of Cu₂O Nanocubes. *Nano Lett.* **2003**, *3*, 231–234. [CrossRef]
33. Kim, D.Y.; Kim, C.W.; Sohn, J.H.; Lee, K.J.; Jung, M.H.; Kim, M.G.; Kang, Y.S. Ferromagnetism of Single-Crystalline Cu₂O Induced through Poly(N-vinyl-2-pyrrolidone) Interaction Triggering d-Orbital Alteration. *J. Phys. Chem. C* **2015**, *119*, 13350–13356. [CrossRef]
34. Zhang, D.; Zhang, H.; Guo, L.; Zheng, K.; Han, X.; Zhang, Z. Delicate control of crystallographic facet-oriented Cu₂O nanocrystals and the correlated adsorption ability. *J. Mater. Chem.* **2009**, *19*, 5220. [CrossRef]
35. Hua, Q.; Cao, T.; Gu, X.; Lu, J.; Jiang, Z.; Pan, X.; Luo, L.; Li, W.; Huang, W. Crystal-Plane-Controlled Selectivity of Cu₂O Catalysts in Propylene Oxidation with Molecular Oxygen. *Angew. Chem. Int. Edit.* **2014**, *53*, 4856–4861. [CrossRef] [PubMed]
36. Zhan, G.; Fan, L.; Zhao, F.; Huang, Z.; Chen, B.; Yang, X.; Zhou, S. Fabrication of Ultrathin 2D Cu-BDC Nanosheets and the Derived Integrated MOF Nanocomposites. *Adv. Funct. Mater.* **2019**, *29*, 1806720. [CrossRef]
37. Yang, Z.; Zhang, S.; Zhao, H.; Li, A.; Luo, L.; Guo, L. Subnano-FeOx Clusters Anchored in an Ultrathin Amorphous Al₂O₃ Nanosheet for Styrene Epoxidation. *ACS Catal.* **2021**, *11*, 11542–11550. [CrossRef]
38. Vithalani, R.; Patel, D.S.; Modi, C.K.; Sharma, V.; Jha, P.K. Graphene Oxide Supported Oxovanadium (IV) Complex for Catalytic Peroxidative Epoxidation of Styrene: An Eye-Catching Impact of Solvent. *Appl. Organomet. Chem.* **2020**, *34*, e5500. [CrossRef]
39. Tan, K.; Iqbal, A.; Adam, F.; Abu Bakar, N.H.H.; Yusop, R.M.; Ahmad, M.N. Synthesis and Characterization of Bubble Wrap-like Hollow Barium Silicate-Carbonate Nanospheres for the Epoxidation of Styrene. *J. Mater. Res. Technol.* **2020**, *9*, 11087–11098. [CrossRef]
40. Liu, J.; Wang, Z.; Jian, P.; Jian, R. Highly Selective Oxidation of Styrene to Benzaldehyde over A Tailor-Made Cobalt Oxide Encapsulated Zeolite Catalyst. *J. Colloid Interf. Sci.* **2018**, *517*, 144–154. [CrossRef]
41. Liu, B.; Wang, P.; Lopes, A.; Jin, L.; Zhong, W.; Pei, Y.; Sui, S.L.; He, J. Au-Carbon Electronic Interaction Mediated Selective Oxidation of Styrene. *ACS Catal.* **2017**, *7*, 3483–3488. [CrossRef]
42. Fu, H.; Huang, K.; Yang, G.; Cao, Y.; Wang, H.; Peng, F.; Wang, Q.; Yu, H. Synergistic Effect of Nitrogen Dopants on Carbon Nanotubes on the Catalytic Selective Epoxidation of Styrene. *ACS Catal.* **2019**, *10*, 129–137. [CrossRef]
43. Walker, K.L.; Dornan, L.M.; Zare, R.N.; Waymouth, R.M.; Muldoon, M.J. Mechanism of Catalytic Oxidation of Styrenes with Hydrogen Peroxide in the Presence of Cationic Palladium(II) Complexes. *J. Am. Chem. Soc.* **2017**, *139*, 12495–12503. [CrossRef] [PubMed]
44. Ghosh, B.K.; Moitra, D.; Chandel, M.; Lulla, H.; Ghosh, N.N. Ag Nanoparticle Immobilized Mesoporous TiO₂-Cobalt Ferrite Nanocatalyst: A Highly Active, Versatile, Magnetically Separable and Reusable Catalyst. *Mater. Res. Bull.* **2017**, *94*, 361–370. [CrossRef]
45. Gunam Resul, M.F.M.; López Fernández, A.M.; Rehman, A.; Harvey, A.P. Development of a Selective, Solvent-Free Epoxidation of Limonene Using Hydrogen Peroxide and a Tungsten-Based Catalyst. *React. Chem. Eng.* **2018**, *3*, 747–756. [CrossRef]
46. Li, H.; Yang, Z.; Lu, S.; Su, L.; Wang, C.; Huang, J.; Zhou, J.; Tang, J.; Huang, M. Nano-Porous Bimetallic CuCo-MOF-74 with Coordinatively Unsaturated Metal sites for Peroxymonosulfate Activation to Eliminate Organic Pollutants: Performance and Mechanism. *Chemosphere* **2021**, *273*, 129643. [CrossRef] [PubMed]

Review

Recent Achievements in the Copper-Catalyzed Arylation of Adamantane-Containing Amines, Di- and Polyamines

Alexei D. Averin ^{1,*}, Svetlana P. Panchenko ¹, Arina V. Murashkina ¹, Varvara I. Fomenko ¹, Daria S. Kuliukhina ¹, Anna S. Malysheva ¹, Alexei A. Yakushev ¹, Anton S. Abel ¹  and Irina P. Beletskaya ^{1,2} 

¹ Department of Chemistry, Lomonosov Moscow State University, Leninskie Gory, 1-3, Moscow 119991, Russia; nevermind1234@list.ru (S.P.P.)

² A.N. Frumkin Institute of Physical Chemistry and Electrochemistry, Russian Academy of Sciences, Leninsky Pr. 31-4, Moscow 119071, Russia

* Correspondence: alexaveron@yandex.ru; Tel.: +7-(495)9391139

Abstract: Rapid development of the copper-catalyzed amination of aryl halides in the beginning of the 21st century, known as the Renaissance of the Ullmann chemistry, laid foundations for the use of this method as a powerful tool for the construction of the C(sp²)-N bond and became a rival of the Buchwald–Hartwig amination reaction. Various applications of this approach are well-documented in a number of comprehensive and more specialized reviews, and this overview in the form of a personal account of the Cu-catalyzed arylation and heteroarylation of the adamantane-containing amines, and di- and polyamines, covers a more specific area, showing the possibilities of the method and outlining general regularities, considering reagents structure, copper source and ligands, scope, and limitations. The material of the last decade is mainly considered, and recent data on the application of the unsupported copper nanoparticles and possibilities of the Chan-Lam reaction as an alternative to the use of aryl halides are also discussed.

Keywords: copper; catalysis; amination; amines; polyamines; aryl halides; adamantane; nanoparticles



Citation: Averin, A.D.; Panchenko, S.P.; Murashkina, A.V.; Fomenko, V.I.; Kuliukhina, D.S.; Malysheva, A.S.; Yakushev, A.A.; Abel, A.S.; Beletskaya, I.P. Recent Achievements in the Copper-Catalyzed Arylation of Adamantane-Containing Amines, Di- and Polyamines. *Catalysts* **2023**, *13*, 831. <https://doi.org/10.3390/catal13050831>

Academic Editors: Yongjun Ji, Liwen Xing and Ke Wu

Received: 31 March 2023

Revised: 23 April 2023

Accepted: 26 April 2023

Published: 1 May 2023



Copyright: © 2023 by the authors. Licensee MDPI, Basel, Switzerland. This article is an open access article distributed under the terms and conditions of the Creative Commons Attribution (CC BY) license (<https://creativecommons.org/licenses/by/4.0/>).

1. Introduction

The beginning of the 20th century was marked by the birth of the copper-mediated reactions of carbon–carbon and carbon–heteroatom bond formation. In the pioneer research carried out by Ullmann and Goldberg, copper powder was shown to provide access to biphenyls [1], aryl amines [2], diaryl ethers [3], and *N*-aryl amides [4]. These reactions employed stoichiometric amounts of copper and strong bases, and demanded very harsh conditions; thus, the substrates' scope was strictly limited. However, the simplicity of the approach allowed for the synthesis of a series of valuable compounds via C–C, C–M, C–O, and C–S bond formation, and some “classical” reactions of this type are still used in industry [5–8].

The need for compounds bearing the *N*-(hetero)aryl moiety cannot be overestimated. They are widely used in the synthesis of pharmaceuticals [9,10] and agrochemicals [11,12], and for the fabrication of modern organic materials [13,14]. It is obvious that convenient, reliable, and inexpensive methods for the synthesis of compounds with the C(sp²)-N bond are always highly demanded. The so-called “Renaissance of the Ullmann chemistry” dates back to the beginning of the 21st century and is associated with the application of the ligands which allowed for the use of copper in catalytic amounts and the application of rather mild reaction conditions. To note, the effect of ketones or esters on the rate of the Ullmann reactions was noted even in 1964 [15]; however, at that time, it was thought to be a result of a better solubility of the copper compounds. In 1997, the reaction of phenols with aryl halides containing triazine fragments at the *ortho* position was reported [16], and this fragment was described as an appended ligand for the copper catalyst. A real breakthrough was a series of works by Buchwald [17], Ma [18], and Taillefer [19] which

used the catalytic systems on the basis of in situ-formed Cu(II) complexes with various ligands. This approach proved to be exceedingly fruitful and further development of the Cu-catalyzed amination and amidation reactions has been decisively linked with the design and investigation of the ligands [20,21]. These ligands can be divided into three main groups: N,N-ligands [22–26], N,O-ligands [27–31], and O,O-ligands [32–36], of which the most widely used and efficient representatives are shown in Figure 1. The role of the anionic ligands, which favor the oxidative addition and thus ensure milder conditions and a wider scope of the aryl halides, was emphasized in [37–39], the oxalamide ligands being essentially efficient for this purpose [40–42].

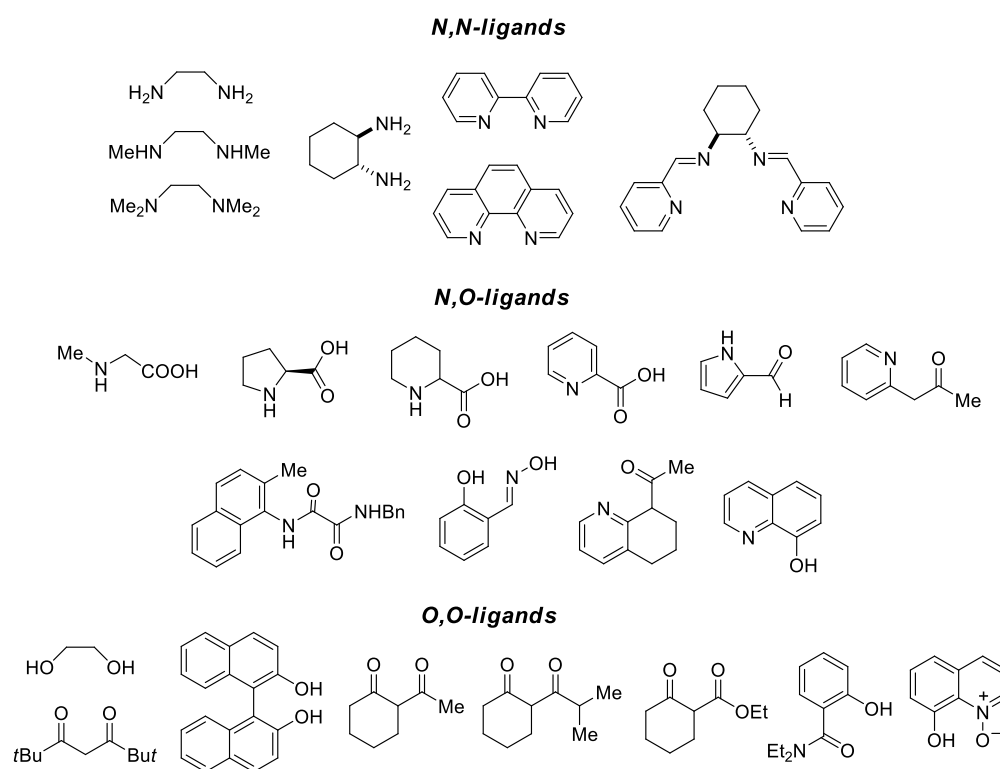


Figure 1. Most important ligands for Cu-catalyzed C–N bond formation.

The development of the copper-catalyzed amination has been already described in several comprehensive reviews. Two of them were published before 2010 by Ma [43] and Taillefer [19]. Two other reviews are dedicated to the comparison of the copper- and palladium-catalyzed amination reactions [44,45]. Further, a more thorough review has been published [46], and some accounts emphasize the application of the method to the synthesis of natural compounds [47,48]. During the last decade, the achievements in the copper-catalyzed amination became a focus of three comprehensive studies [49–51], and special cases of this approach have also been discussed recently [52,53].

One of the important trends in the study of the Cu-catalyzed amination and amidation reactions is the use of heterogeneous and heterogenized copper catalysts immobilized on various supports. The most frequently used copper salt for this purpose is CuI. The nature of supports is versatile, and different organic linkers may serve as the ligands for the copper cation. Cu catalysts are often immobilized on polymer supports [54–60]. For the needs of the development of reusable catalysts, those containing magnetite particles were found to be especially attractive [61–64].

The studies on the mechanism of Cu-catalyzed amination put forward several hypotheses. Taking into consideration the fact that copper in different oxidation states can be successfully employed in catalysis, it was supposed that Cu(I) is a genuine catalytic particle which emerges in the course of the reduction process of Cu(II) compounds [15,65–67]. In some protocols, additional reagents such as ascorbic acid are added to ensure this

reduction [68,69], but many others do not envisage any special reductant [70,71]. In the case of Cu(0), it is thought that, on contrary, its oxidation into Cu₂O gives rise to a catalytically active Cu(I) [65,72]. The main types of proposed mechanisms are the following: (1) oxidative addition of ArHal leading to Cu(III) complex followed by the reductive elimination; (2) formation of the π -complex of aryl halide with Cu(I) followed by the nucleophilic substitution; (3) single electron transfer (SET) or hydrogen atom transfer (HAT); (4) σ -bond metathesis. The majority of researchers support the idea of a key role of Cu(III) intermediate [46,73–77]; for this purpose, some researchers synthesized several stable complexes of Cu(III) in order to study the coordination sphere of the metal cation and to carry out their reactions with nucleophiles [78–80]. Ma investigated a series of reactions without additional ligands and postulated that, in this case, aryl halides, acting as ligands, form the π -complexes with the copper cation [27]. SET and HAT mechanisms involving radicals were thought to be verified [66] by the use of the radical traps which hindered the reactions. At last, metathesis with a four-membered transition state was proposed by Bacon [81]; this mechanism suggests the coordination of the copper cation with the halogen atom of ArHal. It is quite plausible that, with different reagents and in the presence of various ligands, different mechanisms can be actualized.

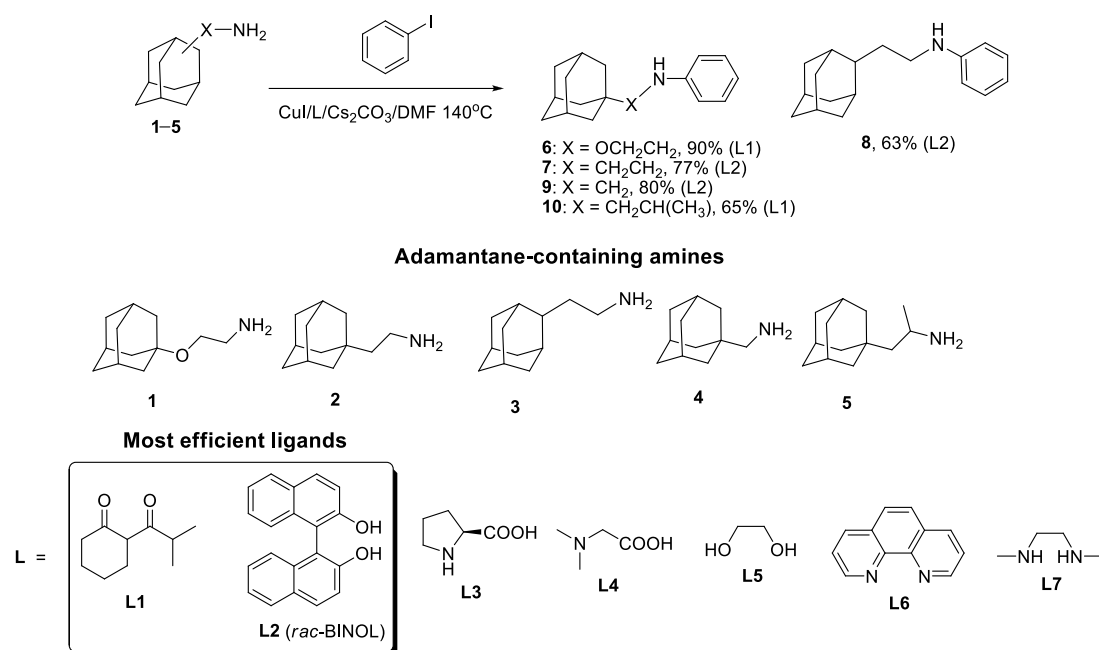
Our research interests in the field of Cu-catalyzed amination cover the reactions with adamantane-containing amines, diamines, oxadiazines, and polyamines. These substrates are interesting due to their often complicated and unpredictable reactivity in spite of the fact that the reactions proceed at primary amino groups. The outcome of the reactions is strongly dependent on the spatial environment of the amino group in the case of adamantaneamines, and the number of methylene groups, or oxygen or nitrogen atoms in the chain for di- and polyamines. Previously, we thoroughly studied the (hetero)arylation of these compounds in the presence of palladium catalysts [21] and found the scope and limitations of this approach. In the following investigations, we compared the possibilities of the application of a much cheaper copper and found the regularities of this process. Our ongoing research deals with the employment of the copper nanoparticles instead of the homogeneous CuI-catalyzed reactions as well as the search for new applications of the Chan-Lam reaction; the present review will describe all of these versions of the C(sp²)-N bond formation. The main objective of this review is to show the scope and limitations of the copper catalysis with regard to the arylation and heteroarylation of these amines, and the following aspects will be addressed: the dependence of the most appropriate catalytic system on the nature of reagents, possibilities of *N,N'*-di(hetero)arylation of the diamines, oxadiazines, and polyamines, the use of unsupported copper nanoparticles, and the character of the Chan-Lam amination employing adamantaneamines, diamines and oxadiazines.

2. CuI-Catalyzed Arylation of Adamantane-Containing Amines

Adamantane-containing amines and their derivatives are well-known for their versatile biological activity; it is sufficient to mention that amantadine (adamantane-1-amine hydrochloride) has been used as an antiviral and antiparkinsonian drug for decades [82], memantine for the treatment of Alzheimer's disease [83], and bromantane (N-(4-bromophenyl)adamantane-2-amine) [84] and its fluorine-containing analogue [85] as neurostimulation agents. Thus, it is quite natural that, previously, we paid much attention to the elaboration of efficient methods of *N*-(hetero)arylation of the adamantane-containing amines employing Pd(0)-catalyzed amination reactions.

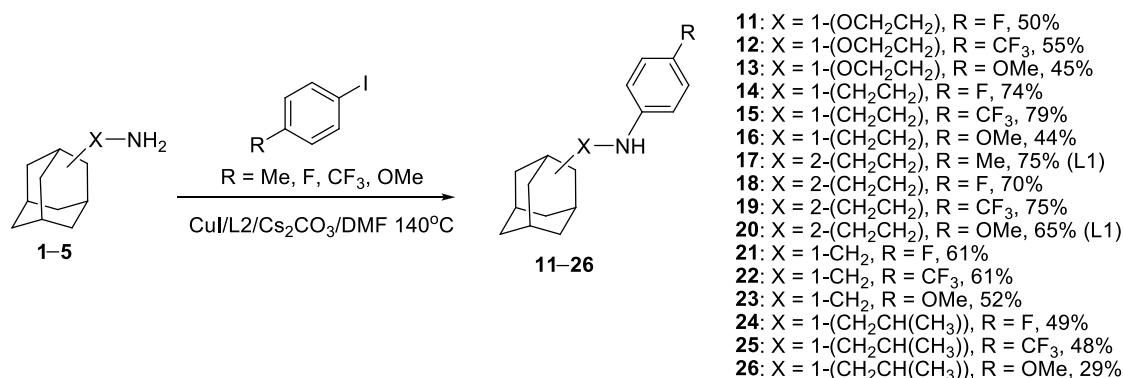
In the trend of replacing expensive palladium catalysis with much cheaper copper-catalyzed reactions, we carried out an investigation of the arylation of a series of adamantane-containing amines, 1–5, differing by the steric hindrances at the amino group, with a model iodobenzene in the presence of various copper catalysts (Scheme 1) [86]. Several widely employed ligands, L1–L7, were tested in the reaction and two of them, L1 (2-isobutyrylcyclohexanone) and L2 (*rac*-BINOL (BINOL = 2,2'-bi(1-naphthol)), both O,O-type, were found to be the most efficient in the reactions run in DMF at 140 °C and catalyzed

by a standard CuI in the presence of Cs₂CO₃. Other solvents which were tested such as propionitrile (EtCN) gave poorer yields, as well as did other copper sources (CuBr, CuOAc, CuOTf, Cu₂O, and CuO). Depending on the structure of the amine, they provided the yields of the *N*-arylation products in the range of 63–90% and were further used for the reactions with adamantane-containing amines. The highest yield (compound **6**, 90%) was observed in the reaction with the amine **1**, in which the amino group is located furthest from the adamantane core. The attempt to use bromobenzene instead of iodobenzene resulted in a dramatic diminishing of the product yield.



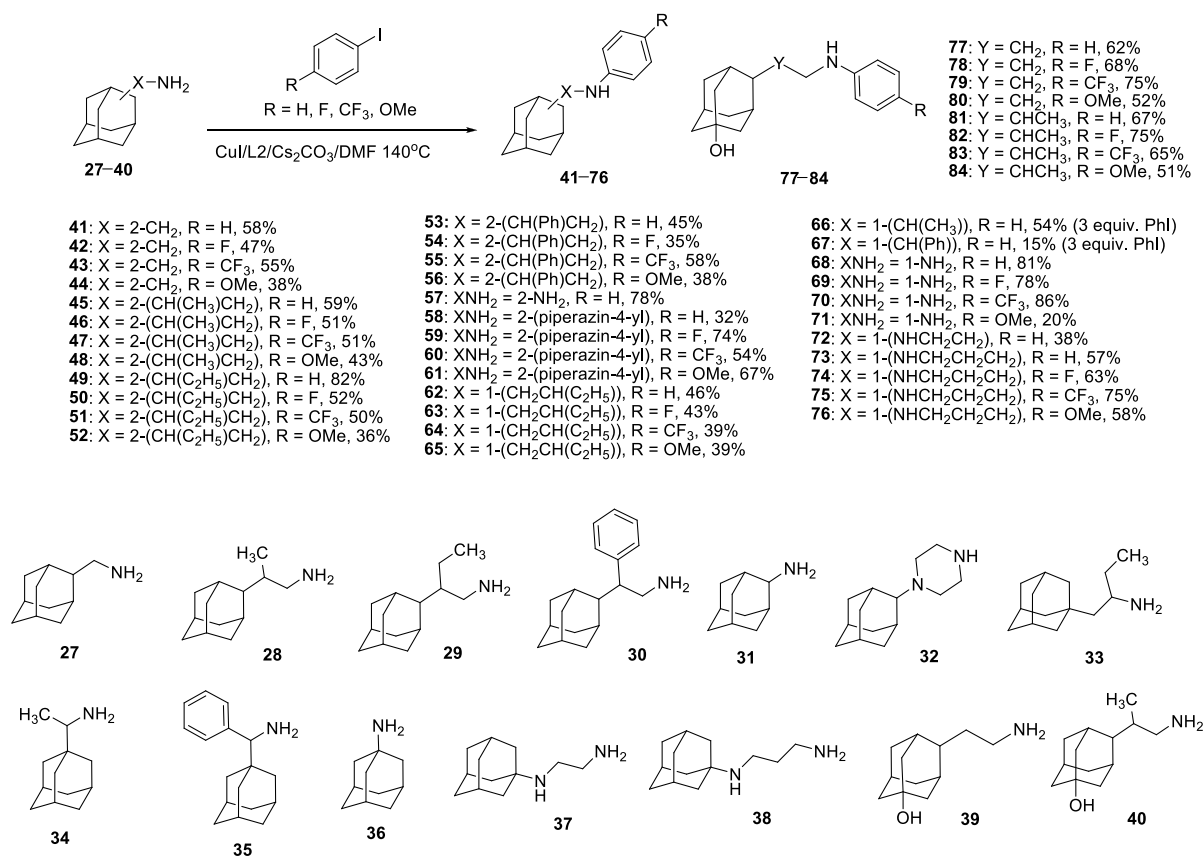
Scheme 1. CuI-catalyzed *N*-arylation of the adamantane-containing amines with iodobenzene.

The same amines, **1–5**, were introduced in the reactions with *para*-substituted iodobenzenes containing typical electron donor and electron withdrawing substituents (Scheme 2). It was interesting to follow the dependence of the yields of the *N*-arylated products; however, in the majority of cases, they ranged from 50 to 75%, and the advantage of the electron deficient 4-iodotrifluoromethylbenzene over electron donor 4-iodoanisole was quite moderate. Thus, in the reactions of **1–4**, CF₃-containing products **12**, **15**, **19**, and **22** were obtained in 55–79% yields, while MeO-containing products **13**, **16**, **20**, and **23** were synthesized in 44–65% yields. Only more sterically hindered amine **5** gave generally lower yields with all of the iodobenzenes which were tested (compounds **24–26**).



Scheme 2. CuI-catalyzed *N*-arylation of the adamantane-containing amines with *para*-substituted iodobenzenes.

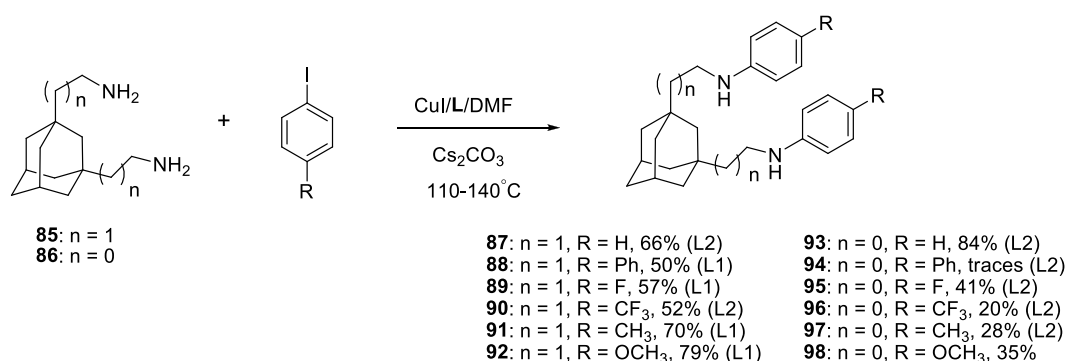
The extension of the series of the adamantane-containing amines (compounds 27–40) was undertaken to reveal the dependence of the amines' structure on the outcome of the copper-catalyzed *N*-arylation (Scheme 3) [87]. The reactions were run under optimized conditions with iodobenzene and its several *p*-substituted analogues. The amines 27–29, 31, 32, 36, and 38–40 provided similar results as described above, obviously, due to a lack of notable steric hindrances. The yields of the corresponding derivatives with the methoxy group were somewhat lower and ranged from 36 to 58%. To note, the presence of the hydroxyl group in the amines 39 and 40 did not alter its good reactivity in the *N*-arylation reactions. In the case of the amines 30 and 33, steric hindrances were more pronounced, which led to diminished yields of the corresponding products 53–56 and 62–65. Amines 34 and 35 were less reactive and the use of three equiv. of iodobenzene was inevitable, allowing for a 54% yield of the product 66, but only a 15% yield of 67. The reactivity of the amine 37 was also substantially lower than that of its analogue, 38, probably due to the presence of the ethylenediamine moiety in the first, which could better bind copper than the $\text{NCH}_2\text{CH}_2\text{CH}_2\text{N}$ fragment in 38, thus removing it from the catalytic cycle.



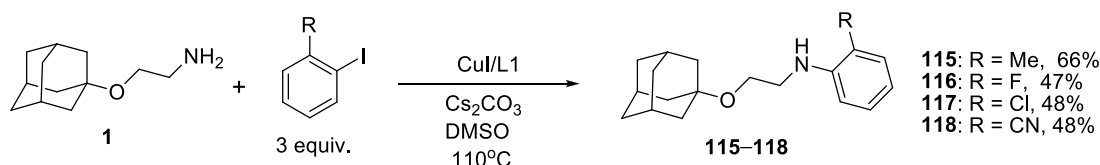
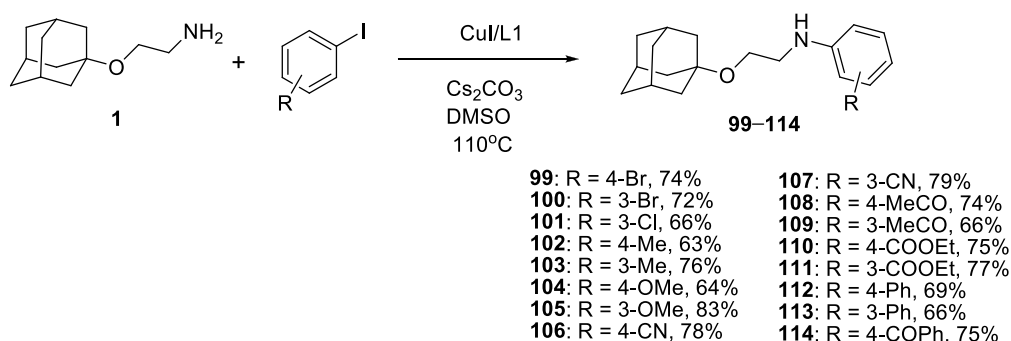
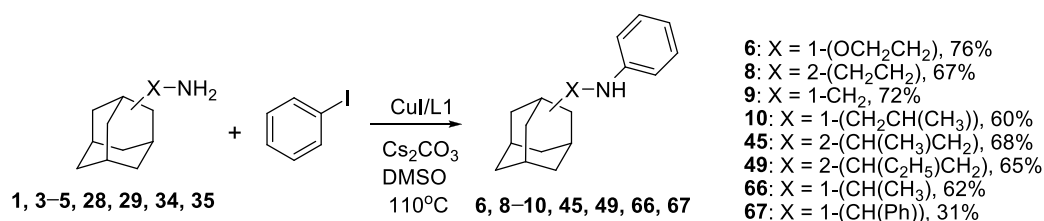
Scheme 3. CuI-catalyzed *N*-arylation of a variety of adamantane-containing amines with iodobenzenes.

The possibility to conduct an *N,N'*-diarylation reaction of the adamantane-containing diamines 85 and 86 was shown using several iodobenzenes (Scheme 4) [88]. Depending on the substituent in iodobenzene, ligand L1 or L2 was found to be optimal. Better yields were obtained with the diamine 85, where amino groups are located further from the adamantane core, and the yields of the corresponding derivatives 87–92 ranged from 50 to 79%. It is interesting that the best yield was observed in the reaction with the electron-enriched *p*-iodoanisole (compound 92), probably due to fewer side reactions with this less active iodide. In the reactions with the diamine 86, generally, the yields of the diarylated products were notably lower, and several by-products were isolated, evidencing a substantial contribution of the formation of the amine-imine followed by its transformation into the corresponding aldehyde and subsequent processes.

A special investigation was dedicated to the possibilities of the reactions run in DMSO instead of DMF [89]. The reactions with various amines, **1**, **3–5**, **28**, **29**, **34**, **35**, featuring a different spatial environment of the amino group were carried out with iodobenzene at 110 °C (Scheme 5). The results were quite comparable with those obtained in DMF at 140 °C; moreover, the arylation of the most hindered amines, **34** and **35**, allowed for increasing the yields of the corresponding derivatives, **66** and **67**, when three equiv. of PhI were employed. The reactions of the amine **1** with various *para*- and *meta*-substituted iodobenzenes provided good to high yields of the products **99–114** (63–83%). The influence of the electron properties of the substituents was poorly manifested though the yields in the reactions with the electron donors *p*-iodotoluene and *p*-iodoanisole, and these were among the smallest (63–64%). DMSO also helped to carry out the reactions with much more problematic *ortho*-substituted iodobenzenes (R = Me, F, Cl, CN). Further, 2-iodotoluene, taken in a three-fold excess, gave a 66% yield of the arylation product **115**, while other *o*-substituted iodobenzenes provided 47–48% yields of the corresponding compounds **116–118**.



Scheme 4. CuI-catalyzed *N,N'*-diarylation of the adamantane-containing diamines with iodobenzenes.

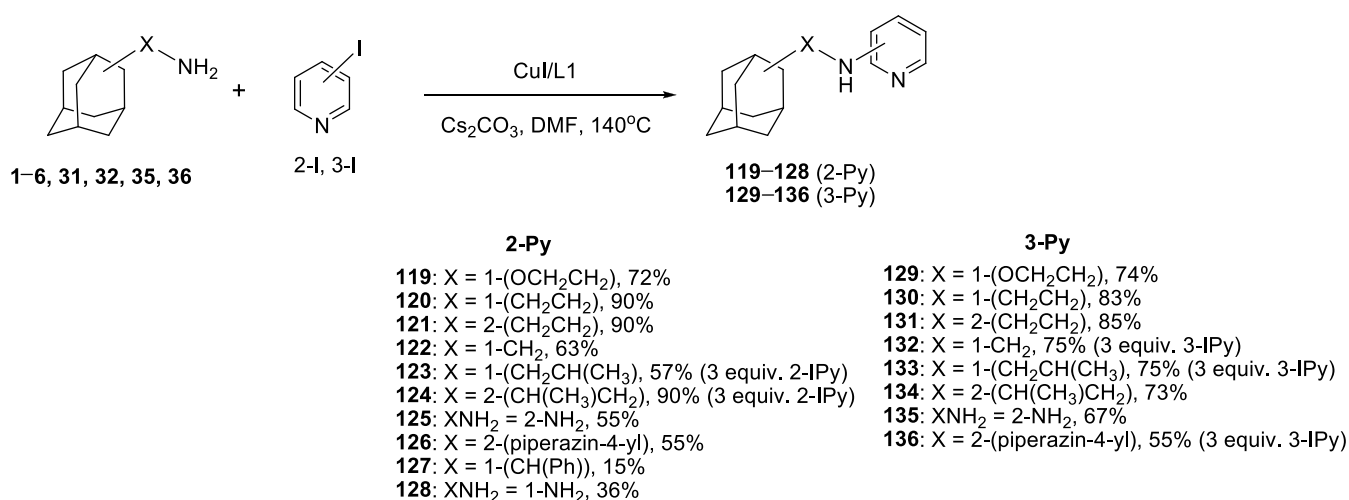


Scheme 5. CuI-catalyzed *N*-arylation of the adamantane-containing amines with iodobenzenes—effect of DMSO.

3. CuI-Catalyzed Heteroarylation of Adamantane-Containing Amines

Molecules which combine adamantane and pyridine moieties in their structure are of great importance due to their versatile biological activities. A 2-aminoadamantyl-containing derivative of pyrrolopyridine known as Peficitinib is used for rheumatoid arthritis treatment [90], and Cu(II) complexes of certain adamantane-substituted pyridines possess anticancer activity [91]. Derivatives of 2-aminopyridine with adamantane fragments were shown to inhibit 11 β -hydrosteroid dehydrogenase 11 β -HSD1 [92–94], and adamantane derivatives of three-substituted pyridine act as antifungal [95] and antinicotinic [96] agents. A great variety of methods exists to introduce heteroaromatic moieties in the adamantane-containing compounds. Interesting radical reactions for the direct transformations of adamantane have been described in a recent review [97]. Thus, quinolinyl-substituted adamantane was obtained via a radical process [98], and modern photocatalytic [99] and photoredox [100] processes were applied for the introduction of quinoline and trifluoromethylpyridine structural fragments into adamantane moiety.

We investigated the possibilities of the Cu(I)-catalyzed amination of 2- and 3-iodopyridines (Scheme 6). Ligands L1–L4 were tested and the best efficiency of L1 was undoubtedly shown. The reactivity of 2-iodopyridine was compared with that of 2-bromopyridine, and while the first afforded a 72% yield in the reaction with the amine **1**, the latter provided 57% of the *N*-pyrid-2-yl containing product **119**. A series of the adamantane-containing amines was tested in the reaction with 2-iodopyridine, and those with the unhindered amino group provided good to high yields of the target products (55–90%) [101]. In the case of the more sterically demanding amines **4** and **5**, the use of three equiv. of PhI was necessary to increase the yields of **123** and **124**; the more hindered amines **35** and **36** provided low yields of the corresponding products **127** and **128** (15 and 36%, respectively).

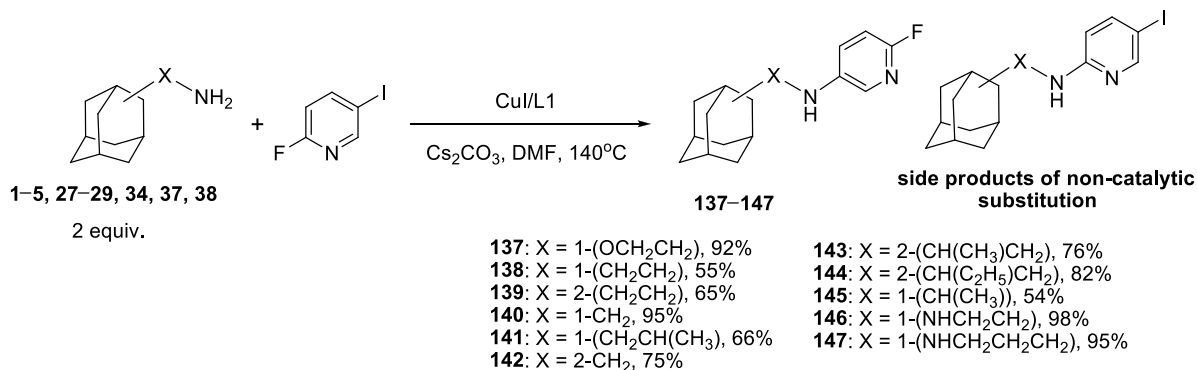


Scheme 6. CuI-catalyzed *N*-heteroarylation of the adamantane-containing amines with 2- and 3-iodopyridines.

Similar results were obtained with 3-iodopyridine (Scheme 6). Amines **1–3**, **28**, and **31** afforded 67–85% yields of the *N*-heteroarylated products and, in the case of the more sterically hindered amines **4** and **5**, the application of three equiv. of PhI was required to increase the yields of compounds **132**, **133**. To note, the secondary cyclic amino group in the piperazinyl derivative of adamantane **32** turned out to be less reactive than the primary amino groups, and it also demanded the use of PhI excess.

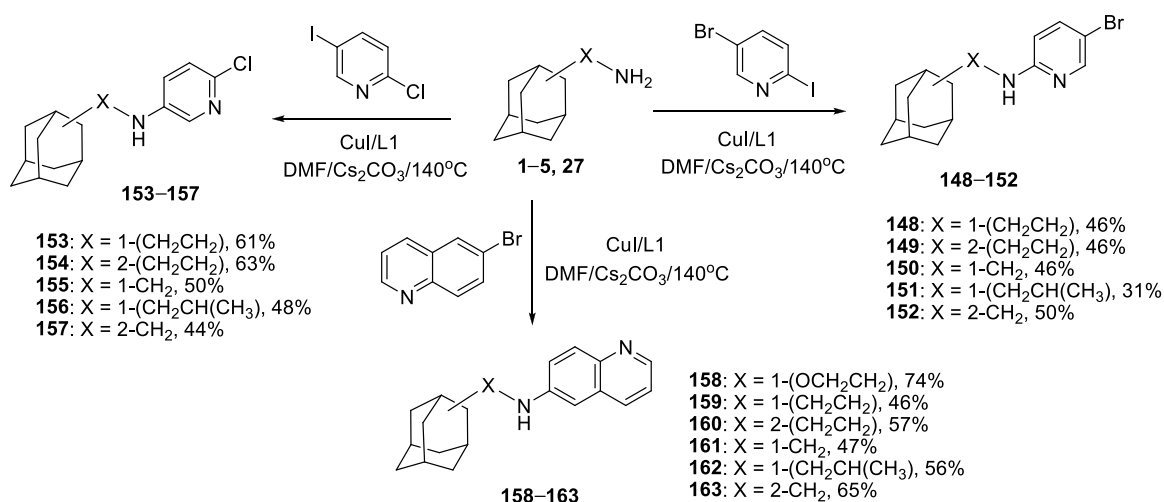
As a special case, we studied the amination of 2-fluoro-5-iodopyridine with a series of adamantane-containing amines (Scheme 7) [102]. The main peculiarity of this process is the competition of the Cu(I)-catalyzed substitution of the iodine atom and the non-catalytic substitution of the fluorine atom. In the case of the application of 10 mol% catalyst and 1:1 ratio of the reagents, generally, only the mixtures of the products were obtained, but the

use of 20 mol% catalyst and two-fold amount of the amine led to a substantial increase in the yields of the target 5-amino-2-fluoropyridines. In some cases (compounds **137**, **140**, **146**, and **147**), they reached 92–98%, and it is noteworthy that enough reluctant amines such as **34** and **37** successfully participated in this reaction.



Scheme 7. CuI-catalyzed *N*-heteroarylation of the adamantane-containing amines with 2-fluoro-5-iodopyridine.

The amines **1–5** and **27** were introduced in the reactions with other dihalopyridines to explore the selectivity of the iodine substitution (Scheme 8). The reactions with 2-bromo-5-iodopyridine turned out to be totally non-selective, and the amination of the isomeric 5-bromo-2-iodopyridine led to the corresponding products of the iodine substitution **148–152** in moderate yields (31–50%). The amination of 2-chloro-5-iodopyridine with the same amines produced compounds **153–157** in somewhat higher yields (44–63%). Nevertheless, the presence of much-less reactive additional halogen atoms (Cl, Br) diminished the selectivity of the amination process, giving rise to unidentified by-products.



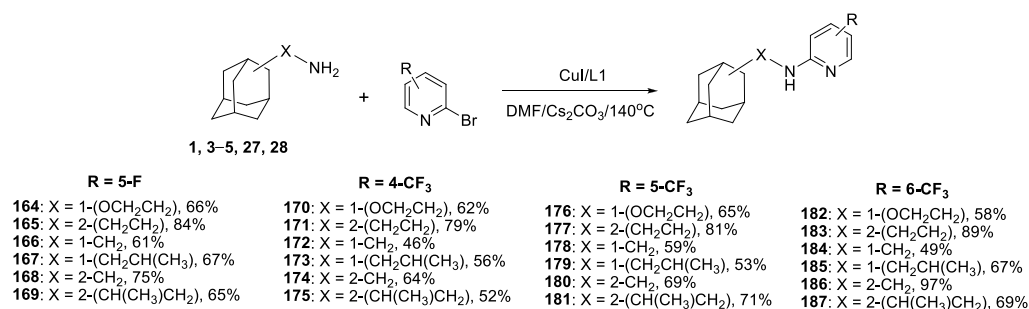
Scheme 8. CuI-catalyzed *N*-heteroarylation of the adamantane-containing amines with 5-bromo-2-iodopyridine, 2-chloro-5-iodopyridine, and 6-bromoquinoline.

Though 3-bromopyridine was found to be unreactive in Cu(I)-catalyzed amination, 6-bromoquinoline was successfully aminated by a series of adamantane-containing amines, and the yields of the products **158–163** varied from 46 to 74%. In all of the abovementioned processes, the CuI/L1 catalytic system was the most efficient.

It is well known that the adamantane derivatives bearing fluorine substituents are of substantial interest for a drug design. Indeed, compounds combining adamantane and fluoroaryl moieties display antituberculosis [103] and antiinflammatory [104] activities, as they inhibit tropoisomerase II [105] and purino receptor P2RX7 [106]. Adamantane deriva-

tives with trifluoromethyl substituent inhibit 11 β -HSD1 [93,107], melanin concentrating hormone MHC1 [108], and the ligands of cannabinoid receptor CB2 [109].

In this regard, we studied the heteroarylation of several adamantane-containing amines, **1**, **3–5**, **27**, and **28**, with fluoro- and trifluoromethyl-substituted 2-bromopyridines [110,111]. The reactions were run with 2-bromo-3-fluoro-, 5-fluoropyridines, and 3-, 4-, 5-, and 6-trifluoromethylsubstituted 2-fluoropyridines using the optimized CuI/L1 catalytic system (Scheme 9). It was found that 2-bromo-3-fluoropyridine and especially 2-bromo-3-trifluoromethylpyridine were not reactive enough under copper catalysis conditions due to steric hindrances at the bromine atom; thus, they were aminated using alternative Pd(0)-catalyzed reactions. The other 2-bromopyridines allowed for good to high yields of the corresponding products. The best results were obtained with the amine **3**, as it produced *N*-pyridyl derivatives **165**, **171**, **177**, and **183** in 79–89% yields. Among the CF₃ derivatives, 2-bromo-6-trifluoromethylpyridine allowed for the formation of the amination products in the highest yields (up to 97% in the case of **186**). Probably, the reactivity of the bromine atom in this compound was optimal: on one hand, enough for the amination reaction to proceed at a sufficient rate, on the other hand, allowing for avoidance of the formation of many by-products in the course of other catalytic processes.



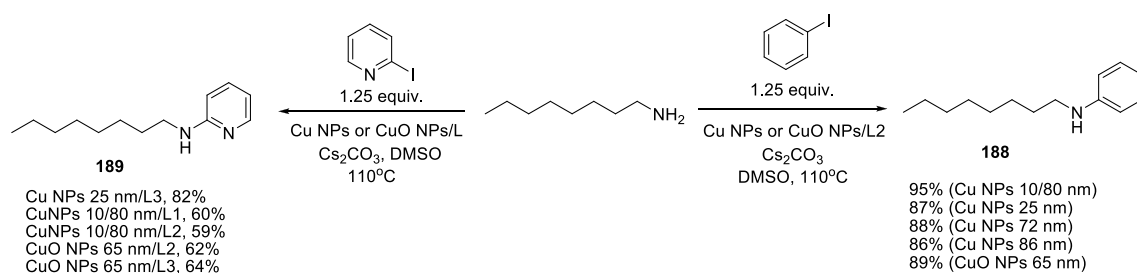
Scheme 9. CuI-catalyzed *N*-heteroarylation of the adamantane-containing amines with fluoro- and trifluoromethyl-substituted 2-bromopyridines.

4. C–N Bond Formation Using Unsupported Copper Nanoparticles

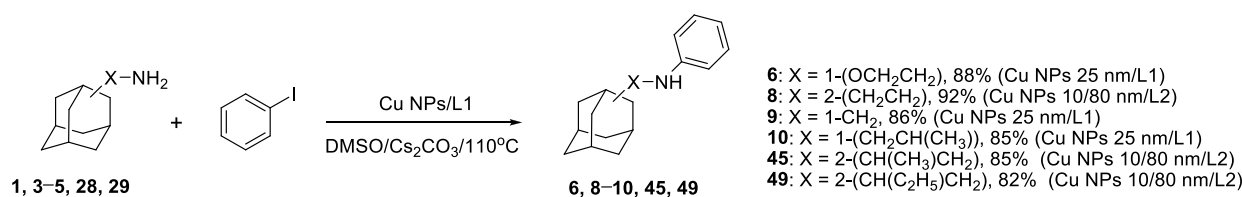
A special case is the use of copper nanoparticles (Cu NPs) in catalytic C–N bond formation. Often, copper and copper oxide nanoparticles immobilized on various supports are used, such as nanocatalysts immobilized on silica gel [112] and maghemite-silica magnetic support [113]; the following supports are also well-known: TiO₂ [114], graphene [115], and multiwall carbon nanotubes (MWCNTs) [116]. The use of unsupported copper nanoparticles in amination reactions is quite rare, and mainly CuO NPs were described for this purpose [117–121].

We began an investigation of the possibilities of the unsupported copper and copper oxide nanoparticles to promote the arylation of various amines, including adamantane-containing compounds. At first, the optimal conditions for the Cu-catalyzed amination of PhI with a model *n*-octylamine were established (Scheme 10) using copper nanoparticles of various average sizes: 10/80 nm (mixture of two fractions), 25 nm, 72 nm, 86 nm, and CuO 65 nm [122,123]. The reactions were run in DMSO or DMF at 110 °C or 140 °C, and a variety of ligands were tested. For the arylation with iodobenzene, L2 was found to be the best choice, as it allowed for the synthesis of *N*-octylaniline **188** in 86–95% yields. The best result (82%) for the heteroarylation of *n*-octylamine with 2-iodopyridine was obtained using the Cu NPs 25 nm/L3 catalytic system, and other combinations of nanoparticles and ligands gave poorer yields. The possibilities of the catalyst recycling were revealed to be strongly dependent on the copper source, and the best result was obtained with the Cu NPs 25 nm/L1 system (up to eight cycles without loss of the catalyst's activity).

Optimized conditions were applied to the arylation of a variety of adamantane-containing amines, **1**, **3–5**, **28**, and **29**, with iodobenzene (Scheme 11) [89].

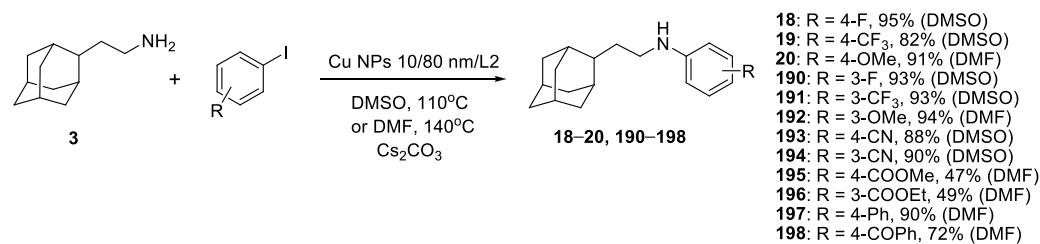


Scheme 10. Initial studies of the (hetero)arylation of a model *n*-octylamine with iodobenzene and 2-iodopyridine using unsupported Cu and CuO nanoparticles.



Scheme 11. *N*-arylation of the adamantane-containing amines with iodobenzene using unsupported Cu NPs.

The results were encouraging, as the yields of the target products (85–92%) were substantially higher than those obtained with CuI catalyst (65–76%, Scheme 5). The application of various substituted iodobenzenes for the arylation of amine **3** in the presence of another efficient system Cu NPs 10/80 nm/L2 (Scheme 12) was equally successful, and the yields of many products reached 90% and more (**18**, **20**, **190–192**, **194**, and **197**). Some of these reactions gave better results in DMSO at 110 °C, and others successfully proceeded in DMF at 140 °C. It is clearly seen that the high yields could be obtained both with electron donor and electron withdrawing substituents in iodobenzenes. The experiments on catalyst recycling demonstrated the possibility of the use of Cu NPs 25 nm/L1 for the arylation of amine **3** with iodobenzene at least in seven cycles without a decrease in the product's yield.

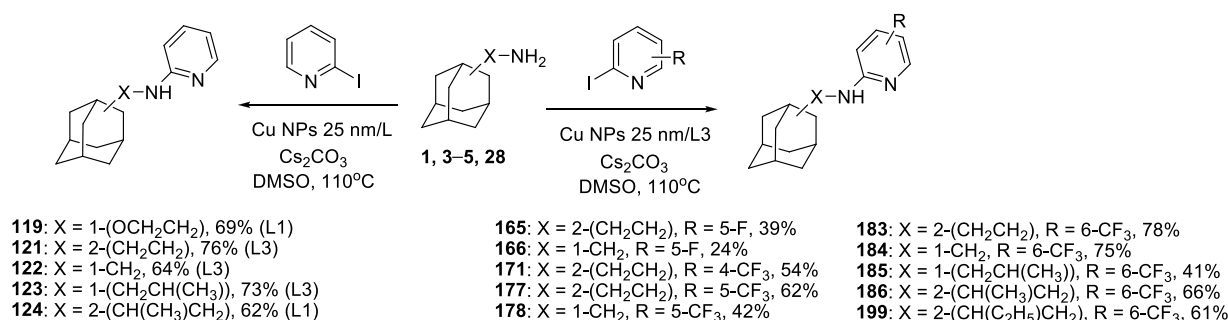


Scheme 12. *N*-arylation of the adamantane-containing amine **3** with substituted iodobenzenes using unsupported Cu NPs.

The *N*-heteroarylation of the adamantane-containing amines turned out to be more problematic (Scheme 13) [124]. The reactions of the amines **1**, **3–5**, and **28** with 2-iodopyridine gave 62–76% yields and it was noted that the effect of the ligand (L1 or L3) was dependent on the structure of the amine. In the reactions with the fluorine-containing 2-bromopyridines, the Cu NPs 25 nm/L3 catalytic system was found to be the best; however, the yields of the products ranged from humble, 24% (**166**), to high, 75–78% (**183**, **184**). Generally, as in the reactions catalyzed by CuI/L1, the best results were obtained with 2-bromo-6-trifluoromethylpyridine.

While copper nanoparticles were more efficient than CuI in the *N*-arylation of the adamantane-containing amines with iodoarenes, they provided lower yields with bromoarenes under the same conditions, e.g., the attempts to introduce 6-bromoquinoline in the amination with several amines in the presence of Cu NPs/L1 resulted in 11–25% yields of the corresponding products **158**, **160**, and **161**, while these reactions catalyzed by

the CuI/L1 system provided 47–74% yields (Scheme 8). However, the application of Cu NPs/L2 for these reactions provided stable 70–75% yields of the products.

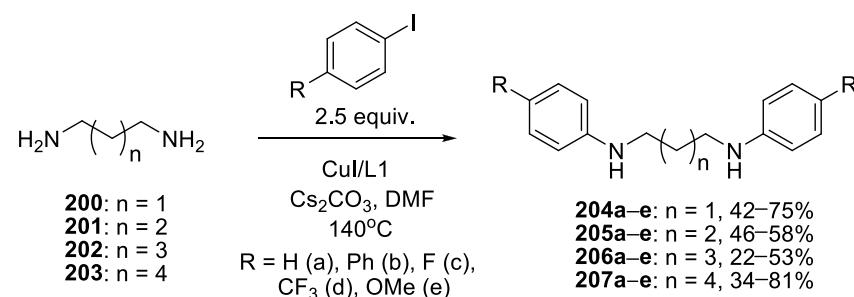


Scheme 13. *N*-heteroarylation of the adamantane-containing amines with substituted iodopyridines using unsupported Cu NPs.

5. *N,N'*-Diarylation of the Di- and Polyamines Using Cu(I) Catalysis

Naturally occurring diamines such as putrescine **201**, cadaverine **202**, and some polyamines, are biologically active compounds which play a key role in cells' proliferation and apoptosis [125], and more and more attention is attracted to their *N*-aryl derivatives [126–128], E.g., such derivatives of putrescine and cadaverine showed cytotoxic and antiproliferative activity [129], *N*-(*p*-tolyl) substituted cadaverine, and hexane-1,6-diamine demonstrated an affinity to NMDA receptors and antileishmaniasis activity [130,131].

We were mainly interested in the synthesis of *N,N'*-diarylsubstituted diamines and, for this purpose, conducted a series of reactions of the diamines **200–203** with iodobenzene and some *p*-substituted derivatives (Scheme 14) [132]. The catalytic system CuI/L1 was shown to be optimal and the yields of the reaction products **204–207** reached 70–80% in the best cases. It was noted that the electron-enriched *p*-iodoanisole was less reactive, giving 20–50% yields of the target compounds **204e–207e**; on the contrary, the reactions with electron-deficient 4-iodobenzotrifluoride provided enough high yields of the compounds **204d–207d**.

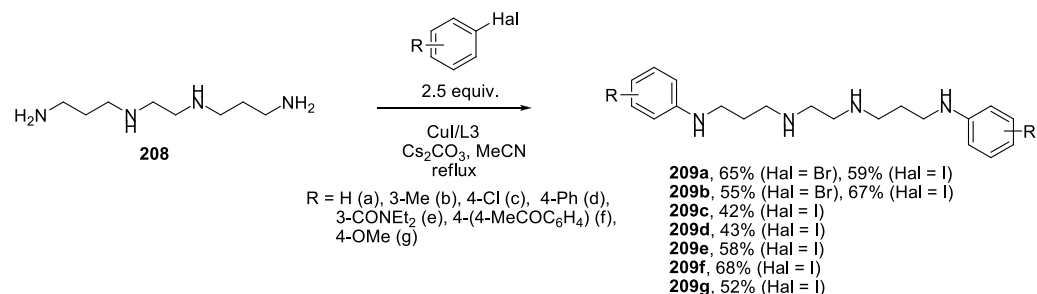


Scheme 14. CuI-catalyzed *N,N'*-diarylation of the diamines **200–203** with substituted iodobenzenes.

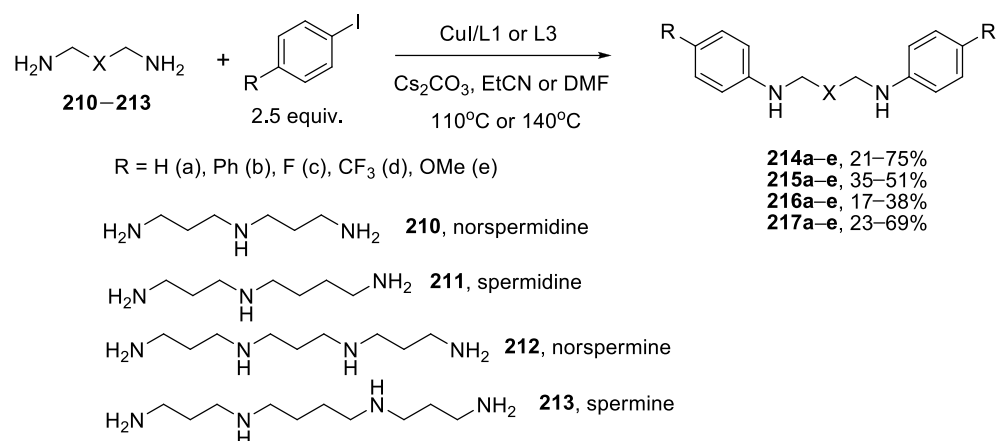
The investigation of the *N,N'*-diarylation of the tetraamine **208** with iodobenzene and a number of aryl iodides revealed that the best ligand in this case was L3 with MeCN as a solvent (Scheme 15) [133]. Bromobenzene was shown to be equally reactive with this tetraamine, which could be due to the coordination of copper to the tetraamine, resulting in a higher reactivity of the catalytic species. On the other hand, it caused the side reaction of the *N*-arylation of the secondary amino groups in the tetraamine, and moderate to good yields of the target compounds **209a–g** (42–67%) were obtained independently of the electron properties of the substituents in iodobenzenes.

Further, several iodobenzenes were introduced in the reactions with the naturally occurring tri- and tetra-amines **210–213** (Scheme 16). The yields of the target *N,N'*-diaryl derivatives **214–217** varied substantially depending on the nature of the polyamines and substituents in the aryl iodides. To note, in the case of **210** and **212**, containing only

trimethylenediamine moieties, the CuI/L3/EtCN catalytic system was more efficient, while in the reactions of **211** and **213** with tetramethylenediamine fragments, CuI/L1/DMF was found to act better. Again, *p*-iodoanisole provided the lowest yields of the target compounds, and the *N,N'*-diarylation of **210** and **213** generally proceeded more smoothly and resulted in higher yields of the products compared to the two other polyamines.



Scheme 15. CuI-catalyzed *N,N'*-diarylation of the tetraamine **208** with substituted halobenzenes.

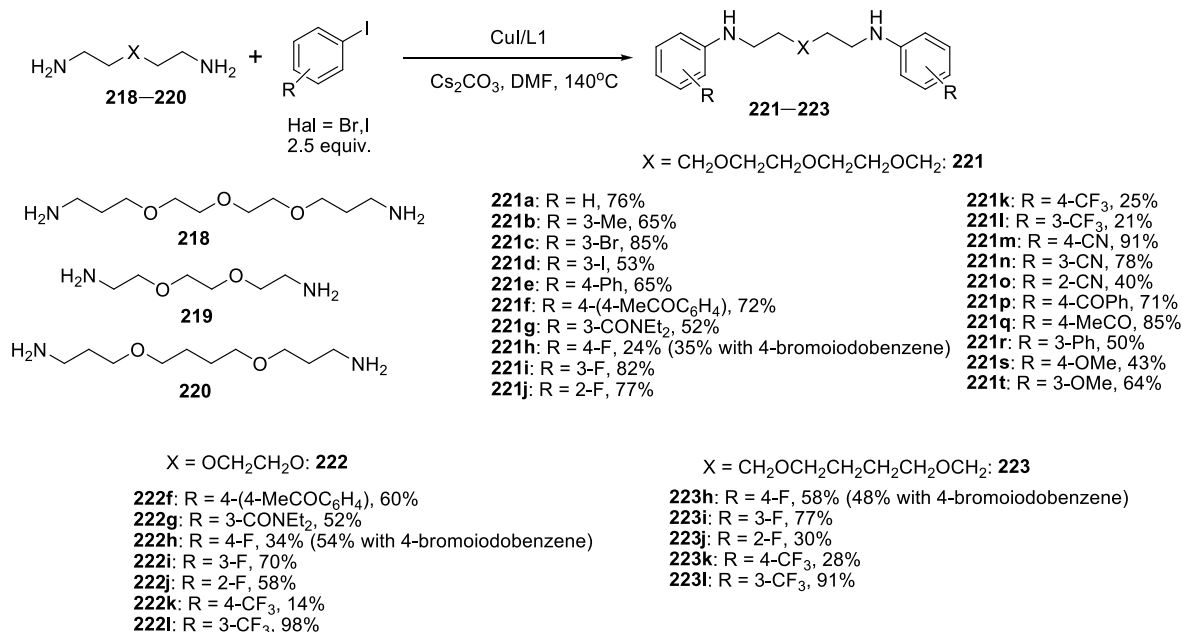


Scheme 16. CuI-catalyzed *N,N'*-diarylation of the tri and tetra-amines **210–213** with substituted iodobenzenes.

Oxadiazines, due to their hydrophilicity and chelating ability, are employed as flexible linkers for the synthesis of biologically active compounds. The structure and the length of the linker can modify the activity [134], and linkers can be incorporated in the organic molecules [135–138] or serve as a bidentate ligand for binding two Pd or Pt complexes [139].

We investigated the *N,N'*-diarylation of three different oxadiazines, **218–220**, varying their length, and number of oxygen atoms and methylene groups between N and O atoms (Scheme 17) [140]. CuI/L1 in DMF was shown to be the most active catalytic system, and trioxadiazine **218** was reacted with a large series of aryl iodides. In the majority of cases, the yields were good to high, attaining 91% in the case of **221m** (with 4-CN substituent in the phenyl ring). A lower, 43%, yield was recorded for the product **221s**, obtained from the electron-enriched *p*-iodoanisole, and, suddenly, the reactions with *p*-fluoroiodobenzene and 4-iodobenzotrifluorides gave very small yields of the target compounds **221h,k**. Similar observations were true for the two other oxadiazines, **219** and **220**, which also encountered difficulties upon reacting with these aryl iodides, especially with the latter one. On the contrary, much higher yields were observed in the reactions with *o*-fluoroiodobenzene (77% yield of **221j** and 58% yield of **222j**).

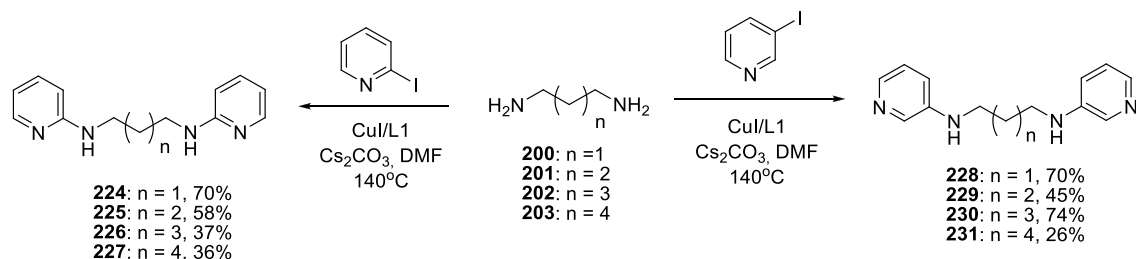
Special investigations were also carried out to verify the absence of the side *N,N'*-diarylation process, which is common for palladium-catalyzed amination reactions. For this purpose, diamines and oxadiazines were reacted with 10 equiv. of PhI and only the traces of the polyarylated derivatives were detected in the reaction mixtures in several cases. On the other hand, it helped to increase the yields of some *N,N'*-diphenyl derivatives to 80–90%.



Scheme 17. CuI-catalyzed *N,N'*-diarylation of the oxadiazines **218–220** with substituted iodobenzenes.

6. *N,N'*-Diheteroarylation of Di- and Polyamines Using Cu(I) Catalysis

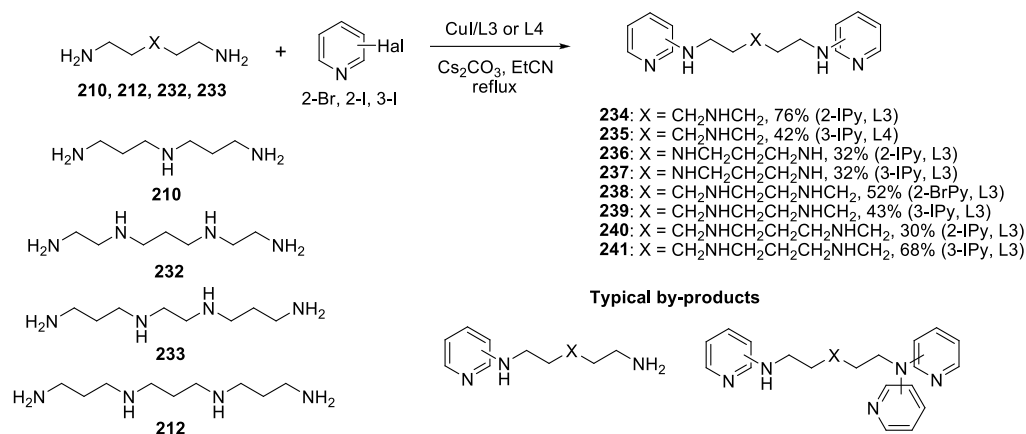
The next part of our research was dedicated to the *N,N'*-heteroarylation of the di- and poly-amines. The diamines **200–203** reacted with 2- and 3-iodopyridines in the presence of the CuI/L1 catalytic system, and the yields of the target dipyridinyl derivatives were dependent on the nature of the diamines and were the highest for the shortest diamine (compounds **224** and **228**) (Scheme 18) [141]. The use of 20 mol% catalyst was crucial for the *N,N'*-diheteroarylation; however, in many cases, monopyridinyl derivatives were also isolated.



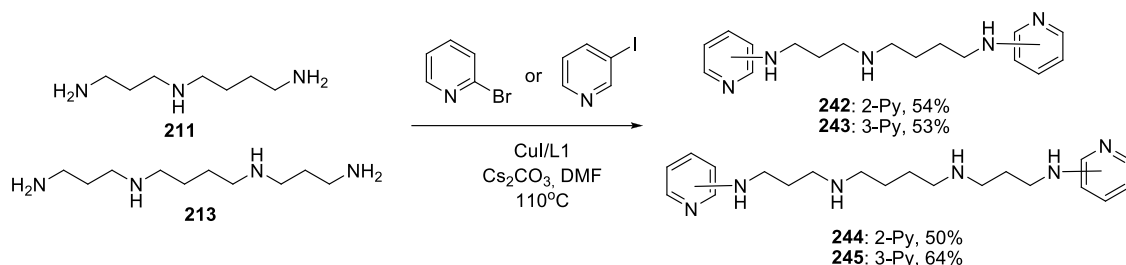
Scheme 18. CuI-catalyzed *N,N'*-diheteroarylation of the diamines **200–203** with 2- and 3-iodopyridines.

More complicated were the reactions of tri- and tetraamine **210**, **212**, **232**, and **233** with 2- and 3-iodopyridines due to many side reactions such as the heteroarylation of the secondary amino group and the *N,N*-diheteroarylation of the primary amino group (Scheme 19) [142].

In several cases, the formation of great amounts of monopyridinyl derivatives was observed. Almost in every case, the adjustment of the catalytic system was needed, including the ligands (L3 or L4), the catalyst loading, and a proper choice between 2-iodopyridine and less-active 2-bromopyridine. As a result, it was possible to obtain the *N,N'*-di(pyridine-2-yl) derivative of the triamine **234** and the *N,N'*-di(pyridine-3-yl) derivative of the tetraamine **241** in good yields (76 and 68%, respectively), while other products, **235–240**, were isolated in moderate yields: 30–52%. Spermidine **211** and spermine **213** reacted better with 2-bromopyridine and 3-iodopyridine, providing 50–64% yields of **242–245** (Scheme 20), but they demanded the application of the another catalytic system, i.e., CuI/L1/DMF, due to their lower reactivity, probably due to the presence of the tetramethylenediamine moieties [141].

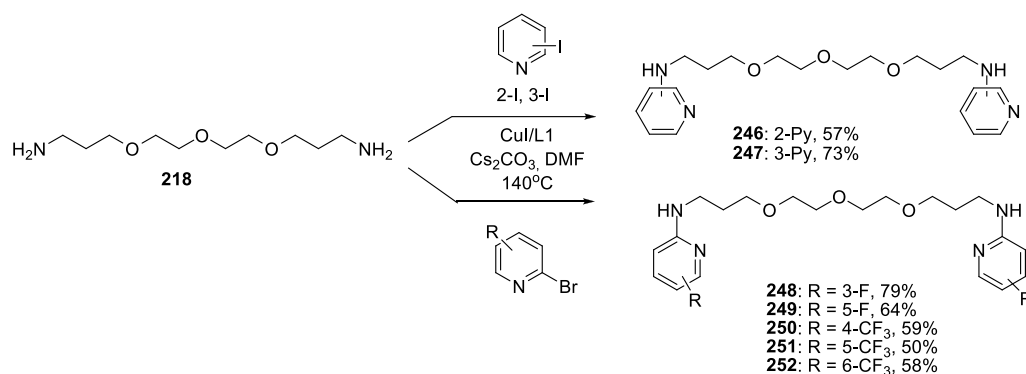


Scheme 19. CuI-catalyzed *N,N'*-diheteroarylation of the tetraamines **210**, **212**, **232**, and **233** with 2- and 3-iodopyridines.



Scheme 20. CuI-catalyzed *N,N'*-diheteroarylation of the naturally occurring triamine **211** and tetraamine **213** with 2- and 3-iodopyridines.

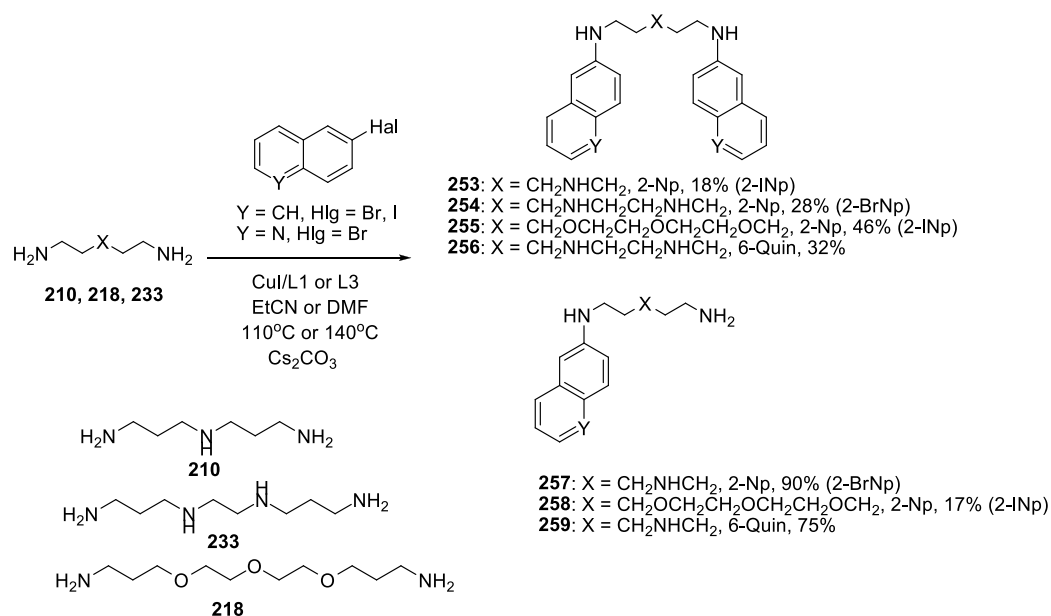
The *N,N'*-diheteroarylation of the trioxadiazine **218** with 2- and 3-iodopyridines as well as fluoro- and trifluoromethylsubstituted 2-bromopyridine was successful in the presence of CuI/L1 (Scheme 21), giving good to high yields of the desired compounds. Notable is the 79% yield of the compound **248**, the product of the reaction with 2-bromo-3-fluoropyridine; in this case, the substitution at the *ortho*-position was unexpectedly very efficient.



Scheme 21. CuI-catalyzed *N,N'*-diheteroarylation of the trioxadiazine **218** with 2- and 3-iodopyridines and substituted 2-bromopyridine.

The possibility of introducing simple fluorophore groups such as naphthalene and quinoline in the polyamines was shown using several exemplary reactions (Scheme 22) [143]. Triamine **210** reacted with 2-iodonaphthalene to give only an 18% yield of the target diaryl derivative **253**, while tetraamine **233** was able to produce the corresponding compound **254** in a 28% yield using less-active 2-bromonaphthalene. Note that the reaction of **210** with 2-bromonaphthalene afforded only monoaryl derivative **257** in 90% yields and the reac-

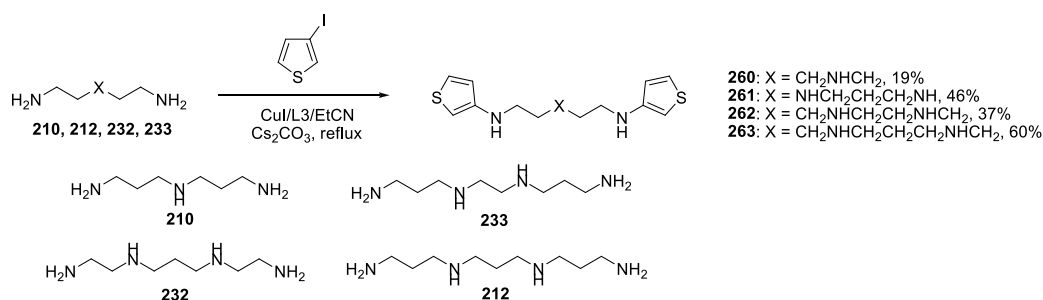
tion of the tetraamine **233** with a more active 2-iodonaphthalene was totally non-selective. Similar results were obtained when reacting tri- and tetra-amines with 6-bromoquinoline (formation of monoquinolinyl derivative of the triamine **259** and *N,N'*-diquinolinyl derivative of the tetraamine **256**). These facts demonstrate a strong dependence of the reactivity of polyamines on the number of ethylenediamine and trimethylenediamine fragments in their structure, as well as on the activity of (hetero)aryl halides.



Scheme 22. CuI-catalyzed *N,N'*-di(hetero)arylation of the polyamines **210**, **218**, and **233** with 2-bromo- and 2-iodonaphthalenes and 6-bromoquinoline.

Trioxadiazamine **218** was less active and helped to produce its *N,N'*-dinaphthyl derivative **255** in a higher yield (46%) using 2-iodonaphthalene.

The reactions of the triamine **210** and several tetraamines **212**, **232**, and **233** with 3-iodothiophene were run in the presence of CuI/L3 in boiling EtCN, and the yields of the desired *N,N'*-diheteroaryl derivatives **260–263** were also strongly dependent on the nature of the starting polyamines (Scheme 23) [144]. The highest yield (60%) was obtained with the tetraamine **212**, possessing only trimethylenediamine moieties.

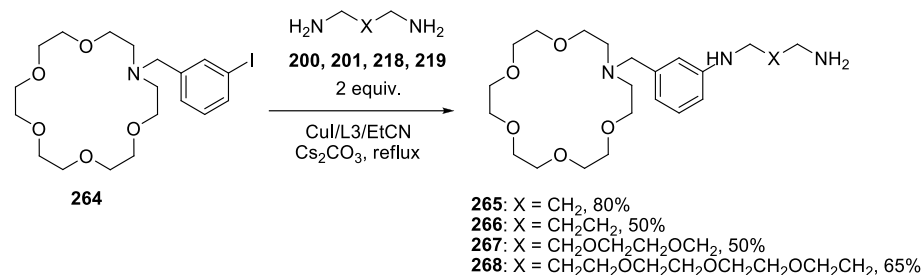


Scheme 23. CuI-catalyzed *N,N'*-di(hetero)arylation of the polyamines with 3-iodothiophene.

7. Copper-Catalyzed Amination in the Modifications of the Aza- and Diazacrown Ethers

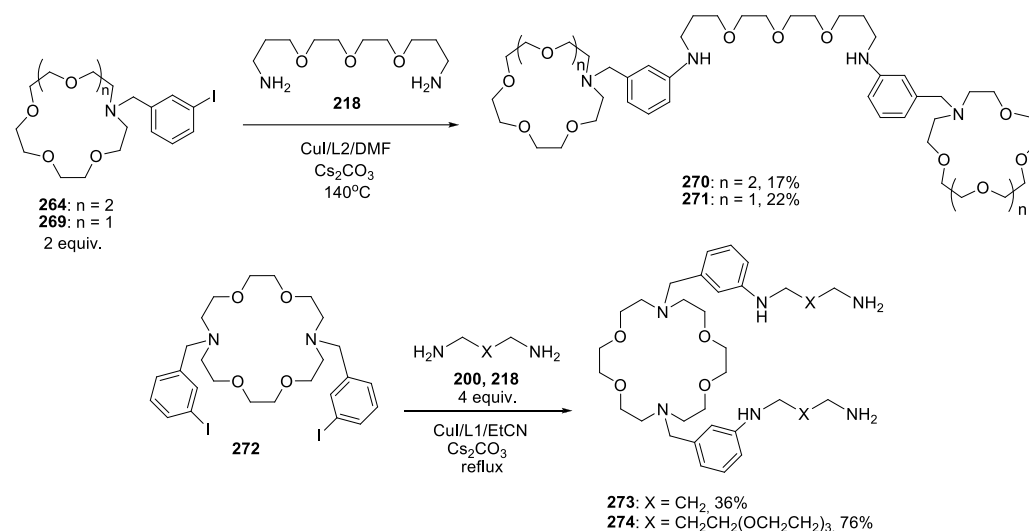
Our investigations of the synthesis of the macrocycles definitely showed that copper catalysis is not applicable to this process, as all macrocyclization reactions require diluted enough conditions and Cu-catalyzed amination normally proceeds at 0.25–0.5 M concentrations of the reagents. However, it can be used for some modifications of the macrocycles possessing iodobenzyl substituents. It was shown to be possible to synthesize diamino

derivatives of the azacrown ethers using this approach (Scheme 24). The reactions of *N*-(3-iodobenzyl)-substituted 1-aza-18-crown-6 **264** were successfully aminated with the excess of the diamines **200** and **201**, and the oxadiazines **218** and **219** to give the corresponding derivatives **265–268** in 50–80% yields [145].



Scheme 24. CuI-catalyzed amination of 3-iodobenzyl-substituted 1-aza-18-crown-6 ether **264**.

Note that the isomeric *N*-(4-iodobenzyl) derivative was much less reactive and provided 20% or less yields of the monoamination products. This method can be employed in the synthesis of bismacrocylic compounds with the trioxadiazine linkers **270** and **271**; in this case the excess of azacrown derivatives should be used (Scheme 25). Also, the diamination of the *N,N'*-di(3-iodobenzyl) derivative of diazacrown **272** was carried out using an excess of propane-1,3-diamine **200** and trioxadiazine **218**, with the yields of the corresponding products **273** and **274** being 36 and 76%, respectively.



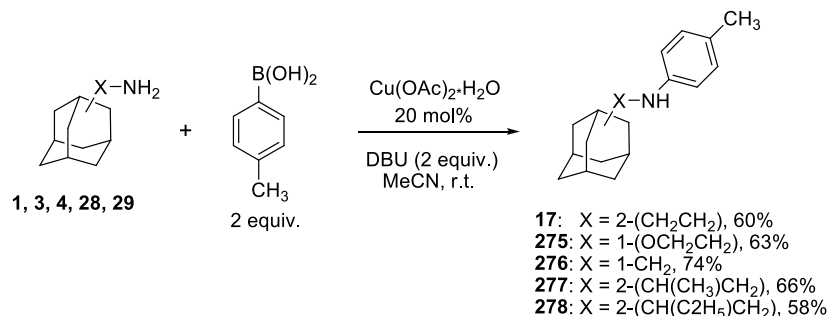
Scheme 25. CuI-catalyzed *N,N'*-diarylation and diamination of the derivatives of the aza- and diazacrown ethers.

The attempts to apply the analogous reactions to the iodobenzyl derivatives of porphyrins were not successful and the introduction of the diamine and oxadiazine moieties in these compounds could be achieved only using Pd-catalyzed amination reactions [146].

8. Chan-Lam Reactions for the Arylation of Adamantane-Containing Amines, Diamines and Oxadiazines

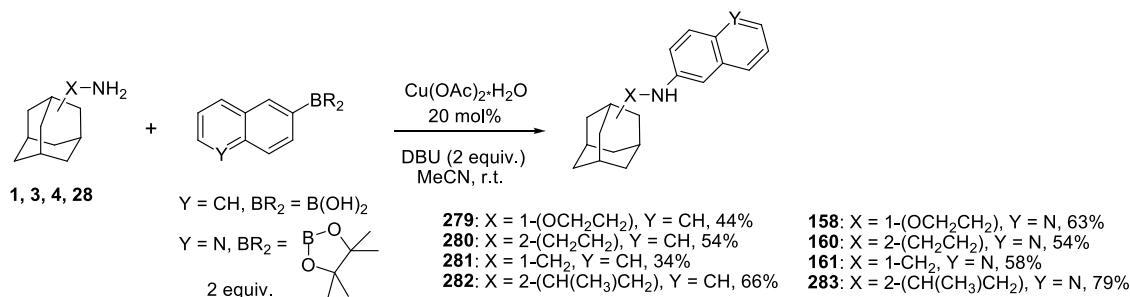
At the present time, the amines' arylation with arylboronic acids and their derivatives known as the Chan–Lam reaction has been developed steadily [147], and we also explored this alternative to arylation with aryl halides. At first, we optimized the reaction conditions using a model *p*-tolylboronic acid in the reactions with various adamantane-containing amines (Scheme 26). Standard copper (II) acetate in MeCN in the presence of DBU (2 equiv.)

and the use of *p*-tolylboronic acid excess were found to provide the highest yields. They ranged from 58 to 74% for the *N*-tolyl derivatives **17**, **275–278**.



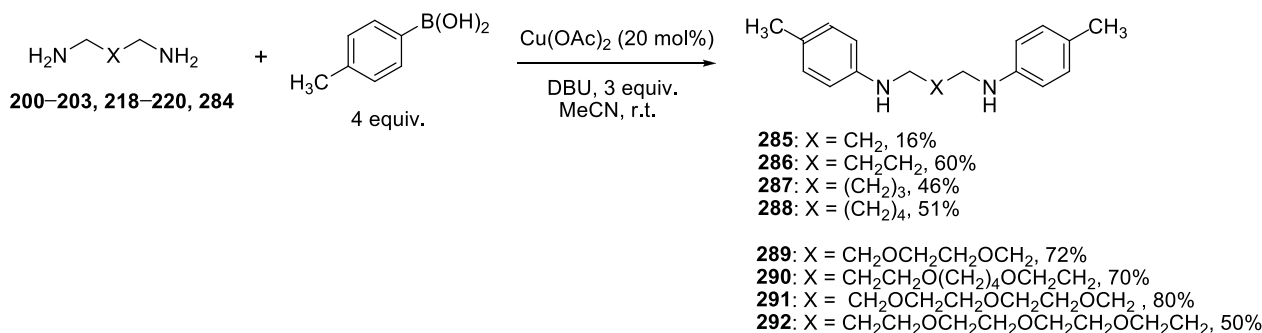
Scheme 26. Chan–Lam *N*-arylation of the adamantane-containing amines with the model *p*-tolylboronic acid.

The possibility of introducing naphthalene and quinoline moieties in the adamantane-containing amines using this method was also shown (Scheme 27). The reactions with 2-naphthalenylboronic acid gave 34–66% yields of the corresponding derivatives **279–282**, while the reactions with 6-quinolinyl picolinyl borate produced the compounds **158**, **160**, **161**, and **283** in 54–79% yields.



Scheme 27. Introduction of the naphthyl and quinolinyl substituents to adamantane-containing amines via Chan–Lam reaction.

At the next step, the conditions for the *N,N'*-diarylation of the diamines **200–203** and the oxadiazines **218–220**, **284** were elaborated (four equiv. of *p*-tolylboronic acid and three equiv. of DBU), and the corresponding target compounds **285–288** and **289–292** were synthesized (Scheme 28) [148]. Except for the propane-1,3-diamine **200** with the shortest chain, which obviously formed an inert complex with the Cu(II) cation, the other diamines and all of the oxadiazines provided good to high yields of the *N,N'*-diarylated products (46–80%). Thus, the Chan–Lam reaction can be judged as a valuable prospective addition to the previously developed methods for the introduction of the aryl and heteroaryl substituents in the adamantane-containing amines, diamines, and oxadiazines.



Scheme 28. *N,N'*-diarylation of the diamines and oxadiazines with the model *p*-tolylboronic acid.

9. Conclusions and Prospects

The results presented in this review clearly demonstrate wide possibilities of copper-catalyzed amination reactions for the synthesis of *N*-(hetero)aryl derivatives of the valuable adamantane-containing amines, diamines, oxadiazines, and polyamines. The reactions catalyzed by the most commonly used CuI were shown to proceed in DMF at 140 °C or in DMSO at 110 °C in the presence of O,O-ligands (2-isobutyrylcyclohexanone and *rac*-BINOL), in the case of the adamantane-containing amines, diamines, and oxadiazines or in the presence of N,O ligands (proline, *N,N*-dimethylglycine) in the case of tri- and tetra-amines. Under these conditions, iodoarenes and iodopyridines were found to be substantially more reactive than their bromosubstituted analogues, although with certain exclusions. Thus, bromobenzene and 2-bromopyridine were suitable for reactions with some polyamines, and more reactive F- and CF₃-substituted 2-bromopyridines were successfully employed in reactions with the adamantane-containing amines. The majority of the adamantane-containing amines were found to normally participate in the copper-catalyzed *N*-(hetero)arylation reactions; nevertheless, several bulky amines with enough hindered amino groups were reluctant in this process and could provide target products in normal yields only in the Pd-catalyzed amination reactions. Copper-catalyzed amination has an important advantage over its Pd-catalyzed alternative, as it does not afford *N,N*-diarylation products even in the presence of a great excess of the aryl halide. On the other hand, some drawbacks should be mentioned such as insufficient yields of the *N,N'*-diaryl compounds in certain cases due to the formation of substantial amounts of mono-derivatives. Another drawback is a possibility of the side reaction of the secondary dialkylamino group arylation in linear polyamines. At last, the reactions need concentrated solutions making macrocyclization reactions impossible.

The possibility of using commercially available Cu and CuO nanoparticles for reactions with the adamantane-containing amines has been investigated recently, and the possibility of obtaining high yields of the *N*-aryl derivatives was demonstrated. An important advantage of this approach is the possibility of reuse of the catalyst for up to seven cycles without a loss of reactivity. Further development of this method is required to engage di- and poly-amines in (hetero)arylation using copper nanoparticles. Equally, it is important to continue investigations revealing the action of nano catalysts, metal leaching during the reaction, and catalyst reusability to study the dependence of the catalyst activity on the ligands and solvents employed. This first successful syntheses of the arylated adamantane-containing amines, diamines, and oxadiazines under the conditions of the Chan–Lam reaction indicate a need to further search for its scope and limitations with our compounds and the application of the copper nanocatalysts in this process.

Author Contributions: Conceptualization, A.D.A. and I.P.B.; investigation, S.P.P., A.V.M., V.I.F., D.S.K., A.S.M. and A.A.Y.; writing—original draft preparation, A.D.A. and A.S.A.; writing—review and editing, A.S.A., A.D.A. and I.P.B.; funding acquisition, A.D.A. All authors have read and agreed to the published version of the manuscript.

Funding: This work was supported by the Russian Science Foundation (grant no. 22-23-00518).

Data Availability Statement: Not applicable.

Conflicts of Interest: The authors declare no conflict of interest.

References

1. Ullmann, F.; Bielecki, J. Ueber Synthesen in der Biphenylreihe. *Ber. Dtsch. Chem. Ges.* **1901**, *34*, 2174–2185. [CrossRef]
2. Ullmann, F. Ueber eine neue Bildungsweise von Diphenylaminderivaten. *Ber. Dtsch. Chem. Ges.* **1903**, *36*, 2382–2384. [CrossRef]
3. Ullmann, F.; Sponagel, P. Ueber Phenylirung von Phenolen. *Justus Liebigs Ann. Chem.* **1906**, *350*, 83–107. [CrossRef]
4. Goldberg, I. Ueber Phenylirungen bei Gegenwart von Kupfer als Katalysator. *Ber. Dtsch. Chem. Ges.* **1906**, *39*, 1691–1692. [CrossRef]
5. Lindley, J. Tetrahedron report number 163: Copper assisted nucleophilic substitution of aryl halogen. *Tetrahedron* **1984**, *40*, 1433–1456. [CrossRef]

6. Kunz, K.; Scholz, U.; Ganzer, D. Renaissance of Ullmann and Goldberg Reactions—Progress in Copper Catalyzed C-N-, C-O- and C-S-Coupling. *Synlett* **2003**, *2003*, 2428–2439. [CrossRef]
7. Fanta, P.E. The Ullmann Synthesis of Biaryls. *Synthesis* **1974**, *1974*, 9–21. [CrossRef]
8. Tuong, T.D.; Hida, M. Mechanism of the Ullmann Condensation. I. Kinetic and Thermodynamic Studies. *Bull. Chem. Soc. Jpn.* **1970**, *43*, 1763–1768. [CrossRef]
9. Affouard, C.; Crockett, R.D.; Diker, K.; Farrell, R.P.; Gorins, G.; Huckins, J.R.; Caille, S. Multi-Kilo Delivery of AMG 925 Featuring a Buchwald–Hartwig Amination and Processing with Insoluble Synthetic Intermediates. *Org. Proc. Res. Dev.* **2015**, *19*, 476–485. [CrossRef]
10. Ku, Y.-Y.; Chan, V.S.; Christesen, A.; Grieme, T.; Mulhern, M.; Pu, Y.-M.; Wendt, M.D. Development of a Convergent Large-Scale Synthesis for Venetoclax, a First-in-Class BCL-2 Selective Inhibitor. *J. Org. Chem.* **2019**, *84*, 4814–4829. [CrossRef]
11. Yang, Q.; Zhao, Y.; Ma, D. Cu-Mediated Ullmann-Type Cross-Coupling and Industrial Applications in Route Design, Process Development, and Scale-up of Pharmaceutical and Agrochemical Processes. *Org. Proc. Res. Dev.* **2022**, *26*, 1690–1750. [CrossRef]
12. Evendar, P.; Qu, R.-Y.; Kang, W.-M.; He, B.; Yang, G.-F. Palladium-Catalyzed Cross-Coupling Reactions: A Powerful Tool for the Synthesis of Agrochemicals. *J. Agric. Food. Chem.* **2018**, *66*, 8914–8934. [CrossRef] [PubMed]
13. Chen, J.; Yan, W.; Townsend, E.J.; Feng, J.; Pan, L.; Del Angel Hernandez, V.; Faul, C.F.J. Tunable Surface Area, Porosity, and Function in Conjugated Microporous Polymers. *Angew. Chem. Int. Ed.* **2019**, *58*, 11715–11719. [CrossRef]
14. Astridge, D.D.; Hoffman, J.B.; Zhang, F.; Park, S.Y.; Zhu, K.; Sellinger, A. Polymer Hole Transport Materials for Perovskite Solar Cells via Buchwald–Hartwig Amination. *ACS Appl. Polym. Mater.* **2021**, *3*, 5578–5587. [CrossRef]
15. Weingarten, H. Mechanism of the Ullmann Condensation. *J. Org. Chem.* **1964**, *29*, 3624–3626. [CrossRef]
16. Nicolaou, K.C.; Boddy, C.N.C.; Natarajan, S.; Yue, T.Y.; Li, H.; Bräse, S.; Ramanjulu, J.M. New Synthetic Technology for the Synthesis of Aryl Ethers: Construction of C-O-D and D-O-E Ring Model Systems of Vancomycin. *J. Am. Chem. Soc.* **1997**, *119*, 3421–3422. [CrossRef]
17. Marcoux, J.-F.; Doye, S.; Buchwald, S.L. A General Copper-Catalyzed Synthesis of Diaryl Ethers. *J. Am. Chem. Soc.* **1997**, *119*, 10539–10540. [CrossRef]
18. Ma, D.; Zhang, Y.; Yao, J.; Wu, S.; Tao, F. Accelerating Effect Induced by the Structure of α -Amino Acid in the Copper-Catalyzed Coupling Reaction of Aryl Halides with α -Amino Acids. Synthesis of Benzolactam-V8. *J. Am. Chem. Soc.* **1998**, *120*, 12459–12467. [CrossRef]
19. Monnier, F.; Taillefer, M. Catalytic C–C, C–N, and C–O Ullmann-Type Coupling Reactions. *Angew. Chem. Int. Ed.* **2009**, *48*, 6954–6971. [CrossRef]
20. Beletskaya, I.P.; Cheprakov, A.V. Copper in cross-coupling reactions: The post-Ullmann chemistry. *Coord. Chem. Rev.* **2004**, *248*, 2337–2364. [CrossRef]
21. Beletskaya, I.P.; Averin, A.D. Metal-catalyzed reactions for the C(sp²)–N bond formation: Achievements of recent years. *Russ. Chem. Rev.* **2021**, *90*, 1359. [CrossRef]
22. Goodbrand, H.B.; Hu, N.-X. Ligand-Accelerated Catalysis of the Ullmann Condensation: Application to Hole Conducting Triarylaminates. *J. Org. Chem.* **1999**, *64*, 670–674. [CrossRef]
23. Gujadhur, R.K.; Bates, C.G.; Venkataraman, D. Formation of Aryl–Nitrogen, Aryl–Oxygen, and Aryl–Carbon Bonds Using Well-Defined Copper(I)-Based Catalysts. *Org. Lett.* **2001**, *3*, 4315–4317. [CrossRef] [PubMed]
24. Surry, D.S.; Buchwald, S.L. Diamine ligands in copper-catalyzed reactions. *Chem. Sci.* **2010**, *1*, 13–31. [CrossRef] [PubMed]
25. Klapars, A.; Huang, X.; Buchwald, S.L. A General and Efficient Copper Catalyst for the Amidation of Aryl Halides. *J. Am. Chem. Soc.* **2002**, *124*, 7421–7428. [CrossRef] [PubMed]
26. Antilla, J.C.; Baskin, J.M.; Barder, T.E.; Buchwald, S.L. Copper–Diamine-Catalyzed N-Arylation of Pyrroles, Pyrazoles, Indazoles, Imidazoles, and Triazoles. *J. Org. Chem.* **2004**, *69*, 5578–5587. [CrossRef]
27. Ma, D.; Cai, Q.; Zhang, H. Mild Method for Ullmann Coupling Reaction of Amines and Aryl Halides. *Org. Lett.* **2003**, *5*, 2453–2455. [CrossRef]
28. Zhang, H.; Cai, Q.; Ma, D. Amino Acid Promoted CuI-Catalyzed C–N Bond Formation between Aryl Halides and Amines or N-Containing Heterocycles. *J. Org. Chem.* **2005**, *70*, 5164–5173. [CrossRef]
29. Jiang, Q.; Jiang, D.; Jiang, Y.; Fu, H.; Zhao, Y. A Mild and Efficient Method for Copper-Catalyzed Ullmann-Type N-Arylation of Aliphatic Amines and Amino Acids. *Synlett* **2007**, *2007*, 1836–1842. [CrossRef]
30. Fan, M.; Zhou, W.; Jiang, Y.; Ma, D. Assembly of Primary (Hetero)Arylamines via CuI/Oxalic Diamide-Catalyzed Coupling of Aryl Chlorides and Ammonia. *Org. Lett.* **2015**, *17*, 5934–5937. [CrossRef]
31. Gao, J.; Bhunia, S.; Wang, K.; Gan, L.; Xia, S.; Ma, D. Discovery of N-(Naphthalen-1-yl)-N'-alkyl Oxalamide Ligands Enables Cu-Catalyzed Aryl Amination with High Turnovers. *Org. Lett.* **2017**, *19*, 2809–2812. [CrossRef] [PubMed]
32. Kwong, F.Y.; Klapars, A.; Buchwald, S.L. Copper-Catalyzed Coupling of Alkylamines and Aryl Iodides: An Efficient System Even in an Air Atmosphere. *Org. Lett.* **2002**, *4*, 581–584. [CrossRef] [PubMed]
33. Jiang, D.; Fu, H.; Jiang, Y.; Zhao, Y. CuBr/rac-BINOL-Catalyzed N-Arylations of Aliphatic Amines at Room Temperature. *J. Org. Chem.* **2007**, *72*, 672–674. [CrossRef] [PubMed]
34. Shafir, A.; Buchwald, S.L. Highly Selective Room-Temperature Copper-Catalyzed C–N Coupling Reactions. *J. Am. Chem. Soc.* **2006**, *128*, 8742–8743. [CrossRef]

35. Shafir, A.; Lichtor, P.A.; Buchwald, S.L. N- versus O-Arylation of Aminoalcohols: Orthogonal Selectivity in Copper-Based Catalysts. *J. Am. Chem. Soc.* **2007**, *129*, 3490–3491. [CrossRef]
36. Kwong, F.Y.; Buchwald, S.L. Mild and Efficient Copper-Catalyzed Amination of Aryl Bromides with Primary Alkylamines. *Org. Lett.* **2003**, *5*, 793–796. [CrossRef]
37. Bernhardson, D.J.; Widlicka, D.W.; Singer, R.A. Cu-Catalyzed Couplings of Heteroaryl Primary Amines and (Hetero)aryl Bromides with 6-Hydroxypicolinamide Ligands. *Org. Proc. Res. Dev.* **2019**, *23*, 1538–1551. [CrossRef]
38. Modak, A.; Nett, A.J.; Swift, E.C.; Haibach, M.C.; Chan, V.S.; Franczyk, T.S.; Shekhar, S.; Cook, S.P. Cu-Catalyzed C–N Coupling with Sterically Hindered Partners. *ACS Catal.* **2020**, *10*, 10495–10499. [CrossRef]
39. Kim, S.-T.; Strauss, M.J.; Cabré, A.; Buchwald, S.L. Room-Temperature Cu-Catalyzed Amination of Aryl Bromides Enabled by DFT-Guided Ligand Design. *J. Am. Chem. Soc.* **2023**, *145*, 6966–6975. [CrossRef]
40. Zhou, W.; Fan, M.; Yin, J.; Jiang, Y.; Ma, D. CuI/Oxalic Diamide Catalyzed Coupling Reaction of (Hetero)Aryl Chlorides and Amines. *J. Am. Chem. Soc.* **2015**, *137*, 11942–11945. [CrossRef]
41. Chen, Z.; Ma, D. Cu/N,N'-Dibenzyloxalamide-Catalyzed N-Arylation of Heteroanilines. *Org. Lett.* **2019**, *21*, 6874–6878. [CrossRef] [PubMed]
42. Li, S.; Huang, X.; Gao, Y.; Jin, J. Oxalamide/Amide Ligands: Enhanced and Copper-Catalyzed C–N Cross-Coupling for Triarylamine Synthesis. *Org. Lett.* **2022**, *24*, 5817–5824. [CrossRef] [PubMed]
43. Ma, D.; Cai, Q. Copper/Amino Acid Catalyzed Cross-Couplings of Aryl and Vinyl Halides with Nucleophiles. *Acc. Chem. Res.* **2008**, *41*, 1450–1460. [CrossRef] [PubMed]
44. Beletskaya, I.P.; Cheprakov, A.V. The Complementary Competitors: Palladium and Copper in C–N Cross-Coupling Reactions. *Organometallics* **2012**, *31*, 7753–7808. [CrossRef]
45. Senra, J.D.; Aguiar, L.C.S.; Simas, A.B.C. Recent Progress in Transition-Metal-Catalyzed C–N Cross-Couplings: Emerging Approaches Towards Sustainability. *Curr. Org. Synth.* **2011**, *8*, 53–78. [CrossRef]
46. Sambigioglio, C.; Marsden, S.P.; Blacker, A.J.; McGowan, P.C. Copper catalysed Ullmann type chemistry: From mechanistic aspects to modern development. *Chem. Soc. Rev.* **2014**, *43*, 3525–3550. [CrossRef] [PubMed]
47. Evano, G.; Blanchard, N.; Toumi, M. Copper-Mediated Coupling Reactions and Their Applications in Natural Products and Designed Biomolecules Synthesis. *Chem. Rev.* **2008**, *108*, 3054–3131. [CrossRef]
48. Okano, K.; Tokuyama, H.; Fukuyama, T. Copper-mediated aromatic amination reaction and its application to the total synthesis of natural products. *Chem. Commun.* **2014**, *50*, 13650–13663. [CrossRef]
49. Lee, J.; Panek, J.S. Application of Copper-Mediated C–N Bond Formation in Complex Molecules Synthesis. In *Copper-Mediated Cross-Coupling Reactions*; John Wiley & Sons Inc.: Hoboken, NJ, USA, 2013; pp. 589–641. [CrossRef]
50. Junge, K.; Wienhöfer, G.; Beller, M.; Tlili, A.; Evano, G.; Taillefer, M.; Kempe, R.; Malbertz, C.; Klankermayer, J. New Trends in Organometallic Catalysts. In *Applied Homogeneous Catalysis with Organometallic Compounds: A Comprehensive Handbook in Three Volumes*, 3rd ed.; Cornils, B., Herrmann, W.A., Beller, M., Paciello, R., Eds.; John Wiley & Sons Inc.: Hoboken, NJ, USA, 2017.
51. Shaughnessy, K.H.; Ciganek, E.; De Vasher, R.B.; Denmark, S.E. *Copper-Catalyzed Amination of Aryl and Alkenyl Electrophiles*; John Wiley & Sons Inc.: Hoboken, NJ, USA, 2017.
52. Neetha, M.; Saranya, S.; Ann Harry, N.; Anilkumar, G. Recent Advances and Perspectives in the Copper-Catalysed Amination of Aryl and Heteroaryl Halides. *ChemistrySelect* **2020**, *5*, 736–753. [CrossRef]
53. Weidlich, T.; Špryncová, M.; Čegan, A. Copper-Catalyzed Reactions of Aryl Halides with N-Nucleophiles and Their Possible Application for Degradation of Halogenated Aromatic Contaminants. *Catalysts* **2022**, *12*, 911. [CrossRef]
54. Hosseinzadeh, R.; Aghili, N.; Tajbakhsh, M. SBA-15 Immobilized Phenanthroline–Copper(I) Complex as a Recyclable Efficient Catalyst for N-Arylation of Amides and N–H Heterocycles with Aryl Halides. *Catal. Lett.* **2016**, *146*, 193–203. [CrossRef]
55. Niakan, M.; Asadi, Z.; Zare, S. Preparation, Characterization and Application of Copper Schiff base Complex Supported on MCM-41 as a Recyclable Catalyst for the Ullmann-type N-arylation Reaction. *ChemistrySelect* **2020**, *5*, 40–48. [CrossRef]
56. Veisi, H.; Hamelian, M.; Hemmati, S.; Dalvand, A. CuI catalyst heterogenized on melamine-pyridines immobilized SBA-15: Heterogeneous and recyclable nanocatalyst for Ullmann-type CN coupling reactions. *Tetrahedron Lett.* **2017**, *58*, 4440–4446. [CrossRef]
57. Hemmati, S.; Ahany Kamangar, S.; Yousefi, M.; Hashemi Salehi, M.; Hekmati, M. Cu(I)-anchored polyvinyl alcohol coated-magnetic nanoparticles as heterogeneous nanocatalyst in Ullmann-type C–N coupling reactions. *Appl. Organomet. Chem.* **2020**, *34*, e5611. [CrossRef]
58. Islam, M.; Mondal, S.; Mondal, P.; Roy, A.S.; Tuhina, K.; Mobarok, M.; Paul, S.; Salam, N.; Hossain, D. An Efficient Recyclable Polymer Supported Copper(II) Catalyst for C–N Bond Formation by N-Arylation. *Catal. Lett.* **2011**, *141*, 1171–1181. [CrossRef]
59. Arundhathi, R.; Kumar, D.C.; Sreedhar, B. C–N Bond Formation Catalysed by CuI Bonded to Polyaniline Nanofiber. *Eur. J. Org. Chem.* **2010**, *2010*, 3621–3630. [CrossRef]
60. Islam, S.M.; Salam, N.; Mondal, P.; Roy, A.S.; Ghosh, K.; Tuhina, K. A highly active reusable polymer anchored copper catalyst for C–O, C–N and C–S cross coupling reactions. *J. Mol. Catal. A Chem.* **2014**, *387*, 7–19. [CrossRef]
61. Esmaeilpour, M.; Sardarian, A.R.; Firouzabadi, H. Dendrimer-encapsulated Cu(II) nanoparticles immobilized on superparamagnetic Fe₃O₄@SiO₂ nanoparticles as a novel recyclable catalyst for N-arylation of nitrogen heterocycles and green synthesis of 5-substituted 1H-tetrazoles. *Appl. Organomet. Chem.* **2018**, *32*, e4300. [CrossRef]

62. Chouhan, G.; Wang, D.; Alper, H. Magnetic nanoparticle-supported proline as a recyclable and recoverable ligand for the CuI catalyzed arylation of nitrogen nucleophiles. *Chem. Commun.* **2007**, *45*, 4809–4811. [CrossRef]
63. Zahmatkesh, S.; Esmaeilpour, M.; Javidi, J. 1,4-Dihydroxyanthraquinone–copper(II) supported on superparamagnetic Fe₃O₄@SiO₂: An efficient catalyst for N-arylation of nitrogen heterocycles and alkylamines with aryl halides and click synthesis of 1-aryl-1,2,3-triazole derivatives. *RSC Adv.* **2016**, *6*, 90154–90164. [CrossRef]
64. Sardarian, A.R.; Eslahi, H.; Esmaeilpour, M. Copper(II) Complex Supported on Fe₃O₄@SiO₂ Coated by Polyvinyl Alcohol as Reusable Nanocatalyst in N-Arylation of Amines and N(H)- Heterocycles and Green Synthesis of 1H-Tetrazoles. *ChemistrySelect* **2018**, *3*, 1499–1511. [CrossRef]
65. Paine, A.J. Mechanisms and models for copper mediated nucleophilic aromatic substitution. 2. Single catalytic species from three different oxidation states of copper in an Ullmann synthesis of triaryl amines. *J. Am. Chem. Soc.* **1987**, *109*, 1496–1502. [CrossRef]
66. Aalten, H.L.; van Koten, G.; Grove, D.M.; Kuilman, T.; Piekstra, O.G.; Hulshof, L.A.; Sheldon, R.A. The copper catalyzed reaction of sodium methoxide with aryl bromides. A mechanistic study leading to a facile synthesis of anisole derivatives. *Tetrahedron* **1989**, *45*, 5565–5578. [CrossRef]
67. Komori, T.; Satoh, N.; Yokoshima, S.; Fukuyama, T. Copper-Mediated Aryl Amination: In Situ Generation of an Active Copper(I) Species. *Synlett* **2011**, *2011*, 1859–1862. [CrossRef]
68. Meng, F.; Zhu, X.; Li, Y.; Xie, J.; Wang, B.; Yao, J.; Wan, Y. Efficient Copper-Catalyzed Direct Amination of Aryl Halides Using Aqueous Ammonia in Water. *Eur. J. Org. Chem.* **2010**, *2010*, 6149–6152. [CrossRef]
69. Quan, Z.; Xia, H.; Zhang, Z.; Da, Y.; Wang, X. Copper-Catalyzed Amination of Aryl Halides with Aqueous Ammonia under Mild Conditions. *Chin. J. Chem.* **2013**, *31*, 501–506. [CrossRef]
70. Fantasia, S.; Windisch, J.; Scalone, M. Ligandless Copper-Catalyzed Coupling of Heteroaryl Bromides with Gaseous Ammonia. *Adv. Synth. Catal.* **2013**, *355*, 627–631. [CrossRef]
71. Shang, Z.; Yang, L.; Chang, G. Synthesis of high-performance polymers via copper-catalyzed amination of dibromoarenes with primary aromatic ether diamines. *Macromol. Res.* **2015**, *23*, 937–943. [CrossRef]
72. Jiao, J.; Zhang, X.-R.; Chang, N.-H.; Wang, J.; Wei, J.-F.; Shi, X.-Y.; Chen, Z.-G. A Facile and Practical Copper Powder-Catalyzed, Organic Solvent- and Ligand-Free Ullmann Amination of Aryl Halides. *J. Org. Chem.* **2011**, *76*, 1180–1183. [CrossRef]
73. Sperotto, E.; van Klink, G.P.M.; van Koten, G.; de Vries, J.G. The mechanism of the modified Ullmann reaction. *Dalton Trans.* **2010**, *39*, 10338–10351. [CrossRef]
74. Mansour, M.; Giacomazzi, R.; Ouali, A.; Taillefer, M.; Jutand, A. Activation of aryl halides by Cu⁰/1,10-phenanthroline: Cu⁰ as precursor of CuI catalyst in cross-coupling reactions. *Chem. Commun.* **2008**, *45*, 6051–6053. [CrossRef] [PubMed]
75. Guo, Z.; Guo, J.; Song, Y.; Wang, L.; Zou, G. Hemilabile-coordinated copper promoted amination of aryl halides with ammonia in aqueous ethylene glycol under atmosphere pressure. *Appl. Organomet. Chem.* **2009**, *23*, 150–153. [CrossRef]
76. Lefèvre, G.; Franc, G.; Adamo, C.; Jutand, A.; Ciofini, I. Influence of the Formation of the Halogen Bond ArX—N on the Mechanism of Diketonate Ligated Copper-Catalyzed Amination of Aromatic Halides. *Organometallics* **2012**, *31*, 914–920. [CrossRef]
77. Xiang, S.-K.; Zhang, D.-X.; Hu, H.; Shi, J.-L.; Liao, L.-G.; Feng, C.; Wang, B.-Q.; Zhao, K.-Q.; Hu, P.; Yang, H.; et al. Synthesis of N-Arylamides by Copper-Catalyzed Amination of Aryl Halides with Nitriles. *Adv. Synth. Catal.* **2013**, *355*, 1495–1499. [CrossRef]
78. Huffman, L.M.; Stahl, S.S. Carbon–Nitrogen Bond Formation Involving Well-Defined Aryl–Copper(III) Complexes. *J. Am. Chem. Soc.* **2008**, *130*, 9196–9197. [CrossRef] [PubMed]
79. Casitas, A.; King, A.E.; Parella, T.; Costas, M.; Stahl, S.S.; Ribas, X. Direct observation of CuI/CuIII redox steps relevant to Ullmann-type coupling reactions. *Chem. Sci.* **2010**, *1*, 326–330. [CrossRef]
80. Casitas, A.; Ribas, X. The role of organometallic copper(III) complexes in homogeneous catalysis. *Chem. Sci.* **2013**, *4*, 2301–2318. [CrossRef]
81. Bacon, R.G.R.; Karim, A. Metal ions and complexes in organic reactions. Part XV. Copper-catalyzed substitutions of aryl halides by phthalimide ion. *J. Chem. Soc. Perkin Trans.* **1973**, 272–278. [CrossRef]
82. Wanka, L.; Iqbal, K.; Schreiner, P.R. The Lipophilic Bullet Hits the Targets: Medicinal Chemistry of Adamantane Derivatives. *Chem. Rev.* **2013**, *113*, 3516–3604. [CrossRef]
83. Sonkusare, S.K.; Kaul, C.L.; Ramarao, P. Dementia of Alzheimer’s disease and other neurodegenerative disorders—Memantine, a new hope. *Pharmacol. Res.* **2005**, *51*, 1–17. [CrossRef]
84. Grekhova, T.V.; Gainetdinov, R.R.; Sotnikova, T.D.; Krasnykh, L.M.; Kudrin, V.S.; Sergeeva, S.A.; Morozov, I.S. Effect of bromantane, a new immunostimulating agent with psychostimulating activity, on the release and metabolism of dopamine in the striatum of freely moving rats. A microdialysis study. *Bull. Exp. Biol. Med.* **1995**, *119*, 294–296. [CrossRef]
85. Morozov, I.S.; Klimova, N.V.; Lavrova, L.N.; Avdyunina, N.I.; Pyatin, B.M.; Troitskaya, V.S.; Bykov, N.P. N-adamantyl derivatives of aromatic amines. Part I. Synthesis and neurotropic activity of N-(adamant-2-yl)anilines. *Pharm. Chem. J.* **1998**, *32*, 1–4. [CrossRef]
86. Panchenko, S.P.; Abel, A.S.; Averin, A.D.; Maloshitskaya, O.A.; Savelyev, E.N.; Orlinson, B.S.; Novakov, I.A.; Beletskaya, I.P. Arylation of adamantanamines: VIII. Optimization of the catalytic system for copper-catalyzed arylation of adamantane-containing amines. *Russ. J. Org. Chem.* **2017**, *53*, 1497–1504. [CrossRef]
87. Averin, A.D.; Panchenko, S.P.; Abel, A.S.; Maloshitskaya, O.A.; Butov, G.M.; Savelyev, E.N.; Orlinson, B.S.; Novakov, I.A.; Beletskaya, I.P. Arylation of adamantanamines: IX. Copper(I)-catalyzed arylation of adamantane-containing amines. *Russ. J. Org. Chem.* **2017**, *53*, 1788–1798. [CrossRef]

88. Panchenko, S.P.; Abel, A.C.; Averin, A.D.; Maloshitskaya, O.A.; Savelyev, E.N.; Orlinson, B.S.; Novakov, I.A.; Beletskaya, I.P. CuI-catalyzed N,N'-diarylation of diamines of adamantane series. *Russ. Chem. Bull.* **2016**, *65*, 1550–1555. [CrossRef]
89. Murashkina, A.V.; Averin, A.D.; Panchenko, S.P.; Abel, A.S.; Maloshitskaya, O.A.; Savelyev, E.N.; Orlinson, B.S.; Novakov, I.A.; Correia, C.R.D.; Beletskaya, I.P. Comparison of the Catalytic Activities of Copper(I) Iodide and Copper Nanoparticles in the N-Arylation of Adamantane-Containing Amines. *Russ. J. Org. Chem.* **2022**, *58*, 15–24. [CrossRef]
90. Kivitz, A.J.; Gutierrez-Ureña, S.R.; Poiley, J.; Genovese, M.C.; Kristy, R.; Shay, K.; Wang, X.; Garg, J.P.; Zubrzycka-Sienkiewicz, A. Peficitinib, a JAK Inhibitor, in the Treatment of Moderate-to-Severe Rheumatoid Arthritis in Patients With an Inadequate Response to Methotrexate. *Arthritis Rheumatol.* **2017**, *69*, 709–719. [CrossRef]
91. Leovac, V.M.; Rodić, M.V.; Jovanović, L.S.; Joksović, M.D.; Stanojković, T.; Vujčić, M.; Sladić, D.; Marković, V.; Vojinović-Ješić, L.S. Transition Metal Complexes with 1-Adamantoyl Hydrazones—Cytotoxic Copper(II) Complexes of Tri- and Tetradentate Pyridine Chelators Containing an Adamantane Ring System. *Eur. J. Inorg. Chem.* **2015**, *2015*, 882–895. [CrossRef]
92. Ryu, J.H.; Kim, S.; Han, H.Y.; Son, H.J.; Lee, H.J.; Shin, Y.A.; Kim, J.-S.; Park, H.-g. Synthesis and biological evaluation of picolinamides as potent inhibitors of 11 β -hydroxysteroid dehydrogenase type 1 (11 β -HSD1). *Bioorg. Med. Chem. Lett.* **2015**, *25*, 695–700. [CrossRef]
93. Rohde, J.J.; Pliushchev, M.A.; Sorensen, B.K.; Wodka, D.; Shuai, Q.; Wang, J.; Fung, S.; Monzon, K.M.; Chiou, W.J.; Pan, L.; et al. Discovery and Metabolic Stabilization of Potent and Selective 2-Amino-N-(adamant-2-yl) Acetamide 11 β -Hydroxysteroid Dehydrogenase Type 1 Inhibitors. *J. Med. Chem.* **2007**, *50*, 149–164. [CrossRef]
94. Sorensen, B.; Rohde, J.; Wang, J.; Fung, S.; Monzon, K.; Chiou, W.; Pan, L.; Deng, X.; Stolarik, D.; Frevert, E.U.; et al. Adamantane 11- β -HSD-1 inhibitors: Application of an isocyanide multicomponent reaction. *Bioorg. Med. Chem. Lett.* **2006**, *16*, 5958–5962. [CrossRef] [PubMed]
95. Liu, S.; Qian, P.; Wan, F.-X.; Shi, Y.-H.; Jiang, L. Design, synthesis, and biological activity of novel 2-(pyridin-3-yl)ethan-1-one oxime ethers bearing adamantane moiety. *J. Chin. Chem. Soc.* **2019**, *66*, 330–334. [CrossRef]
96. Collins, K.C.; Janda, K.D. Investigating Hapten Clustering as a Strategy to Enhance Vaccines against Drugs of Abuse. *Bioconjug. Chem.* **2014**, *25*, 593–600. [CrossRef] [PubMed]
97. Weigel, W.K., III; Dang, H.T.; Feceub, A.; Martin, D.B.C. Direct radical functionalization methods to access substituted adamantanes and diamondoids. *Org. Biomol. Chem.* **2022**, *20*, 10–36. [CrossRef]
98. Zhou, L.; Togo, H. Introduction of Heteroaromatic Bases onto Cycloalkanes with BPO. *Eur. J. Org. Chem.* **2019**, *2019*, 1627–1634. [CrossRef]
99. Zhao, H.; Li, Z.; Jin, J. Green oxidant H₂O₂ as a hydrogen atom transfer reagent for visible light-mediated Minisci reaction. *New J. Chem.* **2019**, *43*, 12533–12537. [CrossRef]
100. Perry, I.B.; Brewer, T.F.; Sarver, P.J.; Schultz, D.M.; DiRocco, D.A.; MacMillan, D.W.C. Direct arylation of strong aliphatic C–H bonds. *Nature* **2018**, *560*, 70–75. [CrossRef]
101. Abel, A.S.; Averin, A.D.; Anokhin, M.V.; Maloshitskaya, O.A.; Butov, G.M.; Savelyev, E.N.; Orlinson, B.S.; Novakov, I.A.; Beletskaya, I.P. Arylation of adamantanamines: VII. Copper(I)-catalyzed N-heteroarylation of adamantane-containing amines with halopyridines. *Russ. J. Org. Chem.* **2015**, *51*, 301–308. [CrossRef]
102. Abel, A.S.; Kotovshchikov, Y.N.; Averin, A.D.; Maloshitskaya, O.A.; Savelyev, E.N.; Orlinson, B.S.; Novakov, I.A.; Beletskaya, I.P. Problem of Regioselectivity in the Amination of 2-Fluoro-5-iodopyridine with Adamantylalkyl Amines. *Heterocycles* **2019**, *99*, 1342–1354. [CrossRef]
103. Scherman, M.S.; North, E.J.; Jones, V.; Hess, T.N.; Grzegorzewicz, A.E.; Kasagami, T.; Kim, I.-H.; Merzlikin, O.; Lenaerts, A.J.; Lee, R.E.; et al. Screening a library of 1600 adamantyl ureas for anti-Mycobacterium tuberculosis activity in vitro and for better physical chemical properties for bioavailability. *Bioorg. Med. Chem.* **2012**, *20*, 3255–3262. [CrossRef]
104. Al-Omar, M.A.; Al-Abdullah, E.S.; Shehata, I.A.; Habib, E.E.; Ibrahim, T.M.; El-Emam, A.A. Synthesis, Antimicrobial, and Anti-inflammatory Activities of Novel 5-(1-Adamantyl)-4-arylideneamino-3-mercapto-1,2,4-triazoles and Related Derivatives. *Molecules* **2010**, *15*, 2526–2550. [CrossRef] [PubMed]
105. Yu, X.; Zhang, M.; Annamalai, T.; Bansod, P.; Narula, G.; Tse-Dinh, Y.-C.; Sun, D. Synthesis, evaluation, and CoMFA study of fluoroquinophenoxazine derivatives as bacterial topoisomerase IA inhibitors. *Eur. J. Med. Chem.* **2017**, *125*, 515–527. [CrossRef] [PubMed]
106. O'Brien-Brown, J.; Jackson, A.; Reekie, T.A.; Barron, M.L.; Werry, E.L.; Schiavini, P.; McDonnell, M.; Munoz, L.; Wilkinson, S.; Noll, B.; et al. Discovery and pharmacological evaluation of a novel series of adamantyl cyanoguanidines as P2X7 receptor antagonists. *Eur. J. Med. Chem.* **2017**, *130*, 433–439. [CrossRef] [PubMed]
107. Udagawa, S.; Sakami, S.; Takemura, T.; Sato, M.; Arai, T.; Nitta, A.; Aoki, T.; Kawai, K.; Iwamura, T.; Okazaki, S.; et al. Discovery of novel 7-membered cyclic amide derivatives that inhibit 11beta-hydroxysteroid dehydrogenase type 1. *Bioorg. Med. Chem. Lett.* **2013**, *23*, 1617–1621. [CrossRef] [PubMed]
108. Berglund, S.; Egner, B.J.; Gradén, H.; Gradén, J.; Morgan, D.G.A.; Inghardt, T.; Giordanetto, F. Optimization of piperidin-4-yl-urea-containing melanin-concentrating hormone receptor 1 (MCH-R1) antagonists: Reducing hERG-associated liabilities. *Bioorg. Med. Chem. Lett.* **2009**, *19*, 4274–4279. [CrossRef]
109. Brogi, S.; Corelli, F.; Di Marzo, V.; Ligresti, A.; Mugnaini, C.; Pasquini, S.; Tafi, A. Three-dimensional quantitative structure–selectivity relationships analysis guided rational design of a highly selective ligand for the cannabinoid receptor 2. *Eur. J. Med. Chem.* **2011**, *46*, 547–555. [CrossRef]


110. Lyakhovich, M.S.; Murashkina, A.V.; Averin, A.D.; Abel, A.S.; Maloshitskaya, O.A.; Savelyev, E.N.; Orlinson, B.S.; Beletskaya, I.P. Arylation of Adamantanamines: X. Palladium- and Copper-Catalyzed Heteroarylation of Adamantane-Containing Amines with Bromopyridines. *Russ. J. Org. Chem.* **2019**, *55*, 737–747. [CrossRef]
111. Lyakhovich, M.S.; Murashkina, A.V.; Panchenko, S.P.; Averin, A.D.; Abel, A.S.; Maloshitskaya, O.A.; Savelyev, E.N.; Orlinson, B.S.; Novakov, I.A.; Beletskaya, I.P. Arylation of Adamantanamines: XI. Comparison of the Catalytic Efficiency of Palladium and Copper Complexes in Reactions of Adamantanamines with Fluorinated 2-Bromopyridines. *Russ. J. Org. Chem.* **2021**, *57*, 768–783. [CrossRef]
112. Hajipour, A.R.; Dordahan, F.; Rafiee, F.; Mahdavi, M. C–N cross-coupling reaction catalysed by efficient and reusable CuO/SiO₂ nanoparticles under ligand-free conditions. *Appl. Organomet. Chem.* **2014**, *28*, 809–813. [CrossRef]
113. Nador, F.; Volpe, M.A.; Alonso, F.; Radivoy, G. Synthesis of N-aryl imidazoles catalyzed by copper nanoparticles on nanosized silica-coated maghemite. *Tetrahedron* **2014**, *70*, 6082–6087. [CrossRef]
114. Mitrofanov, A.Y.; Murashkina, A.V.; Martín-García, I.; Alonso, F.; Beletskaya, I.P. Formation of C–C, C–S and C–N bonds catalysed by supported copper nanoparticles. *Catal. Sci. Technol.* **2017**, *7*, 4401–4412. [CrossRef]
115. Mondal, P.; Sinha, A.; Salam, N.; Roy, A.S.; Jana, N.R.; Islam, S.M. Enhanced catalytic performance by copper nanoparticle–graphene based composite. *RSC Adv.* **2013**, *3*, 5615–5623. [CrossRef]
116. Gopiraman, M.; Ganesh Babu, S.; Khatrri, Z.; Kai, W.; Kim, Y.A.; Endo, M.; Karvembu, R.; Kim, I.S. An efficient, reusable copper-oxide/carbon-nanotube catalyst for N-arylation of imidazole. *Carbon* **2013**, *62*, 135–148. [CrossRef]
117. Khalil, A.; Jouiad, M.; Khraisheh, M.; Hashaikheh, R. Facile Synthesis of Copper Oxide Nanoparticles via Electrospinning. *J. Nanomater.* **2014**, *2014*, 438407. [CrossRef]
118. Jammi, S.; Sakthivel, S.; Rout, L.; Mukherjee, T.; Mandal, S.; Mitra, R.; Saha, P.; Punniyamurthy, T. CuO Nanoparticles Catalyzed C–N, C–O, and C–S Cross-Coupling Reactions: Scope and Mechanism. *J. Org. Chem.* **2009**, *74*, 1971–1976. [CrossRef]
119. Suramwar, N.V.; Thakare, S.R.; Karade, N.N.; Khaty, N.T. Green synthesis of predominant (111) facet CuO nanoparticles: Heterogeneous and recyclable catalyst for N-arylation of indoles. *J. Mol. Catal. A Chem.* **2012**, *359*, 28–34. [CrossRef]
120. Rout, L.; Jammi, S.; Punniyamurthy, T. Novel CuO Nanoparticle Catalyzed C–N Cross Coupling of Amines with Iodobenzene. *Org. Lett.* **2007**, *9*, 3397–3399. [CrossRef]
121. Reddy, K.H.V.; Satish, G.; Ramesh, K.; Karnakar, K.; Nageswar, Y.V.D. An efficient synthesis of N-substituted indoles from indoline/indoline carboxylic acid via aromatization followed by C–N cross-coupling reaction by using nano copper oxide as a recyclable catalyst. *Tetrahedron Lett.* **2012**, *53*, 3061–3065. [CrossRef]
122. Murashkina, A.V.; Kuliukhina, D.S.; Averin, A.D.; Abel, A.S.; Savelyev, E.N.; Orlinson, B.S.; Novakov, I.A.; Correia, C.R.D.; Beletskaya, I.P. A comparison of homogeneous and heterogeneous copper catalyzed arylation of amines. *Mendeleev Commun.* **2022**, *32*, 91–93. [CrossRef]
123. Fomenko, V.I.; Murashkina, A.V.; Averin, A.D.; Shesterkina, A.A.; Beletskaya, I.P. Unsupported Copper Nanoparticles in the Arylation of Amines. *Catalysts* **2023**, *13*, 331. [CrossRef]
124. Kuliukhina, D.S.; Averin, A.D.; Panchenko, S.P.; Abel, A.S.; Savelyev, E.N.; Orlinson, B.S.; Novakov, I.A.; Correia, C.R.D.; Beletskaya, I.P. CuI and Copper Nanoparticles in the Catalytic Amination of 2-Halopyridines. *Russ. J. Org. Chem.* **2022**, *58*, 167–174. [CrossRef]
125. Pegg, A.E.; Casero, R.A. Current Status of the Polyamine Research Field. In *Polyamines: Methods and Protocols*; Pegg, A., Casero, R., Jr., Eds.; Humana Press: Totowa, NJ, USA, 2011; Volume 720, pp. 3–35. [CrossRef]
126. Díaz, J.E.; Bisceglia, J.Á.; Mollo, M.C.; Orelli, L.R. 1,*n*-Diamines. Part 2: Synthesis of acyclic and heterocyclic N-arylputrescine derivatives. *Tetrahedron Lett.* **2011**, *52*, 1895–1897. [CrossRef]
127. Bisceglia, J.Á.; García, M.B.; Massa, R.; Magri, M.L.; Zani, M.; Gutkind, G.O.; Orelli, L.R. Synthesis, characterization and biological activity of bis(3-Aryl-1-hexahydropyrimidinyl)methanes. Novel heterocyclic polyamine derivatives. *J. Heterocycl. Chem.* **2004**, *41*, 85–90. [CrossRef]
128. Haffner, C.D.; Thomson, S.A.; Guo, Y.; Petrov, K.; Larkin, A.; Banker, P.; Schaaf, G.; Dickerson, S.; Gobel, J.; Gillie, D.; et al. Substituted N-{3-[(1,1-dioxido-1,2-benzothiazol-3-yl)(phenyl)amino]propyl}benzamide analogs as potent Kv1.3 ion channel blockers. Part 2. *Bioorg. Med. Chem. Lett.* **2010**, *20*, 6989–6992. [CrossRef] [PubMed]
129. Burns, M.R.; LaTurner, S.; Ziemer, J.; McVean, M.; Devens, B.; Carlson, C.L.; Graminski, G.F.; Vanderwerf, S.M.; Weeks, R.S.; Carreon, J. Induction of apoptosis by aryl-substituted diamines: Role of aromatic group substituents and distance between nitrogens. *Bioorg. Med. Chem. Lett.* **2002**, *12*, 1263–1267. [CrossRef] [PubMed]
130. Bergeron, R.J.; Weimar, W.R.; Wu, Q.; Feng, Y.; McManis, J.S. Polyamine Analogue Regulation of NMDA MK-801 Binding: A Structure–Activity Study. *J. Med. Chem.* **1996**, *39*, 5257–5266. [CrossRef] [PubMed]
131. da Costa, C.F.; Coimbra, E.S.; Braga, F.G.; dos Reis, R.C.N.; da Silva, A.D.; de Almeida, M.V. Preparation and antileishmanial activity of lipophilic N-alkyl diamines. *Biomed. Pharmacother.* **2009**, *63*, 40–42. [CrossRef] [PubMed]
132. Panchenko, S.P.; Averin, A.D.; Anokhin, M.V.; Maloshitskaya, O.A.; Beletskaya, I.P. Cu(I)-catalyzed N,N'-diarylation of natural diamines and polyamines with aryl iodides. *Beilstein J. Org. Chem.* **2015**, *11*, 2297–2305. [CrossRef]
133. Anokhin, M.V.; Averin, A.D.; Beletskaya, I.P. Copper-Catalyzed Arylation of Oxadiazines and Polyamines. *Eur. J. Org. Chem.* **2011**, *2011*, 6240–6253. [CrossRef]

134. Albert, J.; Bosque, R.; Cadena, M.; D'Andrea, L.; Granell, J.; González, A.; Quirante, J.; Calvis, C.; Messeguer, R.; Badía, J.; et al. A New Family of Doubly Cyclopalladated Diimines. A Remarkable Effect of the Linker between the Metalated Units on Their Cytotoxicity. *Organometallics* **2014**, *33*, 2862–2873. [CrossRef]
135. Li, S.A.; Cadelis, M.M.; Sue, K.; Blanchet, M.; Vidal, N.; Brunel, J.M.; Bourguet-Kondracki, M.-L.; Copp, B.R. 6-Bromoindolglyoxylamido derivatives as antimicrobial agents and antibiotic enhancers. *Bioorg. Med. Chem.* **2019**, *27*, 2090–2099. [CrossRef]
136. Liew, L.P.P.; Pearce, A.N.; Kaiser, M.; Copp, B.R. Synthesis and in vitro and in vivo evaluation of antimalarial polyamines. *Eur. J. Med. Chem.* **2013**, *69*, 22–31. [CrossRef] [PubMed]
137. Devi, J.; Devi, S.; Kumar, A. Synthesis, antibacterial evaluation and QSAR analysis of Schiff base complexes derived from [2,2'-(ethylenedioxy)bis(ethylamine)] and aromatic aldehydes. *MedChemComm* **2016**, *7*, 932–947. [CrossRef]
138. Vennerstrom, J.L.; Ager, A.L.; Dorn, A.; Andersen, S.L.; Gerena, L.; Ridley, R.G.; Milhous, W.K. Bisquinolines. 2. Antimalarial N,N-Bis(7-chloroquinolin-4-yl)heteroalkanediamines. *J. Med. Chem.* **1998**, *41*, 4360–4364. [CrossRef] [PubMed]
139. Chtchigrovsky, M.; Eloy, L.; Jullien, H.; Saker, L.; Ségal-Bendirdjian, E.; Poupon, J.; Bombard, S.; Cresteil, T.; Retailleau, P.; Marinetti, A. Antitumor *trans-N*-Heterocyclic Carbene–Amine–Pt(II) Complexes: Synthesis of Dinuclear Species and Exploratory Investigations of DNA Binding and Cytotoxicity Mechanisms. *J. Med. Chem.* **2013**, *56*, 2074–2086. [CrossRef]
140. Lyakhovich, M.S.; Averin, A.D.; Grigorova, O.K.; Roznyatovsky, V.A.; Maloshitskaya, O.A.; Beletskaya, I.P. Cu(I)- and Pd(0)-Catalyzed Arylation of Oxadiazines with Fluorinated Halogenobenzenes: Comparison of Efficiency. *Molecules* **2020**, *25*, 1084. [CrossRef]
141. Panchenko, S.P.; Averin, A.D.; Lyakhovich, M.S.; Abel, A.S.; Maloshitskaya, O.A.; Beletskaya, I.P. CuI-catalyzed heterarylation of natural di- and polyamines with halopyridines. *Russ. Chem. Bull.* **2017**, *66*, 1611–1617. [CrossRef]
142. Anokhin, M.V.; Averin, A.D.; Panchenko, S.P.; Maloshitskaya, O.A.; Buryak, A.K.; Beletskaya, I.P. Copper(I)-Catalyzed Amination of Halogenopyridines with Polyamines. *Helv. Chim. Acta* **2015**, *98*, 47–59. [CrossRef]
143. Anokhin, M.V.; Averin, A.D.; Panchenko, S.P.; Maloshitskaya, O.A.; Beletskaya, I.P. CuI-mediated modification of polyamines with fluorophore groups. *Mendeleev Commun.* **2015**, *25*, 245–247. [CrossRef]
144. Anokhin, M.V.; Averin, A.D.; Panchenko, S.P.; Maloshitskaya, O.A.; Beletskaya, I.P. Copper(I)-catalyzed amination of halothiophenes with polyamines. *Russ. J. Org. Chem.* **2014**, *50*, 923–927. [CrossRef]
145. Yakushev, A.A.; Averin, A.D.; Anokhin, M.V.; Maloshitskaya, O.A.; Lamaty, F.; Beletskaya, I.P. Copper-catalyzed amination in the synthesis of polyoxadiazine derivatives of aza- and diazacrown ethers. *Macroheterocycles* **2014**, *7*, 358–364. [CrossRef]
146. Yakushev, A.A.; Averin, A.D.; Maloshitskaya, O.A.; Syrbu, S.A.; Koifman, O.I.; Beletskaya, I.P. Palladium- and Copper-Catalyzed Amination of Halogenophenyl Substituted Porphyrins for the Synthesis of Porphyrin-Azacrown Ethers Conjugates and Evaluation of Their Sensing Properties. *Macroheterocycles* **2016**, *9*, 65–72. [CrossRef]
147. West, M.J.; Fyfe, J.W.B.; Vantourout, J.C.; Watson, A.J.B. Mechanistic Development and Recent Applications of the Chan–Lam Amination. *Chem. Rev.* **2019**, *119*, 12491–12523. [CrossRef] [PubMed]
148. Kuliukhina, D.S.; Yakushev, A.A.; Malysheva, A.S.; Averin, A.D.; Beletskaya, I.P. Synthesis of N,N'-Diaryl Diamines and Oxadiazines via Chan–Lam Amination. *Russ. J. Org. Chem.* **2022**, *58*, 1752–1758. [CrossRef]

Disclaimer/Publisher's Note: The statements, opinions and data contained in all publications are solely those of the individual author(s) and contributor(s) and not of MDPI and/or the editor(s). MDPI and/or the editor(s) disclaim responsibility for any injury to people or property resulting from any ideas, methods, instructions or products referred to in the content.

Review

Progress on the Cu-Catalyzed 1,4-Conjugate Addition to Thiochromones

Fenghai Guo^{1,2,*} , Jayla A. Young¹, Mina S. Perez¹, Holden A. Hankerson¹ and Alex M. Chavez¹

¹ Department of Chemistry, Winston-Salem State University, 601 S. Martin Luther King Jr. Dr., Winston-Salem, NC 27110, USA

² Biomedical Research Infrastructure Center, Winston-Salem State University, Winston-Salem, NC 27110, USA

* Correspondence: guof@wssu.edu

Abstract: Carbon–carbon bond formation is one of the most important tools in synthetic organic chemists’ toolbox. It is a fundamental transformation that allows synthetic chemists to synthesize the carbon framework of complex molecules from inexpensive simple starting materials. Among the many synthetic methodologies developed for the construction of carbon–carbon bonds, organocopper reagents are one of the most reliable organometallic reagents for this purpose. The versatility of organocuprate reagents or the reactions catalyzed by organocopper reagents were demonstrated by their applications in a variety of synthetic transformations including the 1,4-conjugate addition reactions. Sulfur-containing heterocyclic compounds are a much less studied area compared to oxygen-containing heterocycles but have gained more and more attention in recent years due to their rich biological activities and widespread applications in pharmaceuticals, agrochemicals, and material science. This paper will provide a brief review on recent progress on the synthesis of an important class of sulfur-heterocycles-2-alkylthiochroman-4-ones and thioflavanones via the conjugate additions of Grignard reagents to thiochromones catalyzed by copper catalysts. Recent progress on the synthesis of 2-substituted thiochroman-4-ones via alkynylation and alkenylation of thiochromones will also be covered in this review.

Keywords: organocopper reagents; Cu catalysts; 1,4-conjugate addition; sulfur heterocycles; thiochromone; thioflavanones; 2-alkylthiochroman-4-ones



Citation: Guo, F.; Young, J.A.; Perez, M.S.; Hankerson, H.A.; Chavez, A.M.

Progress on the Cu-Catalyzed 1,4-Conjugate Addition to Thiochromones. *Catalysts* **2023**, *13*, 713. <https://doi.org/10.3390/catal13040713>

Academic Editors: Yongjun Ji, Liwen Xing and Ke Wu

Received: 23 March 2023

Revised: 5 April 2023

Accepted: 6 April 2023

Published: 8 April 2023



Copyright: © 2023 by the authors. Licensee MDPI, Basel, Switzerland. This article is an open access article distributed under the terms and conditions of the Creative Commons Attribution (CC BY) license (<https://creativecommons.org/licenses/by/4.0/>).

1. Introduction

Carbon–carbon bond formation is one of the most important tools in synthetic organic chemists’ toolbox. It is a fundamental transformation that allows synthetic chemists to synthesize the carbon framework of complex molecules from inexpensive simple starting materials. Among the many synthetic approaches developed for the construction of carbon–carbon bonds, organocopper reagents are one of the most reliable organometallic reagents for this purpose [1–8]. A wide range of organocopper reagents were developed for carbon–carbon bond formations [2]. Organometallic reagents catalyzed by copper (I) salts or/and organocopper reagents were successfully employed to construct carbon–carbon bonds sp , sp^2 , and sp^3 carbon centers [2]. The applications of cuprate reagents in a variety of synthetic transformations including the 1,4-conjugate addition reactions further demonstrated their versatility and usefulness [2,3]. Although the conjugate addition of stoichiometric amount of organocuprates to thiochromones were also reported [9,10], this review will focus on recent progress on the conjugate additions of organocopper reagents to thiochromones especially those using catalytic amount of copper (I) salts in the synthesis of an important class of sulfur-heterocycles-2-alkylthiochroman-4-ones and thioflavanones. Other synthetic approaches to 2-alkylthiochroman-4-ones and thioflavanones were well summarized in a recent review article [11] and this review aims to provide more details on the progress on synthesis of 2-substituted thiochroman-4-ones via conjugate addition of Grignard reagents catalyzed by copper salts. This review also aims to give an introduction

to the history, development of the organocuprates and especially their applications in the synthesis 2-substituted thiochroman-4-ones. Progress on the synthesis of 2-substituted thiochroman-4-ones via alkynylation and alkenylation of thiochromones will also be covered in this review as they represent a nice addition to the existing synthetic approaches towards the synthesis of 2-substituted thiochroman-4-ones.

Sulfur-containing heterocycles are important due to their widespread presence in numerous bioactive natural products as well as pharmaceuticals [12–15]. They have widespread applications in many areas including biology, medicinal chemistry, food chemistry, and material science [16–22]. The improvement of the bioavailability and bioactivity was reported by the isosteric replacement of an oxygen atom by a sulfur atom [23], but sulfur-containing heterocyclic compounds are a much less studied area compared to oxygen-containing heterocycles. Due to their widespread applications and rich biological activities, the development towards an efficient synthetic approach to sulfur-containing compounds received more and more interest from both industry and academia. This paper will provide a brief review on recent progress on the synthesis of an important class of sulfur-heterocycles-2-alkylthiochroman-4-ones and thioflavanones via the conjugate additions of Grignard reagents to thiochromones catalyzed by copper catalysts. Recent reports on the synthesis of 2-alkynyl thiochroman-4-ones and 2-alkenylation thiochromones will also be covered in this review. This review aims to cover recent progress on the addition of alkyl, aryl, alkenyl, to thiochromones via 1,4-conjugate addition of Grignard reagents as well as the formal conjugate addition of alkynyl groups to thiochromones catalyzed of Cu (I) salts.

1.1. Introduction to the Pioneering Studies on Organocopper Reagents

Among the many synthetic approaches developed for the construction of carbon–carbon bonds, organocopper reagents are one of the most reliable organometallic reagents for this purpose [1–8]. Among the earliest examples of organocopper chemistry is Glaser’s employment of alkynylcopper reagents in the synthesis of diynes from terminal alkynes in 1870 [24]. Other pioneering studies on organocopper chemistry include the copper-catalyzed Ullmann biaryl synthesis [25] and aryl ether synthesis [26]. Only after more than 50 years later, in 1923, Reich successfully used copper (I) Iodide and phenyl magnesium bromide (**1**) to prepare phenyl copper [27] (i.e., **2**, Figure 1). This was groundbreaking in terms of the development of organocopper reagents, as this was the first preparation of a stoichiometric organocopper reagent and, thus, it marked the beginning of organocopper chemistry.

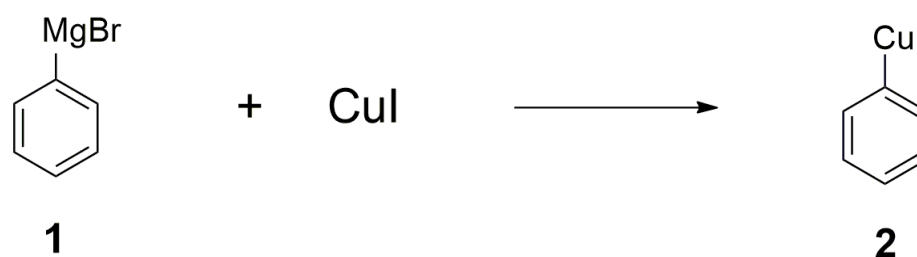


Figure 1. Phenyl copper prepared from phenyl magnesium bromide.

Since the groundbreaking preparation of phenyl copper, much progress in the field of organocopper reagents was reported. For example, more than a decade later, Gilman and Straley demonstrated the synthetic potential of a mono-organocopper reagent when they successfully prepared the first mono-alkylcopper reagent (i.e., ethylcopper) from copper (I) iodide (CuI) and ethyl magnesium iodide (EtMgI) [28] in 1936. Five years later, Karasch [29] discovered the 1,4-conjugate addition of Grignard reagents to α , β -unsaturated ketones catalyzed by copper (I) chloride. This is a very important discovery as it showed that copper (I) salts such as CuCl can selectively affect the 1,4-conjugate addition of Grignard reagents to α , β -unsaturated ketones over 1,2-addition to carbonyl group. Later, the first organocuprate reagent, lithium dimethylcuprate (Me_2CuLi), was prepared and used in the acylation

reactions for ketone synthesis by Gilman in 1952 [30]. These lithium dialkylcuprates were later named “Gilman” reagents in honor of Gilman for his pioneering contributions in this area (Figure 2).

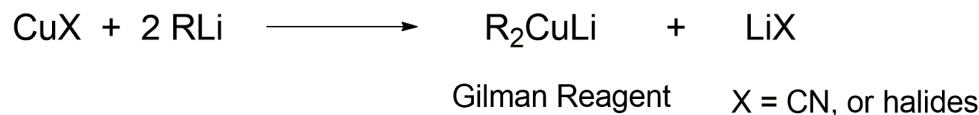


Figure 2. The First Dialkylcuprate Reagent Prepared by Gilman.

Stoichiometric lithium dialkylcuprates (i.e., R_2CuLi) were later used by House and Whitesides to effect 1,4-conjugate addition to α , β -enones [31]. This reaction was highly chemoselective (i.e., 1,4-adduct vs. 1,2-adduct), affording an excellent chemical yield (1,4-adduct vs. 1,2-adduct) and high reproducibility [31]. Thus, this reaction by House and coworkers further demonstrated that cuprates are the reactive species in Karasch’s CuCl catalyzed 1,4-addition of MeMgBr to α , β -enones. Although the reactive species was not clear at that time, Karsch observed that Grignard reagents underwent 1,4-conjugate addition to α , β -enones instead of 1,2-addition to afford the 1,4-adducts selectively in the presence of only 1% copper (I) salt [29]. Grignard reagents usually underwent the 1,2-addition pathway over 1,4-addition without addition of copper (I) salt. This pioneering discovery opens the door for many synthetic applications of copper-catalyzed Grignard reagents. Although there are problems of reproducibility, copper-catalyzed Grignard reactions are highly synthetically useful due to the readily availability from commercial sources as well as the easy preparation of Grignard reagents from corresponding halides. Later, the reproducibility problem can be solved by using highly pure, and stable copper salts such as $\text{CuBr}\cdot\text{SMe}_2$ and CuCN that are soluble. The utility of copper-catalyzed Grignard reagents increases with the reproducibility problem minimized. One of the drawbacks of organocuprates is they usually require the stoichiometric amount of Cu (I) salts. Using excess copper (I) salt is always less appealing from an environmental consideration. If problems such as low reproducibility and the competing side reactions (i.e., competition of 1,2-addition by organolithium and Grignard reagents) can be solved, it is always more appealing to develop and use procedures that only require catalytic amount of copper (I) salt than stoichiometric amount of organocuprate reagents. This paper will provide a brief review on recent progress on the conjugate additions of Grignard reagents to thiochromones catalyzed by copper catalysts as they provide a quick entry into an important class of sulfur-heterocycles-2-alkylthiochroman-4-ones and thioflavanones. The progress on the 1,4-additions of alkenyl Grignard reagents promoted by TMSOTf and the formal conjugate addition of alkynyl groups to thiochromones catalyzed by Cu (I) salts will also be covered as they represent nice addition to the existing synthetic approaches to 2-substituted thiochroman-4-ones.

Organocopper reagents can be readily prepared from a copper (I) salt and the corresponding Grignard reagents or organolithium reagents. This can be carried out by adding one equivalent of organolithium reagent (RLi) or Grignard reagents (RMgX) to a copper (I) salt. Organocopper reagents could be very efficient reagents based on the organic group transferred, as only one valuable ligand is required here. However, the synthetic applications of this reagent were very limited at the early stage of discovery because of the insoluble nature of some organocopper reagents and, thus, lack of reactivity. For example, methyl copper is a yellow polymeric precipitate [32] in diethyl ether and, as a result, not very reactive, which limited its synthetic applications. Recent advances in combining Lewis acids, such as TMSCl or $\text{BF}_3\cdot\text{OEt}_2$, with organocuprates such as alkylcopper reagents led to improved reactivity of these reagents and, thus, made them more useful tools for modern organic synthesis [2].

Although the conjugate addition of stoichiometric amount of organocuprates to thiochromones were also reported, [9,10] this paper will focus on recent progress on the conjugate additions of organocopper reagents to thiochromones, especially those using

a catalytic amount of copper (I) salts in the synthesis of an important class of sulfur-heterocycles-2-alkylthiochroman-4-ones and thioflavanones. The ability to add alkenyl and alkynyl groups are highly desirable in organic synthesis. This review will also cover the recent progress on the synthesis of 2-alkynyl thiochroman-4-ones via the Cu-catalyzed formal conjugate addition of alkynyl groups to thiochromones and 2-alkenylation thiochromones via 1,4-additions of alkenyl Grignard reagents promoted by TMSOTf.

1.2. Significance of Sulfur-Containing Heterocycles-Thiochromanone Derivatives

Due to their wide presence in numerous pharmaceutical active molecules as well as in many bioactive natural products [12–15], sulfur-containing heterocycles played a very important role in our daily lives. Sulfur-containing heterocycles are also widely used in areas, such as medicinal chemistry, material science, food industry, and biology in recent years [16–22]. Although improved bioavailability and bioactivity of compounds are expected via the isosteric replacement of an oxygen atom by a sulfur atom [23], heterocyclic compounds contained sulfur are a much less studied area compared to heterocycles contained oxygen. The development of efficient synthetic approaches to sulfur-containing compounds received more and more interest both in industry and academia in recent years. This is mostly due to the rich biological activities that sulfur-containing compounds display as well as their widespread applications in many areas including pharmaceutical, agrochemical, biology, food chemistry, and other areas. Sulfur-containing heterocycles were found to display rich biological activities. For example, they were found to display cytotoxic effects on tumor cells in vitro [33], cytotoxic activities and the in vitro antileishmanial [34]. Sulfur heterocycles were also reported to be able to kill tumor cells by inducing tumor cell apoptosis [35]. The sulfur analogues of flavonoids, i.e., thioflavonoids, [36–39], were reported to possess rich biological activities. They were reported to have the ability to inhibit nitric oxide production, and to display antimicrobial, antifungal, and antioxidant properties, etc. [40–48]. Thiochromanones, i.e., thiochroman-4-ones, 2-substituted thiochroman-4-ones such as 2-alkylthiochroman-4-ones, and 2-arylthiochroman-4-ones (thioflavanone), are vital precursors and valuable synthons for the synthesis of thiochromanone derivatives for the study of biological activities [49–56].

2. Cu-Catalyzed Conjugate Addition of Grignard Reagents to Thiochromones

Carbon–carbon bond formation is one of the most important transformations in the synthesis of carbon framework of complex molecules in organic synthesis. Carbon–carbon bond formation is one of the most important tools in a synthetic organic chemist’s toolbox.

Among the many synthetic approaches developed for the efficient construction of carbon–carbon bonds, the 1,4-conjugate addition reaction of various organometallic reagents, including Grignard reagents (RMgX, X = Br, Cl, I), represented one of the most reliable synthetic methods for this purpose in organic synthesis [57]. It is well known that Grignard reagents usually undergo 1,2-addition to α , β -unsaturated carbonyl compounds selectively over 1,4-addition pathway without the addition of catalysts, such as Cu (I) salts. It was reported that Cu (I) salts effectively catalyzed the 1,4-conjugate addition of Grignard reagents to carbonyl compounds [29,57]. This kind of Cu (I) salt catalyzed reaction of Grignard reagents usually gave excellent regioselectivity (i.e., 1,4-addition vs. 1,2-addition pathway) as exclusive 1,4-adducts were observed [29,57]. Recently, a unified approach to 2-substituted thiochroman-4-ones-2-alkyl thiochroman-4-ones, 2-aryl thiochroman-4-ones (thioflavanones) via Cu-catalyzed 1,4-conjugate addition of Grignard reagents to thiochromones was reported by our research group (Figure 3) [58]. This unified approach took advantage of the readily available of Grignard reagents, the ease in preparation from corresponding halide compounds, and the broad scope of Grignard reagents (Figure 3) [58].

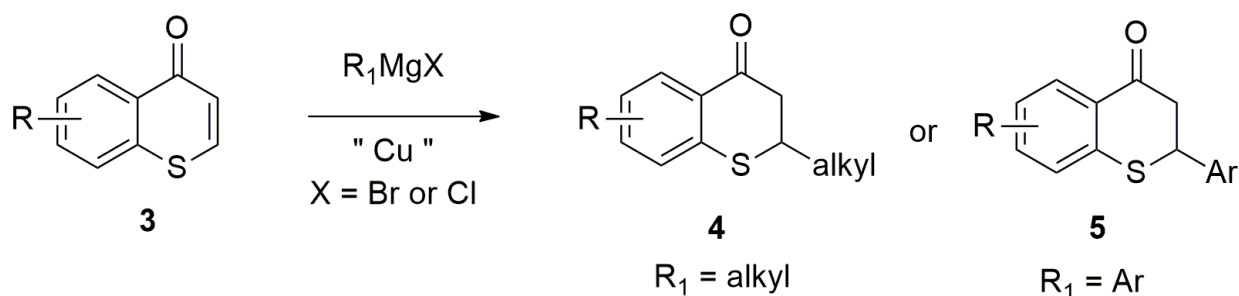


Figure 3. Copper-Catalyzed Conjugate Addition of Grignard Reagents to Thiochromones.

The investigation started with *n*-butylmagnesium chloride with thiochromone **3A** (Figure 4). It was reported that an excellent yield (89%) of 1,4-adduct, 2-*n*-butylthiochroman-4-one **4a** can be attained when TMSCl was used as the additive with 2.0 equivalent of LiCl and 1.0 equivalent of CuCN (Figure 4). The optimization of reaction conditions found that the use of 0.2 equivalent of CuCN·2LiCl offered the highest yield of 1,4-adduct with TMSCl as the additive. When a smaller amount of CuCN·2LiCl (0.1 equivalent) was used, no significant change of the yield of 1,4-adduct **4a** (85% vs. 89%) was observed [58].

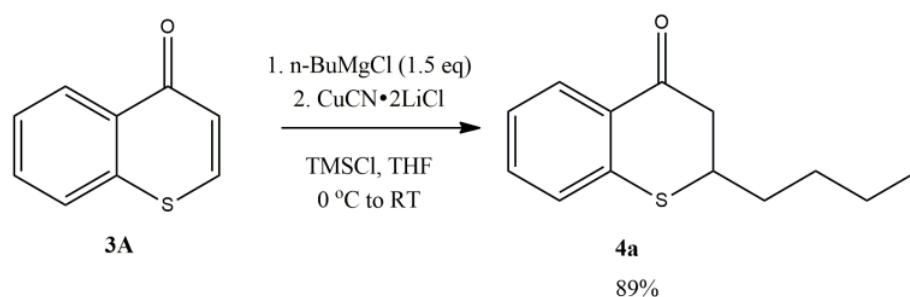


Figure 4. Copper-Catalyzed Conjugate Addition of *n*-BuMgCl to Thiochromones.

With this optimal reaction condition found, the scope of Grignard reagents was then investigated. A broad scope of Grignard reagents added to thiochromone **3A** to in 1,4-addition fashion to afford 1,4-adducts **4a–h** with good chemical yields (Figure 5, 64–88%). Simple Grignard reagents underwent 1,4-conjugate addition to thiochromone **3A** smoothly to deliver 1,4-adducts **4a–4d** with excellent efficiency (Figure 5, 75–88%). Steric bulkier Grignard reagents were less reactive and afford lower yields presumably due to steric hindrance (Figure 5, **4e**, 69% and **4f**, 64%). Grignard reagents prepared from corresponding cyclic halides also worked well (Figure 5, **4g**, 82% and **4h**, 85%) [58].

Under these optimal reaction conditions, aromatic Grignard reagents also underwent conjugate addition to thiochromones smoothly (Figure 6). PhMgBr added to thiochromone **3A** to in 1,4-addition fashion with high efficiency (Figure 6, **5a**, 89%). Grignard reagents with electron-donating groups such as “-Me”, “-OMe” on the aromatic ring were found to be effective too (**5b–d**, 80–90%). Grignard reagents with strong electron-withdrawing groups such as “-CF₃” on the aromatic ring also worked well in 1,4-addition fashion (**5e**, 70%). Grignard reagents prepared from extended aryl bromides also underwent 1,4-conjugate addition to thiochromone **3A** smoothly to afford 1,4-adducts with high chemical yields (**5f**, 84%; **5g**, 78%). Furthermore, Grignard reagents prepared from corresponding aromatic heterocycle halides such as 2-furylmagnesium bromide and 2-thienylmagnesium bromide were also tolerated (**5h**, 79%; **5i**, 75%, Figure 6) [58].

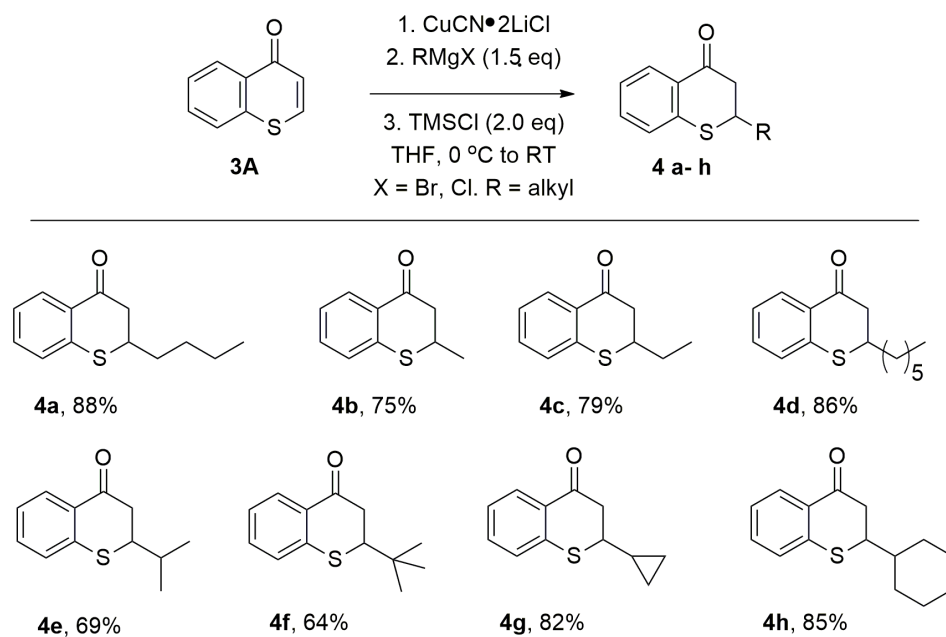


Figure 5. Copper-Catalyzed Conjugate Addition of RMgX to Thiochromones.

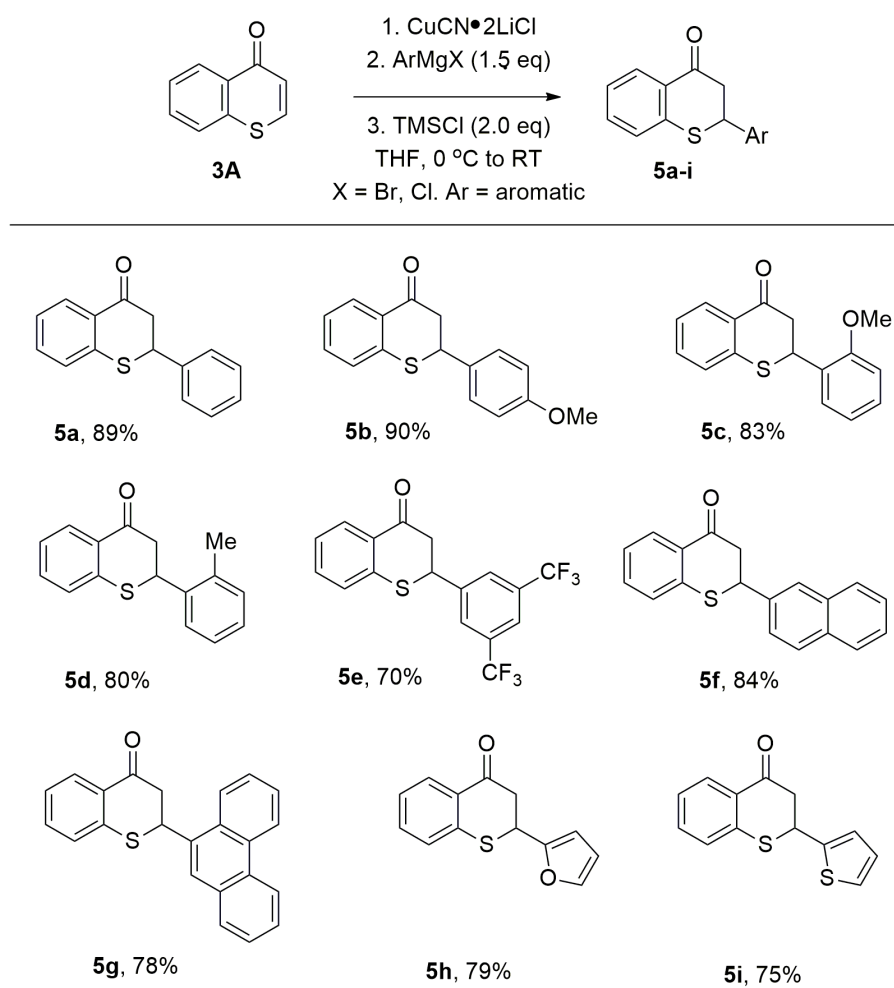


Figure 6. Copper-Catalyzed Conjugate Addition of ArMgX to Thiochromones.

A broad scope of thiochromones worked well under the reported optimal reaction condition (Figure 7). It was reported that *n*-BuMgCl underwent 1,4-conjugate addition to thiochromones **3B–3P** smoothly (Figure 7, **4Ba–4Oa**, 73–86%). Thiochromones bearing simple alkyl groups reacted well to afford **4Ba–4Da** in good yields (80–84%). The steric hindered *t*-butyl group were also tolerated to afford 1,4-adduct **4Ea** with 75% yield. *N*-BuMgCl also added to thiochromones bearing halides on the aromatic ring (i.e., F, Br, and Cl) to deliver 1,4-adducts in good yields (Figure 7). *N*-BuMgCl also underwent 1,4-conjugate addition with thiochromones with two halides on the aromatic ring, such as 6,8-difluorothiochromanone and 6,8-dichlorothiochromone with good efficiency (**4Ka**, 73% and **4La**, 77%, Figure 7). Thiochromones bearing electron-donating groups, such as MeO-, also worked well (Figure 7, **4Ma**, 86%; **4Oa**, 85%). Extended thiochromone **3P** also worked well (Figure 7, **4Pa**, 71%) [58].

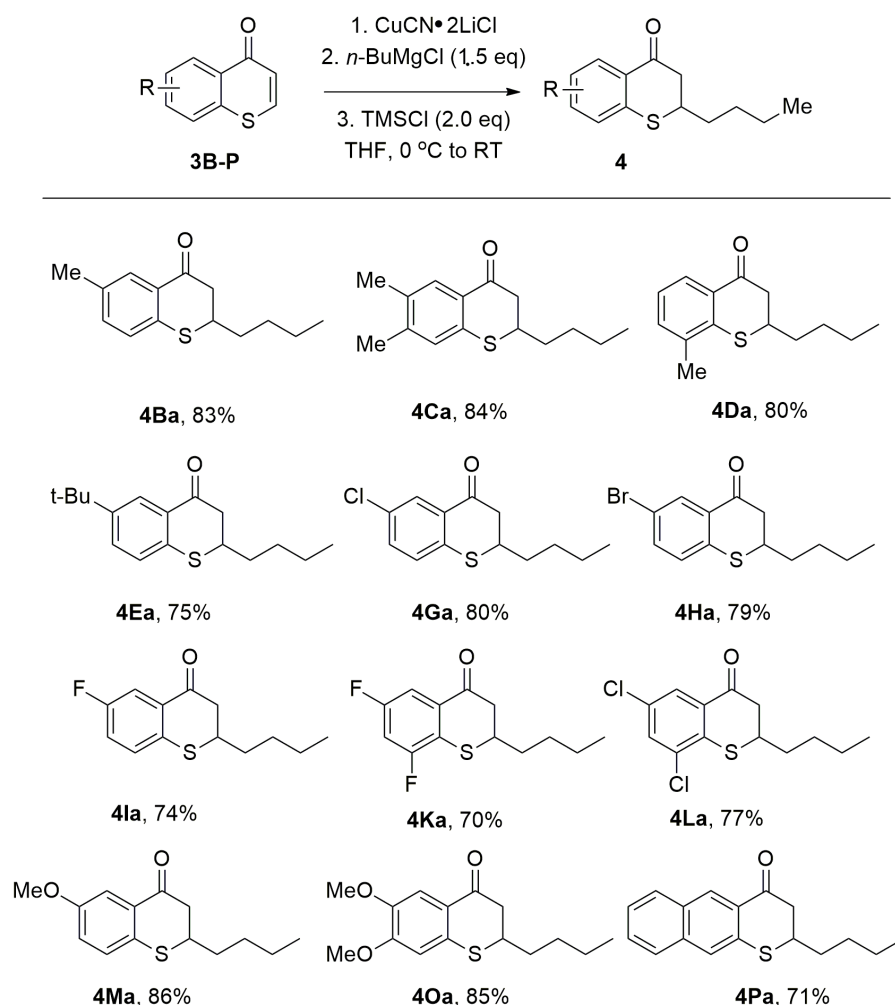


Figure 7. Copper-Catalyzed Conjugate Addition of ArMgX to Thiochromones.

With the employment of PhMgBr, the scope of substituted thiochromones was also explored to synthesize various thioflavanones, an important class of thiochromone derivatives with rich biological activities. Thiochromones bearing electron-donating or electron-withdrawing groups on the aromatic ring were investigated with PhMgBr. PhMgBr added to thiochromones **3B–3P** in 1,4-addition fashion smoothly to afford 1,4-adducts-thioflavanones in good yields (Figure 8). For example, with simple alkyl groups on the aromatic ring of thiochromones, thioflavanones **5Ba–3Ea** can be isolated in good yields (Figure 8, 83–88%). Thiochromone bearing bulky groups (*i*-Pr) were also tolerated (Figure 8, **5Fa**, 77%). PhMgBr also worked well with thiochromones bearing halides (i.e., F, Br, and Cl) on the aromatic ring (Figure 8, **5Ga–5Ia**, 78–82%). PhMgBr also underwent 1,4-

conjugate addition with thiochromones with two halides on the aromatic ring, such as 6,8-difluorothiochromanone and 6,8-dichlorothiochromone with good efficiency (Figure 8, **5Ka**, 70% and **5La**, 76%). Electron-donating groups, such as MeO-, also underwent smooth 1,4-conjugate addition to thiochromones to deliver 1,4-adducts in excellent chemical yields (**5Ma**, 84% and **5Na**, 83%). PhMgBr also adds to 8-substituted thiochromones (8-*i*-Pr, 8-MeO-) with good yields (**5Fa**, 77%, **5Ma**, 81%). This indicates that the steric hindrance was not a problem here. Thiochromones with extended aromatic structures also underwent 1,4-conjugate addition with PhMgBr with high efficiency (Figure 8, **5Oa**, 81%; **5Pa**, 80%) [58].

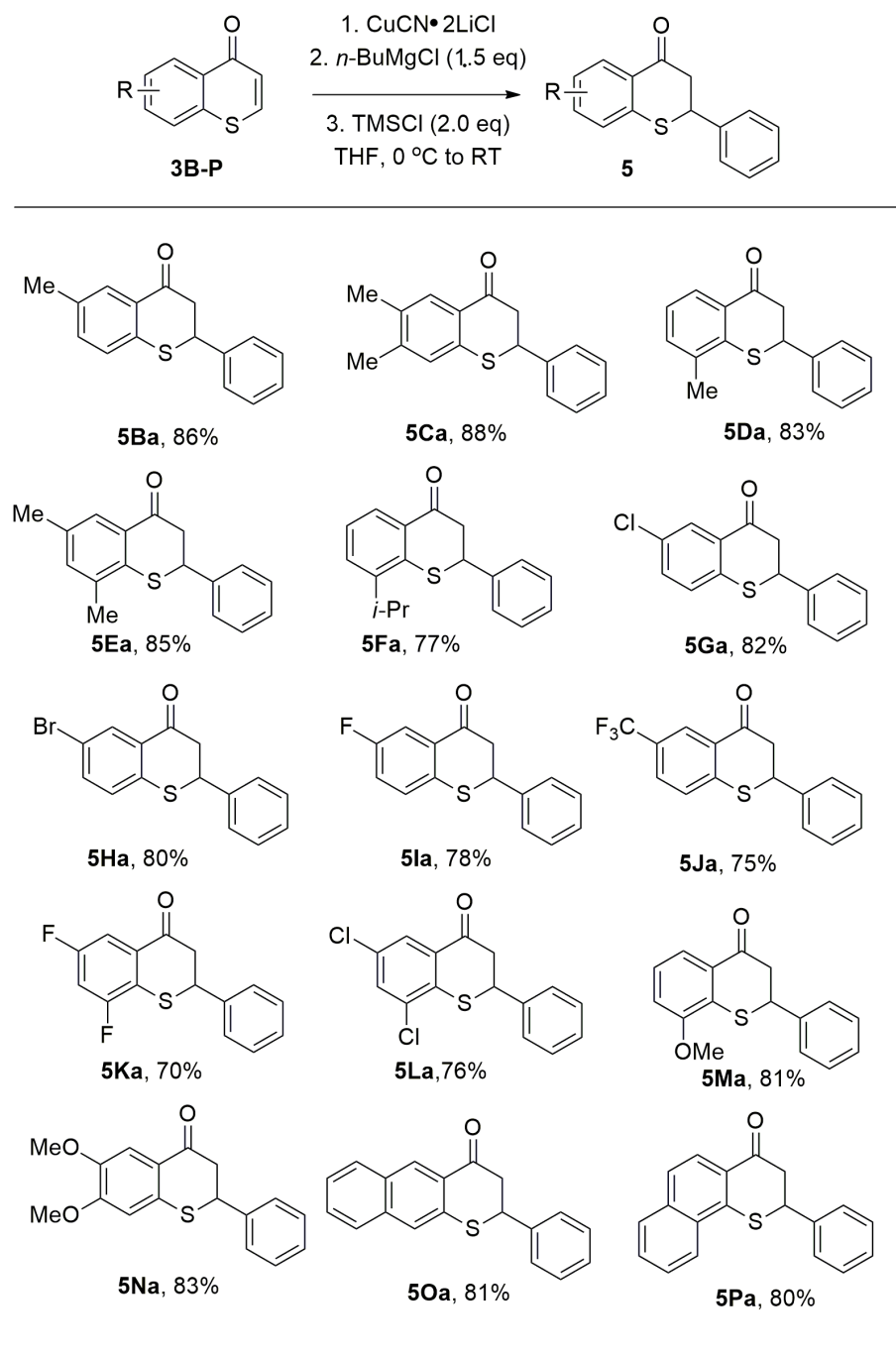


Figure 8. Synthesis of thioflavanones.

3. Enantioselective Cu-Catalyzed Conjugate Addition of Grignard Reagents to Thiochromones

Recently, an enantioselective Cu-catalyzed conjugate addition of Grignard reagents to thiochromones was also reported [59]. The screening of the reaction conditions found that a combination of copper salt, $\text{Cu}[\text{MeCN}]_4\text{PF}_6$, and chiral ligand, (*R,S*)-PPF- P^tBu_2 , in DCM with TMSiCl as the additive offered the best chemical yield (73%) as well as the best enantioselectivity (82% ee) of 1,4-adduct **4b** (Figure 9).

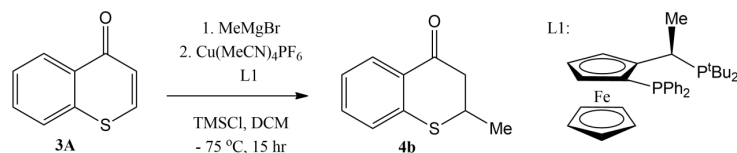


Figure 9. Enantioselective Cu-catalyzed conjugate addition of MeMgBr to thiochromones.

The optimal reaction condition was ultimately determined to be 0.2 mmol thiochromones in 4 mL DCM with 5 mol% $\text{Cu}[\text{MeCN}]_4\text{PF}_6$ and 6 mol% (*R,S*)-PPF- P^tBu_2 at $-75\text{ }^\circ\text{C}$ using TMSi as the additive [59]. With this optimal reaction in hand, both the scopes of thiochromones and Grignard reagents were explored. Thiochromones with electron donating groups such as MeO or Me undergo conjugate addition with MeMgBr smoothly to afford 1,4-adducts **7a–g** in good to moderate yields and enantioselectivities (Figure 10, 59–99% yields, and 72–87% ee). Lower enantioselectivities were observed with thiochromones with F, Cl, Br, CF_3 groups (**7h–m**, 38–73% ee, Figure 10). Thiochromones with extended aromatic group also reacted with MeMgBr to afford 1,4 adduct **7n** in 69% yield and 66% ee (Figure 10). Alkyl Grignard reagents except MeMgBr gave modest to good yields (41–92%) but with poor enantioselectivities (1–18% ee) [59].

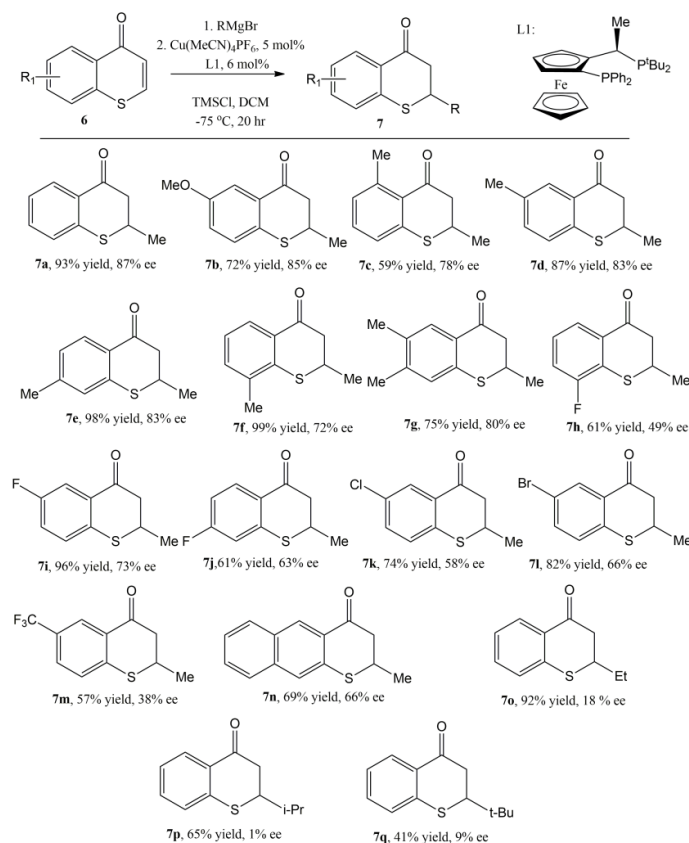


Figure 10. The Scope of Enantioselective Cu-catalyzed conjugate addition to thiochromones.

4. Alkynylation and Alkenylation of Thiochromones

4.1. Enantioselective Cu-Catalyzed Alkynylation of Thiochromones

Cu-catalyzed alkynylation of thiochromones was also reported recently by Wang's research group in 2020 [60]. The ability to incorporate the alkynyl functional group is important for research in pharmaceuticals and agrochemicals, as well as for functionalized materials. This method provided a unique approach by introducing alkyne functional groups onto thiochromanones, which will offer new opportunities for studying biological activities and further applications in materials science and other fields for these sulfur-containing heterocycles. It was found that the best yield (95%) and enantioselectivity (92% ee) of 1,4-adduct **9a** can be attained with thiochromone **8a** and phenylacetylene when more hindered phosphoramidite ligand **L2** was used (Figure 11). It was found that the additive TMSOTf is important for the success of this alkynylation reaction, as it activates the thiochromone substrates to form corresponding 4-[(trimethylsilyl)oxy]thiochromenylium as key intermediate for this reaction. TMSOTf also serves as a counteranion to stabilize the reactive complex as it was reported that a remarkable anion effect from trimethylsilyl salt was observed and the highest reactivity and enantioselectivity were achieved with the less coordinating triflate (OTf) group [60].

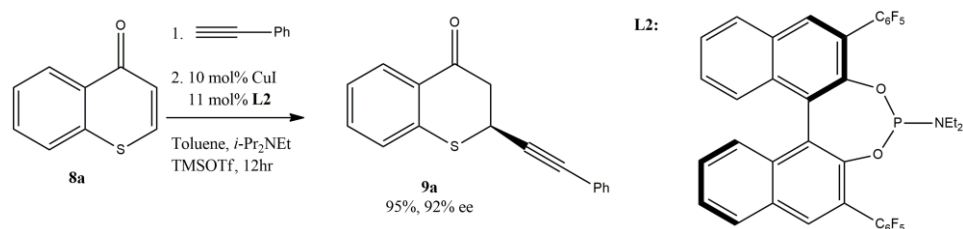


Figure 11. Enantioselective Cu-catalyzed alkynylation of thiochromones.

The scope of arylacetylene was investigated with thiochromone **8b** (Figure 12) and it was found that arylacetylenes bearing both electron-withdrawing and electron-donating groups on the aromatic ring were tolerated to furnish 1,4-adducts **9** in good to excellent yields and enantioselectivities (12 examples, 62–97% yield, 73–94% ee, Figure 12). Additionally, the scope of substituted thiochromones were also investigated. It was reported that both electron-withdrawing and electron-donating groups on the aromatic ring of the substituted thiochromones worked well. However, no significant difference on the reactivity and enantioselectivity between the electron-withdrawing and electron-donating groups on the aromatic ring of the substituted thiochromones were observed [60].

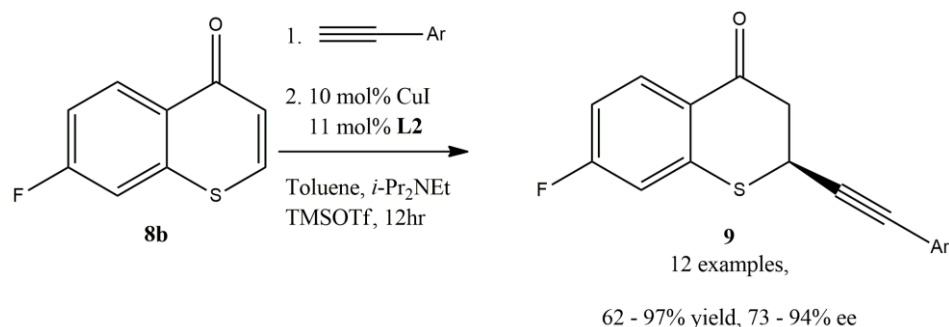


Figure 12. The scope of arylacetylenes for the enantioselective Cu-catalyzed alkynylation of thiochromones.

4.2. Alkenylation of Thiochromones with Alkenyl Grignard Reagents

Langer and coworkers reported the alkenylation of thiochromones and chromones with alkenyl Grignard reagents [61]. In their study on the structure–activity relationship of 2-vinylchroman-4-one, 2-vinylchroman-4-ones, and related analogs, the synthesis of

2-alkenylthiochroman-4-ones via the TMSOTf-mediated reaction of thiochromones with vinylmagnesium bromide and 2-(isopropenyl) magnesium bromide were successfully developed (Figure 13). It was noted that the presence of TMSOTf was the key to the success of this reaction. It was mentioned that without the addition of TMSOTf, the reaction of vinylmagnesium bromide and chromone led to complex mixture of compounds due to the competing 1,2-addition to carbonyl group instead of the desired 1,4-addition. The direct addition of alkenyl Grignard reagents to thiochromone and derivatives in the presence of TMSOTf provided a direct synthetic approach to 2-alkenylthiochroman-4-ones by introducing alkene including vinyl functional groups onto thiochromanones. It was found that both vinyl magnesium bromide and 2-(isopropenyl) magnesium bromide worked well with thiochromone to afford 1,4-adducts in modest to good yields (Figure 13). For example, vinyl magnesium bromide added to thiochromone and 6-chlorothiochromone in the presence of TMSOTf to deliver 1,4-adducts-2-vinylthiochroman-4-one **11a** (66%) and 6-chloro-2-vinylthiochroman-4-one **11b** (42%). However, 2-(isopropenyl) magnesium bromide also worked well with both thiochromone and 6-chlorothiochromone under TMSOTf-mediated reaction condition (Figure 13) [61].

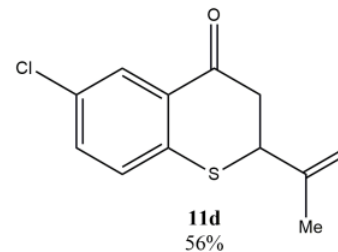
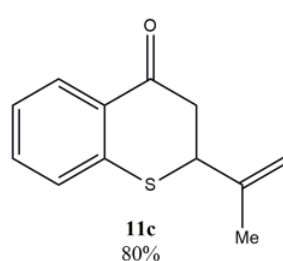
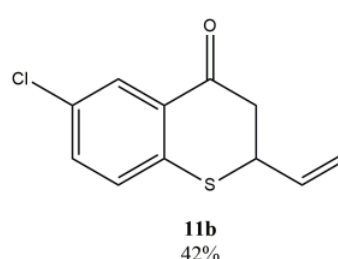
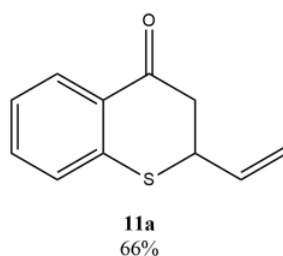
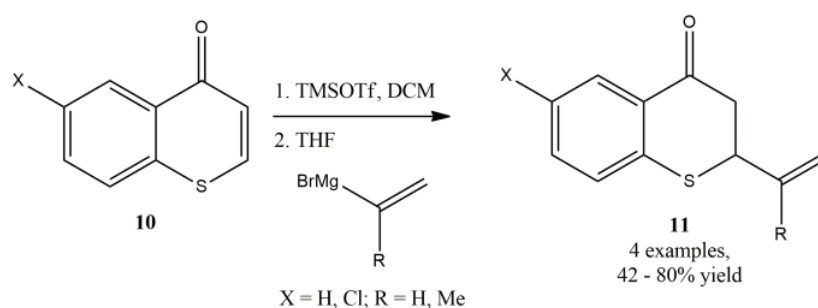


Figure 13. Alkenylation of thiochromones with alkenyl Grignard reagents.

5. Mechanism on the Cu-Catalyzed Conjugate Addition of Grignard Reagents to Thiochromones

The mechanism on the 1,4-conjugate addition reactions of cuprate reagents [i.e., $\text{Me}_2\text{CuLi}\cdot\text{LiCN}$ and $\text{Me}_2\text{CuLi}\cdot\text{LiI}$] with 2-cyclohexen-1-one **12** in THF were investigated by Bertz and Ogle [62]. Different π -complexes (i.e., **14**) of cuprate reagents with 2-cyclohexen-1-one was identified in THF using rapid-injection NMR techniques (Figure 14). It was

assumed that the contact ion-pairs (CIPs) are the reactive species and, thus, a heterodimeric structure of the contact ion-pair (CIP) **13** in THF was proposed [62].

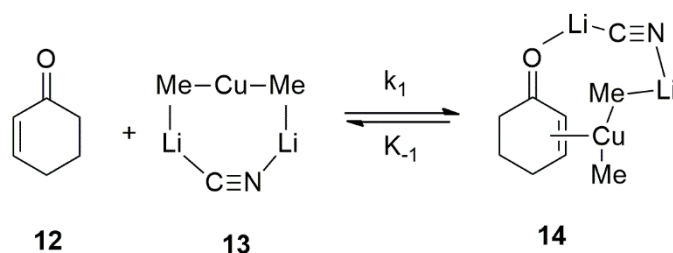


Figure 14. Investigation on Mechanism of Cu-catalyzed conjugate addition of Organocuprates using Rapid-injection NMR techniques.

The plausible mechanism on the copper-catalyzed 1,4-conjugate addition reactions of Grignard reagents [i.e., RMgX , $\text{X} = \text{Br}, \text{Cl}$] with thiochromones **15** in THF would involve the formation of similar π -complexes **17** (Figure 15). The reactive species likely would be the heterodimeric structure of the contact ion-pair (CIP) **16** in THF (Figure 15).

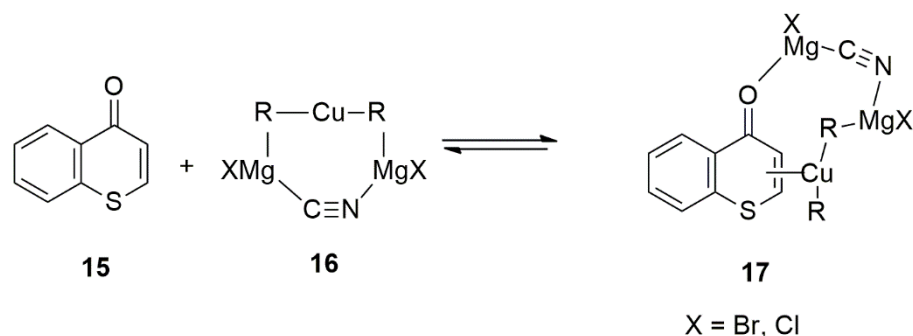


Figure 15. Plausible Reactive Intermediates in Cu-catalyzed Conjugate Addition to Thiochromones.

Lewis acids such as TMSCl were reported to greatly accelerate the organocuprate reactions [63,64]. With the Cu-catalyzed 1,4-conjugate addition of Grignard reagents, it is likely that TMSCl stabilized the π -complex **17** by converting it to a reactive tetravalent copper species **18**, which is capable of a rapid reductive elimination to form 1,4-adduct (Figure 16).

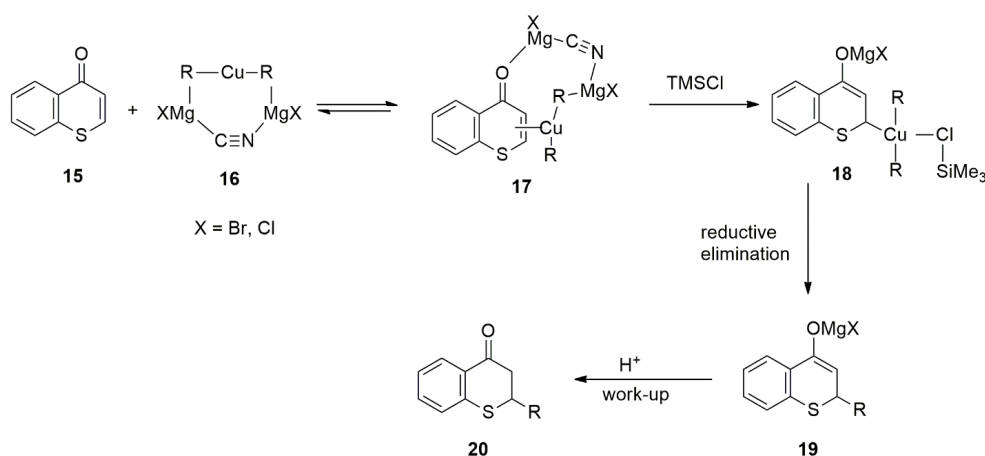


Figure 16. The Role of TMSCl in the Conjugate Addition of Grignard Reagents to Thiochromones.

6. Discussions—Challenges and Perspectives

Sulfur-heterocycles are much less studied compared to their corresponding oxygen counterparts. For example, the reactivities of thiochromones and the oxygen counterpart chromones are very different. Thiochromones are usually less reactive due to a higher degree of electron delocalization of lone pair on the sulfur atom, and this places higher electron density on the Michael acceptors and makes it less electron deficient comparing to oxygen counterparts, thus reducing the reactivity towards organometallic reagents. Recent advances in the synthetic approaches towards the successful synthesis of 2-substituted thiochroman-4-ones including 2-alkylthiochroman-4-ones, 2-arylthiochroman-4-ones (thioflavanones), 2-alkenyl thiochroman-4-ones, and 2-alkynyl thiochroman-4-ones all involved the use of Lewis acids such as TMSOTf, TMSCl, and TMSI [58–61]. The progress highlighted the importance of Lewis acids in activating thiochromones and, thus, increased reactivities. These recent advances further demonstrated the versatility of Cu-catalyzed reactions to include the 1,4-conjugate addition reactions to heterocyclic Michael acceptors such as thiochromones. The copper-catalyzed 1,4-conjugate addition of Grignard reagents are appealing due to the readily availability of Grignard reagents, the ease in preparation from corresponding halide compounds and the broad scope of Grignard reagents that will enable the synthesis of a large library of analogs for biological screening. The Cu-catalyzed conjugate addition of organometallic reagents offered a quick entry into an important class of sulfur-heterocycles, 2-substituted thiochroman-4-ones from common starting materials-thiochromones. The ability to add all three different carbon centers (sp , sp^2 , sp^3) such as alkyl, aryl, alkenyl, and alkynyl groups are important and showcase the versatility of these transformations including copper-catalyzed 1,4-addition of Grignard reagents [58,59], the copper-catalyzed formal conjugate addition of alkynyl groups [60] as well as the addition of alkenyl Grignard reagents to thiochromone promoted by TMSOTf [61]. These recent advances on the 1,4-addition or formal 1,4-addition to thiochromones are important, as they enable a quick entry into large varieties of 2-substituted thiochroman-4-ones, an important class of S-heterocycles known for their biological activities. One of the challenges in the reaction of organocuprate reagents is that it often requires stoichiometric amount of copper salts. It would always be more desirable to develop 1,4-conjugate addition of organometallic reagents including Grignard reagents using catalytic amount of copper salts. There are still challenges in developing a more general Cu-catalyzed enantioselective 1,4-conjugate addition of alkyl Grignard reagents to thiochromones that will offer high enantioselectivity for a broader scope of both Grignard reagents as well as thiochromones. A broader scope of alkenyl and alkynyl Grignard reagents that would lead to 2-alkenyl, 2-alkynyl substituted thiochroman-4-ones with excellent enantioselectivities are also desirable.

7. Conclusions

Carbon–carbon bond formation is one of the most important transformations in the synthesis of carbon framework of complex molecules in organic synthesis. Among the many synthetic methodologies for carbon–carbon bond formation, organocopper reagents are one of the most reliable organometallic reagents for this purpose. The versatility of Cu-catalyzed reactions was demonstrated by their applications in a variety of synthetic transformations, including the 1,4-conjugate addition reactions. The Cu-catalyzed conjugate addition of organometallic reagents offered straightforward access to an important class of sulfur-heterocycles, 2-alkylthiochroman-4-ones and thioflavanones, from common starting materials-thiochromones. This paper provided a brief review on recent progress on the synthesis of an important class of sulfur-heterocycles-2-alkylthiochroman-4-ones and thioflavanones via the conjugate additions of Grignard reagents to thiochromones catalyzed by copper catalysts. Recent progress on the synthesis of 2-alkynyl thiochroman-4-ones via the Cu-catalyzed formal conjugate addition of alkynyl groups to thiochromones and 2-alkenylation thiochromones via 1,4-additions of alkenyl Grignard reagents promoted by TMSOTf were also covered in this review. These recent progresses on the addition of alkyl, aryl, and alkenyl to thiochromones via 1,4-conjugate addition of Grignard reagents as well

as the formal conjugate addition of alkynyl groups to thiochromones catalyzed of Cu (I) salts provides a quick entry into 2-substituted thiochroman-4-ones, an important class of S-heterocycles known for their biological activities.

Author Contributions: This is a review article. Conceptualization F.G.; writing the original draft F.G.; Review and editing, F.G., J.A.Y., M.S.P., H.A.H. and A.M.C. All authors have read and agreed to the published version of the manuscript.

Funding: This research was funded by NIH—National Institute of General Medical Sciences (award no. R16GM145541) and NSF HBCU-EiR (award no. 1831339).

Data Availability Statement: Not applicable.

Acknowledgments: This work was generously supported by NIH—National Institute of General Sciences (award no. R16GM145541). We would also like to thank NSF HBCU-UP EiR (award no. 1831339) for their generous financial support.

Conflicts of Interest: The authors declare no conflict of interest.

References

- Breit, B.; Schmidt, Y. Directed reactions of organocopper reagents. *Chem. Rev.* **2008**, *108*, 2928. [CrossRef]
- Taylor, R.J.K. (Ed.) *Organocopper Reagents: A Practical Approach*; Oxford University Press: Oxford, UK, 1994.
- Krause, N. (Ed.) *Modern Organocopper Chemistry*; John Wiley & Sons: New York, NY, USA, 2002.
- Krause, N.; Hoffmann-Röder, A. Recent advances in catalytic enantioselective Michael additions. *Synthesis* **2001**, *2001*, 171. [CrossRef]
- Lipshutz, B.H. *Organometallics in Synthesis: A Manual*; Schlosser, M., Ed.; Chapter 4; John Wiley & Sons: Chichester, UK, 1994; p. 283.
- Krause, N.; Gerold, A. Regio- and Stereoselective Syntheses with Organocopper Reagents. *Angew. Chem. Int. Ed. Engl.* **1997**, *36*, 186. [CrossRef]
- Alexakis, A.; Benhaim, C. Enantioselective copper-catalysed conjugate addition. *Eur. J. Org. Chem.* **2002**, *2002*, 3221. [CrossRef]
- Harutyunyan, S.R.; Hartog, T.D.; Geurts, K.; Minnaard, A.J.; Feringa, B.L. Catalytic asymmetric conjugate addition and allylic alkylation with Grignard reagents. *Chem. Rev.* **2008**, *108*, 2824. [CrossRef]
- Guo, F.; Jeffries, M.C.; Graves, B.N.; Graham, S.A.; Pollard, D.A.; Pang, G.; Chen, H.Y. A rapid entry into thioflavanones via conjugate additions of diarylcuprates to thiochromones. *Tetrahedron* **2017**, *73*, 5745–5750. [CrossRef]
- Bass, S.A.; Parker, D.M.; Bellinger, T.J.; Eaton, A.S.; Dibble, A.S.; Koroma, K.L.; Sekyi, S.A.; Pollard, D.A.; Guo, F. Development of Conjugate Addition of Lithium Dialkylcuprates to Thiochromones: Synthesis of 2-Alkylthiochroman-4-ones and Additional Synthetic Applications. *Molecules* **2018**, *23*, 1728. [CrossRef]
- In Lee, J. Synthetic Approaches to 2-Alkylthiochroman-4-ones and Thioflavanones. *Bull. Korean Chem. Soc.* **2021**, *42*, 852–862. [CrossRef]
- Damani, L.A. (Ed.) *Sulphur-Containing Drugs and Related Organic Compounds*; Wiley: New York, NY, USA, 1989.
- Clayden, J.; MacLellan, P. Asymmetric synthesis of tertiary thiols and thioethers. *Beilstein J. Org. Chem.* **2011**, *7*, 582–595. [CrossRef]
- Ingall, A.H. Thiopyrans and Fused Thiopyrans. In *Comprehensive Heterocyclic Chemistry*; Katritzky, A.R., Rees, C.W., Eds.; Pergamon Press: Oxford, UK, 1984; Volume 3, p. 885.
- Schneller, S.W. Thiochromanones and Related Compounds. In *Advances in Heterocyclic Chemistry*; Katritzky, A.R., Boulton, A.J., Eds.; Academic Press: New York, NY, USA, 1975; Volume 18, p. 59.
- Acton, A.Q. (Ed.) *Sulfur Compounds: Advances in Research and Application*; Scholarly Editions: Atlanta, GA, USA, 2012.
- Nielsen, S.F.E.; Nielsen, O.; Olsen, G.M.; Liljefors, T.; Peters, D. Novel Potent Novel Potent Ligands for the Central Nicotinic Acetylcholine Receptor: Synthesis, Receptor Binding, and 3D-QSAR Analysis. *J. Med. Chem.* **2000**, *43*, 2217–2226. [CrossRef]
- Smith, B.R.; Eastman, C.M.; Njardarson, J.T. Beyond C, H, O and N! Analysis of the Elemental Composition of U.S. FDA Approved Drug Architectures. *J. Med. Chem.* **2014**, *57*, 9764–9773. [CrossRef] [PubMed]
- Takimiya, K.; Osaka, I.; Mori, T.; Nakano, M. Organic Semiconductors Based on [1]Benzothieno[3,2-*b*][1]benzothiophene Substructure. *Acc. Chem. Res.* **2014**, *47*, 1493–1502. [CrossRef] [PubMed]
- Joyce, N.I.; Eady, C.C.; Silcock, P.; Perry, N.B.; Van Klink, J.W. Fast Phenotyping of LFS-Silenced (Tearless) Onions by Desorption Electrospray Ionization Mass Spectrometry (DESI-MS). *J. Agric. Food Chem.* **2013**, *61*, 1449–1456. [CrossRef] [PubMed]
- Mishra, A.; Ma, C.Q.; Bauerle, P. Functional Oligothiophenes: Molecular Design for Multidimensional Nanoarchitectures and Their Applications. *Chem. Rev.* **2009**, *109*, 1141–1276. [CrossRef]
- Lin, D.Y.; Zhang, S.Z.; Block, E.; Katz, L.C. Encoding social signals in the mouse main olfactory bulb. *Nature* **2005**, *434*, 470–477. [CrossRef]
- Wermuth, C.G. Molecular variations based on isosteric replacements. In *The Practice of Medicinal Chemistry*; Wermuth, C.G., Ed.; Academic Press: San Diego, CA, USA, 1996; pp. 203–237.
- Glaser, C. Ber. 2, 422 (1869); C. Glaser. *Liebigs Ann. Chem.* **1870**, *154*, 159.


25. Ullmann, F. Ber. deut. Chem. Ges. 29, 1878 (1896). *Liebigs Ann. Chem.* **1904**, 332, 38. [CrossRef]
26. Ullmann, F.; Sponagel, P. Ueber die phenylirung von phenolen. *Chem. Ber.* **1905**, 38, 2211–2212. [CrossRef]
27. Reich, R. Nouveaux composés organométalliques: Le cuivre phényle et l'argent phényle. *Compt. Rend.* **1923**, 177, 322.
28. Gilman, H.; Straley, J.M. Relative reactivities of organometallic compounds. XIII. Copper and silver. *Rec. Trav. Chim.* **1936**, 55, 821. [CrossRef]
29. Kharasch, M.S.; Tawney, P.O. Factors determining the course and mechanisms of Grignard reactions. II. The effect of metallic compounds on the reaction between isophorone and methylmagnesium bromide. *J. Am. Chem. Soc.* **1941**, 63, 2308–2316. [CrossRef]
30. Gilman, H.; Jones, R.G.; Woods, L.A.J. The preparation of methylcopper and some observations on the decomposition of organocopper compounds. *Org. Chem.* **1952**, 17, 1630. [CrossRef]
31. House, H.O.; Respass, W.L.; Whitesides, G.M.J. The chemistry of carbanions. XII. The role of copper in the conjugate addition of organometallic reagents¹. *Org. Chem.* **1966**, 31, 3128. [CrossRef]
32. Lipshutz, B.H.; Sengupta, S. Organocopper reagents: Substitution, conjugate addition, carbo/metallocupration, and other reactions. *Org. React.* **1992**, 41, 135.
33. Choi, E.J.; Lee, J.I.; Kim, G.-H. Evaluation of the anticancer activities of thioflavanone and thioflavone in human breast cancer cell lines. *Int. J. Mol. Med.* **2012**, 29, 252–256. [PubMed]
34. Vargas, E.; Echeverri, F.; Vélez, I.D.; Robledo, S.M.; Quiñones, W. Synthesis and Evaluation of Thiochroman-4-one Derivatives as Potential Leishmanicidal Agents. *Molecules* **2017**, 22, 2041. [CrossRef]
35. Zhao, J.; Li, H.-Z.; Suo, H.; Wang, Y.; Yang, C.; Ma, Z.; Liu, Y. Cytotoxic effect of three novel thiochromanone derivatives on tumor cell in vitro and underlying mechanism. *Glob. Adv. Res. J. Med. Sci.* **2014**, 3, 240–250.
36. Harborne, J.B. *The Flavonoids: Advances in Research Since 1980*; Chapman and Hall: New York, NY, USA, 1988.
37. Harborne, J.B.; Williams, C.A. Anthocyanins and other flavonoids. *Nat. Prod. Rep.* **1995**, 12, 639–657. [CrossRef]
38. Pietta, P.G. Flavonoids as antioxidants. *J. Nat. Prod.* **2000**, 63, 1035–1042. [CrossRef] [PubMed]
39. Andersen, O.M.; Markham, K.R. (Eds.) *Flavonoids: Chemistry, Biochemistry and Applications*; Taylor & Francis: London, UK, 2006.
40. Philipp, A.; Jirkovsky, I.; Martel, R.R. Synthesis and antiallergic properties of some 4*H*, 5*H*-pyrano[3,2-*c*][1]benzopyran-4-one, 4*H*,5*H*-[1]benzothiopyrano[4,3-*b*]pyran-4-one, and 1,4-dihydro-5*H*-[1]benzothiopyrano[4,3-*b*]pyridine-4-one derivatives. *J. Med. Chem.* **1980**, 23, 1372–1376. [CrossRef]
41. Ramalingam, K.; Thyvelikath, G.X.; Berlin, K.D.; Chesnut, R.W.; Brown, R.A.; Durham, N.N.; Ealick, S.E.; Van der Helm, D. Synthesis and biological activity of some derivatives of thiochroman-4-one and tetrahydrothiapyran-4-one. *J. Med. Chem.* **1977**, 20, 847–850. [CrossRef] [PubMed]
42. Wang, H.K.; Bastow, K.F.; Cosentino, L.M.; Lee, K.H. Antitumor Agents. 166. Synthesis and Biological Evaluation of 5,6,7,8-Substituted-2-phenylthiochromen-4-ones. *J. Med. Chem.* **1996**, 39, 1975–1980. [CrossRef]
43. Holshouser, M.H.; Loeffler, L.J.; Hall, I.H. Synthesis of peptides by the solid-phase method. 6. Neurotensin, fragments, and analogs. *J. Med. Chem.* **1981**, 24, 853–858. [CrossRef]
44. Dhanak, D.; Keenan, R.M.; Burton, G.; Kaura, A.; Darcy, M.G.; Shah, D.H.; Ridgers, L.H.; Breen, A.; Lavery, P.; Tew, D.G.; et al. Benzothiopyran-4-one based reversible inhibitors of the human cytomegalovirus (HCMV) protease. *Bioorg. Med. Chem. Lett.* **1998**, 8, 3677–3682. [CrossRef]
45. Nussbaumer, P.; Lehr, P.; Billich, A. 2-Substituted 4-(Thio)chromenone 6-*O*-Sulfamates: Potent Inhibitors of Human Steroid Sulfatase. *J. Med. Chem.* **2002**, 45, 4310–4320. [CrossRef]
46. Kataoka, T.; Watanabe, S.; Mori, E.; Kadomoto, R.; Tanimura, S.; Kohno, M. Synthesis and structure-activity relationships of thioflavone derivative as specific inhibitors of the ERK-MAP kinase signaling pathway. *Bioorg. Med. Chem.* **2004**, 12, 2397–2407. [CrossRef] [PubMed]
47. Soni, D.V.; Jacobberger, J.W. Gene modulation by Cox-1 and Cox-2 specific inhibitors in human colorectal carcinoma cancer cells. *Cell Cycle.* **2004**, 3, 349–357.
48. Bondock, S.; Metwally, M.A. Thiochroman-4-ones: Synthesis and reactions. *J. Sulfur Chem.* **2008**, 29, 623–653. [CrossRef]
49. Dalla Via, L.; Marciani Magno, S.; Gia, O.; Marini, A.M.; Da Settimo, F.; Salerno, S.; La Motta, C.; Simorini, F.; Taliani, S.; Lavecchia, A.; et al. Benzothiopyranoindole-Based Antiproliferative Agents: Synthesis, Cytotoxicity, Nucleic Acids Interaction, and Topoisomerases Inhibition Properties. *J. Med. Chem.* **2009**, 52, 5429–5441. [CrossRef]
50. Bates, D.K.; Li, K. Stannous Chloride-Mediated Reductive Cyclization-Rearrangement of Nitroarenyl Ketones. *J. Org. Chem.* **2002**, 67, 8662–8665. [CrossRef] [PubMed]
51. Aramaki, Y.; Seto, M.; Okawa, T.; Oda, T.; Kanzaki, N.; Shiraishi, M. Synthesis of 1-Benzothiepine and 1-Benzazepine Derivatives as Orally Active CCR5 Antagonists. *Chem. Pharm. Bull.* **2004**, 52, 254–258. [CrossRef] [PubMed]
52. Dike, S.Y.; Ner, D.H.; Kumar, A. A New Enantioselective Chemoenzymatic Synthesis of R-(−)Thiazesim Hydrochloride. *Bioorg. Med. Chem. Lett.* **1991**, 1, 383–386. [CrossRef]
53. Phippen, C.B.W.; McErlean, C.S.P. A 1,5-Benzothiazepine Synthesis. *Tetrahedron Lett.* **2011**, 52, 1490–1492. [CrossRef]
54. Li, W.; Schlepfforst, C.; Daniliuc, C.; Glorius, F. Asymmetric Hydrogenation of Vinylthioethers: Access to Optically Active 1,5-Benzothiazepine Derivatives. *Angew. Chem. Int. Ed.* **2016**, 55, 3300–3303. [CrossRef]
55. Fang, X.; Li, J.; Wang, C.J. Organocatalytic Asymmetric Sulfa-Michael Addition of Thiols to α,β -Unsaturated Hexafluoroisopropyl Esters: Expedient Access to (*R*)-Thiazesim. *Org. Lett.* **2013**, 15, 3448–3451. [CrossRef]

56. Fukata, Y.; Asano, K.; Matsubara, S. Facile Net Cycloaddition Approach to Optically Active 1,5-Benzothiazepines. *J. Am. Chem. Soc.* **2015**, *137*, 5320–5323. [CrossRef]
57. Ortiz, P.; Lanza, F.; Harutyunyan, S.R. 1,2- Versus 1,4-Asymmetric Addition of Grignard Reagents to Carbonyl Compounds. In *Progress in Enantioselective Cu(I)-catalyzed Formation of Stereogenic Centers*; Harutyunyan, S.R., Ed.; Springer Press: Basel, Switzerland, 2016; pp. 99–134.
58. Bellinger, T.J.; Harvin, T.; Pickens-Flynn, T.; Austin, N.; Whitaker, S.H.; Tang Yuk Tutein, M.L.C.; Hukins, D.T.; Deese, N.; Guo, F. Conjugate Addition of Grignard Reagents to Thiochromones Catalyzed by Copper Salts: A Unified Approach to Both 2-Alkylthiochroman-4-One and Thioflavanone. *Molecules* **2020**, *25*, 2128. [CrossRef]
59. Luo, S.; Meng, L.; Yang, Q.; Wang, J. Cu-Catalyzed Conjugate Addition of Grignard Reagents to Thiochromones: An Enantioselective Pathway for Accessing 2-Alkylthiochromanones. *Synlett* **2018**, *29*, 2071–2075.
60. Meng, L.; Ngai, K.Y.; Chang, X.; Lin, Z.; Wang, J. Cu(I)-Catalyzed Enantioselective Alkynylation of Thiochromones. *Org. Lett.* **2020**, *22*, 1155–1159. [CrossRef] [PubMed]
61. Hoettecke, N.; Rotzöll, S.; Albrecht, U.; Lalk, M.; Fischer, C.; Langer, P. Synthesis and antimicrobial activity of 2-alkenylchroman-4-ones, 2-alkenylthiochroman-4-ones and 2-alkenylquinol-4-ones. *Bioorg. Med. Chem.* **2008**, *16*, 10319–10325. [CrossRef]
62. Bertz, S.H.; Cope, S.; Murphy, M.; Ogle, C.A.; Taylor, B.J. Rapid injection NMR in mechanistic organocopper chemistry. Preparation of the elusive copper (III) intermediate. *J. Am. Chem. Soc.* **2007**, *129*, 7208–7209. [CrossRef] [PubMed]
63. Corey, E.J.; Boaz, N.W. Evidence for a reversible d, π -complexation, β -cupration sequence in the conjugate addition reaction of Gilman reagents with α , β -enones. *Tetrahedron Lett.* **1985**, *26*, 6015–6018. [CrossRef]
64. Bertz, S.H.; Miao, G.; Rossiter, B.E.; Snyder, J.P. Effect of TMSCl on the Conjugate Addition of Organocuprates to α -enones: A New Mechanism. *J. Am. Chem. Soc.* **1995**, *117*, 11023–11024. [CrossRef]

Disclaimer/Publisher's Note: The statements, opinions and data contained in all publications are solely those of the individual author(s) and contributor(s) and not of MDPI and/or the editor(s). MDPI and/or the editor(s) disclaim responsibility for any injury to people or property resulting from any ideas, methods, instructions or products referred to in the content.

Review

Recent Advances of Cu-Based Catalysts for NO Reduction by CO under O₂-Containing Conditions

Xiaoli Chen ¹, Yaqi Liu ¹, Yan Liu ¹, Dianxing Lian ¹, Mohaoyang Chen ¹, Yongjun Ji ^{1,*}, Liwen Xing ^{2,*} , Ke Wu ^{2,*} and Shaomian Liu ^{3,*}¹ School of Light Industry, Beijing Technology and Business University, Beijing 100048, China² College of Chemistry and Materials Engineering, Beijing Technology and Business University, Beijing 100048, China³ Institute of Process Engineering, Chinese Academy of Sciences, Beijing 100190, China

* Correspondence: yjji@btbu.edu.cn (Y.J.); xingliwen@btbu.edu.cn (L.X.); wuke@btbu.edu.cn (K.W.); shaomianliu@163.com (S.L.)

Abstract: Selective catalytic reduction of NO_x by CO (CO-SCR) to both N₂ and CO₂ is a promising way to simultaneously remove two harmful gases, CO and NO_x, in automobile and factory exhaust gases. The development of efficient catalysts is the key challenge for the technology to be commercialized. The low-cost Cu-based catalysts have shown promising performance in CO-SCR, but there are some technical problems that obstruct their practical implementation, such as high reduction temperature and low O₂, H₂O, and SO₂ resistance. This paper provides a comprehensive overview and insights into CO-SCR under O₂-containing conditions over the Cu-based catalysts, including catalytic performances of non-supported, supported mono-metallic, supported bimetallic, and supported multi-metallic Cu-based catalysts. In addition, the effects of O₂ concentration, reaction temperature, H₂O, and SO₂ on the catalytic performance are discussed. Furthermore, the reaction mechanism of CO-SCR on Cu-based catalysts is briefly summarized. Lastly, challenges and perspectives with respect to this reaction are discussed. We hope this work can provide theoretical guidance for the rational design of efficient Cu-based catalysts in the CO-SCR reaction for commercial applications.

Keywords: Cu-based catalysts; CO + NO; catalytic performances; O₂ resistance; H₂O and SO₂ resistance



Citation: Chen, X.; Liu, Y.; Liu, Y.; Lian, D.; Chen, M.; Ji, Y.; Xing, L.; Wu, K.; Liu, S. Recent Advances of Cu-Based Catalysts for NO Reduction by CO under O₂-Containing Conditions. *Catalysts* **2022**, *12*, 1402. <https://doi.org/10.3390/catal12111402>

Academic Editor: Carlo Santoro

Received: 12 October 2022

Accepted: 7 November 2022

Published: 9 November 2022

Publisher's Note: MDPI stays neutral with regard to jurisdictional claims in published maps and institutional affiliations.



Copyright: © 2022 by the authors. Licensee MDPI, Basel, Switzerland. This article is an open access article distributed under the terms and conditions of the Creative Commons Attribution (CC BY) license (<https://creativecommons.org/licenses/by/4.0/>).

1. Introduction

Nitrogen oxides (NO_x), the major component of air pollutants, can cause a series of environmental issues, such as acid rain [1], photochemical smog [2], and the destruction of the ozone layer [3]. NO_x are mainly from the exhaust emissions of automobiles [4] and factories [5]. With the enhanced environmental protection consciousness and tightening of the environmental regulations on emission control, NO_x removal has become imperative. Among various denitrification technologies, selective catalytic reduction of NO_x with NH₃ (the so-called NH₃-SCR) is the most used. However, this technology still has many shortcomings [6], such as ammonia storage [7], leakage, and high cost [8]. In contrast, CO, which also widely exists in flue gas and automobile exhaust, has low corrosivity and low requirements for equipment [9]. Therefore, the use of CO as a reducing agent to selectively reduce NO_x (CO-SCR) is more promising since it can simultaneously control the emissions of two harmful gases [10].

Noble metals (Pt, Pd, Rh, Ir, Ru, and Au), which have rich surface adsorption sites, high catalytic activity, and O₂ resistance, have been widely explored as CO-SCR catalytic active components. Among them, Pt [11], Pd [12], and Ir [13] are the most used. Recently, our group reported an efficient Ir₁/m-WO₃ catalyst with single Ir atoms anchored on the mesoporous WO₃ [14]. This Ir₁/m-WO₃ catalyst containing only 1 wt.% Ir loading exhibited exceptional catalytic performance in the presence of 2 vol.% O₂, achieving 73% NO conversion and 100% N₂ selectivity at 350 °C. Its superior activity can be attributed

to the following reasons: (i) isolated Ir single atoms and the maximized Ir-WO₃ interfaces promote the adsorption and activation of NO, and (ii) the accessible mesopores in m-WO₃ enhance the transport of both NO and CO. Despite the success achieved for noble metals, their high cost and poor low-temperature performance make them uncompetitive economically and technically in practical applications [15]. Therefore, low-cost transition metal-based catalysts have attracted widespread attention [16]. Among them, Cu-based [17,18], Fe-based [19], and Co-based [20] catalysts are widely studied.

Compared with other transition metal catalysts, Cu-based catalysts exhibit relatively better catalytic performance in the presence of O₂, showing high application potential. Many supported Cu-based catalysts such as Cu/CeO₂-Fe₂O₃ [21], CuO/CeO₂-Fe₂O₃ [22], Cu/Fe₂O₃-CeO₂/ZrO₂ [23], and CuO_x/CeO₂ [24] exhibit excellent catalytic performance, with NO conversion usually surpassing 90% at 200 °C. Moreover, non-supported catalysts such as CuCeO_x [25] and Cu₁Ce_{0.5}Fe_{1.5}O_{4.25} [18] also have high denitrification efficiency at 100–200 °C. However, the reaction conditions of the above catalysts are O₂-free. As we know, real exhaust gases contain a large amount of O₂ [10], which preferentially reacts with CO or NO to form CO₂ and NO₂, resulting in poor catalytic activity. Additionally, SO₂ and H₂O poisoning of Cu-based catalysts is another obstacle for CO-SCR technology [21,26]. Therefore, developing efficient Cu-based catalysts for CO-SCR under O₂-containing conditions, especially with low reduction temperature and strong anti-SO₂ and H₂O poisoning ability, is the key to promoting its industrial application on a large scale.

In previous reviews, Du et al. [27] summarized research advances of CuO-CeO₂ catalysts for catalytic elimination of CO and NO, focusing on the analysis of the reaction mechanism and key factors influencing the catalytic activity. Wang et al. [28] systematically summarized the reaction mechanism and anti-inactivation measures of CO-SCR over Cu-based catalysts and proposed some optimization strategies for designing catalysts with high catalytic activity. However, in these reviews, much attention is paid to the research progress of the Cu-based catalysts under O₂-free conditions, and rarely to the case in the presence of oxygen, which represents the real industrial operating conditions. This review focuses on various types of Cu-based catalysts for NO reduction by CO under O₂-containing conditions and systematically analyzes the research status, including their catalytic performances, influencing factors on the catalytic activity, and catalytic mechanism, as shown in Figure 1. Finally, challenges and perspectives with respect to this reaction are discussed. We believe this work will attract wide interest from both academia and industry, and promote the development of CO-SCR process catalysts and thus push this technology to be commercialized.

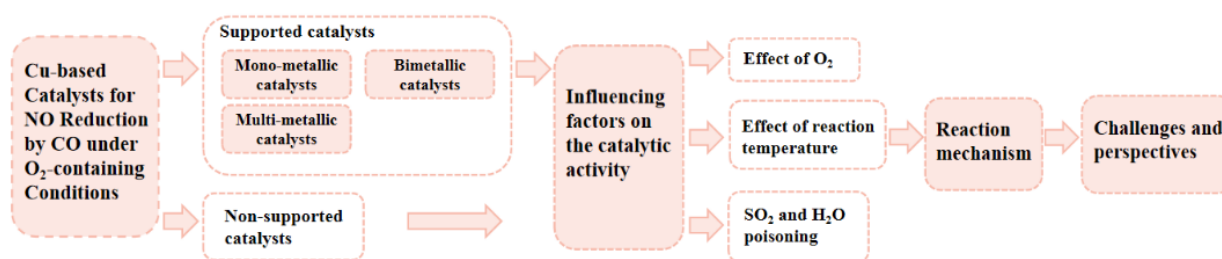


Figure 1. Schematic illustration of the review of Cu-based catalysts for NO reduction by CO under O₂-containing conditions.

2. Cu-Based Catalysts

2.1. Supported Catalysts

Compared to non-supported catalysts, supported catalysts have obvious advantages, such as high dispersion of active components and low amount. Among multifarious catalysts reported for CO-SCR, supported Cu-based catalysts are the most extensively studied and have considerable application potential [29]. In this section, various types of supported Cu-based catalysts and their catalytic behavior in NO reduction by CO in the

presence of O₂ are summarized. Table 1 gives the catalytic performances of supported Cu-based catalysts for NO + CO reaction in the presence of O₂ reported in the literature.

Table 1. Catalytic activity of various supported Cu-based catalysts for the NO + CO + O₂ reaction.

Type	Sample	T _{max} ^a (°C)	η _{NO} ^b (%)	S _{N2} ^c (%)	ψ(NO) ^d (%)	ψ(CO) (%)	ψ(O ₂) (%)	F (mL min ⁻¹) ^e	GHSV (mL g _{Ag} ⁻¹ h ⁻¹) ^f	Ref.
Mono-metallic catalysts	0.5%Cu/Al ₂ O ₃	500	—	—	1	1	0.5	100	30,000	[30]
	CuO/TiO ₂	500	54	—	5	5	0.12	50	75,000 h ⁻¹	[26]
	5Cu/AlPO ₄	400	78	48	0.2	1.5	0.65	60	36,000	[31]
	Cu/SmCeO ₂ /TiO ₂	300	50	—	0.05	1	10	50	10,000 h ⁻¹	[32]
	Cu/Ce _{0.1} Al	400	100	—	0.06	0.12	0.1	30	18,000	[33]
	CuO/Al ₂ O ₃	500	30	—	1	1	0.5	100	30,000 h ⁻¹	[34]
	Cu/Al ₂ O ₃	500	—	—	1	1	0.5	100	30,000	[35]
Bimetallic catalysts	Pt-Cu@M-Y	350	43	53	0.05	0.1	1	667	10,000 h ⁻¹	[36]
	Ce-Cu-BTC	250	90	—	0.1	0.1	5	—	—	[37]
	Fe ₂ Cu ₁ /RHA	100	100	100	0.056	0.056	8.9	2400	11,220 h ⁻¹	[38]
	Cu ₁ :Ce ₃ /Al ₂ O ₃	420	71.8	—	0.025	0.5	5	300	360,000	[39]
	Cu ₁ :Ce ₃ /CNT	220	96	—	0.025	0.5	0.3	300	12,600 h ⁻¹	[40]
	K/Cu/SmCe@TiO ₂	330	97	—	0.05	1	10	50	10,000 h ⁻¹	[41]
	Cu-Mn/Al ₂ O ₃	180	78	85	0.055	0.9	16	—	10,000 h ⁻¹	[42]
Multi-metallic catalysts	CuCoO _x /TiO ₂	200	60	—	0.1	1	2	1200	20,000 h ⁻¹	[43]
	CuCoCe/2D-VMT	200	70	97	0.05	0.1	1	—	102,000 h ⁻¹	[44]
	Cu-Ni-Ce/AC	150	99.8	—	0.4	4	5	1000	30,000 h ⁻¹	[45]
	Cu-Ce-Fe-Co/TiO ₂	200	93	—	0.02	1	6	—	10,000 h ⁻¹	[46]
	Cu-Ce-Fe-Mn/TiO ₂	200	82	—	0.02	0.02	1	—	10,000 h ⁻¹	[46]

^a T_{max}: Temperature corresponding to maximum NO conversion. ^b η_{NO}: The conversion of NO. ^c S_{N2}: The selectivity of N₂. ^d ψ(NO): The NO concentration in the feeding gas. ^e F: The volume flow rate of the feeding gas. ^f GHSV: Gas weight hourly space velocity.

2.1.1. Mono-Metallic Catalysts

The loading state of the metal, the nature of the support, and the interaction between the metal and the support will all affect the catalytic performance. Yamamoto et al. [30] studied the effects of supported elements, supports, and calcination temperature on the catalytic performance of NO-CO-O₂ reaction. The Cu-based catalysts with different supports and loading amounts were investigated in detail, and the results suggest that 0.5 wt.% Cu/Al₂O₃ exhibited the highest catalytic performance. The support γ-Al₂O₃ itself can reduce NO to N₂O but not N₂, possessing a limited capability for the reduction of NO. Therefore, the addition of Cu to Al₂O₃ promotes the formation of N₂. Additionally, the calcination temperature of the catalyst and Cu loading could affect the catalytic activity. When the calcination temperature was too high (>500 °C), the Cu species on the surface could slowly form aggregated Cu species, which preferentially oxidize CO without reducing NO_x, thereby resulting in a sharp decrease in catalytic performance. Moreover, when the Cu loading was 3 wt.%, the polymer-like Cu species were mainly present on the surface of the support. If the Cu loading was further increased to more than 5 wt.%, CuO species appeared on the catalyst surface. Both the polymer-like Cu species and CuO species mainly facilitate CO oxidation. With the 0.5 wt.% Cu loading, there was the generation of atomically dispersed Cu²⁺ species on γ-Al₂O₃. In this case, the oxidation activity of CO was weak, and a large amount of residual CO could interact with NO. Thus, the reduction activity of NO by CO is the highest. Nevertheless, Sierra-Pereira et al. [26] found that for CuO/TiO₂, its activity increased with Cu loading from 2 wt.% to 10 wt.% in NO-CO-O₂ reaction, and 10 wt.% CuO/TiO₂ exhibited the highest catalytic performance, achieving 54% NO conversion at 500 °C.

In addition to the above single metal oxide support, metal oxide composite supports were also applied to optimize the denitration performance of Cu-based catalysts. AlPO₄, which has two different types of surface hydroxyl groups, (AlOH) and (POH), is a kind of stable material with large specific surface area and acid properties [47]. Kacimi et al. [31] prepared a series of Cu/AlPO₄ catalysts with different Cu loadings by Cu(II) ion complexes

exchange, which leads to the formation of well-dispersed Cu(II) amino species. Among these catalysts, 5Cu/AlPO₄, containing the largest amount of dispersed surface Cu(II) species, exhibited the best catalytic performance, achieving 90% NO conversion at 300 °C. Venegas et al. [32] reported that the Cu/SmCeO₂@TiO₂ catalyst with Cu supported on core-shell-structured SmCeO₂@TiO₂ achieved 50% NO conversion at 500 °C in the presence of 10 vol.% O₂. Its superior catalytic performance was because CeO₂ possessed excellent redox properties through the transfer between Ce³⁺ and Ce⁴⁺, thus increasing the oxidation activity of the Cu/SmCeO₂@TiO₂ catalyst. Moreover, the addition of Sm helped to maintain the thermal stability of the CeO₂ phase. Core-shell-structured CeO₂@TiO₂ nanoparticles could also stabilize the involved Cu phase, preventing its migration and sinterization, and thus leading to higher activities [48]. Bai et al. [33] synthesized an efficient CuO/CeO₂-Al₂O₃ catalyst, which exhibited excellent catalytic performance and superior resistance to O₂ and SO₂ for CO-SCR. The incorporation of Ce⁴⁺ was conducive to the enrichment of Cu atoms and the generation of synergistic oxygen vacancies on the surface of the catalyst, which improved the redox performance of the catalyst. Moreover, Cu²⁺ was favorable for the CO adsorption, while the unpaired electrons in the CeO₂-Al₂O₃ support were favorable for the adsorption of NO.

2.1.2. Bimetallic Catalysts

Chen et al. [43] synthesized a series of CuCoO_x/TiO₂ catalysts and found that the CuCoO_x/TiO₂ catalyst able to generate the CuCo₂O₄ spinel exhibited the highest catalytic activity, reaching 98.9% NO conversion at 200 °C and in the absence of O₂. However, when 2 vol.% O₂ was introduced, the NO conversion decreased sharply to 60%. Liu et al. [42] investigated the denitration performance of various transition metals supported on Al₂O₃ pellets under O₂-rich conditions (16 vol.%). Among these catalysts, Cu-Mn/Al₂O₃ with a molar ratio Cu:Mn of 1.5 displayed the best catalytic activity, achieving nearly 78% NO conversion and 85% N₂ selectivity at 180 °C. Based on the density functional theory calculation, it was demonstrated that Mn had better O₂ resistance and Cu had better H₂O resistance. López et al. [41] prepared a novel core-shell-structured K/Cu/SmCe@TiO₂ catalyst, giving 97% NO conversion at 330 °C in the presence of excess O₂ (10 vol.%). The interaction between highly dispersed Cu species and K promoted the reduction of NO. Gholami et al. [40] found that the catalytic activity of the Cu1:Ce3/CNT catalyst (carbon nanotubes) was much better than that of the Cu1:Ce3/AC catalyst (activated carbon) in the presence of O₂ (0.3 vol.%, O₂/CO ≥ 0.6). The Cu1:Ce3/CNT catalyst displayed the highest NO conversion of 96% at 220 °C, attributed to its high concentration of surface oxygen vacancies (SOVs), high Cu⁺ species content, superior reducing capability, and the synergistic effect between SOV and Cu⁺ species. Furthermore, Gholami et al. [39] investigated the denitration performance of a string of Cu1:Ce3 catalysts supported on various supports (CNTs, AC, TiO₂, γ-Al₂O₃, and SiC) in the presence of excess O₂ (5 vol.%), and found that Cu1:Ce3/Al₂O₃ catalyst possessed the highest catalytic performance, with 71.8% NO conversion at 420 °C, mainly ascribed to the enrichment of catalytically active centers of Cu on the Al₂O₃ support. Interestingly, it was observed that with the increase in O₂ concentration from 2% to 5%, the conversion of NO increased slightly. This was because the more O₂ was adsorbed on the catalyst surface, the more adsorbed O was provided. The adsorbed O then reacted with the adsorbed CO to form CO₂, which thus led to the generation of oxygen vacancies for the adsorption and dissociation of NO further. Moreover, this adsorbed O could also react with NO to NO₂, which was quickly reduced by CO to N₂. Metal organic frameworks (MOFs) have broad application prospects in the field of catalysis, due to their huge surface area, tailored compositions, and variable structures [49,50]. Zhang et al. [37] prepared the Cu-BTC (BTC = benzene-1,3,5-tricarboxylate) and Ce-Cu-BTC catalysts, which are three-dimensional (3D) porous MOFs (their SEM images are shown in Figure 2a,b). Cu-BTC only exhibited 50% NO conversion at 250 °C, while Ce-modified Cu-BTC catalysts could achieve much higher NO conversion of 91%. Owing to the incorporation of Ce³⁺, the Ce-Cu-BTC catalyst had more SOVs, conducive to enhancing

the adsorption of NO_x on the surface of catalysts, as evidenced by the in situ DRIFTS spectrum (Figure 2c,d). The enhanced NO_x adsorption ultimately improved the catalytic activity for CO-SCR.

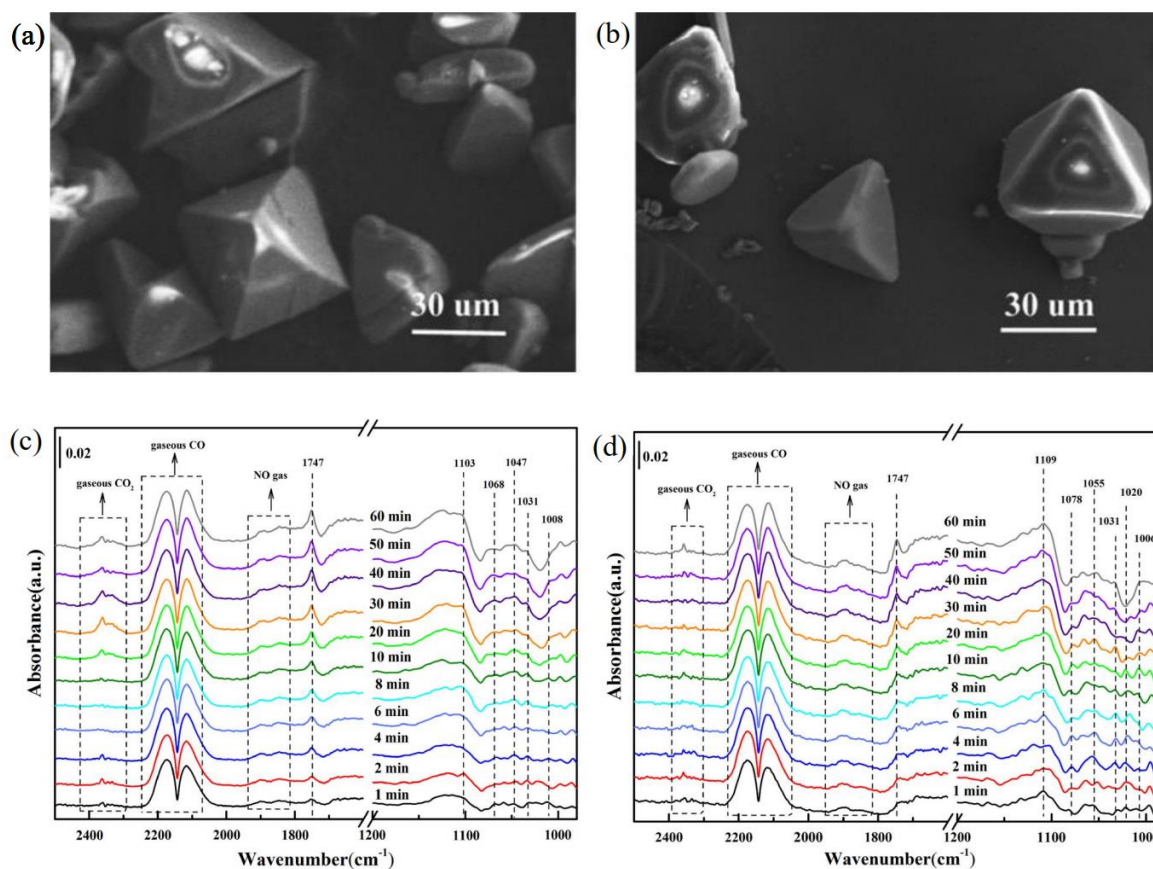


Figure 2. SEM images of (a) Cu-BTC and (b) Ce-Cu-BTC. In situ DRIFTS spectra of CO + NO + O₂ co-adsorption on the surface of (c) Cu-BTC and (d) Ce-Cu-BTC at 150 °C, where NO = 1000 ppm, CO = 1000 ppm, 5 vol.% O₂, and equilibrium gas was N₂. Reproduced from [37] with permission.

Recently, our group used a simple impregnation method followed by reduction with H₂ to synthesize a Pt-Cu@M-Y catalyst, which consists of sub-nanometric Pt on Cu nanoparticles confined in the NaOH-modified Y-zeolite. The Pt-Cu@M-Y catalyst with only 0.04 wt.% Pt loading showed superior catalytic activity for NO + CO reaction, with NO conversion and N₂ selectivity nearly 100% at 250 °C. This enhanced activity originated from the synergistic catalysis of Pt and Cu, in which NO was mainly adsorbed on sub-nanometric Pt, and the generated interfaces between Cu nanoparticles and surface CuO_x species served as the dissociation sites of NO. However, when 1 vol.% O₂ was introduced (O₂/CO = 10), the NO conversion decreased to 43% and N₂ selectivity dropped to 53% at 350 °C, due to the preferential oxidation of CO and NO by O₂ at high temperatures.

2.1.3. Multi-Metallic Catalysts

Pan et al. [46] synthesized a series of Cu-based and Mn-based catalysts by the wet impregnation method and applied them to the CO-SCR reaction. It was found that Cu-Ce-Fe-Co/TiO₂ and Mn-Ce-Fe-Co/TiO₂ exhibited better catalytic activity in the absence of O₂, both reaching full NO conversion at 250 °C. However, the presence of O₂ largely restricts the NO reduction efficiency. Comparatively, Cu-Ce-Fe-Co/TiO₂ showed better tolerance to O₂ than Mn-Ce-Fe-Co/TiO₂. When 6 vol % O₂ was fed, the Cu-Ce-Fe-Co/TiO₂ catalyst still exhibited 93% NO conversion and 74.3% NO_x conversion at 200 °C ([NO] = 200 ppm, [CO] = 200 ppm), indicating that only a part of NO was oxidized. The enhanced catalytic

performance of Cu-Ce-Fe-Co/TiO₂ may owe to its superior reducibility, more oxygen vacancies, and better oxygen mobility. Wang et al. [45] synthesized a Cu-Ni-Ce/AC catalyst by the ultrasonic equal volume impregnation method. This catalyst exhibited extremely high catalytic activity in the presence of O₂ (5 vol.%), reaching 99.8% NO conversion at 150 °C. In this case, the doping of Ce promoted the uniform dispersion of Cu and Ni and formed many reaction units on the surface of the catalyst, enhancing the adsorption abilities of CO and NO and thus improving the catalytic performance. Two-dimensional (2D) vermiculite (VMT) is a natural layered clay mineral with a unique two-dimensional structure and high-temperature stability, widely used as a support and applied in the fields of photocatalysis and heterogeneous catalysis. Liu et al. [44] synthesized a CuCoCe/2D-VMT catalyst by the impregnation method. It exhibited superior catalytic activity in the coexistence of 1 vol.% O₂ and 5 vol.% H₂O, reaching 70% NO conversion and 97% N₂ selectivity at 200 °C. They found that the doping of Ce could reduce the reduction temperature and promote the formation of oxygen vacancies, giving the CuCoCe/2D-VMT sample more active centers, thus improving its catalytic performance. This deduction was confirmed by the Raman spectrum (Figure 3a), in which the CuCoCe/2D-VMT sample had a higher concentration of oxygen vacancies than the CuCo/2D-VMT sample. Similar results were also obtained by XPS characterization. As shown in Figure 3b, CuCoCe/2D-VMT had more adsorbed oxygen (denoted as O_β).

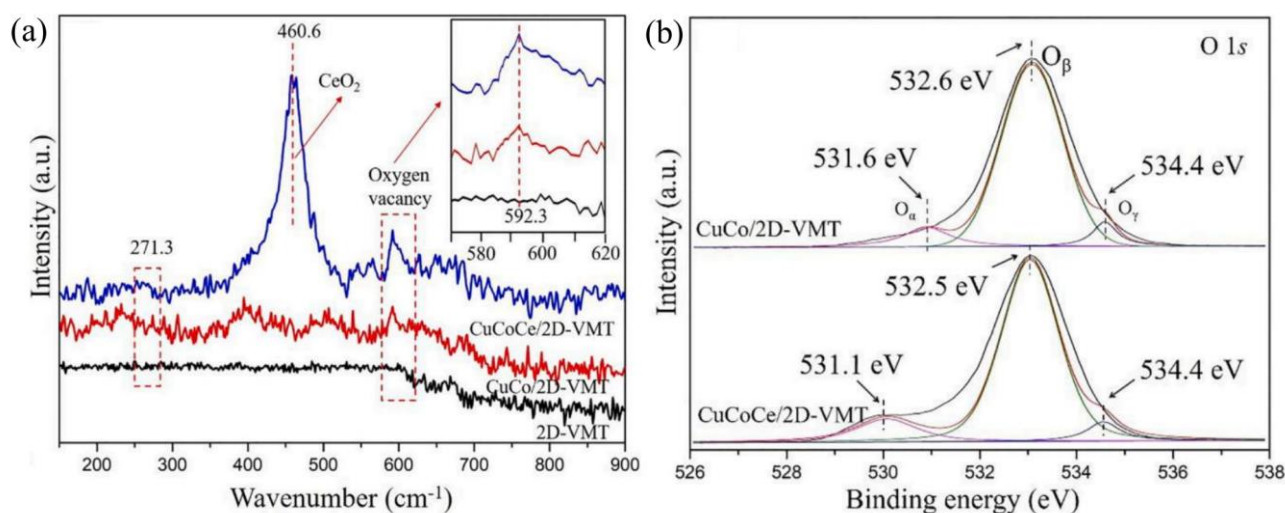


Figure 3. (a) Raman spectra of CuCoCe/2D-VMT, CuCo/2D-VMT, and 2D-VMT catalysts and (b) XPS spectra of O 1s. Reproduced from [44] with permission.

2.2. Non-Supported Catalysts

Besides a large number of reported Cu-based supported catalysts, some non-supported Cu-based catalysts also have certain O₂ resistance in the CO-SCR reaction. Mehandjiev et al. [51] first reported that CuCo₂O₄ had the ability to reduce NO by CO in the presence of O₂. Furthermore, Panayotov et al. [52] found that Cu_xCo_{3-x}O₄ spinels possessed excellent catalytic performance for CO-SCR under O₂-containing conditions than CuO and Co₃O₄. Additionally, in the presence of 650 ppm O₂, the catalytic activity increased with the Cu content. Ivanka et al. [53] prepared CuO-MnO_x (1.5 < x < 2) catalysts by coprecipitation and studied their catalytic performance in the presence of O₂. They found that the degree of NO conversion to N₂ achieved by CuO-MnO_x (Cu/Cu + Mn up to 0.53) under O₂-containing conditions was similar to that under O₂-free conditions. This could be explained as follows. After the introduction of O₂, NO quickly reacted with it to produce NO₂. Moreover, the reduction of NO₂ by CO was faster than CO oxidation. Therefore, N₂ and CO₂ were finally generated. Sun et al. [54] synthesized the CuCe mixed metal oxides, which showed superior NO conversion and N₂ selectivity, both maintaining more than 90% in a wide temperature window in the absence of O₂. Nevertheless, when 1% O₂ was introduced, the

NO conversion dropped rapidly to 0 within 3.5 h. The NO conversion could gradually recover to the initial value after the O₂ was stopped. This result indicated that CO preferentially reacts with O₂, resulting in the decrease in NO conversion in the presence of O₂. Wen et al. [55] synthesized mixed CuCeMgAlO oxides by coprecipitation, which possessed higher NO conversion than CuMgAlO and CeMgAlO for NO + CO + O₂ reaction. The superior catalytic performance of CuCeMgAlO can be explained by the synergistic effect generated by the interaction of Cu and Ce. In addition, when 1% H₂O was introduced, the NO conversion over CuCeMgAlO was significantly improved from 50% to 100% at 250 °C, but both CuMgAlO and CeMgAlO lost their catalytic activity completely. Moreover, when 500 ppm SO₂ was introduced, the NO conversion dropped rapidly over CuMgAlO and CeMgAlO; however, CuCeMgAlO still maintained 100% NO conversion at 720 °C. This suggests that CuCeMgAlO possesses high activity for NO + CO + O₂ reaction and excellent resistance to H₂O and SO₂ poisoning.

3. Influencing Factors on Catalytic Activity

There is a certain amount of O₂, SO₂, and H₂O in flue gas and automobile exhaust, which will affect the activity of the catalysts. In addition, the temperature is also an important factor. In this section, the effects of O₂, temperature, SO₂ and H₂O on the catalytic activity of Cu-based catalysts for NO reduction by CO are summarized, as shown in Figure 4.

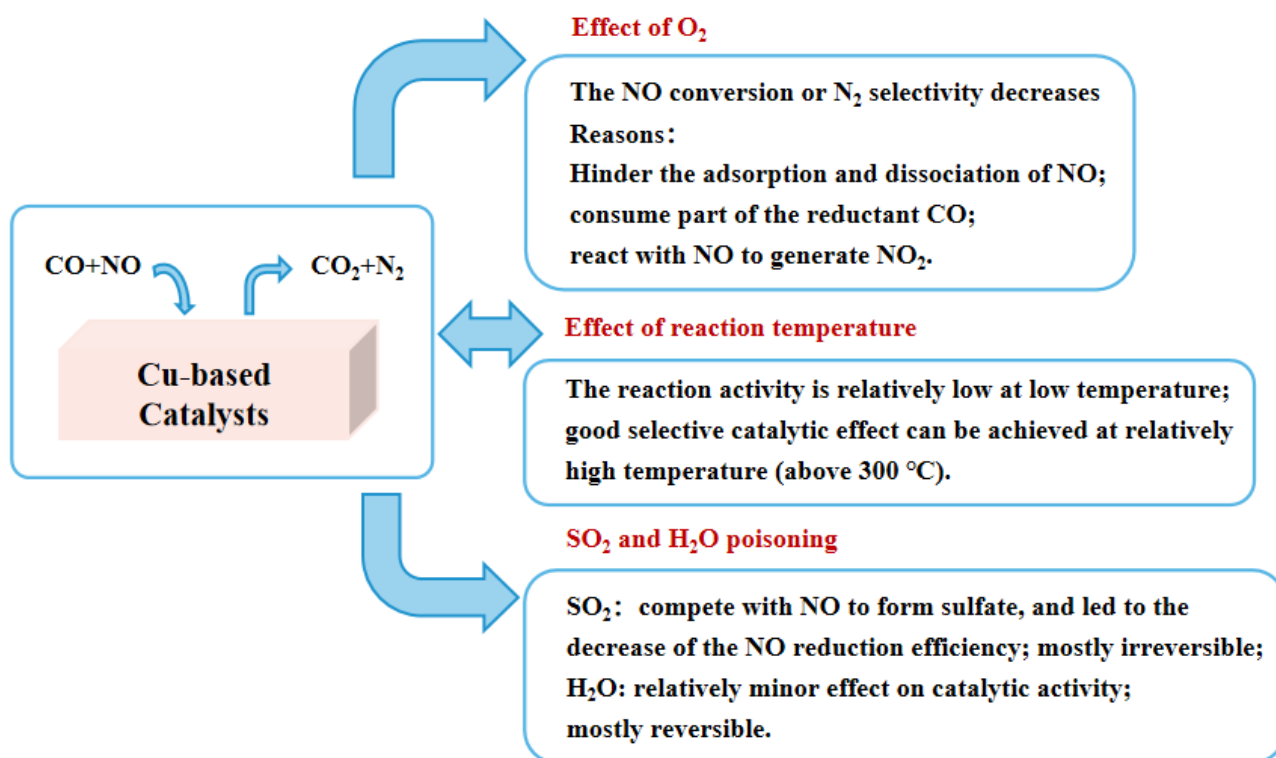


Figure 4. Effect of O₂, reaction temperature, SO₂, and H₂O on the catalytic activity of Cu-based catalysts for NO reduction by CO.

3.1. Effect of O₂

Currently, the published literature mainly studies the CO-SCR mechanism of Cu-based catalysts in the absence of O₂. Research on the catalytic performance of Cu-based catalysts in the presence of O₂ is rare and mainly focuses on the reaction conditions of low O₂ concentration ($\leq 1\%$). For instance, Wen et al. [35] prepared the Cu/Ce/Mg/Al/O mixed oxides catalyst, which could enable full NO conversion at 315 °C in the presence of 0.5% O₂ (O₂/CO = 0.36). Yamamoto et al. [30] investigated the effect of O₂ concentration on

the denitration performance of the 0.5 wt.% Cu/Al₂O₃ catalyst for CO-SCR. The results showed that in the absence of O₂, the amount of N₂ generated was high, but when the O₂ concentration increased, the amount of N₂ decreased gradually. At the same time, after O₂ was introduced, the conversion of CO increased sharply, reaching nearly 100% at 0.5% O₂. Moreover, with the increase in CO conversion, the amount of N₂ generated decreased, but the amount of N₂O and NO₂ remained unchanged, which indicates that O₂ preferentially reacted with CO, so the amount of reducing agent CO decreased, resulting in the decrease in NO conversion. When the O₂ concentration exceeded 0.5%, the amount of N₂ generated was also less and less, while the NO₂ amount increased with increasing O₂ concentration, which indicates that more and more NO is oxidized by O₂. However, the amount of NO₂ generated was much less than that of N₂ generated in the absence of O₂, indicating that most NO has not reacted with O₂, which may be because O₂ occupies the adsorption site of NO. Sun et al. [54] also observed the same phenomenon that CuCe mixed metal oxide catalysts enabled nearly full NO conversion at 250 °C in the absence of O₂, and after 1% O₂ was introduced, the NO conversion gradually dropped to 0. Therefore, O₂ existing in the CO-SCR reaction system has an inhibitory effect on NO reduction. Gholami et al. [39] investigated the effect of O₂ (2% or 5%) on the denitration performance of the Cu1:Ce3/Al₂O₃ catalyst for the CO-SCR reaction system, and found that compared with the case without O₂, the conversion of NO decreased from 59.3% to nearly 40% after 2% O₂ was introduced at 300 °C, but increased to 43.3% when 5% O₂ was introduced. They believe that this is because more O₂ is adsorbed on the surface of the catalyst and then cleaved to O_(ad), thereby promoting the formation of NO₂, which can further rapidly react with CO to form N₂ and CO₂. However, they did not provide specific information on the selectivity of N₂. In addition, some scholars also explored the CO-SCR denitration activity of the Cu-based catalysts in the presence of excess O₂. Venegas et al. [32] found that the NO conversion of the Cu/SmCeO₂/TiO₂ catalyst reached 50% in the presence of 10% O₂ at 300 °C. López et al. [41] reported that the K/Cu/SmCe@TiO₂ catalyst delivered 97% NO conversion at 330 °C in the presence of 10% O₂. However, none of them provided details on the selectivity of N₂, which directly reflects the effectiveness of the catalyst. Therefore, it is necessary to study the adsorption and dissociation centers of O₂ on the surface of Cu-based catalysts and reveal its inhibition mechanism in combination with existing characterization and analysis methods. Furthermore, the relationship between the catalytic activity and support, surface active oxygen species, and defect structure should be further investigated to improve the O₂ resistance of Cu-based catalysts.

3.2. Effect of Reaction Temperature

In addition to O₂ resistance, CO-SCR also faces the challenge of low-temperature performance. As described, although noble metals have superior O₂ resistance [56–58], their high cost and poor low-temperature performance make them unsuitable for the treatment of large-scale industrial tail gas [59,60]. In contrast, transition metal-based catalysts, especially Cu-based catalysts, have been widely studied for their low-temperature activity and low cost [61]. Under O₂-containing conditions, the minimum temperature at which the Cu-based catalyst achieves the best catalytic effect is mainly 200–300 °C, as shown in Table 1. Most published studies did not provide data on the selectivity of N₂. Even in only a few studies reporting N₂ selectivity, it requires a relatively high reduction temperature to achieve a better catalytic effect. For example, under the reaction conditions of 0.1% CO, 0.05% NO, and 1% O₂, the Pt-Cu@M-Y catalyst [36] could achieve 43% NO conversion and 53% N₂ selectivity at 350 °C. In the presence of 0.65 vol.% O₂, the Cu/AlPO₄ catalyst [31] could achieve 78% NO conversion and 48% N₂ selectivity at 400 °C. Therefore, it is necessary to improve the low-temperature activity and N₂ selectivity of the Cu-based catalysts under O₂-rich conditions in the future.

3.3. SO₂ and H₂O Poisoning

The presence of SO₂ and H₂O in the flue gas also has a certain impact on the catalytic performance of the catalysts. Some studies have revealed that SO₂ could adsorb on the surface of the catalysts and compete with NO to form sulfate [62]. The deposition of sulfate led to a decrease in the NO reduction efficiency, and this process is mostly irreversible. On the other side, the effect of H₂O on the catalyst activity is minor [21]. Sierra Pereira and Urquieta-González studied the effect of SO₂ or H₂O on the catalytic activity of Cu/TiO₂ for CO + NO reaction [26]. In the absence of SO₂ and H₂O, Cu/TiO₂ exhibited high NO conversion. After SO₂ was introduced for 30 min, the activity of Cu/TiO₂ decreased from approximately 55% to 0. Even if SO₂ was removed from the feed gas, the activity cannot be recovered at all, as shown in Figure 5a. The results indicate that SO₂ poisoning of Cu/TiO₂ catalyst is irreversible. This phenomenon was attributed to the formation of metal sulfates on the surface of catalysts, which blocked the active site. Compared with SO₂, H₂O has a relatively weak effect on the catalytic activity, as shown in Figure 5b. The introduction of 10 wt.% H₂O led to a reduction in NO conversion from 60% to 40%. After the elimination of H₂O, the activity of Cu/TiO₂ could be recovered. Liu et al. [44] reported that CuCoCe/2D-VMT exhibited superior catalytic activity in the presence of O₂ (1 vol.%) and H₂O (5 vol.%), enabling full NO conversion to N₂ at 300 °C. When a small amount of SO₂ (50 ppm or 100 ppm) was introduced, the catalytic activity decreased slightly, and soon reached a plateau. After SO₂ was removed, the activity gradually returned to the initial value. It is known that SO₂ can occupy some active sites, resulting in a slight decrease in NO conversion. However, adding a certain amount of SO₂ can achieve the balance between the SO₂ adsorption and the SO₂ reduction by CO, so the conversion of NO remains stable. Moreover, the 2D-VMT has a high specific surface area, which can provide storage space for the generated sulfate. Furthermore, Ce preferentially adsorbs SO₂ to protect the Cu active site. When a large amount of SO₂ is introduced, the balance between SO₂ adsorption and reduction is broken, so the catalytic activity continues to decrease. It may be that a large amount of SO₂ reacts with H₂O to produce stable sulfate, which occupies the active site, resulting in the irreversible deactivation of the CuCoCe/2D-VMT catalyst.

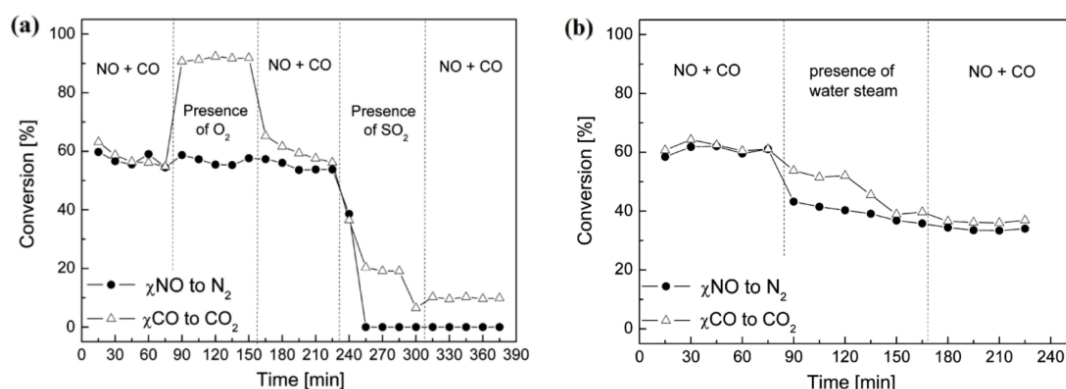
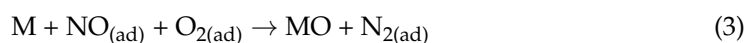
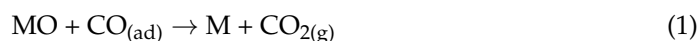


Figure 5. The effect of O₂ or SO₂ (a) and H₂O (b) on the catalytic performance for the CO-SCR reaction over Cu/TiO₂. Reproduced from [26] with permission.

Some studies also reported that SO₂ and/or H₂O have no significant effect on catalytic activity. Pan et al. investigated the catalytic activity of Cu-Ce-Fe-Co/TiO₂ for CO + NO reaction in the presence of SO₂ or H₂O, and found that after 50 ppm SO₂ or 10% H₂O addition to the feed gas, NO conversion on Cu-Ce-Fe-Co/TiO₂ did not exhibit significant changes and remained stable. This phenomenon is attributed to the special spinel structure of the Cu-Co-based catalysts, which preferentially adsorbs NO and CO compared with SO₂. This is also consistent with the findings of Chen et al. [44]. However, after simultaneously introducing SO₂ and H₂O, the activity of Cu-Ce-Fe-Co/TiO₂ decreased from approximately 95% to 60%. After SO₂ and H₂O were removed, the activity gradually recovered to about 80%.

4. Reaction Mechanism

At present, the widely accepted redox reaction mechanisms of CO-SCR catalysts are the Langmuir–Hinshelwood (L-H) mechanism and the Eley–Rideal (E-R) mechanism [63]. The E-R mechanism means that the reaction proceeds through the interaction between the adsorbed species and the gaseous reactant, while the L-H mechanism is when the reaction is performed by the adsorbed components [64]. The L-H mechanism is usually preferred because the reaction attempts may be enormous [65], which is generally accepted by researchers for metal oxide catalysts [63]. First, CO is adsorbed to the surface of the catalyst and reacts with lattice oxygen to form oxygen vacancies (CO catalytic oxidation). Next, the o-terminal of NO is adsorbed on the oxygen vacancy, and then N–O breaks to form $N_{(ad)}$ (ad stands for an adsorbed state) and new lattice oxygen. However, oxygen vacancies can also be occupied by O_2 , leading to catalyst deactivation in the presence of O_2 . Finally, $N_{(ad)}$ transforms into N_2 or N_2O by reacting with another $N_{(ad)}$ or another NO. N_2O can be subsequently adsorbed to oxygen vacancies and then form new lattice oxygen and N_2 . The reaction formula is as follows:



Zhang et al. [37] found that the model reaction $NO + CO + O_2$ over Ce–Cu–BTC follows the L-H mechanism, as shown in Figure 6a. NO is preferentially adsorbed on the active site of Ce–Cu–BTC to form various adsorbed NO species. CO is mainly adsorbed to the Ce^{3+} sites on the catalyst surface. The adsorbed NO species can react with the adsorbed CO species to form different intermediates. The interaction between Cu and Ce is conducive to the formation of more Cu^+ , which can promote the conversion of the N_2O intermediate to N_2 .

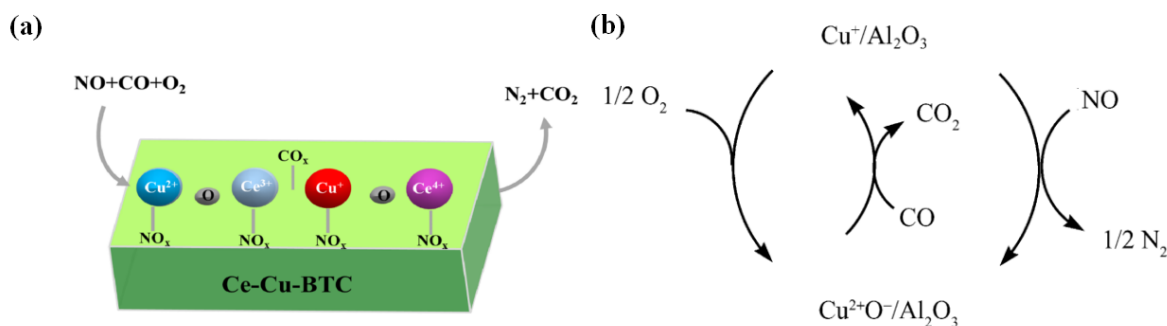


Figure 6. The reaction mechanism of Ce–Cu–BTC (a) and low-loaded CuO/Al_2O_3 (0.5 wt.% Cu) (b) for CO-SCR in the presence of O_2 . Reproduced from [34,37] with permission.

Many researchers [66,67] believe that O_2 is preferentially adsorbed and dissociated at the active site, which hinders the further adsorption and dissociation of NO, so the catalytic performance of the catalysts decreases with the increase in O_2 concentration. In addition, the increased surface coverage of $O_{(ad)}$ after dissociation increases the contact probability with $CO_{(ad)}$, and directly consumes part of the reductant CO, which is also regarded as an important reason for the decline in NO conversion. Amano et al. [34] found that under O_2 -containing conditions, the reaction mechanism of CuO/Al_2O_3 with different Cu loading is significantly different. When the loading amount of Cu is very small (0.5 wt.%), there is a single electron redox behavior, which is the cycle of Cu^{2+} and Cu^+ . It is considered as the reaction mechanism of NO reduction by CO in the presence of O_2 , as shown in Figure 6b. However, when the loading of Cu reaches 3 wt.%, Cu^{2+} is more easily reduced to metallic Cu^0 ; the latter is more conducive to CO oxidation than NO reduction.

On the other hand, it is also reported that O_2 has a positive effect on CO-SCR because the dissociated $O_{(ad)}$ can combine with the adsorbed NO to form NO_2 , which can further rapidly react with CO to form N_2 and CO_2 . Fukuda et al. [68] found that after introducing O_2 , the catalytic performance of $Cu_2O/\gamma-Al_2O_3$ for the CO+NO reaction was improved. Spassova et al. [53] deem that O_2 is adsorbed to the surface of the catalyst and then cleaved to $O_{(ad)}$, which then reacts with $CO_{(ad)}$ and NO to CO_2 and NO_2 , and finally, NO_2 reacts with CO to produce CO_2 and N_2 . Similarly, Gholami [29] also believes that under O_2 -containing conditions, O_2 is adsorbed on the catalyst surface and then cleaved to $O_{(ad)}$, which reacts with CO to CO_2 , and then NO is adsorbed on the generated oxygen vacancy and decomposed into $N_{(ad)}$ and $O_{(ad)}$. Subsequently, $N_{(ad)}$ reacts with another $N_{(ad)}$ to generate N_2 , and $O_{(ad)}$ reacts with another NO form NO_2 . Finally, NO_2 reacts with CO to produce N_2 and CO_2 .

5. Conclusions and Perspectives

In recent years, the selective catalytic reduction of NO with CO as the reductant is one of the research hotspots in the denitrification field. Research on the application of Cu-based catalysts in NO-CO reaction system has increased year by year, mainly focusing on O_2 -free or hypoxic conditions. When the O_2 concentration increases, the NO conversion or N_2 selectivity decreases significantly, and the selective catalytic activity of the catalysts decreases. This stems from the following reasons: (i) O_2 is preferentially adsorbed and dissociated at the active site, which hinders the adsorption and dissociation of NO; (ii) $O_{(ad)}$ reacts with CO, which directly consumes part of the reductant CO; and (iii) $O_{(ad)}$ reacts with NO, resulting in the decrease in N_2 selectivity. Therefore, it is necessary to investigate the relationship between the structural change in crystal defects and the type of oxygen species on the surface of Cu-based catalysts, and the type of NO and CO adsorbed species, so as to deeply understand the reaction process of CO-SCR. The influence of O_2 on the crystal structure of the Cu-based catalysts, the electron transfer of metal elements, as well as the dissociation of N-O bonds and O-O bonds should also be studied to explore the reaction mechanism of CO-SCR, so as to improve the O_2 resistance of the catalysts. Follow-up research can be implemented from the following aspects: (1) some in situ methods can be employed to study the real-time structure–activity relationship of the Cu-based catalysts in the future, because in terms of this reaction, to date, there is a lack of in situ characterization methods to monitor the structural changes of the catalysts in the reaction process; (2) it is imperative to develop green and energy-saving strategies to synthesize the Cu-based catalysts, i.e., ball milling, and mechanical mixing, used for CO-SCR. The currently used preparation methods for the Cu-based catalysts are mainly solution-based strategies, such as wet impregnation, precipitation, and sol-gel. These preparation methods involved complex operations, enormous energy, and are not conducive to industrialization. In short, in view of the superior catalytic performance and low cost of Cu-based catalysts, it is urgent to further study how to simultaneously achieve a suitable antioxidant effect, low-temperature activity, and high SO_2/H_2O tolerance to promote the industrial application of the CO-SCR technology.

Author Contributions: Investigation, X.C.; Data curation, X.C.; Writing-review & editing, X.C. and Y.J.; Visualization, Y.L. (Yaqi Liu); Review, Y.L. (Yan Liu) and M.C.; Resources, D.L. and L.X.; Conceptualization, Y.J. and S.L.; Methodology, Y.J. and S.L.; Supervision, Y.J. and S.L.; Project administration, Y.J. and S.L.; Funding acquisition, Y.J. and K.W. All authors have read and agreed to the published version of the manuscript.

Funding: This research was funded by the Research Foundation for Youth Scholars of Beijing Technology and Business University grant number QNJJ2022-23 from K.W.; the Project for Improving the Research Ability of Postgraduate from Beijing Technology and Business University grant number 19008022056 from X.C.; the Research Foundation for Youth Scholars of Beijing Technology and Business University grant number QNJJ2022-22 from L.X.; the National Natural Science Foundation of China grant number 21978299 from Y.J.; the Research Foundation for Advanced Talents of Beijing Technology and Business University grant number 19008020159 from Y.J.

Data Availability Statement: Data sharing not applicable.

Conflicts of Interest: The authors declare no conflict of interest.

References

- Lu, K.; Guo, S.; Tan, Z.; Wang, H.; Shang, D.; Liu, Y.; Li, X.; Wu, Z.; Hu, M.; Zhang, Y. Exploring Atmospheric Free-Radical Chemistry in China: The Self-Cleansing Capacity and the Formation of Secondary Air Pollution. *Natl. Sci. Rev.* **2019**, *6*, 579–594. [CrossRef] [PubMed]
- Wang, C.; Wang, W.; Sardans, J.; An, W.; Zeng, C.; Abid, A.A.; Peñuelas, J. Effect of Simulated Acid Rain on CO₂, CH₄ and N₂O Fluxes and Rice Productivity in a Subtropical Chinese Paddy Field. *Environ. Pollut.* **2018**, *243*, 1196–1205. [CrossRef] [PubMed]
- Granger, P.; Parvulescu, V.I. Catalytic NO_x Abatement Systems for Mobile Sources: From Three-Way to Lean Burn after-Treatment Technologies. *Chem. Rev.* **2011**, *111*, 3155–3207. [CrossRef] [PubMed]
- Asakura, H.; Hosokawa, S.; Ina, T.; Kato, K.; Nitta, K.; Uera, K.; Uruga, T.; Miura, H.; Shishido, T.; Ohyama, J.; et al. Dynamic Behavior of Rh Species in Rh/Al₂O₃ Model Catalyst During Three-Way Catalytic Reaction: An Operando X-Ray Absorption Spectroscopy Study. *J. Am. Chem. Soc.* **2018**, *140*, 176–184. [CrossRef] [PubMed]
- Jaegers, N.R.; Lai, J.-K.; He, Y.; Walter, E.; Dixon, D.A.; Vasiliu, M.; Chen, Y.; Wang, C.; Hu, M.Y.; Mueller, K.T.; et al. Mechanism by Which Tungsten Oxide Promotes the Activity of Supported V₂O₅/TiO₂ Catalysts for NO_x Abatement: Structural Effects Revealed by ⁵¹V MAS NMR Spectroscopy. *Angew. Chem. Int. Edit.* **2019**, *58*, 12609–12616. [CrossRef]
- Wang, L.; Cheng, X.; Wang, Z.; Ma, C.; Qin, Y. Investigation on Fe-Co Binary Metal Oxides Supported on Activated Semi-Coke for NO Reduction by CO. *Appl. Catal. B Environ.* **2017**, *201*, 636–651. [CrossRef]
- Cheng, X.; Bi, X.T. Reaction Kinetics of Selective Catalytic Reduction of NO_x by Propylene over Fe/ZSM-5. *Chem. Eng. J.* **2012**, *211–212*, 453–462. [CrossRef]
- Yang, T.T.; Bi, H.T.; Cheng, X. Effects of O₂, CO₂ and H₂O on NO_x Adsorption and Selective Catalytic Reduction over Fe/ZSM-5. *Appl. Catal. B Environ.* **2011**, *102*, 163–171. [CrossRef]
- Souza, M.S.; Araújo, R.S.; Oliveira, A.C. Optimizing Reaction Conditions and Experimental Studies of Selective Catalytic Reduction of NO by CO over Supported SBA-15 Catalyst. *Environ. Sci. Pollut. Res.* **2020**, *27*, 30649–30660. [CrossRef]
- Xu, Z.; Li, Y.; Lin, Y.; Zhu, T. A Review of the Catalysts Used in the Reduction of NO by CO for Gas Purification. *Environ. Sci. Pollut. Res.* **2020**, *27*, 6723–6748. [CrossRef]
- Fernández, E.; Liu, L.; Boronat, M.; Arenal, R.; Concepcion, P.; Corma, A. Low-Temperature Catalytic NO Reduction with CO by Subnanometric Pt Clusters. *ACS Catal.* **2019**, *9*, 11530–11541. [CrossRef]
- Xing, F.; Jeon, J.; Toyao, T.; Shimizu, K.-i.; Furukawa, S. A Cu-Pd Single-Atom Alloy Catalyst for Highly Efficient NO Reduction. *Chem. Sci.* **2019**, *10*, 8292–8298. [CrossRef]
- Yoshinari, T.; Sato, K.; Haneda, M.; Kintaichi, Y.; Hamada, H. Positive Effect of Coexisting SO₂ on the Activity of Supported Iridium Catalysts for NO Reduction in the Presence of Oxygen. *Appl. Catal. B Environ.* **2003**, *41*, 157–169. [CrossRef]
- Jiang, R.; Liu, S.; Li, L.; Ji, Y.; Li, H.; Guo, X.; Jia, L.; Zhong, Z.; Su, F. Single Ir Atoms Anchored on Ordered Mesoporous WO₃ are Highly Efficient for the Selective Catalytic Reduction of NO with CO under Oxygen-Rich Conditions. *ChemCatChem* **2021**, *13*, 1834–1846. [CrossRef]
- Wang, X.; Li, X.; Mu, J.; Fan, S.; Chen, X.; Wang, L.; Yin, Z.; Tadé, M.; Liu, S. Oxygen Vacancy-Rich Porous Co₃O₄ Nanosheets toward Boosted NO Reduction by CO and CO Oxidation: Insights into the Structure-Activity Relationship and Performance Enhancement Mechanism. *ACS Appl. Mater. Interfaces* **2019**, *11*, 41988–41999. [CrossRef]
- Lv, Y.; Liu, L.; Zhang, H.; Yao, X.; Gao, F.; Yao, K.; Dong, L.; Chen, Y. Investigation of Surface Synergetic Oxygen Vacancy in CuO-CoO Binary Metal Oxides Supported on γ -Al₂O₃ for NO Removal by CO. *J. Colloid Interface Sci.* **2013**, *390*, 158–169. [CrossRef]
- Takagi, N.; Ishimura, K.; Miura, H.; Shishido, T.; Fukuda, R.; Ehara, M.; Sakaki, S. Catalysis of Cu Cluster for NO Reduction by CO: Theoretical Insight into the Reaction Mechanism. *ACS Omega* **2019**, *4*, 2596–2609. [CrossRef]
- Wang, L.; Cheng, X.; Wang, Z.; Sun, R.; Zhao, G.; Feng, T.; Ma, C. Reaction of NO + CO over Ce-Modified Cu-FeO_x Catalysts at Low Temperature. *Energy Fuels* **2019**, *33*, 11688–11704. [CrossRef]
- Li, J.; Wang, S.; Zhou, L.; Luo, G.; Wei, F. NO Reduction by CO over a Fe-Based Catalyst in FCC Regenerator Conditions. *Chem. Eng. J.* **2014**, *255*, 126–133. [CrossRef]
- Simonot, L.; Garin, F.; Maire, G. A Comparative Study of LaCoO₃, Co₃O₄ and a Mix of LaCoO₃-Co₃O₄: II. Catalytic Properties for the CO + NO Reaction. *Appl. Catal. B Environ.* **1997**, *11*, 181–191. [CrossRef]
- Cheng, X.; Zhang, X.; Su, D.; Wang, Z.; Chang, J.; Ma, C. NO Reduction by CO over Copper Catalyst Supported on Mixed CeO₂ and Fe₂O₃: Catalyst Design and Activity Test. *Appl. Catal. B Environ.* **2018**, *239*, 485–501. [CrossRef]
- Zhang, X.; Cheng, X.; Ma, C.; Wang, Z. Effects of the Fe/Ce Ratio on the Activity of CuO/CeO₂-Fe₂O₃ Catalysts for NO Reduction by CO. *Catal. Sci. Technol.* **2018**, *8*, 3336–3345. [CrossRef]
- Zhang, X.; Cheng, X.; Ma, C.; Wang, X.; Wang, Z. Effect of a ZrO₂ Support on Cu/Fe₂O₃-CeO₂/ZrO₂ Catalysts for NO Removal by CO Using a Rotary Reactor. *Catal. Sci. Technol.* **2018**, *8*, 5623–5631. [CrossRef]
- Shi, Q.; Wang, Y.; Guo, S.; Han, Z.-K.; Ta, N.; Li, G.; Baiker, A. NO Reduction with CO over CuO_x/CeO₂ Nanocomposites: Influence of Oxygen Vacancies and Lattice Strain. *Catal. Sci. Technol.* **2021**, *11*, 6543–6552. [CrossRef]

25. Wang, Y.; Jiang, Q.; Xu, L.; Han, Z.-K.; Guo, S.; Li, G.; Baiker, A. Effect of the Configuration of Copper Oxide-Ceria Catalysts in NO Reduction with CO: Superior Performance of a Copper-Ceria Solid Solution. *ACS Appl. Mater. Interfaces* **2021**, *13*, 61078–61087. [CrossRef] [PubMed]
26. Sierra-Pereira, C.A.; Urquieta-González, E.A. Reduction of NO with CO on CuO or Fe₂O₃ Catalysts Supported on TiO₂ in the Presence of O₂, SO₂ and Water Steam. *Fuel* **2014**, *118*, 137–147. [CrossRef]
27. Du, Y.; Gao, F.; Zhou, Y.; Yi, H.; Tang, X.; Qi, Z. Recent Advance of CuO-CeO₂ Catalysts for Catalytic Elimination of CO and NO. *J. Environ. Chem. Eng.* **2021**, *9*, 106372. [CrossRef]
28. Wang, J.; Gao, F.; Dang, P.; Tang, X.; Lu, M.; Du, Y.; Zhou, Y.; Yi, H.; Duan, E. Recent Advances in NO Reduction with CO over Copper-Based Catalysts: Reaction Mechanisms, Optimization Strategies, and Anti-Inactivation Measures. *Chem. Eng. J.* **2022**, *450*, 137374. [CrossRef]
29. Gholami, Z.; Luo, G.; Gholami, F.; Yang, F. Recent Advances in Selective Catalytic Reduction of NO_x by Carbon Monoxide for Flue Gas Cleaning Process: A Review. *Catal. Rev.* **2021**, *63*, 68–119. [CrossRef]
30. Yamamoto, T.; Tanaka, T.; Kuma, R.; Suzuki, S.; Amano, F.; Shimooka, Y.; Kohno, Y.; Funabiki, T.; Yoshida, S. NO Reduction with CO in the Presence of O₂ over Al₂O₃-Supported and Cu-Based Catalysts. *Phys. Chem. Chem. Phys.* **2002**, *4*, 2449–2458. [CrossRef]
31. Kacimi, M.; Ziyad, M.; Liotta, L.F. Cu on Amorphous AlPO₄: Preparation, Characterization and Catalytic Activity in NO Reduction by CO in Presence of Oxygen. *Catal. Today* **2015**, *241*, 151–158. [CrossRef]
32. Venegas, F.; López, N.; Sánchez-Calderón, L.; Aguila, G.; Araya, P.; Guo, X.; Zhu, Y.; Guerrero, S. The Transient Reduction of NO with CO and Naphthalene in the Presence of Oxygen Using a Core-Shell SmCeO₂@TiO₂-Supported Copper Catalyst. *Catal. Sci. Technol.* **2019**, *9*, 3408–3415. [CrossRef]
33. Bai, Y.; Bian, X.; Wu, W. Catalytic Properties of CuO/CeO₂-Al₂O₃ Catalysts for Low Concentration NO Reduction with CO. *Appl. Surf. Sci.* **2019**, *463*, 435–444. [CrossRef]
34. Amano, F.; Suzuki, S.; Yamamoto, T.; Tanaka, T. One-Electron Reducibility of Isolated Copper Oxide on Alumina for Selective NO-CO Reaction. *Appl. Catal. B Environ.* **2006**, *64*, 282–289. [CrossRef]
35. Wen, B.; He, M.; Schrum, E.; Li, C. NO Reduction and CO Oxidation over Cu/Ce/Mg/Al Mixed Oxide Catalyst in FCC Operation. *J. Mol. Catal. A Chem.* **2002**, *180*, 187–192. [CrossRef]
36. Li, L.; Liu, S.; Jiang, R.; Ji, Y.; Li, H.; Guo, X.; Jia, L.; Zhong, Z.; Su, F. Subnanometric Pt on Cu Nanoparticles Confined in Y-Zeolite: Highly-Efficient Catalysts for Selective Catalytic Reduction of NO_x by CO. *ChemCatChem* **2021**, *13*, 1568–1577. [CrossRef]
37. Zhang, Y.; Zhao, L.; Duan, J.; Bi, S. Insights into DeNO_x Processing over Ce-Modified Cu-BTC Catalysts for the CO-SCR Reaction at Low Temperature by in Situ DRIFTS. *Sep. Purif. Technol.* **2020**, *234*, 116081. [CrossRef]
38. Teng, Z.; Huang, S.; Fu, L.; Xu, H.; Li, N.; Zhou, Q. Study of a Catalyst Supported on Rice Husk Ash for NO Reduction with Carbon Monoxide. *Catal. Sci. Technol.* **2020**, *10*, 1431–1443. [CrossRef]
39. Gholami, Z.; Luo, G.; Gholami, F. The Influence of Support Composition on the Activity of Cu:Ce Catalysts for Selective Catalytic Reduction of NO by CO in the Presence of Excess Oxygen. *New J. Chem.* **2020**, *44*, 709–718. [CrossRef]
40. Gholami, Z.; Luo, G. Low-Temperature Selective Catalytic Reduction of NO by CO in the Presence of O₂ over Cu:Ce Catalysts Supported by Multiwalled Carbon Nanotubes. *Ind. Eng. Chem. Res.* **2018**, *57*, 8871–8883. [CrossRef]
41. López, N.; Aguila, G.; Araya, P.; Guerrero, S. Highly Active Copper-Based Ce@TiO₂ Core-Shell Catalysts for the Selective Reduction of Nitric Oxide with Carbon Monoxide in the Presence of Oxygen. *Catal. Commun.* **2018**, *104*, 17–21. [CrossRef]
42. Liu, K.; Yu, Q.; Qin, Q.; Wang, C. Selective Catalytic Reduction of Nitric Oxide with Carbon Monoxide over Alumina-Pellet-Supported Catalysts in the Presence of Excess Oxygen. *Environ. Technol.* **2018**, *39*, 1878–1885. [CrossRef] [PubMed]
43. Chen, X.; Zhang, J.; Huang, Y.; Tong, Z.; Huang, M. Catalytic Reduction of Nitric Oxide with Carbon Monoxide on Copper-Cobalt Oxides Supported on Nano-Titanium Dioxide. *J. Environ. Sci.* **2009**, *21*, 1296–1301. [CrossRef]
44. Liu, Z.; Yu, F.; Pan, K.; Zhou, X.; Sun, R.; Tian, J.; Wan, Y.; Dan, J.; Dai, B. Two-Dimensional Vermiculite Carried CuCoCe Catalysts for CO-SCR in the Presence of O₂ and H₂O: Experimental and DFT Calculation. *Chem. Eng. J.* **2021**, *422*, 130099. [CrossRef]
45. Wang, D.; Huang, B.; Shi, Z.; Long, H.; Li, L.; Yang, Z.; Dai, M. Influence of Cerium Doping on Cu-Ni/Activated Carbon Low-Temperature CO-SCR Denitration Catalysts. *RSC Adv.* **2021**, *11*, 18458–18467. [CrossRef]
46. Pan, K.L.; Young, C.W.; Pan, G.T.; Chang, M.B. Catalytic Reduction of NO by CO with Cu-Based and Mn-Based Catalysts. *Catal. Today* **2020**, *348*, 15–25. [CrossRef]
47. Rebenstorf, B.; Lindblad, T.; Andersson, S.L.T. Amorphous AlPO₄ as Catalyst Support 2. Characterization of Amorphous Aluminum Phosphates. *J. Catal.* **1991**, *128*, 293–302. [CrossRef]
48. Li, G.; Tang, Z. Noble Metal Nanoparticle@Metal Oxide Core/Yolk-Shell Nanostructures as Catalysts: Recent Progress and Perspective. *Nanoscale* **2014**, *6*, 3995–4011. [CrossRef]
49. Kaur, R.; Kaur, A.; Umar, A.; Anderson, W.A.; Kansal, S.K. Metal Organic Framework (MOF) Porous Octahedral Nanocrystals of Cu-BTC: Synthesis, Properties and Enhanced Adsorption Properties. *Mater. Res. Bull.* **2019**, *109*, 124–133. [CrossRef]
50. Wang, B.; Xie, L.-H.; Wang, X.; Liu, X.-M.; Li, J.; Li, J.-R. Applications of Metal-Organic Frameworks for Green Energy and Environment: New Advances in Adsorptive Gas Separation, Storage and Removal. *Green Energy Environ.* **2018**, *3*, 191–228. [CrossRef]
51. Mehandjiev, D.; Panayotov, D.; Khristova, M. Catalytic Reduction of NO with CO over Cu_xCo_{3-x}O₄ Spinel. *React. Kinet. Catal. Lett.* **1987**, *33*, 273–277. [CrossRef]
52. Panayotov, D.; Khristova, M.; Mehandjiev, D. Application of the Transient Response Technique to the Study of CO + NO + O₂ Interaction on Cu_xCo_{3-x}O₄ Catalysts. *J. Catal.* **1995**, *156*, 219–228. [CrossRef]

53. Spassova, I.; Khristova, M.; Panayotov, D.; Mehandjiev, D. Coprecipitated CuO-MnO_x Catalysts for Low-Temperature CO-NO and CO-NO-O₂ Reactions. *J. Catal.* **1999**, *185*, 43–57. [CrossRef]
54. Sun, R.; Yu, F.; Wan, Y.; Pan, K.; Li, W.; Zhao, H.; Dan, J.; Dai, B. Reducing N₂O Formation over CO-SCR Systems with CuCe Mixed Metal Oxides. *ChemCatChem* **2021**, *13*, 2709–2718. [CrossRef]
55. Wen, B.; He, M. Study of the Cu-Ce Synergism for NO Reduction with CO in the Presence of O₂, H₂O and SO₂ in FCC Operation. *Appl. Catal. B Environ.* **2002**, *37*, 75–82. [CrossRef]
56. Gao, F.; Wang, Y.; Goodman, D.W. CO/NO and CO/NO/O₂ Reactions over a Au-Pd Single Crystal Catalyst. *J. Catal.* **2009**, *268*, 115–121. [CrossRef]
57. Hu, Q.; Cao, K.; Lang, Y.; Chen, R.; Chu, S.; Jia, L.; Yue, J.; Shan, B. Improved NO-CO Reactivity of Highly Dispersed Pt Particles on CeO₂ Nanorod Catalysts Prepared by Atomic Layer Deposition. *Catal. Sci. Technol.* **2019**, *9*, 2664–2672. [CrossRef]
58. Song, Y.-J.; Jesús, Y.M.L.-D.; Fanson, P.T.; Williams, C.T. Kinetic Evaluation of Direct NO Decomposition and NO-CO Reaction over Dendrimer-Derived Bimetallic Ir-Au/Al₂O₃ Catalysts. *Appl. Catal. B Environ.* **2014**, *154–155*, 62–72. [CrossRef]
59. Liu, N.; Chen, X.; Zhang, J.; Schwank, J.W. Drifts Study of Photo-Assisted Catalytic CO + NO Redox Reaction over CuO/CeO₂-TiO₂. *Catal. Today* **2015**, *258*, 139–147. [CrossRef]
60. Yao, X.; Xiong, Y.; Sun, J.; Gao, F.; Deng, Y.; Tang, C.; Dong, L. Influence of MnO₂ Modification Methods on the Catalytic Performance of CuO/CeO₂ for NO Reduction by CO. *J. Rare Earths* **2014**, *32*, 131–138. [CrossRef]
61. Wang, L.; Wang, Z.; Cheng, X.; Zhang, M.; Qin, Y.; Ma, C. In Situ DRIFTS Study of the NO + CO Reaction on Fe-Co Binary Metal Oxides over Activated Semi-Coke Supports. *RSC Adv.* **2017**, *7*, 7695–7710. [CrossRef]
62. Ma, K.; Guo, K.; Li, L.; Zou, W.; Tang, C.; Dong, L. Cavity Size Dependent SO₂ Resistance for NH₃-SCR of Hollow Structured CeO₂-TiO₂ Catalysts. *Catal. Commun.* **2019**, *128*, 105719. [CrossRef]
63. Liu, K.; Yu, Q.; Liu, J.; Wang, K.; Han, Z.; Xuan, Y.; Qin, Q. Selection of Catalytically Active Elements for Removing NO and CO from Flue Gas at Low Temperatures. *New J. Chem.* **2017**, *41*, 13993–13999. [CrossRef]
64. Harris, J.; Kasemo, B. On Precursor Mechanisms for Surface Reactions. *Surf. Sci.* **1981**, *105*, L281–L287. [CrossRef]
65. Baxter, R.J.; Hu, P. Insight into Why the Langmuir-Hinshelwood Mechanism Is Generally Preferred. *J. Chem. Phys.* **2002**, *116*, 4379–4381. [CrossRef]
66. Wang, A.; Ma, L.; Cong, Y.; Zhang, T.; Liang, D. Unique Properties of Ir/ZSM-5 Catalyst for NO Reduction with CO in the Presence of Excess Oxygen. *Appl. Catal. B Environ.* **2003**, *40*, 319–329. [CrossRef]
67. Zhu, R.; Guo, M.; He, J. NO Reactions over Ir-Based Catalysts under Oxygen-Rich Conditions. *Fuel Process. Technol.* **2013**, *108*, 63–68. [CrossRef]
68. Fukuda, R.; Sakai, S.; Takagi, N.; Matsui, M.; Ehara, M.; Hosokawa, S.; Tanaka, T.; Sakaki, S. Mechanism of NO-CO Reaction over Highly Dispersed Cuprous Oxide on γ -Alumina Catalyst Using a Metal-Support Interfacial Site in the Presence of Oxygen: Similarities to and Differences from Biological Systems. *Catal. Sci. Technol.* **2018**, *8*, 3833–3845. [CrossRef]

MDPI
St. Alban-Anlage 66
4052 Basel
Switzerland
www.mdpi.com

Catalysts Editorial Office
E-mail: catalysts@mdpi.com
www.mdpi.com/journal/catalysts



Disclaimer/Publisher's Note: The statements, opinions and data contained in all publications are solely those of the individual author(s) and contributor(s) and not of MDPI and/or the editor(s). MDPI and/or the editor(s) disclaim responsibility for any injury to people or property resulting from any ideas, methods, instructions or products referred to in the content.



Academic Open
Access Publishing

mdpi.com

ISBN 978-3-0365-9042-4